D. Lee R. H. Pletcher

Application of Viscous-Inviscid Interaction Methods to Transonic Turbulent Flows

November 1986

Submitted to:
National Aeronautics and Space Administration
Ames Research Center
Moffett Field, California
NASA Grant No. NAG-2-152

HTL-42, CFD-16
ISU-ERI-Ames-87055

final report

College of Engineering
Iowa State University

Any opinions, findings, and conclusions or recommendations expressed in this publication are those of the authors and do not necessarily reflect the views of the National Aeronautics and Space Administration.

HTL-42, CFD-16
Project 1568
ISU-ERI-Ames-87055

D. Lee R. H. Pletcher

Application of Viscous-Inviscid Interaction Methods to Transonic Turbulent Flows

Final Report

11/1/81 - 11/30/86
R. H. Pletcher, Principal Investigator

Supported by the National Aeronautics and Space Administration, NASA Grant No. NAG-2-152

Heat Transfer Laboratory
Department of Mechanical Engineering
Computational Fluid Dynamics Center

engineering research institute
iowa state university

TABLE OF CONTENTS

LIST OF FIGURES

LIST OF TABLES

ABSTRACT

Two different viscous-inviscid interaction schemes have been developed for the analysis of steady, turbulent, transonic, separated flows over axisymmetric bodies. The viscous and inviscid solutions are coupled through the displacement concept using a transpiration velocity approach. In the semi-inverse interaction scheme, the viscous and inviscid equations are solved in an explicitly separate manner and the displacement thickness distribution is iteratively updated by a simple coupling algorithm. In the simultaneous interaction method, local solutions of viscous and inviscid equations are treated simultaneously, and the displacement thickness is treated as an unknown and is obtained as a part of the solution through a global iteration procedure.

The inviscid flow region is described by a direct finite-difference solution of a velocity potential equation in conservative form. The potential equation is solved on a numerically generated mesh by an approximate factorization (AF2) scheme in the semi-inverse interaction method and by a successive line overrelaxation (SLOR) scheme in the simultaneous interaction method.

The boundary-layer equations are used for the viscous flow region. The continuity and momentum equations are solved inversely in a coupled manner using a fully implicit finite-difference scheme. The energy equation is solved uncoupled. The FLARE approximation is used in the reversed flow region and its effectiveness is studied by using a windward differencing scheme.

The two-layer algebraic turbulence model proposed by Cebeci and Smith (1974) and a new one-half equation turbulence model proposed by Johnson and King (1985) are utilized to describe the Reynolds stress in turbulent flow calculations. Parameters affecting the convergence rate of the interaction procedure are discussed. The calculation schemes are evaluated by studying 1) an incompressible, laminar, separated flow over a flat plate with a trough, 2) a turbulent, transonic, separated flow over an axisymmetric boattail with a solid cylindrical plume simulator, 3) a turbulent, transonic, separated flow over an axisymmetric bump attached to a circular cylinder. The predictions are compared with experimental data and other available numerical results. The simultaneous interaction method becomes more efficient and reliable than the semi-inverse method as the separation size grows. The prediction obtained by the Johnson-King model is generally in good agreement with the measurements, but disagreement is noticeable after the reattachment point.

NOMENCLATURE

a	speed of sound
a_1	constant in turbulence model, Equation (2.68)
a^*	critical speed of sound
A	metric quantity of coordinate transformation, Equation (3.35)
A_j, a_j	coefficients appearing in the finite-difference expressions
A_1, A_2, A_3	metric quantities of coordinate transformation, Equation (3.27)
A2,A4,A5	metric quantities of coordinate transformation, Equations (13.1), (13.2) and (13.5)
A^+	Van Driest damping parameter
$[A]_j$	2×2 coefficient matrix, Equations (2.129) and (2.130)
AX_j, AY_j	coefficients appearing in the finite-difference expressions
b	exponent, Equation (4.1)
B	metric quantity of coordinate transformation, Equation (3.35)
B_j, b_j	coefficients appearing in the finite-difference expressions
$[B]_j$	2×2 coefficient matrix, Equations (2.129) and (2.130)
BX_j, BY_j	coefficients appearing in the finite-difference expressions
$c_{f\infty}$	skin-friction coefficient based on free stream dynamic pressure
c_p	specific heat at constant pressure
c_v	specific heat at constant volume
C	FLARE constant
C	metric quantity of coordinate transformation, Equation (3.33)
C	chord length
C_{dif}	constant in turbulence model, Equation (2.73)

C_E	Eckert type parameter, Equation (2.98)
$C_{i,j}$	correction array
C_j, c_j	coefficients appearing in the finite-difference expressions
C_M	coefficient defined in Equation (4.7)
C_ℓ	Chapman-Rubesin type parameter, Equation (2.98)
C_p	pressure coefficient
C_1, C_2	empirical constants, Equation (2.11)
$[C]_j$	2×1 matrix, Equations (2.129) and (2.130)
CX_j, CY_j	coefficients appearing in the finite-difference expressions
d_m	maximum boattail diameter
D	Van Driest damping function
D_j, d_j	coefficients appearing in the finite-difference expressions
D_m	diffusion term of the turbulent kinetic energy
$[D]_j$	2×2 coefficient matrix, Equations (2.129) and (2.130)
DX_j, DY_j	coefficients appearing in the finite-difference expressions
E_j, e_j	coefficients appearing in the finite-difference expressions
E^{+1}, E^{-1}	shift operators, Equation (3.80)
f	body force
$f_{i,j}$	intermediate correction array
f_1, f_2, f_3	empirical functions in turbulent flow
F	dimensionless x component velocity, U/U_e
g	function used in coordinate transformation, Equation (2.92)
$g_{i,j}$	intermediate correction array
G	dimensionless total enthalpy, I/I_e
h	enthalpy

H	total enthalpy
H_j, h_j	coefficients appearing in the finite-difference expressions
I	dimensionless total enthalpy, H/u_∞^2
I_ρ	parameter, Equation (2.137)
J	Jacobian of coordinate transformation, Equation (3.27)
k	thermal conductivity, Equation (2.12)
k	turbulent kinetic energy, Equation (2.65)
K	$\Delta\eta_+/\Delta\eta_-$
ℓ	mixing length
L	dissipation length scale, Equation (2.68)
L	complete differential operator, Equation (3.39)
L_e	length of the computational domain in the x-coordinate
m	displacement thickness parameter, Equation (2.104)
m_t	shear-layer coordinate parameter, Equation (3.15)
m^*	effective displacement thickness parameter, $m-m_t$
M	Mach number
M_τ	Mach number parameter, Equation (2.39)
M^*	dimensionless Mach number, Equation (4.6)
N	pressure gradient parameter, Equation (2.51)
N	linear differential operator, Equation (3.39)
N_j	dimensionless diffusion term, Equation (2.111)
$N_{1,j}, N_{2,j}$	dimensionless diffusion terms, Equation (2.121)
N_3, N_4	coefficients appearing in the finite-difference expressions
p	pressure
p_j, p_{1j}	coefficients appearing in the finite-difference expressions

p^+	dimensionless pressure gradient parameter, Equation (2.39)
P	dimensionless pressure
Pr	Prandtl number
Pr_t	turbulent Prandtl number
q	magnitude of the velocity
q	heat flux
Q_1, Q_2	coefficients appearing in the finite-difference expressions
r	radius
r_e	radius of the outer boundary, Figure 6
r_o	radius of the body surface
R	gas constant, Equation (2.9)
R	dimensionless radius
Re	Reynolds number
$Re_{\theta k}$	Reynolds number based on the kinetic momentum thickness, Equation (2.57)
R_i, R_j, R_ℓ	metric quantities of coordinate transformation, Equations (3.79) and (4.9)
R_{max}	maximum residual
s	arc length
S	entropy
S_j, s_j	coefficients appearing in the finite-difference expressions
t	time
t	normal distance from the shear-layer coordinate to the body surface
t_a	depth of a trough, Equation (5.1)
T	temperature
T_o	stagnation temperature

u	x component velocity
u_i, u_j, u_k	velocity components in a Cartesian system
u_τ	friction velocity, Equation (2.37)
u^+	dimensionless velocity, Equation (2.37)
U	dimensionless x component velocity in Chapter II, u/u_∞
U	contravariant ξ component velocity in Chapter III
$[U]_j$	2×1 unknown matrix, Equations (2.129) and (2.130)
v	y component velocity
v_o	transpiration velocity, Equation (3.12)
v_t	characteristic turbulent velocity
V	dimensionless y component velocity in Chapter II, $vRe_\infty^{\frac{1}{2}}/u_\infty$
V	contravariant η component velocity in Chapter III
V	velocity vector
W	dimensionless velocity, Equation (2.100)
x	coordinate in streamwise direction
x_e	outflow boundary position in x coordinate, Figure 6
x_i, x_j, x_k	Cartesian coordinates
x_o	inflow boundary position in x coordinate, Figure 6
X	dimensionless x coordinate
y	coordinate in normal direction
y^+	dimensionless y coordinate, Equation (2.37)
Y	dimensionless y coordinate
z	parameter defined in Equation (2.56)

Greek symbols

α	turbulence model parameter, Equation (2.54)

α	acceleration parameter, Equation (3.40)
α_H, α_L	upper and lower limits of α sequence
$\alpha_1, \alpha_2, \alpha_3$	parameters in coordinate transformation
β	pressure gradient parameter, Equation (2.98)
β_c	heat transfer parameter, Equation (2.39)
γ	ratio of specific heat
γ_i	Klebanoff's intermittency function
δ	boundary-layer thickness
δ	central-difference operator
δ_{ij}	Kronecker delta function
δ^*	displacement thickness, Equation (2.32)
δ_k^*	kinematic displacement thickness, Equation (2.53)
δ	forward-difference operator
δ	backward-difference operator
δ_ϕ	change in ϕ between two iterations
Δr	$r_{i+\frac{1}{2}} - r_{j-\frac{1}{2}}$
Δx	$x_i - x_{i-1}$
$\Delta\eta_+$	$\eta_{j+1} - \eta_j$
$\Delta\eta_-$	$\eta_j - \eta_{j-1}$
$\Delta\xi_+$	$\xi_{i+1} - \xi_i$
$\Delta\xi_-$	$\xi_i - \xi_{i-1}$
η	transformed coordinate
ε	convergence criterion for global iteration procedure
ε_c	convergence criterion for general iteration procedure
ε_d	rate of dissipation of turbulent kinetic energy, Equation (2.66)

θ	inverse of square root of $-u'v'$
θ_k	kinetic momentum thickness, Equation (2.58)
κ	von Karman constant, Equation (2.46)
λ	parameter for time-dissipation term
λ_1, λ_2	coefficients appearing in the finite-difference expressions
μ	molecular viscosity
μ_t	turbulent viscosity
μ	dimensionless viscosity
μ_t	dimensionless turbulent viscosity
ξ	transformed coordinate
π	parameter defined in Equation (2.55)
Π	stress tensor
ρ	density
ρ_o	stagnation density
ρ, ρ	retarded density
ρ	dimensionless density
σ	turbulence modeling parameter, Equation (2.63)
τ	shear stress
τ	viscous stress tensor
ν	kinematic viscosity
ϕ	velocity potential
ψ	stream function
ω	relaxation parameter

Subscripts

e	edge of the boundary layer

eq	equilibrium conditions
i	inner part of boundary layer
i	x or ξ-index
I	viscous flow
j	y or η-index
m	value of quantity where -u'v' is a maximum
n	normal component
new	new converged value
o	outer part of boundary layer
old	old value obtained at previous iteration
opt	optimum value
w	wall
∞	free stream conditions

Superscripts

k	sequence level
n	iteration level
*	designates a modified coefficient
$( )'$	fluctuation in turbulent flow, mass-averaged variable, Equation (2.15)
$( )''$	fluctuation in turbulent flow, time-averaged variable, Equation (2.13)
$\bar{( )}$	time-averaged value, Equation (2.14)
$\tilde{( )}$	mass-averaged value, Equation (2.16)
$\bar{( )}$	dimensionless quantity in Chapter III
$\hat{( )}$	quantity transformed by Prandtl transposition theorem
$\hat{( )}$	provisional variable used in Newton linearization

I. INTRODUCTION

A. Overview of the Problem

Encouraging progress has been made in recent years in the prediction of complex flow fields. However, much more work needs to be done to develop and verify reliable predictive schemes in several areas of application. One of the difficult problems in present day aerodynamics is the accurate prediction of complex turbulent flows occurring in the transonic speed regime. Transonic flows occur in many important aerodynamic applications of current technological interest including flows over airfoil and engine components. This is largely because many modern commercial and military aircraft cruise very efficiently at transonic speeds.

While transonic flow fields contain a variety of interesting and unique characteristics, they are especially characterized by the two main complicating features of mixed subsonic/supersonic flow and substantial viscous effects. In a typical transonic flow, a subsonic freestream is accelerated over a convex body surface to form an embedded region of supersonic flow adjacent to the body surface. This supersonic region is generally terminated by a shock wave that recompresses the flow as the flow returns to the subsonic speed. The strength and extent of the shock wave increase with freestream Mach number. From a mathematical point of view, the transonic flow must be described by a nonlinear equation or set of equations of mixed elliptic/hyperbolic type, because a subsonic flow region is described by an elliptic

equation and supersonic region is described by a hyperbolic equation. The boundaries between the elliptic and hyperbolic regions must be obtained as a part of the solution.

Viscous effects are also important in the transonic flow. The interaction between a viscous (or boundary) layer and a shock wave is a very complicated phenomenon. The principal interaction between the shock wave and the boundary layer arises from the displacement thickness effect which leads to a thickened effective body causing significant changes to the surface pressures and forces. In the inviscid flow region, the pressure increases discontinuously across the shock wave. However, in the inner part of the boundary layer which has subsonic velocity, this abrupt increase of the pressure cannot occur. Instead, the overall pressure rise takes place over several boundary-layer thicknesses. Although the shock wave penetrates the boundary layer and generates a significant normal pressure gradient, it is considerably weakened and finally vanishes as it reaches the sonic line in the lower part of the boundary layer. The flow under the sonic line is retarded by this adverse pressure gradient and boundary layer is substantially thickened.

If the strength of retarding influences is sufficiently strong, the boundary layer separates from the body surface increasing the streamwise spread of the pressure rise. A typical example of the transonic flow with the interaction between the normal shock wave and the boundary layer is schematically illustrated in Figure 1. When the overall pressure rise is sufficient to cause separation, an outgoing weak

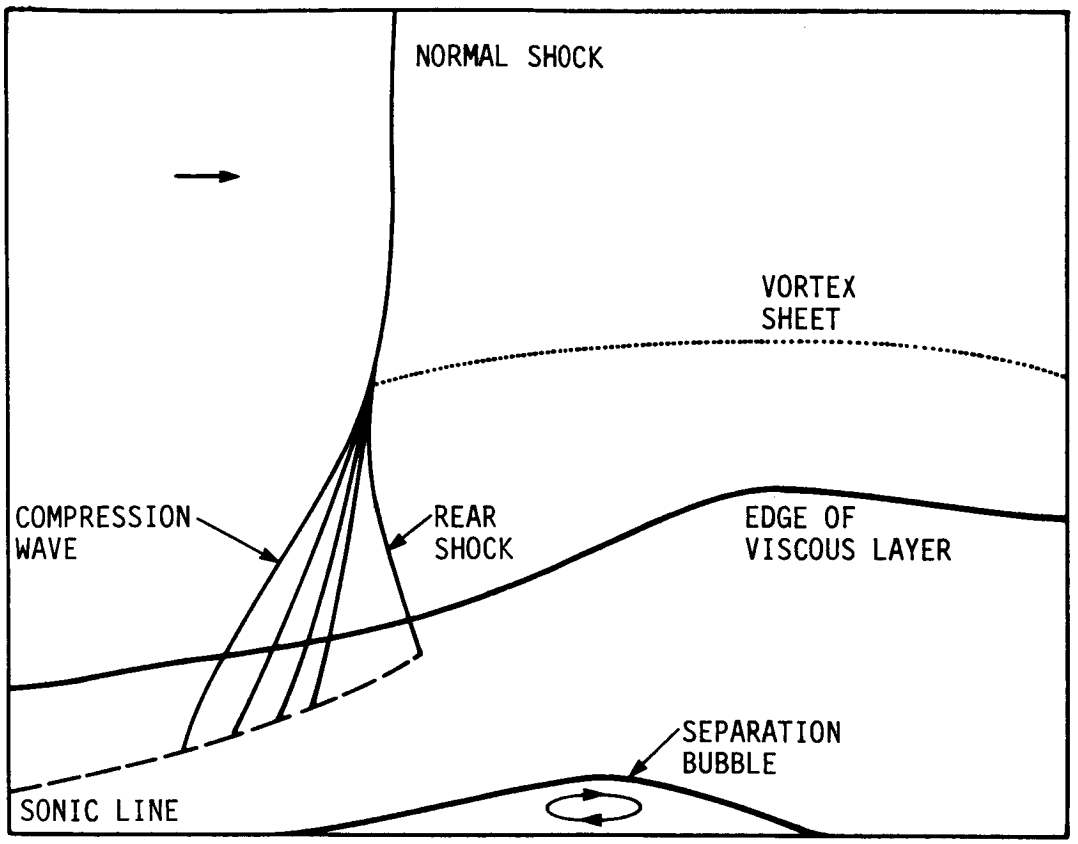

FIGURE 1. Transonic flow field through the interaction

compression wave is generated. Although the compression wave downstream of the separation is barely perceptible, it joins the nearly normal strong shock some distance outside the boundary layer. To achieve continuity of pressure and flow direction downstream of this intersection, an incoming weak oblique shock is generated, and a vortex sheet with a rapid entropy rise across it runs downstream from the intersection. Because of a nonuniform entropy increase across the shock wave, the flow outside the boundary layer immediately downstream of the weak trailing shock is still supersonic, but with further pressure rise as the flow continues downstream the supersonic tongue diminishes and finally vanishes (Green, 1970).

The presence of separation can significantly affect the entire flow field. For example, the existence of separation on an airfoil can change the lift and drag coefficients considerably so as to degrade the control effectiveness of the aircraft. Also, the flow reattachment gives rise to heating rates which can far exceed those for an attached boundary layer. Therefore, the mechanism of the separation and reattachment in transonic flow fields has received a great deal of attention in the aerodynamic design process, though it is still far from being fully understood. Generally, the process of separation is believed to depend only on the properties of the approaching flow stream. However, the flow inside the separation bubble is thought to be subject to both upstream and downstream influences, thus having elliptic characteristics. The size of a separation bubble usually depends on the magnitude of the pressure rise, the nature of the disturbance which

causes it, the Mach number, and the Reynolds number of the initial flow (Green, 1970). However, the size of separation caused by a normal shock wave is so influenced by the interaction with the far field that a correlation of separation size with the main flow parameters is very difficult to obtain. Such an interaction process is complex and our present understanding of this phenomenon is very incomplete.

The complexity of the governing equations that need to be solved to predict transonic flows depends on the flow phenomena in question. If the shock wave is sufficiently weak that the flow does not separate, the viscous effects are often insignificant. In this case, a fairly accurate description of the pressure distribution can be obtained from solving the equations for inviscid flow only, perhaps even the transonic small disturbance (TSD) form of the equations. If the shock wave is strong enough to cause separation, the governing equations must include viscous effects. The optimum (in terms of cost and accuracy) computational strategy for the latter case has not been established. The broad classes of competing methods can be labeled as global or zonal.

In the global approach, no assumptions are necessary about the type or nature of interaction in the flow field. All regions are computed simultaneously with a single set of equations, such as the Navier-Stokes equations. The Navier-Stokes equations are generally regarded as the basic equations describing most flow phenomena of practical aerodynamic interest. The physical phenomena encountered in transonic flows, including mixed subsonic/supersonic flow, shock waves, boundary layer,

separation and turbulence can be mathematically represented by the time-dependent Navier-Stokes equations. The numerical solution of the time-dependent Navier-Stokes equations for practical turbulent flow problems is, however, presently not feasible with existing computers due to the small characteristic length and time scales of the turbulent motion. Thus, some form of averaging of the governing equations and turbulence modeling are required. Current practice, as well as much research in turbulent flows, is based on the use of the time-averaged Navier-Stokes (Reynolds) equations with turbulence modeling. Often, the predictions based on this approach have failed to predict flow details accurately, but shortcomings are frequently attributed to the grid arrangement or the turbulence model.

In the zonal approach, the flow region is divided into subregions which have distinct flow characteristics and each subregion is described by an appropriately reduced set of governing equations. As in many flow situations, the transonic flow field can be divided into the thin shear (boundary) layer near solid boundaries and inviscid flow elsewhere, assuming that the Reynolds number is sufficiently large. Most commonly, the Euler equations or the potential equation have been used for the inviscid flow region and either an integral or finite-difference representation of the boundary-layer equations for the viscous flow region. It is often possible to solve these two sets of equations interactively in a consistent manner using what has become known as the viscous-inviscid interaction approach. Applications of viscous-inviscid interaction schemes based on the above idea to transonic turbulent

separated flows can be found in numerous works. Predictions based on this approach generally compare well with the solutions based on the time-averaged Navier-Stokes equations, but solutions from both approaches often exhibit disagreement with experimental measurements for transonic separated turbulent flows. These discrepancies in solutions based on the viscous-inviscid interaction approach have been attributed to inadequate turbulence modeling or errors associated with the standard boundary-layer approximation which neglects the normal pressure gradient across the boundary layer.

The accuracy and reliability of turbulent flow predictions are very much constrained by the accuracy and generality of the turbulence model used to evaluate the Reynolds stresses and heat flux quantities. To a large extent, turbulence modeling is the pacing item in the quest for improved predictions. Despite considerable research effort, completely satisfactory turbulence models have not been identified for many complex flows, especially those containing regions of flow reversal. The lack of generality is a major shortcoming of turbulence models. Many of the studies for viscous transonic flows have used variants of a simple algebraic turbulence model (Deiwert, 1976; Baldwin and Lomax, 1978; Carter, 1981). Recently, more complex models which solve additional differential equations for turbulence parameters have been used. Surprisingly, complex models that show better overall predictions in many incompressible cases do not provide significant improvement over simple algebraic models for transonic flows with large separation.

A long range goal of computational fluid dynamics is the development of methods which are predictive; that is, methods which can be used with reasonable confidence in the absence of confirming experimental data. To support this goal, the development of turbulence models with reasonable generality could be helpful. Until this has been achieved, the identification of models which work well for particular classes of flows (with their accompanying range of applicability and limitations) would prove useful for design purposes.

The present study deals with both computational and turbulence modeling aspects of predicting transonic flows with strong interaction. An objective of the study was to advance the state of the art in turbulent flow prediction and to enhance present understanding regarding the range of applicability and limitations of computational approaches and turbulence models for flows containing separated regions.

B. Literature Review

The study of transonic aerodynamics has a long history and a considerable amount of research has been done both experimentally and theoretically. The present review is intended to provide an indication of the state of the art of transonic aerodynamics. It is by no means all inclusive. The emphasis was put on works of two-dimensional transonic flows with strong interaction between the shock wave and the boundary layer, which is closely related to the present study. Experimental studies and analytical works are discussed separately for convenience. A detailed historical review of transonic flow research

can be found in an article by Spreiter (1982).

1. Experimental work

Interest in transonic flows was developed as early as the 1900s, but realistic experiments only began in the 1940s because of technical difficulties in obtaining transonic speeds. However, at present, experimental measurements over a variety of flow conditions and body configurations are available. Still, only a limited number of experimental investigations provide extensive, quantitative measurements of flow properties in the boundary layer which are necessary for understanding the mechanism of the interaction between a shock wave and a boundary layer.

Naturally, most of the transonic flow experiments have focused on airfoil-like geometries. Some of the important works are given below. Liepmann (1946) performed an experimental study for the transonic flow past a 12% circular arc airfoil to examine the effect of the boundary layer upon the shock wave pattern and pressure distribution. Measurements indicated that a change of the boundary layer from the laminar to the turbulent regime resulted in a marked change in shock wave pattern and surface pressure distribution at the same freestream Mach number. Also, the pressure gradient normal to the boundary layer was found to be of the same order as the one parallel to the boundary layer near the base of the shock wave.

Measurements of Ackeret et al. (1947) showed that the boundary-layer displacement thickness increased rapidly at separation so that the surface pressure distribution was significantly modified from what would

be predicted from pure inviscid analysis. According to the measurements of Seddon (1960), the incident normal shock is bifurcated into a strong oblique shock and a weak rear shock due to the viscous interaction. Following the trailing weak rear shock, the supersonic stream is embedded in the subsonic region just outside the boundary layer. In the boundary layer, the flow was shown to undergo successively the three processes of shock compression, displacement and rehabilitation.

Pearcey et al. (1968) carefully examined the scale effects in wind tunnel tests. They suggested that the applicability of the flow model developed on shock induced separation of turbulent boundary layers on an airfoil to full scale behavior could be restricted. Restrictions arise because the trailing edge does not include the interaction that sometimes occurs between the disturbance at the foot of the shock and a subsonic-type rear separation in the continuous adverse gradient further downstream.

McDevitt et al. (1976) performed an experimental study for the transonic flow over an 18% thick circular-arc airfoil. By varying the peak local Mach number from about 1 to 1.4, both weak and strong interactions were observed. Shock induced separation was observed at $M_\infty \simeq 0.78$, and the effect of changes in Reynolds number on the flow field was appreciable at low Reynolds numbers, but this effect was small for Reynolds numbers above 1×10^7 based on the airfoil chord length. For freestream Mach numbers ranging from about 0.76 to 0.78, the airfoil flow field was found to be unsteady. Comparisons of the measurements and numerical solutions of the Navier-Stokes equations suggested that

the development of a more accurate turbulence model was necessary when the interaction is strong and extensive separation is present. The same flow model was tested by Levy (1978) and Seegmiller et al. (1978) at a fixed Reynolds number and the same unsteady motion was observed at the limited range of freestream Mach numbers indicated above.

Johnson and Bachalo (1980) reported an experimental study for a symmetrical NACA 64A010 airfoil at transonic conditions. Measurements were obtained with the freestream Mach number fixed at 0.8 for three different angles of attack to vary the intensity of shock wave/boundary layer interaction. The effect of varying Reynolds number was found to be very small because the transition strip placed at the leading edge nullified the effects of natural transition, thus reducing the sensitivity to Reynolds number. As the angle of attack was increased, the boundary-layer thickness on the airfoil's upper surface significantly increased and the shock wave moved forward. The turbulent flow measurements revealed that the turbulence fluctuations attained equilibrium with the local mean flow more rapidly than previously expected. On this basis, it was suggested that improved turbulence modeling was needed at or very near the separation point and that an algebraic turbulence model based on the local equilibrium assumption can be used downstream of the separation point.

One of the most heavily investigated transonic flow configurations other than the airfoil configuration is the cone-cylinder boattailed afterbody. Shrewsbury (1968) studied the effect of boattail juncture shape on afterbody drag at transonic speed. He tested eight different

afterbody configurations with cylindrical plume simulators for freestream Mach numbers ranging from 0.56 to 1.0 and angles of incidence ranging from 0 to 8 degrees. The experiment was performed with both rounded and sharp sting junctures. A sharp juncture was found to result in a slower pressure recovery on the afterbody. This experiment included measurements for three-dimensional separated flows.

Reubush (1974) conducted an experimental investigation for a series of eight nacelle-mounted isolated circular-arc boattailed afterbodies with both cylindrical plume simulators and real jet exhaust plumes to determine the effectiveness of utilizing solid circular cylinders to simulate jet exhaust plumes. The experiment was conducted at freestream Mach numbers ranging from 0.4 to 1.3 at an angle of attack of 0 degrees with various ratios of simulator diameter to nozzle-exit diameter. Comparisons of the measurements generally indicated that use of one of the larger diameter simulators would approximately result in pressure coefficient distributions and drag coefficients of real jet exhaust plumes at all Mach numbers. A more detailed discussion of these experiments will be given in a later section.

Later, an investigation was conducted by Reubush and Putnam (1976) to determine the effects of variations in Reynolds number on the pressure and drag of similar isolated boattails. They found that as the Reynolds number was increased, the boattail static pressure coefficients in the expansion region of the boattail became more negative, although those pressure coefficients in the recompression region of the boattails became more positive. These two trends were found to be compensating

and there was only a small effect of Reynolds number. Abeyounis (1977) measured the separation point using an oil-flow technique for the same circular-arc boattails, and suggested a correlation between the separation point and the Mach number, but the reattachment point was not measured.

Benek (1979) experimentally investigated transonic flows over two different boattail configurations with solid cylindrical plume simulators for freestream Mach numbers ranging from 0.6 to 1.3 using a laser doppler velocimeter. The two configurations differed in smoothness of the boattail so that one produced a fully attached flow and the other produced substantial separation.

There have been several experimental studies conducted on the flow field over circular-arc bump attached to a plane wall or cylinder. This configuration has the advantage of generating thick, extensive separation compared to the airfoil geometry so that more information can be obtained about the turbulent boundary-layer flow in the immediate vicinity of the separation point.

Alber et al. (1973) measured the turbulent transonic separated flow generated on the rear portion of a two-dimensional circular-arc model mounted on the wind tunnel floor using pitot probes. By varying the freestream Mach number from 0.3 to 0.8, two different types of separation were tested; pressure gradient induced separation and shock wave induced separation. At the lower Mach numbers, no shock was observed and separation induced by the pressure gradient appeared at the aft portion of the bump. As the Mach number was increased up to 1.32,

the separation point moved upstream and the reattachment point moved downstream. Shock induced separation was observed as the peak local Mach number was increased to 1.34. As the Mach number was increased further, the shock and the separation and reattachment points moved downstream. Velocity profiles downstream of the shock wave were also found to be quite different in the pressure gradient induced separation and shock induced separation cases. However, the accuracy of the measurements of velocity profiles in the reversed flow region is uncertain due to possible errors associated with the measuring technique.

Using a Mach Zehnder interferometry, Delery et al. (1976) studied a separated flow with strong viscous-inviscid interaction in a two-dimensional transonic channel in which a 12% thick circular bump profile was placed on the lower channel wall. Their results clearly indicated that the interaction with the shock wave brought on a noticeable thickening of the boundary layer and a noticeable distortion of the velocity distribution. They also found that the appearance of separation depended on the shock intensity and the velocity profile shape.

Delery (1983) investigated flows resulting from the interaction of shock wave and turbulent boundary layer occurring in a two-dimensional transonic channel. The turbulent boundary layer was developed on the channel walls and the bumps were placed on both upper and lower channel wall to accelerate the flow to supersonic speed. It was found that the first part of the interaction process entailed a very large production

of turbulence having a very strong anisotropy. In this zone, the normal stresses in the momentum and turbulent energy equations were considered to be important. He reported that the downstream relaxation toward a new equilibrium state was a very gradual process due to the long lifetime of the large structures which were formed in the region of intense turbulence production.

Bachalo and Johnson (1979) performed an experimental study for an axisymmetric flow model which consisted of an annular circular-arc bump affixed to a circular cylinder aligned with the flow direction. Measurements were obtained in the NASA Ames 2 × 2 foot transonic wind tunnel at freestream Mach number of 0.875 using a laser velocimeter. The separation and reattachment points were determined using oil flow visualization. The same bump configuration was tested by Horstman and Johnson (1984) at Mach numbers raging from 0.4 to 0.925 in the NASA Ames 6 × 6 foot supersonic wind tunnel where the influence of the tunnel walls would be much smaller than in the previous smaller wind tunnel. For the same test conditions, measurements of the surface pressure distribution obtained in these two wind tunnels were almost identical except that the shock location obtained in the larger tunnel was always about 1% chord length upstream of that in the smaller wind tunnel. As the Mach number was increased up to 0.8, the flow remained subcritical, but a small region of separation was observed. At Mach number slightly over 0.8, a shock wave was formed. As the Mach number was increased further, the shock location remained almost the same, but the separated region grew rapidly. More detailed observations will be given in a

later section.

2. Analytical work

a. General Since transonic flow is governed by a nonlinear equation or set of equations, analytical studies were very limited in the early days of transonic aerodynamics. Therefore, early studies of transonic flows depended very heavily on experiments and there were only few theoretical results. More recently, due to the general availability of digital computers, many numerical studies have been conducted and these have accelerated understanding of transonic phenomena.

Numerical studies of transonic flows can generally be divided into two categories depending on whether viscous effects are accounted for or not. Early studies were typified by the solution of the inviscid subset of the Navier-Stokes equations, such as the transonic small disturbance equation solved by Murman and Cole (1971) for two-dimensional flow and Bailey and Ballhaus (1972) for three-dimensional flow, the potential equation, solved by Jameson (1974), and the Euler equations, solved by Magnus and Yoshihara (1970). Comprehensive reviews concerning this approach can be found in articles by Yoshihara and Spee (1982), Nixon and Kerlick (1982), Holst (1983), and South (1985). These fully inviscid analyses often produce approximate descriptions of the transonic flow field including the pressure distribution and shock wave location. However, they fail to provide an accurate description when separation occurs due to shock wave penetration or a strong adverse pressure gradient. As observed in many experiments, viscous effects in transonic separated flows are so significant that a fully inviscid

analysis cannot be used to obtain a reasonable solution in such flows.

The other category consists of numerical methods which include viscous effects. Such methods are usually divided according to two approaches. The first approach is based on the full set or reduced subset of the Navier-Stokes equations and the other is the zonal approach based on the coupling of the viscous and inviscid subsets of the Navier-Stokes equations (the viscous-inviscid interaction method).

b. Navier-Stokes solutions-general Examples of the first approach which generally uses the time dependent Reynolds-averaged or mass-averaged Navier-Stokes equations can be found in numerous studies. An informative review on this approach is contained in an article by Mehta and Lomax (1982). Some of these studies were devoted to an evaluation of the turbulence modeling, generally the algebraic model with or without relaxation type modifications or one or two-equation models, for shock wave/boundary layer interaction flows. Included in such studies are Baldwin et al. (1975), Baldwin and Rose (1975), Deiwert (1976), Viegas and Coakley (1977), Levy (1978), Viegas and Horstman (1979), and Horstman (1983). Generally, higher-order turbulence models such as two-equation models provided a better description of flow details than the algebraic turbulence models. However, differences between these two models became very small in flows with shock induced separation and the overall predictions were in poor agreement with the measurements.

Several studies also utilized a reduced set of equations that falls between the full Navier-Stokes equations and the boundary-layer

equations. Baldwin and Lomax (1978) applied a thin-layer approximation to the Navier-Stokes equations. These equations are somewhat simpler than the Navier-Stokes equations, but a substantial amount of computer effort is still required to solve them. The parabolized Navier-Stokes (PNS) equations have recently gained popularity in many flow calculations (Rudman and Rubin, 1968) because of the use of a space marching technique, but their application to transonic flow has been rare. Recently, however, Khosla and Lai (1984) developed a global PNS technique to calculate transonic separated flows.

c. Navier-Stokes solutions-boattails and bumps A more detailed description of previous studies conducted with the above approaches on flows of present interest, the boattail afterbody and bump configurations, is given below. Holst (1977) and Swanson (1980) solved the time-dependent, Reynolds-averaged Navier-Stokes equations using an explicit finite-difference method for axisymmetric boattail flows measured by Reubush (1974). Both studies used a two-layer algebraic turbulence model with a relaxation formula to account for the nonequilibrium effects of the interacted turbulent flow. Predictions agreed much better with experimental data than results of equilibrium turbulence models, but the predictions in the reversed flow region were not satisfactory. This suggests that the improvement of the turbulence modeling is needed especially in the separated flow region.

Deiwert (1981) used the thin-layer form of the Reynolds-averaged Navier-Stokes equations, developed by Pulliam and Steger (1980), to calculate flows over several different axisymmetric boattail

configurations experimentally tested by Shrewsbury (1968), Reubush (1974) and Benek (1979). A two-layer algebraic turbulence model introduced by Baldwin and Lomax (1978) was used. Results agreed well qualitatively, but quantitatively some discrepancies were observed in the separated flow region; surface pressure was overpredicted in the pressure recovery region. These discrepancies were attributed to poor turbulence modeling, effects of artificial viscosity, and the influence of grid point distribution.

Khosla and Rubin (1983) applied a composite velocity formulation in solving the Navier-Stokes equations for Reubush's boattail flow. This formulation used a multiplicative composite of the appropriate velocity representations for the inviscid and viscous flow regions. As a result, the equations were structured so that far from the surface of the body the continuity equation reduced to the potential equation and the momentum equations led to the Bernoulli equation. Swanson et al. (1983) extended this method to transonic flow calculations by using the artificial compressibility method for embedded supersonic regions. A two-layer algebraic turbulence model proposed by Cebeci and Smith (1974) was used with the relaxation model suggested by Shang et al. (1976). Results showed favorable agreement with experimental data but the pressure was still overpredicted in the large separated flow region.

Solutions of the time-dependent, Reynolds-averaged Navier-Stokes equations were obtained by Johnson et al. (1982) for the flow over an axisymmetric bump attached to a cylinder, experimentally measured by Bachalo and Johnson (1979). The two-equation (k-ω) turbulence model

proposed by Wilcox and Rubesin (1980) and the algebraic Cebeci-Smith turbulence model were used. Even though the two-equation model resulted in slightly better predictions than the Cebeci-Smith model, both models produced essentially the same results. Particularly, the shock locations predicted by both models were in poor agreement with the measurements. The authors suggested that this large discrepancy was due to the rapid increase in the turbulent shear stresses in the vicinity of the shock.

Using the same Navier-Stokes equations, Horstman and Johnson (1984) recalculated this flow for a wider range of freestream Mach numbers and compared with their new measurements. At the outer boundary, freestream conditions were assumed instead of the inviscid solid wall (slip) boundary condition. They also used the two-equation (k-ε) model of Jones and Launder (1972) with a longitudinal curvature correction. The change of the outer boundary condition resulted in a vast improvement in calculated results, which indicated that the measurements were free from effects of the wind tunnel wall. A slight improvement was observed by using the k-ε turbulence model, but the pressure was still overpredicted in the recovery region and the separated region was predicted very poorly compared to experimental measurements. The computations showed no separation for freestream Mach numbers up to 0.8, while the experiment showed separation at all Mach numbers tested. For the larger freestream Mach numbers, the predictions of the separation points were relatively good, while the calculated reattachment points were significantly upstream of the measured points.

Sahu and Danberg (1985) used the thin-layer Navier-Stokes equations to predict the transonic separated flow over the same axisymmetric bump model. The computations were made with the algebraic turbulence model of Baldwin and Lomax (1978) and the two-equation (k-ε) turbulence model of Chien (1982). The calculated surface pressure distributions with both turbulence models were almost identical throughout the interaction region. The shock location was well predicted, but the pressure was significantly overpredicted downstream of the shock by both models and the pressure plateau was not captured by either model. They thought that this large discrepancy was due to the poor grid spacing in the redeveloping region. But the large error in prediction may also be caused by inadequate turbulence modeling. The large difference between the predictions of the two turbulence models was noticeable in the predicted skin-friction coefficients downstream of the reattachment point. The two-equation model resulted in a very strange sharp peak downstream of the reattachment point. The predicted reattachment point was located about 15% of the bump chord length upstream of the measured point. Therefore, the accuracy of the k-ε turbulence model of Chien (1982) is somewhat questionable for this flow.

The Johnson-King turbulence model was used by Johnson (1985) in solutions to the Navier-Stokes equations for axisymmetric bump flows of Bachalo and Johnson (1979). Calculated results were compared with the measurements for a wide range of freestream Mach numbers and were generally observed to be in very good agreement with the measurements. However, a slight overprediction of the displacement thickness was

noticeable downstream of bump-sting juncture, and a slow recovery of the flow toward the equilibrium state was evident downstream of the reattachment point. Still, the Johnson-King turbulence model was found to provide very good overall predictions for flows with strong interaction. The model requires very little more computational effort than the equilibrium, algebraic models.

d. Viscous-inviscid interaction-general Poor predictions by the fully inviscid numerical schemes and the high computing cost of Navier-Stokes solutions have accelerated the development of the viscous-inviscid interaction approach in recent years. A more comprehensive discussion of this approach can be found in the recent reviews by Le Balleur (1981a), Lock (1981), and Melnik (1981). This approach generally requires the iterative matching of the viscous and inviscid solutions through displacement thickness coupling. In the initial development stage, the classical direct matching method was used as can be found in the works of Bauer et al. (1975), Bavitz (1975), and Collyer and Lock (1979). The direct interaction method cannot be applied to separated flows because the boundary-layer solution breaks down at the point of separation. In order to overcome this singularity problem, several asymptotic and empirical ideas were developed (Reubush and Putnam, 1976; Wilmoth, 1977). However, these methods could not provide significantly accurate solutions due to built-in empiricism.

The separation singularity problem in the boundary-layer equations can be eliminated by the use of an inverse method. With the inverse method, prescribing the displacement thickness (Catherall and Mangler,

1966) or skin friction (Klineberg and Steger, 1974), the boundary-layer solution becomes regular. However, the displacement thickness or skin-friction distributions are not known and must be obtained as a part of solution if the method is to be predictive. Carter and Wornom (1975) coupled an inverse boundary-layer solution with an inverse solution of Cauchy integral equation for the incompressible flow calculations. This approach has received little support because of its slow convergence rate. Also, it would seem difficult to implement an inverse formulation for transonic inviscid flow.

Le Balleur (1978) introduced a semi-inverse interaction method for the calculation of transonic separated flow in which an inverse solution to the integral boundary-layer equations was coupled to a direct inviscid solution. A similar approach was developed by Carter (1979) and Kwon and Pletcher (1979) in their incompressible separated flow analyses, except that the boundary-layer equations were solved in a finite-difference form. This approach was also extended to calculations of transonic flows in many applications.

The integral form of the boundary-layer equations has been used with various inviscid flow formulations. Whitfield et al. (1981) and Murman and Bussing (1984) used the Euler equations; Lee and Van Dalsem (1981) used the full potential equation; Melnik and Brook (1985) used the full potential equation with an entropy correction. The interaction schemes of Carter (1981), Van Dalsem and Steger (1983), and Murphy and King (1983) used the finite-difference form of the boundary-layer equations for the viscous region and the full potential equation for the

inviscid region. Although these schemes gave reasonable predictions for some transonic flows, discrepancies between calculated and measured surface pressure distributions were often observed in separated flow regions.

In a series of numerical studies by Carter and Hafez (1982) and Carter et al. (1983), attempts were made to account for normal pressure gradients and the effects of embedded shocks. A compressible stream function formulation was used for the inviscid flow to take into account the rotational flow effects in the outer region of the boundary layer downstream of the shock. The results indicated that for transonic shock induced separation, the effects of displacement thickness interaction dominated over those produced by embedded shocks and normal pressure gradients. It was concluded that the correct turbulence modeling is more important in obtaining good predictions than inclusion of normal pressure gradients.

In another approach to the interaction problems known as the simultaneous interaction method, local solutions for the pressure and displacement thickness are obtained simultaneously so that they can mutually satisfy the local viscous and inviscid relations. Most of the early applications of this approach were in fully supersonic or subsonic flow cases where the outer inviscid flow can be described by a simple linear theory or an integral relation (Lees and Reeves, 1964; Crimi and Reeves, 1976; Veldman, 1979, 1981; Davis and Werle, 1981; Davis, 1984). Moses et al. (1978), on the other hand, used an integral method for the boundary-layer equations and a finite-difference method for the solution

of the Laplace equation for stream function in the inviscid flow region for a laminar incompressible flow.

A similar approach using the integral method for the boundary-layer equations was then extended to steady transonic flows by Wai and Yoshihara (1981) and to unsteady problems by Houwink and Veldman (1984) and Le Balleur (1984). A fully finite-difference simultaneous interaction method was first introduced by Edwards and Carter (1985) for laminar incompressible separated calculations. In some of the above studies based on the simultaneous interaction approach, the simultaneous solution procedure is followed by the pure inviscid or viscous calculations (Veldman, 1981; Veldman and Lindhout, 1983; Edwards and Carter, 1985). This approach is often called a quasi-simultaneous interaction method.

e. Viscous-inviscid interaction-boattails and bumps The following is a more detailed review of calculation results obtained using the viscous-inviscid interaction approach for the boattail and bump flows. Chow et al. (1975) applied a conventional direct viscous-inviscid interaction approach to calculate the transonic flow over axisymmetric boattail bodies tested by Reubush (1974). The full potential equation was solved for the inviscid flow region using the line relaxation scheme of South and Jameson (1973). The direct solution of the integral boundary-layer equations was used for the viscous flow. Inviscid solutions were obtained over the equivalent body which was obtained by adding the displacement thickness to the original body to account for the viscous effects. The displacement thickness was

adjusted using a underrelaxation factor of 2/3 after each solution sweep of the viscous and inviscid equations. The full potential equation was found to yield better agreement with the experimental results than the transonic small disturbance equation. However, the direct calculation method was not applicable to separated flow.

Reubush and Putnam (1976) also employed a direct interaction method to calculate the separated flow over the same axisymmetric boattail configuration. The inviscid flow region was calculated by a linearized potential flow (panel) method, developed by Hess and Smith (1967) for incompressible flows, with a compressibility correction. Therefore, this method was limited to a fully subsonic flow. The viscous flow region was described by the integral formulation of the boundary-layer equations developed by Reshotko and Tucker (1957). To avoid the singularity problem occurring at the point of separation, a discriminating streamline method, developed by Presz (1974), was used. This discriminating streamline, which separates the reversed flow region from the outer boundary layer so that the boundary layer is treated as fully attached, was also used as an effective solid body surface. The discriminating streamline was given as a conical surface diverging from the model surface at an angle which was dependent primarily on the local Mach number at the point of separation. A straight line curve fit to the experimental data of Presz was used to determine the divergence angle. The separation point, which was extremely critical to the solution, was determined from the empirical relation of Page (1961). Then the viscous and inviscid flow regions were solved sequentially in a

direct mode to update the displacement thickness and surface pressure distribution until convergence was obtained. Results showed reasonable agreement with experimental data, but still large discrepancies were evident in flows with higher Mach numbers. This method is not regarded as a truly predictive one because the divergence angle is entirely dependent on the experimental data and the separation point is determined empirically. A similar approach was used by Presz et al. (1978).

The above method was extended by Wilmoth (1977) to transonic calculations by using the line relaxation method of South and Jameson (1973) for the finite-difference solution of the full potential equation. Also, the discriminating streamline was given as a straight line connecting the predetermined separation and reattachment points. The separation point was taken from the oil flow measurements of Abeyounis (1977) and the reattachment point was assumed to be at the point of maximum surface pressure. Therefore, this method cannot be regarded as a truly predictive one, either. Better predictions were obtained with the experimentally determined discriminating streamline than with the empirically determined one. Also, it was found that the prediction was very sensitive to the shape and location of discriminating streamline. This suggests the need for a truly predictive method in which the separated region can be found as a part of the solution. Results also indicated that the conservative differencing of the potential equation might be necessary when viscous effects were included. A similar direct interaction approach was used

by Cosner and Bower (1977), but predictions in flows with significant separation were poor.

Dash and Pergament (1978) used a finite-difference formulation of the boundary-layer equations in their direct interaction scheme. The inviscid region was also described by the full potential equation. Instead of a solid plume simulator, a jet entrainment correction was used to yield an effective plume boundary. They employed the two-layer algebraic and two-equation (k-ε^2) turbulence models. The k-ε^2 model provided better overall results. However, no consideration was given to solving separated flow.

Kuhn (1980) applied the semi-inverse viscous-inviscid interaction approach to calculate the same boattail flows. The relaxation method used by Wilmoth (1977) was used for the direct solution of the inviscid flow equations. The integral form of the boundary-layer equations was solved in an inverse mode for the reversed flow region. The displacement surface in the reversed flow region, which was prescribed as a boundary condition for the boundary-layer equations and as an equivalent body surface for the inviscid calculation, was assumed to be conical starting at the separation point. The inviscid and viscous solutions were alternatively repeated until convergence was obtained. The divergence angle and separation point were adjusted in a way to reduce the root mean square error between the inviscid and viscous edge velocities in the iteration process. The calculated results generally agreed well with experimental data. Due to the assumption of linear displacement thickness profile, this method cannot generally be applied

accurately to other cases such as the separated flow over a flat plate.

A semi-inverse interaction method was also used by Carter and Vasta (1982a) to calculate the axisymmetric boattail flows experimentally studied by Reubush (1974) and the axisymmetric bump flow measured by Bachalo and Johnson (1979). The conservative full potential equation was solved by a line relaxation scheme in the inviscid flow region. Unlike the method of Kuhn (1980), the finite-difference method was used to obtain the inverse solution of the boundary-layer equations. The standard first-order boundary-layer analysis was also modified to account for the effects of the normal pressure gradient which may be significant in strongly interacting flows. The viscous and inviscid calculations were coupled using a transpiration velocity boundary condition for the inviscid flow that was related to the streamwise gradient of the displacement thickness following Lighthill (1958). The displacement thickness was updated with a formula suggested by Carter (1979), which was based on the mismatch of the inviscid and viscous edge velocities. With an algebraic turbulence model, the pressure was overpredicted and the separation point was too far downstream. Using the relaxation model of Shang and Hankey (1975), better predictions were observed. Still, predictions in the reversed region appeared to need improvement. The effects of normal pressure gradient were not believed to be of importance for this flow.

Whitfield et al. (1981) calculated the transonic interacting flow over a planar bump, experimentally studied by Altstatt (1977), using the semi-inverse viscous-inviscid interaction method. The time-dependent

Euler equations in conservative form were solved in a finite-volume formulation for the inviscid flow calculation. The boundary-layer equations were solved by an inverse integral technique. The viscous and inviscid calculations were coupled using a transpiration velocity. The update formula for displacement thickness was identical to that used by Carter (1979). Reasonably good agreement between calculated and measured surface pressure data was observed. No specific comparisons for other quantities were available.

A semi-inverse interaction method was used by Carter (1981) to calculate the transonic flow over the axisymmetric bump experimentally studied by Bachalo and Johnson (1979). Carter's scheme utilized a finite-difference inverse procedure for the boundary-layer equations. The full potential equation was solved by a line relaxation technique. The same coupling procedure proposed by Carter (1979) for incompressible flow was used. Predictions obtained with the two-layer algebraic Cebeci-Smith model showed poor agreement with the measurements; the pressure was significantly overpredicted in the vicinity of the bump-sting juncture and the separation point was predicted too far downstream. The discrepancies were attributed to inadequate turbulence modeling. With a reduced value of the Clauser constant in the Cebeci-Smith turbulence model, better predictions were observed. The above studies based on the viscous-inviscid interaction method except for the direct method are summarized in Table 1.

TABLE 1. The summary of previous studies based on the viscous-inviscid interaction method

References	Inter-action	Viscous analysis	Inviscid analysis	Appli-cation
Carter and Wornom (1975)	IV	FD	IN	SB
Le Balleur (1978)	SE	IN	FD	TR
Moses et al. (1978)	SI	IN	FD	SB
Carter (1979)	SE	FD	FD	SB
Kwon and Pletcher (1979)	SE	FD	IN	SB
Veldman (1979)	QS	FD	IN	SB
Kuhn (1980)	SE	FD	FD	TR
Whitfield et al. (1981)	SE	IN	FD	TR
Lee and Van Dalsem (1981)	SE	IN	FD	TR
Carter (1981)	SE	FD	FD	TR
Kwon and Pletcher (1981)	SE	FD	FD	SB
Veldman (1981)	QS	FD	IN	SB
Davis and Werle (1981)	QS	FD	IN	SB
Wai and Yoshihara (1981)	SI	IN	FD	TR
Carter and Hafez (1982)	SE	FD	FD	TR
Carter and Vasta (1982b)	SE	FD	IN	SB
Van Dalsem and Steger (1983)	SE	FD	FD	TR
Murphy and King (1983)	SE	FD	FD	TR
Carter et al. (1983)	SE	FD	FD	TR
Veldman and Lindhout (1983)	QS	FD	IN	SB
Davis (1984)	SI	FD	IN	SB,SP
Houwink and Veldman (1984)	SI	IN	FD	TR
Le Balleur (1984)	SI	IN	FD	TR
Melnik and Brook (1985)	SE	IN	FD	TR
Edwards and Carter (1985)	QS	FD	FD	SB

IV : inverse
SE : semi-inverse
QS : quasi-simultaneous
SI : simultaneous

IN : integral
FD : finite-difference

SB : subsonic
SP : supersonic
TR : transonic

C. Scope and Contributions of the Present Study

Previous studies of transonic flows with strong viscous-inviscid interaction described above have used either the time-averaged Navier-Stokes equations or the zonal (viscous-inviscid interaction) approach. Generally, the Navier-Stokes solutions provide a reasonably good predictions for flows with strong interaction between a shock wave and a boundary layer, and separated flows can be handled without special treatments. However, the numerical solution of Navier-Stokes equations still requires a large computational effort, especially for turbulent flows. Fine grids are often needed to obtain reasonable solutions because the use of wall functions for compressible turbulent flows is not well established. Therefore, turbulent flow calculations usually require large computing times or they exhibit relatively large errors caused by the use of a coarse mesh in order to reduce the computational effort. This situation is expected to improve with time, however, due to continuing improvements in algorithms and computing machines.

The need to improve computational efficiency for transonic flows provided motivation for the present study. Viscous-inviscid interaction methods have been used successfully in the calculation of incompressible separated flows by many investigators. As discussed in the preceding section, predictions obtained by the interaction method showed reasonably good agreement with solutions of the Navier-Stokes equations for strongly interacting transonic flows.

The objective of the present study was to develop an efficient and robust viscous-inviscid interaction scheme that can be used to predict

transonic flows with strong interaction between a shock wave and a boundary layer. First, the limit of applicability and efficiency of the semi-inverse interaction scheme, developed by Kwon and Pletcher (1979) and Carter (1979) was studied. Then a new interaction method was sought to enhance the efficiency and applicability of the overall interaction approach.

In the present semi-inverse interaction method, the flow domain was divided into the irrotational inviscid and viscous regions. The inviscid flow region was described by a direct finite-difference solution of a full potential equation in conservative form. The inviscid solution procedure was based on the iterative approximate factorization (AF2) algorithm which was implemented into the computer code, TAIR, by Dougherty et al. (1981). The TAIR code was modified in a manner that permitted calculation of any specified portion of an axisymmetric flow field having nonperiodic boundary conditions. The boundary-layer equations were solved by an inverse finite-difference method in the viscous flow region. In order to increase the efficiency of the overall interaction scheme and eliminate the possible stagnation point problem of the inviscid solution, a shear-layer coordinate system was adopted as suggested by Carter (1981). Its influence on the final solution and the global convergence behavior was evaluated by using several different shear-layer coordinates.

The viscous solution was coupled with the inviscid solution using the transpiration velocity formulation to account for the displacement effect. The updating algorithm of Carter (1981), which was used to

update the displacement thickness distribution through an iterative procedure based on the mismatch between inviscid and viscous edge velocities, was modified to increase the convergence rate of the global iteration procedure. However, this type of coupling algorithm has been known to be unstable for extensively separated flow regions in a supersonic stream as suggested by Wigton and Holt (1981). This trend has been experienced in the present study. Therefore, the development of a more robust interaction scheme was needed for the prediction of general separated transonic flows with strong interaction.

A new simultaneous viscous-inviscid interaction method was developed in the present study. In this new interaction coupling algorithm, the inviscid and viscous solutions were obtained simultaneously in order to eliminate numerical problems associated with the semi-inverse interaction method in the calculation of extensively separated flow. The simultaneous solution procedure was made possible through a localized implicit treatment of two sets of equations. Therefore, the updated displacement thickness required for a better agreement between the inviscid and viscous pressure distributions was obtained as a part of the iterative solution procedure, not with a separate interaction algorithm as used in the semi-inverse interaction method. To simplify the local treatment of the inviscid solution procedure, the conservative full potential equation was solved by a simple successive line overrelaxation (SLOR) scheme.

The solution procedure for the boundary-layer equations was almost identical to that of the semi-inverse method except that the

displacement thickness was treated as unknown to be obtained as a part of solution. It was found that most of the computing time was taken by the Newton linearization procedure in the boundary-layer equations. A pseudo-time dependent approach was developed to reduce the computing time needed in the linearization procedure. Since the separation was very large in several test cases, there was some concern about the marching procedure of the finite-difference scheme in the reversed flow region. To verify the effectiveness of the FLARE approximation, a windward differencing scheme was also employed in the separated flow region for some of the calculations for the purpose of comparison. The multiple sweep procedure required for the windward differencing was not used separately but was achieved by the global interaction iterative procedure. To the authors' knowledge, the present new interaction scheme is the first simultaneous interaction scheme to be applied to the transonic flow regime employing the finite-difference method for both the inviscid and viscous equations.

These two viscous-inviscid interaction methods were demonstrated by computations of several different flows including the two-dimensional laminar incompressible separated flow over a flat plate with a trough, first numerically studied by Carter and Wornom (1975), turbulent transonic flow over an axisymmetric boattail afterbody with a solid cylindrical plume simulator experimentally tested by Reubush (1974), and the turbulent transonic flow over an axisymmetric bump attached to a cylinder experimentally measured by Bachalo and Johnson (1979).

In the calculation of turbulent transonic flow, turbulence modeling is of great importance if separation exists. In the previous studies employing either the viscous-inviscid interaction method or the Navier-Stokes equations, predictions obtained by both algebraic and two-equation turbulence models were generally in poor agreement with experimental data, specially in the shock induced separated region. These discrepancies are believed to be largely due to shortcomings of turbulence modeling.

The calculated results also suggested that the nonequilibrium effects must be accounted for correctly. Johnson and King (1985) recently proposed a new turbulence model designed especially for turbulent boundary layers in strong adverse pressure gradient with separation. This model makes use of an ordinary differential equation for the maximum Reynolds shear stress which provides a velocity scale for turbulent viscosity. In the present study, this new Johnson-King turbulence model was further evaluated in comparison with the algebraic Cebeci-Smith model. Observations are made about the effect of varying parameters in the Johnson-King model and the influence of the choice of turbulence model on the convergence properties of the numerical scheme.

The contributions of the present study can be summarized as follows:

1. A modification to the semi-inverse interaction method was developed to improve the convergence speed of the global iteration procedure.
2. A shear-layer coordinate system was adopted and its effects upon final solutions and convergence were evaluated.

3. The validity of the FLARE approximation was evaluated in the shock induced separation region by comparing with results obtained with the windward differencing.
4. The pseudo-time dependent approach was developed to reduce the computing time needed for the Newton linearization procedure when the multiple sweeps of the boundary-layer equations were used.
5. A new simultaneous interaction method based on the fully finite-difference scheme was developed for transonic flow to provide a more robust and efficient viscous-inviscid interaction algorithm than the semi-inverse interaction scheme.
6. The Johnson-King model was evaluated in a fully predictive viscous-inviscid interaction calculation scheme.
7. The effect of the choice of turbulence model on the interaction convergence behavior was observed.

In the following chapter, the basic conservation laws needed to derive the governing equations for transonic flows are presented. Also in Chapter II, the viscous analysis based on the boundary-layer equations is presented together with the discussion of turbulence modeling. Next, the inviscid analysis based on the full potential equation formulation is discussed in Chapter III. In Chapter IV, the present viscous-inviscid interaction methods are discussed. Finally, Chapter V presents the calculation results in comparison with the available experimental measurements and other numerical solutions, which is followed by the conclusions in Chapter VI.

II. VISCOUS ANALYSIS

In this chapter, the detailed description of the solution procedure for viscous flows will be presented. The general conservation principles are described first. The governing equations for compressible turbulent boundary-layer flows are then developed from those general conservation statements. Turbulence models for both equilibrium and nonequilibrium flows are discussed. The numerical methods used to solve the equations are also described.

A. Laws of Conservation

The fundamental equations of fluid dynamics are based on three universal laws of conservation of mass, momentum and energy. The governing equations are derived by applying these conservation laws to a uniform, homogeneous fluid without mass-diffusion or finite-rate chemical reactions.

1. Conservation of mass

Using the Eulerian approach, conservation of mass applied to a fluid passing through an infinitesimal, fixed control volume yields the continuity equation which can be written in vector notation as

$$\frac{\partial \rho}{\partial t} + \nabla \cdot (\rho \vec{V}) = 0 \tag{2.1}$$

where ρ is the fluid density and $\vec{V}$ is the fluid velocity vector.

2. Conservation of momentum

Conservation of momentum, which is an application of Newton's second law to a fixed control volume, can be expressed as

$$\frac{\partial}{\partial t}(\rho\vec{V}) + \nabla\cdot\rho\vec{V}\vec{V} = \rho\vec{f} + \nabla\cdot\vec{\Pi} \tag{2.2}$$

where $\vec{f}$ is a body force and $\vec{\Pi}$ is a stress tensor. With a constitutive relation for an isotropic, Newtonian fluid based on Stoke's hypothesis, the stress tensor, $\vec{\Pi}$, is reduced to

$$\Pi_{ij} = - p\delta_{ij} + \tau_{ij} \tag{2.3}$$

where δ_{ij} is the Kronecker delta function ($\delta_{ij} = 1$ if $i = j$ and $\delta_{ij} = 0$ if $i = j$) and τ_{ij} is a viscous stress tensor given by

$$\tau_{ij} = \mu \left[\left(\frac{\partial u_i}{\partial x_j} + \frac{\partial u_j}{\partial x_i}\right) - \frac{2}{3}\,\delta_{ij}\,\frac{\partial u_k}{\partial x_k}\right] \tag{2.4}$$

for Cartesian coordinates.

Substituting Equation (2.3) into Equation (2.2) and using Equation (2.1), the well known Navier-Stokes equation is obtained as

$$\rho\frac{\partial\vec{V}}{\partial t} + \rho\vec{V}\cdot\nabla\vec{V} = \rho\vec{f} - \nabla p + \nabla\cdot\vec{\tau} \tag{2.5}$$

3. Conservation of energy

The conservation law for energy is a statement of the First Law of Thermodynamics for fluid passing through a fixed control volume. This yields the energy equation written in terms of total enthalpy, H, as

$$\rho\frac{\partial H}{\partial t} + \rho\vec{V}\cdot\nabla H = \frac{\partial p}{\partial t} + \nabla\cdot(\vec{\tau}\cdot\vec{V} - \vec{q}) \tag{2.6}$$

H is defined as

$$H = h + \frac{1}{2}\vec{V}\cdot\vec{V} \tag{2.7}$$

where h is enthalpy. Using Fourier's law for heat transfer by conduction, the heat flux vector, $\vec{q}$, can be expressed as

$$\vec{q} = - k\nabla T \tag{2.8}$$

where k is the thermal conductivity.

4. Equation of state

In order to close the above set of conservation equations, the relationships between thermodynamic properties and the transport properties must be specified. Since the fluid of interest is air at transonic speed, the perfect gas equation of state can be applied with little error

$$p = \rho RT \tag{2.9}$$

where R is the gas constant. Also for a perfect gas, the following relationships hold:

$$h = c_p T \qquad \gamma = \frac{C_p}{c_v} \qquad c_v = \frac{R}{\gamma-1} \qquad c_p = \frac{\gamma R}{\gamma-1} \tag{2.10}$$

where c_v is the specific heat at constant volume, c_p is the specific heat at constant pressure and γ is the ratio of specific heats.

For the coefficient of viscosity, Sutherland's equation was used,

$$\mu = C_1 \frac{T^{3/2}}{T + C_2} \tag{2.11}$$

where C_1 and C_2 are constants for a given gas. The thermal conductivity, k, was evaluated by

$$k = \frac{C_p \mu}{Pr} \tag{2.12}$$

where Pr is the Prandtl number, which was assumed to be constant.

B. Turbulent Flows

Most flows occurring in nature and in practical applications are turbulent. The scientific study of turbulent flow spans approximately one century and has resulted in significant progress in many directions. Our understanding of turbulent flow is, however, very incomplete.

Turbulent fluid motion is defined by Hinze (1975) as an irregular condition of flow in which the various quantities show a random variation in time and space coordinates, so that statistically distinct average values can be discerned, and is often characterized with a wide range of frequencies and length scales. The size of the largest scale is determined mainly by the characteristic dimension of the main flow, while the size of the smallest is determined by the fluid viscosity. The large scale motion is believed to carry most of the energy and momentum in turbulence. The energy is continuously transferred from the largest through the intermediate to the smallest scales, where the energy is dissipated as heat (Reynolds, 1974).

The unsteady full Navier-Stokes equations are generally considered to describe turbulent flows as well as laminar flows. When the Navier-Stokes equations are used to obtain the solution for fluid motion, numerical methods must be used instead of analytical procedures because of the highly nonlinear characteristics of the equations. However, time and space scales of turbulent motion are so small that the large number of grid points and the small size of the time steps required to discretize the equations for computer simulation are beyond the capabilities of present day computers at least for practical problems.

The most common practice in the computation of turbulent flows at the present time is to solve the time-averaged Navier-Stokes equations, which are often referred to as the Reynolds equations of motion, in place of the instantaneous equations. These time-averaged equations are derived by replacing the instantaneous quantities by the sum of their time-mean and fluctuating quantities as

$$f = \overline{f} + f'' \tag{2.13}$$

Time-averaged quantities are denoted by overbars and are defined as

$$\overline{f} = \frac{1}{\Delta t} \int_{t}^{t+\Delta t} f(t)\, dt \tag{2.14}$$

where Δt is large compared to the time scale of random fluctuations associated with the turbulence but smaller than the time scale of unsteady mean motion. For a fluctuating quantity, the time average is zero by definition.

For the treatment of compressible flows and mixtures of gases, it is convenient to use the mass-weighted averaging suggested by Favre (1965), which removes density fluctuations from the time-averaged equations of motion. A mass-weighted average is defined by

$$f = \tilde{f} + f' \tag{2.15}$$

where

$$\tilde{f} = \frac{\overline{\rho f}}{\bar{\rho}} \tag{2.16}$$

Hereafter, steady flow is assumed and body forces are neglected. Using Equation (2.15) for the velocity and enthalpy and Equation (2.13) for the density and pressure, the instantaneous quantities in Equations (2.1), (2.5), and (2.6) are replaced with their mean and fluctuating quantities. Using the time-averaging procedure and canceling vanishing terms in those equations, the mean conservation equations for mass, momentum, and energy are obtained as

continuity

$$\nabla\cdot(\bar{\rho}\tilde{V}) = 0 \tag{2.17}$$

momentum

$$\nabla\cdot(\bar{\rho}\tilde{V}\tilde{V}) = -\nabla\bar{p} + \nabla\cdot(\bar{\tau} - \bar{\rho}\overline{V'V'}) \tag{2.18}$$

energy

$$\nabla\cdot(\bar{\rho}\tilde{V}\tilde{H}) = \nabla\cdot(\bar{k}\nabla\bar{T} - \bar{\rho}\overline{H'V'} + \tilde{V}\bar{\tau} + \overline{V'\tau}) \tag{2.19}$$

C. Coordinate System

The coordinate system chosen for the present analysis is presented in Figure 2. In the case of axisymmetric external flows, it is common to use axisymmetric body intrinsic curvilinear coordinates where the abscissa, x, is measured along the body surface and the ordinate, y, is measured normal to the body surface as shown in Figure 2. Also, the radial distance from the axis of symmetry is noted by r.

The boundary-layer approximation, which will be discussed in detail in the following section, is based on the assumption that the dominant viscous shear force is parallel to the body surface. However, when the flow separates, the flow direction may deviate substantially from the direction determined by the tangent to the body surface. If the separated flow region is large, the validity of the boundary-layer approximation might be questioned.

Werle and Verdon (1980) proposed the use of a shear-layer coordinate system, shown in Figure 3, for viscous separated flows over a blunt trailing edge. This coordinate system is chosen so as to align with the predominant direction of the separated viscous flow by adding the thickness t to the original body coordinate as shown in Figure 3. The boundary-layer approximation is then applied with respect to this coordinate system in place of a body-oriented coordinate system. Another important advantage of using this shear-layer coordinate system arises in the calculation of the inviscid flow in a viscous-inviscid interaction procedure. For a body shape with a slope discontinuity, the inviscid flow is solved over the shear-layer coordinate by adding the

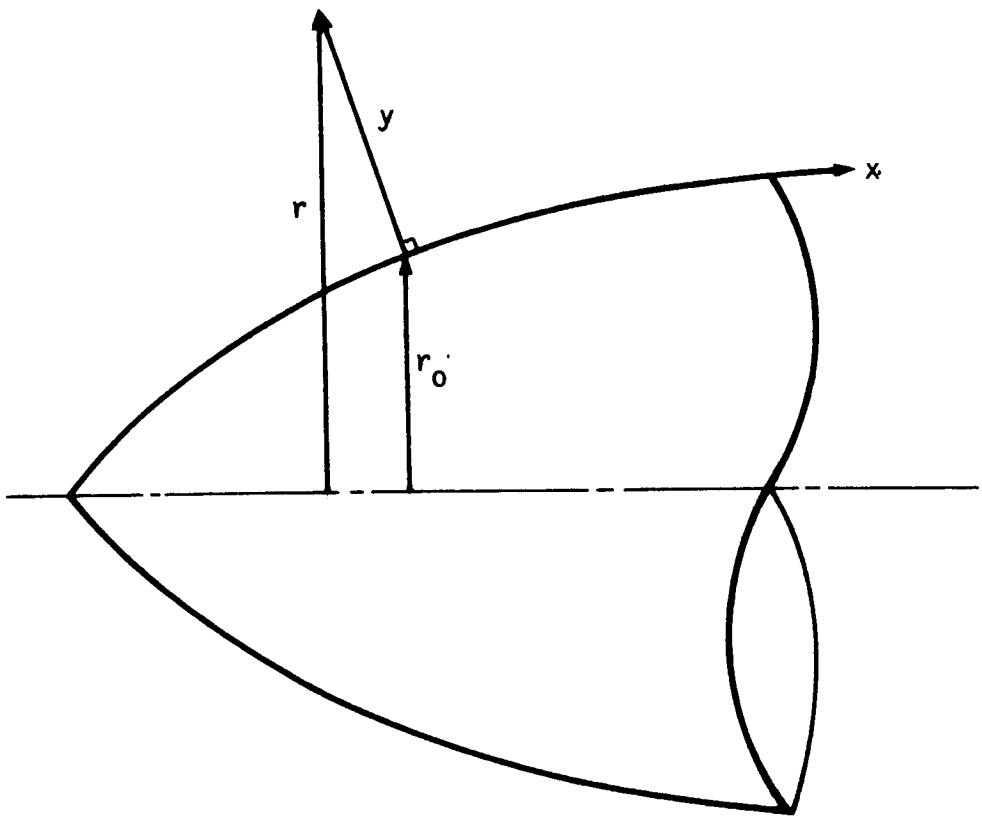

FIGURE 2. Coordinate system for the viscous analysis

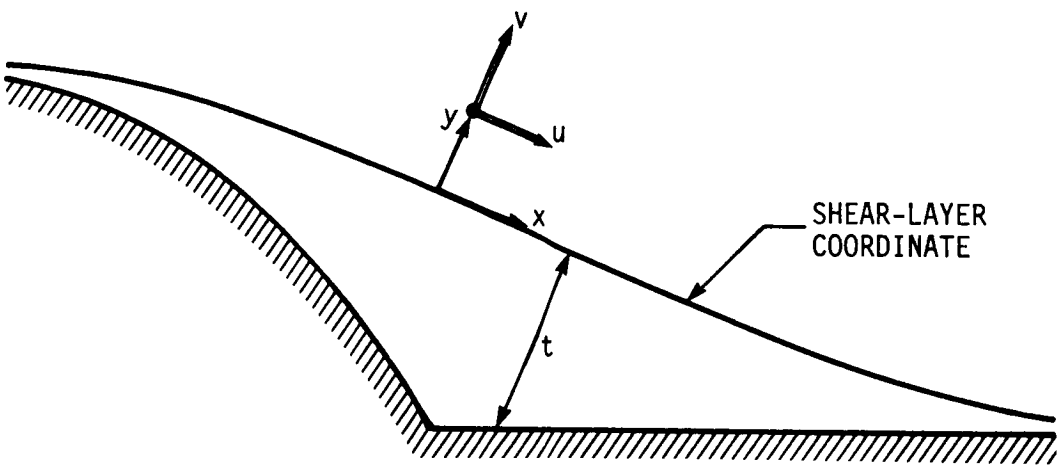

FIGURE 3. Shear-layer coordinate system

thickness t to the actual body surface, which eliminates artificial inviscid stagnation points thus simplifying the inviscid calculation as well as the overall interaction procedure.

As pointed out by Carter (1981), corrections must be made in the viscous-inviscid interaction procedure to account for the change in coordinates. The choice of the shear-layer coordinate direction is arbitrary but it should approximately align with the main direction of flow in viscous regions. Further details on the shear-layer coordinate system will be presented in a later section. Calculations were also made using the body-oriented coordinate system indicated by Figure 2 in the present study.

D. Boundary-Layer Approximation

It is well known from experimental observations that, at large Reynolds numbers, the effects of viscosity become increasingly confined to a narrow region near a solid boundary. In such flow regions, the governing equations can be simplified considerably by using Prandtl's boundary-layer approximation. Assuming that the viscous layer is thin relative to the characteristic dimension of the object immersed in the flow and that the largest viscous term is of the same approximate magnitude as any inertia term, an order of magnitude analysis can be used to obtain a simplified set of equations, i.e., boundary-layer equations.

This order of magnitude reduction for compressible turbulent flow is so lengthy that only the important points will be discussed here (see

Cebeci and Smith (1974)). The analysis is based on the assumption:

$$\frac{\partial}{\partial y} >> \frac{\partial}{\partial x} \qquad u >> v \qquad f >> f' \tag{2.20}$$

To estimate the magnitude of turbulence quantities, experimental observations must be used. For compressible flows, the magnitude of fluctuating terms of density and pressure in addition to velocity and temperature must be estimated. If fluctuations of the pressure and total temperature, T_o, are negligibly small, i.e.,

$$\frac{p'}{\bar{p}} << 1 \qquad \frac{T_o}{\bar{T}_o} << 1 \tag{2.21}$$

where $T_o = T + 0.5\ u^2/c_p$, then temperature fluctuations are nearly isobaric (Bradshaw, 1977) as

$$\frac{\rho'}{\bar{\rho}} = -\frac{T'}{\bar{T}} = (\gamma-1)M^2\ \frac{u'}{\bar{u}} \tag{2.22}$$

In the region near the wall, velocity fluctuations are relatively large, but the Mach number M is usually small. In the outer region where the Mach number is large, velocity fluctuations are generally small. Therefore, density fluctuations are small everywhere across the boundary layer for Mach numbers even up to 5. Even though there is evidence (Kistler and Chen, 1963) that the magnitude of the pressure fluctuation is appreciable at Mach number around 5 and is expected to increase with increasing Mach number, the pressure fluctuations are usually assumed to be negligible and this seems to be a very sound assumption for transonic flows. The effects of compressibility upon fluctuations of transport properties like the viscosity, conductivity and specific heats are not

well understood, but those fluctuations can usually be neglected (Bradshaw and Ferriss, 1971). Consequently, the turbulence structure of the boundary layer for Mach number up through 5 is generally believed to be the same as in the low speed flow, that is, incompressible flow. Also, under the boundary-layer approximation, the following relations between the time-mean and mass-weighted mean values are found (Cebeci and Smith, 1974)

$$\bar{u} = \tilde{u} \qquad \bar{H} = \tilde{H} \tag{2.23}$$

1. Governing equations

With the above boundary-layer approximation, Equations (2.17)-(2.19) are reduced to the following boundary-layer equations for axisymmetric compressible turbulent flows:

continuity

$$\frac{\partial}{\partial x}(\bar{\rho}\bar{u}r) + \frac{\partial}{\partial y}(\bar{\rho}\tilde{v}r) = 0 \tag{2.24}$$

momentum

$$\bar{\rho}\bar{u}\frac{\partial \bar{u}}{\partial x} + \bar{\rho}\tilde{v}\frac{\partial \bar{u}}{\partial y} = -\frac{d\bar{p}}{dx} + \frac{1}{r}\frac{\partial}{\partial y}[r(\bar{\mu}\frac{\partial \bar{u}}{\partial y} - \bar{\rho}\overline{u'v'})] \tag{2.25}$$

energy

$$\bar{\rho}\bar{u}\frac{\partial \bar{H}}{\partial x} + \bar{\rho}\tilde{v}\frac{\partial \bar{H}}{\partial y} = \frac{1}{r}\frac{\partial}{\partial y}\{r[\frac{\bar{\mu}}{Pr}\frac{\partial \bar{H}}{\partial y} - \bar{\rho}\overline{H'v'} + (1 - \frac{1}{Pr})\bar{\mu}\bar{u}\frac{\partial \bar{u}}{\partial y}]\} \tag{2.26}$$

where r is set to unity for a plane two-dimensional case. These equations are also valid for laminar flows when the terms involving the fluctuating quantities are set to zero.

In obtaining the boundary-layer equations, second derivatives of the velocity component in the streamwise, x, direction have been neglected along with the entire momentum equation for the transverse, y, direction. As a result, the pressure gradient in the transverse direction is set to zero and pressure becomes a function of x only. With the velocity component in the streamwise direction at the edge of the boundary layer, u_e, specified as a boundary condition, dp/dx can be evaluated from the inviscid flow equation given by

$$\frac{dp}{dx} = - \rho_e u_e \frac{du_e}{dx} \tag{2.27}$$

The boundary-layer approximation provides very important mathematical advantages: first, the equations become parabolic instead of elliptic so that the streamwise direction becomes the marching direction and the numerical solution procedure becomes much simpler; second, pressure can be impressed upon the boundary layer as a known variable; third, boundary conditions are reduced considerably, notably for v and in the x coordinate direction.

Note that in the case of turbulent flow, new unknown terms are introduced in the boundary-layer equations due to the Reynolds decomposition and averaging process. These terms $- \overline{u'v'}$ and $- \overline{H'v'}$, representing the apparent turbulent shear stress and heat flux quantities, must be modeled using empirical information to close the system of equations. The study of turbulence modeling will be discussed in Section II. E.

2. Boundary conditions

Appropriate boundary conditions are required to solve these governing equations for viscous flow regions. In a standard procedure, initial profiles for u and H are required at the starting plane as well as values of u, v and H at the wall and values of u and H at the boundary layer edge.

This standard procedure, which is referred as a direct method, becomes singular at the point of separation (Goldstein, 1948; Brown and Stewartson, 1969). When the pressure gradient is fixed near separation, the normal component of velocity, v, increases toward infinity at the point of separation. In a finite-difference solution, the magnitude of v at the point of separation is finite with a finite streamwise step size but will increase as the step size is reduced. As a result, the solution will not be unique and will usually fail to converge. This classical separation singularity, which is purely mathematical, can be avoided by the use of an inverse method which was suggested by Catherall and Mangler (1966). It has been used successfully by several investigators in numerical calculations (Klineberg and Steger, 1974; Williams, 1975; Carter, 1978; Kwon and Pletcher, 1979). In the inverse method, a regular solution is obtained through separated flow regions by prescribing the displacement thickness or skin friction in place of pressure gradient or u_e and the pressure gradient is determined as a part of solution.

The initial profiles for velocity and enthalpy at the stagnation point are provided automatically by similarity solutions to the

transformed equations that will be presented in a later section. The typical initial guesses required to obtain these solutions were obtained from freestream conditions, i.e., for $y > -t$,

$$\bar{u}(0,y) = u_\infty \qquad \tilde{v}(0,y) = 0 \qquad \bar{H}(0,y) = H_\infty \tag{2.28}$$

At the solid boundary, the no slip condition was used for the velocity components:

$$\bar{u}(x,-t) = \tilde{v}(x,-t) = 0 \tag{2.29}$$

For the total enthalpy, either the wall value or wall heat flux was specified, i.e.,

$$\bar{H}(x,-t) = H_w(x) \qquad \text{or} \qquad \left.\frac{\partial \bar{H}}{\partial y}\right|_{y=-t} = q_w(x) \tag{2.30}$$

In the direct method, values of the velocity and total enthalpy were prescribed at the outer edge of the boundary layer as

$$\text{as } y \to \infty, \qquad \bar{u}(x,y) \to u_e(x) \qquad \bar{H}(x,y) \to H_e(x) \tag{2.31}$$

where the subscript e refers to conditions at the edge of the boundary layer. The pressure gradient was also determined from the specified $u_e(x)$ as given by Equation (2.27).

The inverse procedure was used for the region interacted with the inviscid flow solution by specifying the displacement thickness which is defined as

$$\delta^* = \int_{-t}^{\infty} \frac{r}{r_o} \left(1 - \frac{\bar{\rho}\bar{u}}{\rho_e u_e}\right) dy \tag{2.32}$$

for axisymmetric compressible flows instead of the value of u at the edge of the boundary layer. The total enthalpy was specified as in the direct method.

Although the inverse method was developed mainly for separated flows, the method can also be used for attached flows. However, in the present study, attached flows were generally computed by the direct method. From now on, for simplicity, the bars and tildes will be omitted from the single mean quantities.

E. Turbulence Modeling

In a previous section the need for turbulence modeling was pointed out. Unfortunately, a universal turbulence model has not been developed to date and it seems very unlikely that one will be developed soon. Therefore, it might be better to find turbulence models which have reasonable accuracy over limited ranges of flow conditions. With such a purpose, it is essential to understand the basic aspects of the structure of turbulent flow before proceeding with the implementation of turbulence models.

1. The structure of the turbulent boundary layer

As discussed in a previous section, the structure of turbulent flow appears to remain almost unchanged for Mach numbers up through 5. It is, therefore, generally sufficient to include compressibility effects implicitly through the mean density variation in turbulence models which work reasonably well for incompressible flows.

The inner and outer regions of an incompressible, constant property turbulent boundary layer along a solid wall generally have quite different characteristics. However, they are strongly coupled by the shear stress profile and general diffusivity of the turbulence. The inner region comprises only a small fraction of a whole boundary layer in terms of thickness, but its influence over the entire boundary layer is significant. Klebanoff and Diehl (1952) experimentally observed that the inner region is generally insensitive to flow conditions far away from the wall and to the upstream conditions and that the mean velocity distribution is strongly dependent on the local conditions such as the wall shear, τ_w, density, ρ, viscosity, μ, and the distance y from the wall. This suggests that the inner region is frequently in a state of near local equilibrium according to Bradshaw (1972). In such a case, the mean flow motion can be described by a rather simple expression known as the law of the wall,

$$u^+ = f_1(y^+) \tag{2.33}$$

by using the wall coordinates defined as

$$u^+ = \frac{u}{u_\tau} \qquad y^+ = \frac{y u_\tau \rho}{\mu} \tag{2.34}$$

where u_τ, which is called the friction velocity, is given by

$$u_\tau = \left(\frac{\tau_w}{\rho}\right)^{\frac{1}{2}} \tag{2.35}$$

The inner region can be further divided into three layers: a viscous sublayer, a buffer region, and a fully turbulent region based on the

relative magnitude of the viscous and turbulent shear stress.

The outer region of the turbulent boundary layer occupies most ($\simeq$ 80%) of the boundary-layer thickness. The mean velocity distribution in this region is generally known to be described by the velocity-defect law:

$$\frac{u_e - u}{u_\tau} = f_2(\frac{y}{\delta}) \tag{2.36}$$

where δ is the boundary-layer thickness. Unlike the inner region, the function f_2 is strongly affected by streamwise pressure gradient. Clauser (1956) discovered that a similarity velocity profile in the outer region can be obtained by choosing proper scaling variables.

The preceding argument is generally applicable to fully attached turbulent boundary layers. When the turbulent flow separates under a strong adverse pressure gradient, the flow is often found to be unsteady, sometimes randomly and sometimes in a quasi-periodic sense. Simpson et al. (1977) observed that the qualitative turbulence structure upstream of the separation is not significantly different from that in flows with zero pressure gradient. As separation is approached, the flow is gradually influenced by the large scale outer flow and finally the motion near the wall is governed by the large eddy motion downstream of the separation point. These turbulent fluctuations in the separated region are of unusually large magnitude compared to the mean velocities. The law of the wall for the mean velocity profile and the local equilibrium argument appear not to be valid for separated flows according to Simpson (1979).

In the wall boundary layer developing downstream of the reattachment point, the mixing layer and the new wall shear layer intersect and result in a complicated turbulence structure. The incoming mixing layer in the outer part of the boundary layer is believed to carry characteristics of the separated region far downstream of reattachment. It has been also observed that it takes quite a long distance for flows to return to the structure of the ordinary turbulent boundary layer (Bradshaw and Wong, 1972). After the reattachment point, the turbulent energy is usually decreasing continuously but the exact reason for this phenomenon is not known.

The above discussion was mainly focused on incompressible flows. As mentioned before, there is evidence that the basic structure of turbulence is not altered significantly by moderate density or temperature fluctuations, which suggests that interaction between the velocity and temperature fluctuations is probably not strong even in flow of moderate Mach numbers (Bradshaw, 1977). Thus for compressible turbulent shear flows, the main coupling between the governing equations occurs through the mean density variation only.

As was the case for incompressible flows, the mean velocity distribution in the inner region can be observed to be somewhat similar by using wall coordinates. Since density and viscosity vary with the position, their values at the wall are used to define the friction velocity and wall coordinates as follows:

$$u^+ = \frac{u}{u_\tau} \qquad y^+ = \frac{y u_\tau \rho_w}{\mu_w} \qquad u_\tau = \left(\frac{\tau_w}{\rho_w}\right)^{\frac{1}{2}} \tag{2.37}$$

It is, however, not easy to obtain a simple law of the wall expression for the mean velocity in the inner region in the compressible case. Analyses of experimental data suggest that law of the wall for compressible flows is significantly affected by compressibility, i.e., effect of high Mach number, pressure gradient and heat transfer at the wall. The usual law of the wall for compressible flows then becomes

$$u^+ = f_3(y^+, \beta_c, M_\tau, p^+) \tag{2.38}$$

where

$$\beta_c = \frac{q_w}{T_w \rho_w C_{pw} u_\tau} \qquad M_\tau = \frac{u_\tau}{a_w} \qquad p^+ = \frac{\nu_e u_e}{u_\tau^3} \frac{du_e}{dx} \tag{2.39}$$

and q_w and a_w are the outward heat transfer rate and speed of sound at the wall (Bradshaw, 1977). Generally, the effects of high Mach number, a hot wall (negative β_c), and a favorable pressure gradient (negative p^+) tend to drive the velocity data $u^+(y^+)$ down below the incompressible logarithmic law (White, 1974). There have been numerous suggestions for the law of the wall function, f_3 (Van Driest, 1951; Maise and McDonald, 1968; Bertram, 1968; Baldwin and MacCormack, 1976; Viegas and Rubesin, 1983). These will not be given here and such a function was not used in the present calculations.

Even though the basic structure of turbulence remains unchanged for flows with a moderate Mach number, the flow pattern might become quite complex due to the intersection of a shock wave with a boundary layer in transonic flows. In the inner part of the boundary layer near the wall where the flow is subsonic, disturbances created by the impingement of

the shock wave cannot be discontinuous and thus are partly propagated upstream. This causes the streamlines upstream in the subsonic region to diverge and the increase of the thickness results in compression waves in the outer supersonic region. These intersect with the shock wave and cause it to bend forward. The pressure rise along the wall is still steep but continuous and takes places over a distance of the order of the boundary-layer thickness. If the pressure rise is sufficiently large, then the boundary layer separates with a more complex flow pattern forming a separation bubble and increasing the streamwise spread of the pressure rise. The complicated structure is primarily due to the mixing of supersonic and subsonic regions.

During the interaction with the shock wave, relatively large shear stress gradients normal to the wall build up in the inner region and are of crucial importance, dragging low energy flow downstream into the region of high pressure. In the outer supersonic layer, the flow is more nearly inviscid and is usually described in terms of wave pattern. The most distinguishing features of this pattern are the refraction of all waves by the rotational supersonic layer and the reflection of all incoming waves when they reach the sonic line. The reflection at the sonic line is compatible with the behavior of the subsonic region (Green, 1970).

If the overall pressure rise associated with the shock wave is not large enough to cause separation, the streamwise extent of the interaction region is then typically two or three times the thickness of the undisturbed boundary layer. In this case, since the upstream

propagation of pressure disturbances is small and the boundary layer remains thin, most of the outgoing compression waves coalesce with the outgoing random shock. Therefore, the effect of the viscous layer upon the pattern of the shock wave is relatively small.

When separation occurs, the flow pattern becomes quite complicated. As shown in Figure 1, separation generally results in bifurcation of the shock wave into a leading and rear shock, generating a vortex sheet with a rapid entropy rise. A separation bubble of slow recirculating flow occurs at the foot of the shock wave in the lower portion of the viscous layer. A strong transonic interaction may involve the additional complication of a tongue of supersonic flow downstream of the shock. This supersonic region embedded in the subsonic region outside the boundary layer is believed to interfere with the normal process of reattachment. As a result, the length of the separated region becomes more sensitive to changes in the overall pressure rise. This appearance of an embedded supersonic zone is consequently associated with the beginning of the phase in which the interaction increasingly affects the pressure at the trailing edge. A more detailed description of the behavior of a transonic turbulent boundary layer subject to strong interaction with shock waves can be found in the articles by Green (1968, 1970).

One of the major difficulties in predicting such a flow is uncertainty about the development of the turbulent shear stress in the region where pressure changes rapidly. This problem becomes serious when there is a severe adverse pressure gradient downstream of the

shock. In this case, the effect of uncertainties in predicting shear stress changes through the shock may be significantly magnified in the region of rising pressure downstream. Hence, as shock strength increases, it becomes more desirable to use a method which takes account of history, i.e., which includes an independent relation for the rate of change of shear stress. However, present understanding of a strongly interacted boundary layer is mainly qualitative and more detailed experimental studies are needed. Thus, present turbulence models are not complete and must be refined through a series of comparisons with experiments.

2. Turbulence modeling

The apparent turbulent stress and heat flux appearing in the Reynolds-averaged boundary-layer equations must be specified in order to predict the mean velocity and temperature distributions across the boundary layer. While relationships among these quantities can be developed into the form of transport equations from the basic conservation laws, more unknown quantities are introduced. These quantities must be evaluated based on empirical hypotheses.

One of the simplest modeling strategies follows the proposal of Boussinesq (1877). Boussinesq assumed that turbulent shear stresses are related to the rate of mean strain via a turbulent viscosity defined by

$$-\rho\overline{u'v'} = \mu_t \frac{\partial u}{\partial y} \tag{2.40}$$

By analogy with the kinetic theory of gases, which provides an accurate

theory for the molecular viscosity, the turbulent viscosity, μ_t, is assumed to be the product of a velocity and a length,

$$\mu_t = \rho v_t \ell \tag{2.41}$$

where v_t and ℓ are characteristic velocity and length scales of the turbulence, respectively. Therefore, the main task in representing the turbulent viscosity is to find appropriate expression for v_t and ℓ.

In a like manner, the apparent turbulent heat flux is related to the turbulent viscosity and the mean flow variables through Boussinesq's turbulent conductivity concept. Using Equation (2.7), the apparent turbulent heat flux in the boundary layer is approximated as

$$\rho\overline{H'v'} = \rho\overline{h'v'} + \rho u\overline{u'v'} \tag{2.42}$$

Using Boussinesq's turbulent conductivity concept and the turbulent Prandtl number,

$$-\rho\overline{h'v'} = \frac{\mu_t}{Pr_t}\frac{\partial h}{\partial y} \tag{2.43}$$

Substituting Equations (2.40) and (2.43) into Equation (2.42), the apparent turbulent heat flux is given as

$$-\rho\overline{H'v'} = \frac{\mu_t}{Pr_t}\frac{\partial H}{\partial y} + (1 - \frac{1}{Pr_t})\mu_t u\frac{\partial u}{\partial y} \tag{2.44}$$

Experimental data suggest that Pr_t is a well behaved function across the flow, and reasonably good predictions have been achieved even with a constant value of Pr_t, for example, 0.9. Note that μ_t and Pr_t are not the physical properties but vary with local flow conditions and

geometry. Although the Boussinesq assumption is not in complete agreement with all available experimental evidence, it appears to be a reasonably good approximation in many engineering flow circumstances.

The models that utilize the Boussinesq assumption are further classified by the number of supplementary partial differential equations which are used to obtain the modeling parameters like ν_t, ℓ or μ_t itself. An ordinary differential equation is usually counted as a half equation and algebraic equations are counted as zero.

The algebraic or zero equation model, which is based on Prandtl's mixing length concept (1926), is the simplest and most popular turbulence model among those utilizing the Boussinesq assumption. In this model, the characteristic scales and the turbulent Prandtl number are given by simple algebraic equations related to the motion of the mean flow. Despite its simplicity, it has proven effective in predicting relatively simple flows. In order to make it more accurate for complicated flow cases, there have been numerous attempts to modify the algebraic equations with semi-empirical relations (Van Driest, 1951; Patankar and Spalding, 1967; Cebeci and Smith, 1974; Deiwert, 1976; Baldwin and Lomax, 1978; see, e.g., Anderson et al., 1984). The major objection to algebraic models is that they are based on a local equilibrium assumption, i.e., the turbulent viscosity is evaluated only in terms of local flow parameters and upstream effects are not considered.

A one-half equation model is considered as the least complex method which can approximately account for the nonequilibrium effects. One of

the modeling parameters or turbulent viscosity itself is controlled by the solution of an ordinary differential equation which can usually be derived from the more general transport equation for the parameters by neglecting variations in one coordinate direction while the other parameters, if any, are governed by algebraic relations. Most of these models employ an ordinary differential equation for the length scale (McDonald and Kreskovsky, 1974; Chan, 1972; Pletcher, 1978) or turbulent viscosity (Shang and Hankey, 1975; Reyhner, 1968).

Obviously, the next step is to use a full partial differential equation for the modeling parameters. The modeling which has become popular in not only academic research but also engineering applications is a two-equation model. One of the most frequently used two-equation model is the k-ε model first proposed by Harlow and Nakayama (1967) and developed further by many others (Jones and Launder, 1972; Ng and Spalding, 1972). Also numerous other two-equation models have been suggested including a k-ω^2 model developed by Wilcox and Rubesin (1980) especially for compressible flows. Most of these two-equation models employ a modeled form of the turbulent kinetic energy equation but use a different dependent variable for the second model transport equation from which the length scale is determined. The disadvantage of two-equation models is the need to make assumptions in evaluating the third-order turbulent correlations in the transport equations.

A Reynolds stress equation model which does not utilize the Boussinesq assumption about turbulent viscosity was pioneered by Rotta (1951) and has been enhanced by Hanjalic and Launder (1972) and many

others. Recently, a large eddy simulation approach which is not based on the Reynolds equations was developed by Deardorff (1970). However, these last two types of models must be refined and tested further before they can be used for engineering predictions.

Transonic turbulent flow is believed to be affected strongly by upstream history effects in the neighborhood of a shock wave. For such flows, two-equation models have been used extensively because they were believed to have a better chance of predicting overall flow structure correctly than local equilibrium models. Surprisingly, most of calculated results of various two-equation models (Coakley and Viegas, 1977; Viegas and Coakley, 1978; Viegas and Horstman, 1979) are not necessarily superior to those of lower-order models. Meanwhile, several one-half equation models have been developed mainly in order to account for nonequilibrium effects and their predictions generally provide a definite improvement over those from algebraic models. In the present study, the zero equation and the one-half equation models were used and they are described in detail in the following sections.

3. Algebraic model

Prandtl (1926) proposed the following mixing-length formulation:

$$\mu_t = \rho \ell^2 \left| \frac{\partial u}{\partial y} \right| \tag{2.45}$$

where ℓ and $\ell|\partial u/\partial y|$ can be thought of as the characteristic length and velocity scales of turbulence, respectively. Evaluation of ℓ in this model varies with the type of flow. For flows along a solid surface, the boundary layer is usually divided into inner and outer regions for

the evaluation of ℓ.

In the inner region close to a solid wall, the mixing length is believed to be proportional to the transverse distance from the wall as

$$\ell_i = \kappa y \tag{2.46}$$

where κ is an empirical constant known as the von Kármán constant. A value of κ of about 0.41 provides good agreement with experimental data taken in simple flows. This distribution of ℓ_i matches correctly with the fully turbulent layer of the inner region excluding the viscous sublayer and buffer layer close to a wall. The expression for mixing length become applicable over the whole inner region by using an empirically determined damping function D, proposed by Van Driest (1956).

$$\ell_i = \kappa D y \tag{2.47}$$

where

$$D = 1 - \exp(-\frac{y^+}{A^+}) \tag{2.48}$$

and y^+ is given by Equation (2.39). A value of 26 is generally used for the damping constant A^+. The expression given by Equation (2.48) is valid only for flows with a negligible pressure gradient. When the pressure gradient is sufficiently adverse as to cause separation, τ_w becomes zero, then D given by Equation (2.48) will become zero so that μ_t will be zero in the inner region. Such a problem can be overcome by defining D based on the maximum velocity gradient rather than the wall value as suggested by Pletcher (1978) and Carter and Wornom (1975).

Then the damping function can be written as

$$D = 1 - \exp\left[-\left(\frac{\rho}{\mu}\left|\frac{\partial u}{\partial y}\right|_{max}\right)^{\frac{1}{2}} \frac{y}{A^+}\right] \tag{2.49}$$

There have been numerous variations suggested for the damping function in order to account for effects of property variations, pressure gradient, blowing, transverse curvature and separation (Cebeci, 1970, 1971, 1973; Kays et al., 1970; Pletcher, 1976). Following Cebeci and Smith (1974) the damping function used in the present study is

$$D = 1 - \exp\left[-\left(\frac{\rho}{\mu}\left|\frac{\partial u}{\partial y}\right|_{max}\right)^{\frac{1}{2}} \frac{yN}{A^+}\right] \tag{2.50}$$

where

$$N = \left[1 - 11.8\left(\frac{\mu_w}{\mu}\right)\left(\frac{\rho}{\rho_w}\right)^2 p^+\right]^{\frac{1}{2}} \tag{2.51}$$

In the outer region of a wall boundary layer, the mixing length is often taken as proportional to the boundary-layer thickness. Another common method is to use the kinematic displacement thickness instead of boundary-layer thickness and the velocity at the outer edge of the boundary layer as the length and velocity scales, respectively:

$$\mu_{to} = \alpha \rho u_e \delta_k^* \tag{2.52}$$

where α is the Clauser constant and is observed to be about 0.0168 and δ_k^* is the kinematic displacement thickness defined by

$$\delta_k^* = \int_0^\infty \frac{r}{r_o}\left(1 - \frac{u}{u_e}\right) dy \tag{2.53}$$

Cebeci and Smith (1974) also recommend a modification to include the effect of low Reynolds number, based on the observation by Coles (1962) as

$$\alpha = 0.0168 \frac{1.55}{1 + \pi} \tag{2.54}$$

where

$$\pi = 0.55 \left[1 - \exp(- 0.243z^{\frac{1}{2}} - 0.298z)\right] \tag{2.55}$$

and

$$z = \frac{Re_{\theta k}}{425} - 1 \tag{2.56}$$

Here $Re_{\theta k}$ is the Reynolds number based on the kinematic momentum thickness defined as

$$Re_{\theta k} = \frac{\rho_w u_e \theta_k}{\mu_w} \tag{2.57}$$

where θ_k is the kinematic momentum thickness defined by

$$\theta_k = \int_0^\infty \frac{r}{r_o} \frac{u}{u_e}(1 - \frac{u}{u_e}) \, dy \tag{2.58}$$

The effect of this modification becomes negligible if $Re_{\theta k}$ is greater than 5000.

As the freestream is approached near the edge of the boundary layer, the turbulence becomes intermittent. Following Klebanoff's (1954) observations, there are intervals of time when the flow is not turbulent near the outer edge of the boundary layer and these intervals become longer as the distance from the wall increases. Including this intermittency factor to the expression for turbulent viscosity for the

outer region, Equation (2.56) becomes

$$\mu_{to} = \alpha \rho u_e \delta_k^* \gamma_i \tag{2.59}$$

where intermittency factor γ_i is given by

$$\gamma_i = [1 + 5.5(\frac{y}{\delta})^6]^{-1} \tag{2.60}$$

and α is given by Equation (2.54). Note that the effect of the transverse curvature was neglected since the boundary-layer thickness is assumed small compared with the radius of the body. Deiwert (1976) used the furthest point across the boundary layer where the velocity is zero in place of usual $y = 0$ for the lower basis needed in evaluating δ_k^* and γ_i in order to avoid an unrealistically large length scale in the reversed flow region. The effect of this modification proved to be insignificant and was not used in the present study.

The above algebraic two-layer model will be referred to as the Cebeci-Smith model hereafter. This Cebeci-Smith model is known to predict rather poorly in separated regions and was not proposed for use in such flows by its originators. This poor prediction is mainly due to the assumption of local equilibrium which implies the neglect of the effects of diffusion and convection of turbulence scales and assumes a balance between the production and dissipation of the turbulent kinetic energy. The sole reason for its use was for reference purposes, simply to indicate the level of performance to be expected from algebraic models which have been perfected for equilibrium or near-equilibrium turbulent flows.

4. Nonequilibrium turbulence model

The aforementioned algebraic model is based on an assumed equilibrium between the mean motion of the flow and its local turbulence. When the flow changes rapidly in the streamwise direction, the turbulence may lag the mean motion. To account for this, models have been developed to utilize transport equations for the turbulence itself. The simpler of such methods use transport equations for variables used in defining a turbulent viscosity, which then can be out of equilibrium with the mean motion. It should be noted, however, that the Reynolds stresses are tied to the mean motion through the Boussinesq approximation and react immediately to changes in the mean motion, even though the effect of this reaction is influenced by the extent of the lag of the turbulent viscosity.

Such models typically employ partial differential equations to take into account the effect of diffusion or convection of turbulence length or velocity scales. Typical of such models is the two-equation model (e.g., k-ε model of Jones and Launder (1972) and k-ω^2 model of Wilcox and Rubesin (1980)). Considering the added numerical complexity and computational effort required to solve additional partial differential equations, the improvement in predictive accuracy over algebraic models has not been encouraging. On the other hand, the effect of flow history on the turbulent viscosity can be approximated with an ordinary differential equation, a so called one-half equation model, and such models have proven effective within a limited range of applicability.

One-half equation models are generally divided into two different types. The first type is purely an empirical relaxation or lag model. The models of this kind are actually equivalent to one-dimensional versions of transport equations for the quantities concerned except that these transport equations are not generally derivable from the Navier-Stokes equations. Included in this type are a relaxation form of an ODE for μ_t itself proposed by Shang and Hankey (1975) and an ODE for length scale in the outer region suggested by Pletcher (1978). The other type utilizes a reduced form of the transport equation for turbulent kinetic energy to define one of the turbulent characteristic scales (McDonald and Kreskovsky, 1974; Chan, 1972).

Very recently, Johnson and King (1985) suggested a new one-half equation model in which the velocity scale is governed by an ODE derivable from the turbulent kinetic energy equation. This model will be referred to as the Johnson-King model and is described below.

The turbulent viscosity is assumed to have a functional form of

$$\mu_t = \mu_{to}[1 - \exp(-\frac{\mu_{ti}}{\mu_{to}})] \tag{2.61}$$

where μ_{ti} and μ_{to} can be thought of as describing the turbulent viscosity in the inner and outer parts of the boundary layer. Equation (2.61) provides a smooth implicit blending of turbulent viscosities in two regions instead of an explicit change at the boundary of two regions.

The inner turbulent viscosity is given by

$$\mu_{ti} = \rho D^2 \kappa y (-\overline{u'v'}_m)^{\frac{1}{2}} \tag{2.62}$$

where the damping function D is the same as given by Equation (2.50) except that A^+ is assigned a value of 15 instead of 26. This adjustment was suggested by Johnson and King (1985) to provide y^4-dependency instead of y^3-dependency of μ_t in the near wall region. Compared with the algebraic Cebeci-Smith model, the major difference is that the velocity scale is based on $(-\overline{u'v'}_m)^{\frac{1}{2}}$, which is provided by the solution of an ODE. Perry and Schofield (1973) suggested that $(-\overline{u'v'}_m)^{\frac{1}{2}}$ provided a much better velocity-defect correlation than did the friction velocity u_τ for flows with adverse pressure gradients.

The outer value of the turbulent viscosity μ_{to} is given by

$$\mu_{to} = \sigma(x)\alpha u_e \delta_k^* \gamma_i \tag{2.63}$$

where $\sigma(x)$ is an unknown parameter which varies with streamwise distance. This form of the outer turbulent viscosity is identical with the Cebeci-Smith model except for the appearance of $\sigma(x)$ which becomes necessary to make the turbulent viscosity consistent with the local flow. In other words, values of $\sigma(x)$ are determined so that $-\overline{u'v'}_m$ resulting from use of μ_t and the mean velocity profile coincides with the value given by the ODE. In this way, the nonequilibrium effect expressed through $-\overline{u'v'}_m$ can be felt in the outer region as well as in the inner region. The details are discussed later.

The streamwise distribution of $-\overline{u'v'}_m$ is determined from the solution of an ordinary differential equation which is derived from the

turbulent kinetic energy equation using assumptions similar to those used by Bradshaw et al. (1967). The equation for the transport of turbulent kinetic energy for a steady compressible boundary layer is given by

$$\rho u\frac{\partial k}{\partial x} + \rho v\frac{\partial k}{\partial y} = -\rho\overline{u'v'}\frac{\partial u}{\partial y} + \frac{\partial}{\partial y}[\mu\frac{\partial}{\partial y}(k + \overline{v'^2})]$$

$$- \frac{\partial}{\partial y}(\rho\overline{kv'} + \overline{pv'}) - \rho\varepsilon_d \qquad (2.64)$$

where k is the turbulent kinetic energy and is defined as

$$k = \frac{1}{2}\,(\overline{u_i'u_i'}) \qquad (2.65)$$

and ε_d is the rate of dissipation of the turbulent kinetic energy and can be approximated as

$$\varepsilon_d \simeq \frac{\mu}{\rho}(\frac{\partial\overline{u_i'}}{\partial x_j})^2 \qquad (2.66)$$

Assuming the path of the maximum turbulent kinetic energy is continuous outside the viscous sublayer and is nearly coincident with the x coordinate, Equation (2.64) can be specialized for the maximum turbulent kinetic energy k_m and reduced approximately to the following form:

$$u_m\frac{dk_m}{dx} = -\overline{u'v'}_m\left.\frac{\partial u}{\partial y}\right|_m - \frac{1}{\rho}\frac{\partial}{\partial y}(\rho\overline{kv'} + \overline{pv'}) - \varepsilon_{d,m} \qquad (2.67)$$

Here, subscript m denotes that the quantity is evaluated where k is maximum in the y direction across the boundary layer. In the above equation, the additional assumption has been made that $-\overline{u'v'}_m$ becomes maximum where k is maximum.

Following the analysis of Bradshaw et al. (1967), additional parameters are defined as

$$a_1 = \frac{\overline{-u'v'}_m}{k_m} \qquad L_m = \frac{(\overline{-u'v'}_m)^{3/2}}{\varepsilon_{d,m}} \tag{2.68}$$

Here L_m corresponds to a dissipation length scale. To simplify the above equation, a_1 is assumed to be constant. Experimental data suggest that a_1 varies between 0.2 and 0.3 and it is reasonable to assume a_1 to be a constant. A value of 0.25 for a_1 was suggested by Johnson and King (1985). Different values of a_1 were also used in the present calculations, and the effect of varying a_1 will be discussed in a later section. Using Equation (2.68), Equation (2.67) can be rearranged to give

$$\frac{d}{dx}(\overline{-u'v'}_m) = \frac{a_1(\overline{-u'v'}_m)}{L_m u_m}\left[L_m \frac{\partial u}{\partial y} - (\overline{-u'v'}_m)^{\frac{1}{2}} - \frac{a_1}{u_m} D_m\right] \tag{2.69}$$

where D_m represents the diffusion term in Equation (2.67).

The first term on the right hand side of Equation (2.69), $L_m(\partial u/\partial y)|_m$, can be interpreted as the square root of the turbulent shear stress that might result when convection and diffusion effects are negligibly small. Thus, this term is replaced as

$$L_m \left.\frac{\partial u}{\partial y}\right|_m = (\overline{-u'v'}_{m,eq})^{\frac{1}{2}} \tag{2.70}$$

This quantity is determined by the equilibrium turbulent viscosity distribution given by

$$\mu_{t,eq} = \mu_{to,eq}[1 - \exp(-\frac{\mu_{ti,eq}}{\mu_{to,eq}})] \tag{2.71-a}$$

$$\mu_{ti,eq} = \rho D^2 \kappa y(-\overline{u'v'}_{m,eq})^{\frac{1}{2}} \tag{2.71-b}$$

$$\mu_{to,eq} = \alpha u_e \delta_k^* \gamma_i \tag{2.71-c}$$

The dissipation length scale L_m is determined as

$$L_m = 0.4\ y_m \qquad \text{for} \quad y_m \leq 0.225\ \delta \tag{2.72-a}$$

$$L_m = 0.09\ \delta \qquad \text{for} \quad y_m > 0.225\ \delta \tag{2.72-b}$$

The turbulent diffusion term D_m must also be modeled in order to solve Equation (2.69). This turbulent diffusion term seems to be important in the region where the flow is recovering toward an equilibrium state. Johnson and King (1985) proposed the following form of D_m based on the bulk convection hypothesis of Townsend (1976):

$$D_m = \frac{C_{dif}(-\overline{u'v'}_m)^{3/2}}{a_1 \delta[0.7-(y/\delta)_m]} |1 - \sigma(x)^{\frac{1}{2}}| \tag{2.73}$$

where C_{dif} is a modeling constant and its suggested value is 0.5.

In order to solve Equation (2.69), it is convenient to define new variables:

$$\theta = (-\overline{u'v'}_m)^{-\frac{1}{2}} \qquad \theta_{eq} = (-\overline{u'v'}_{m,eq})^{-\frac{1}{2}} \tag{2.74}$$

Finally, Equation (2.69) can be rewritten in terms of new variables as follows:

$$\frac{d\theta}{dx} = \frac{a_1}{2u_m L_m}\{1 - \frac{\theta}{\theta_{eq}} + \frac{C_{dif} L_m}{a_1 \delta[0.7-(y/\delta)_m]} |1 - \sigma(x)^{\frac{1}{2}}|\} \qquad (2.75)$$

Equation (2.75) is nonlinear because of the appearance of local parameters as coefficients of θ. Equation (2.69) is linearized by simply using values of those quantities from the previous x station (lagging). Also, in Equations (2.62) and (2.71-b), the values of $(-\overline{u'v'}_m)^{\frac{1}{2}}$ and $(-\overline{u'v'}_{m,eq})^{\frac{1}{2}}$ required to determine μ_{ti} and $\mu_{ti,eq}$ are obtained from the previous x station.

Initial conditions for θ, θ_{eq} and $\sigma(x)$ must be provided before Equation (2.75) can be solved. The flow upstream at the point where this nonequilibrium model starts can be assumed to be in an equilibrium state so that $\mu_t = \mu_{t,eq}$. Therefore, the initial condition is given as

$$\text{at } x = x_o, \qquad \overline{u'v'}_m = \overline{u'v'}_{m,eq} \quad (\text{i.e., } \theta = \theta_{eq}) \qquad (2.76)$$

$$\sigma(x) = 1.0$$

where $-\overline{u'v'}_{m,eq}$ can be easily provided by any equilibrium turbulent viscosity model such as the Cebeci-Smith model. The starting point, x_o, for this closure should not, obviously, be where the Reynolds stress is expected to change rapidly. Therefore, all calculations were initiated using the Cebeci-Smith model from the leading edge and a switch was made to the Johnson-King model at the beginning of the viscous-inviscid interaction region.

The variable $\sigma(x)$ provides a close tie between the turbulent viscosity across the whole boundary layer and the ordinary differential equation for the maximum Reynolds shear stress. The appropriate value of $\sigma(x)$ can be obtained through an iterative process by requiring that $-\overline{u'v'}_m$ obtained from the velocity profile and turbulent viscosity agrees with $-\overline{u'v'}_m$ determined from Equation (2.75). To evaluate μ_t, specifically μ_{to}, an initial guess for $\sigma(x)$ is necessary to begin the iteration process. Normally, the value of $\sigma(x)$ from the previous station was used. Then the intermediate distribution of μ_t, noted by μ_t^*, is determined by Equation (2.61) and the distribution of Reynolds stresses, $-\overline{u'v'}^*$, based on μ_t^* is calculated as

$$-\rho\overline{u'v'}^* = \mu_t^* \frac{\partial u}{\partial y} \tag{2.77}$$

If $-\overline{u'v'}_m^*$ obtained by Equation (2.77) is different from $-\overline{u'v'}_m$ determined from Equation (2.75), the value of $\sigma(x)$ must be modified. The velocity gradient at the point where $-\overline{u'v'}^*$ becomes maximum is then given by

$$\left.\frac{\partial u}{\partial y}\right|_m = \frac{-\rho\overline{u'v'}_m}{\mu_{t,m}^*} \tag{2.78}$$

The turbulent viscosity which gives the same maximum Reynolds stress obtained by Equation (2.75) should be

$$\tilde{\mu}_{t,m} = \frac{-\rho\overline{u'v'}_m}{\left.\frac{\partial u}{\partial y}\right|_m} = \frac{-\overline{u'v'}_m}{-\overline{u'v'}_m^*}\,\mu_{t,m}^* \tag{2.79}$$

The new value of $\sigma(x)$ can then be determined by letting

$$\mu_{t,m}(\sigma) = \tilde{\mu}_{t,m} \tag{2.80}$$

Since the expression for μ_t is nonlinear in terms of $\sigma(x)$, the solution to Equation (2.80) has to be determined by a numerical method. In this study, the simple Newton-Raphson method was applied as

$$\mu_{to,m}^{k+1} = \mu_{to,m}^{k} - \frac{\mu_{t,m}^{k} - \tilde{\mu}_{t,m}}{\left.\frac{\partial \mu}{\partial \mu_{to}}\right|_{m}^{k}} \tag{2.81}$$

where superscript k is the iteration level for the Newton-Raphson method. The converged value of $\mu_{to,m}^{k+1}$ becomes $(\mu_{to,m})_{new}$ and new value of $\sigma(x)$ is given by

$$\sigma_{new} = \sigma_{old} \frac{(\mu_{to,m})_{new}}{(\mu_{to,m})_{old}} \tag{2.82}$$

Since $\tilde{\mu}_{t,m}$ in Equation (2.79) is still dependent on $\mu_{t,m}^{*}$, i.e., the old value of $\sigma(x)$, this procedure of determining $\sigma(x)$ needs to be iteratively repeated.

The solution procedure for this closure can be summarized as follows:

1) For $x < x_o$, the flow is assumed to be in equilibrium so that the turbulent viscosity is provided by the Cebeci-Smith model.
2) At $x = x_o$, initial conditions are given by Equation (2.76) and $\overline{-u'v'}_{m,eq}$ is determined by the Cebeci-Smith model.
3) For $x > x_o$, $\mu_{t,eq}$ and $\overline{-u'v'}_{m,eq}$ are determined by Equation (2.71). Also, $\sigma(x)$ is lagged and $\overline{-u'v'}_{m}$ is calculated by Equation (2.75).

4) μ_t^* is calculated by Equation (2.61) and $-\overline{u'v'}_m^*$ is determined by Equation (2.77) using μ_t^* and the velocity profile.

5) If $-\overline{u'v'}_m \neq -\overline{u'v'}_m^*$, the new $\sigma(x)$ is calculated by Equation (2.82) and step (4) is repeated. Otherwise the procedure moves to step (6).

6) The turbulent viscosity is determined by $\mu_t = \mu_t^*$

This Johnson-King model has never been tested for a wide range of flows, but appears to be very effective in predicting both pressure driven and shock induced separated flows in the present study. However, this model still needs improvement in order to provide a better prediction and this will be discussed in a later section.

Before closing the discussion of turbulence modeling, it should be noted that for turbulent flows, transition from laminar to turbulent flow was assumed to occur at a fixed point near the leading edge and no particular formula for the transition point was used. Also, the apparent turbulent heat flux is modeled by Equation (2.44) with a constant value of the turbulent Prandtl number equal to 0.9.

F. Mathematical Model

Although the boundary-layer equations given by Equations (2.24)-(2.26) are believed to describe the compressible turbulent boundary layer fairly well, they are not in the best form to be solved numerically. The additional modifications and transformations used prior to obtaining the numerical solution are described next.

C-2

1. Prandtl's transposition theorem

The shear-layer coordinate system has been adopted because of several advantages pointed out in Section II. C. The difficulty associated with the use of the shear-layer coordinate is that the body surface does not lie along a coordinate line. According to Werle and Verdon (1980), this difficulty can be avoided by using the Prandtl's transposition theorem (1938). A detailed discussion of this theorem can be found in a article by Glauert (1957). In this transposition theorem, new variables defined by

$$\hat{x} = x \qquad \hat{y} = y + t \qquad \hat{v} = v + u\frac{dt}{dx} \tag{2.83}$$

are introduced into the boundary-layer equations, where t is defined as the distance between the shear-layer coordinate and the body coordinate as shown in Figure 2.

After application of this transposition theorem, the form of the boundary-layer equations does not change and the same boundary conditions are maintained except for the appearance of a caret (∧) over x, y and v. Provided that the magnitude of t is only a fraction of the boundary-layer thickness, the boundary-layer approximation remains valid. The only differences are that the wall boundary conditions, given by Equations (2.29) and (2.30), are prescribed at $\hat{y} = 0$ in place of y = -t and the velocity $\hat{v}$ is no longer the component of velocity in the y direction but becomes the component of velocity normal to lines of constant $\hat{y}$. Therefore, the caret (∧) will be dropped for x, y and v in the equations to follow.

2. Nondimensionalization

Variables in the boundary-layer equations are nondimensionalized as

$$X = \frac{x}{L} \qquad Y = \frac{y}{L} Re_\infty^{\frac{1}{2}} \qquad R = \frac{r}{L}$$

$$U = \frac{u}{u_\infty} \qquad V = \frac{v}{u_\infty} Re_\infty^{\frac{1}{2}} \qquad I = \frac{H}{u_\infty^2} \tag{2.84}$$

$$P = \frac{p}{\rho_\infty u_\infty^2} \qquad \tilde{\rho} = \frac{\rho}{\rho_\infty} \qquad \tilde{\mu} = \frac{\mu}{\mu_\infty} \qquad \tilde{\mu}_t = \frac{\mu_t}{\mu_\infty}$$

where Re_∞ is the Reynolds number based on the freestream value and L is the reference length of unity. Also note that the tildes (~) over the density and viscosities do not mean a mass-weighted average.

Using these nondimensional variables and Boussinesq's turbulent viscosity and turbulent conductivity concepts (see Equations (2.40) and (2.44)), the compressible boundary-layer equations for steady, axisymmetric flows, given by Equations (2.24)-(2.26), become

continuity

$$\frac{\partial}{\partial X}(\tilde{\rho}UR) + \frac{\partial}{\partial Y}(\tilde{\rho}VR) = 0 \tag{2.85}$$

momentum

$$\tilde{\rho}U\frac{\partial U}{\partial X} - \tilde{\rho}V\frac{\partial U}{\partial Y} = \tilde{\rho}_e U_e \frac{dU_e}{dX} + \frac{1}{R}\frac{\partial}{\partial Y}[R(\tilde{\mu} + \tilde{\mu}_t)\frac{\partial U}{\partial Y}] \tag{2.86}$$

energy

$$\tilde{\rho}U\frac{\partial I}{\partial X} - \tilde{\rho}V\frac{\partial I}{\partial Y} = \frac{1}{R}\frac{\partial}{\partial Y}\{R(\frac{\tilde{\mu}}{Pr} + \frac{\tilde{\mu}_t}{Pr_t})\frac{\partial I}{\partial Y}$$

$$+ R[(1 - \frac{1}{Pr})\tilde{\mu} + (1 - \frac{1}{Pr_t})\tilde{\mu}_t]U\frac{\partial U}{\partial Y}\} \tag{2.87}$$

The corresponding boundary conditions, given by Equations (2.28)-(2.31), can be rewritten as

$$\text{at } X = 0, \qquad U = 1.0 \qquad V = 0 \qquad I = I_\infty \tag{2.88}$$

$$\text{at } Y = 0, \qquad U = V = 0 \tag{2.89}$$

$$I = I_w \qquad \text{or} \qquad \left.\frac{\partial I}{\partial Y}\right|_w \text{ specified}$$

$$\text{as } Y \to \infty, \qquad U \to U_e \qquad I \to I_e \tag{2.90}$$

3. Coordinate transformation

The boundary-layer equations in the form of Equations (2.85)-(2.87) are formidable nonlinear coupled partial differential equations even for a very simple geometry. Therefore, there have been a number of efforts to simplify the equations, especially in the pre-computer era. Among these earlier works, a number of transformations relating compressible boundary layers to equivalent incompressible flows can be found useful even today.

The density variation can be accounted for by using a stream function, but the variable viscosity requires the introduction of a second similarity type variable. It was discovered by Illingworth (1950) that it was convenient to account for viscosity and density effects separately in the similarity variables. Lees (1956) combined the Illingworth transformation and Mangler transformation (1948) for axisymmetric flow and this transformation is often called the Illingworth-Levy-Lees-Dorodnitsyn transformation. This transformation

was modified by including the transverse curvature terms following the lead of Probstein and Elliott (1956). Such a transformation was used by Cebeci and Smith (1974), Carter (1978, 1981) and Lee and Pletcher (1985) for the analysis of compressible turbulent flows.

The stream function for compressible axisymmetric flow is defined as

$$\frac{\partial \psi}{\partial X} = - \tilde{\rho} V R \qquad \frac{\partial \psi}{\partial Y} = \tilde{\rho} U R \tag{2.91}$$

Use of equation (2.91) replaces the continuity equation. The similarity type independent variables are defined as

$$\xi = \int_0^X \tilde{\rho}_e \tilde{\mu}_e U_e R_o^2 dX \qquad \eta = \frac{U_e}{g(\xi)} \int_0^Y \tilde{\rho} R dY \tag{2.92}$$

where the normalizing function, $g(\xi)$, can be chosen arbitrarily. This transformation removes most of the effects of compressibility from the governing equations. Following Illingworth's work, when the direct method was used, $g(\xi)$ is given by

$$g(\xi) = (2\xi)^{\frac{1}{2}} \tag{2.93}$$

so that the singularity at $\xi = 0$ can be removed. As a result, the calculation can be started without difficulty at a leading edge or at a stagnation point. When the inverse method was used, $g(\xi)$ was taken to be equal to the displacement thickness (Carter, 1978). This choice tended to keep the number of grid points within the boundary layer nearly constant.

Defining new dependent variables,

$$F = \frac{U}{U_e} \qquad G = \frac{I}{I_e} \tag{2.94}$$

Equations (2.85)-(2.87) become

continuity

$$gF = \frac{\partial \psi}{\partial \eta} \tag{2.95}$$

momentum

$$g^2 F\frac{\partial F}{\partial \xi} - g\frac{\partial \psi}{\partial \xi}\frac{\partial F}{\partial \eta} = g^2\beta(G - F^2) + \frac{\partial}{\partial \eta}[C_\ell(1 + \frac{\mu_t}{\mu})\frac{\partial F}{\partial \eta}] \tag{2.96}$$

energy

$$g^2 F\frac{\partial G}{\partial \xi} - g\frac{\partial \psi}{\partial \xi}\frac{\partial G}{\partial \eta} = \frac{\partial}{\partial \eta}[\frac{C_\ell}{Pr}(1 + \frac{\mu_t Pr}{\mu\ Pr_t})\frac{\partial G}{\partial \eta}]$$

$$+ C_E\frac{\partial}{\partial \eta}\{C_\ell[(1 - \frac{1}{Pr}) + (1 - \frac{1}{Pr_t})\frac{\mu_t}{\mu}]F\frac{\partial F}{\partial \eta}\} \tag{2.97}$$

where the nondimensional pressure gradient parameter, β, and the Chapman-Rubesin (1949) type parameter, C_ℓ, are defined as

$$\beta = \frac{1}{M_e}\frac{dM_e}{d\xi} \qquad C_\ell = \frac{\rho\mu}{\rho_e\mu_e}(\frac{R}{R_o})^2 \tag{2.98}$$

and assuming H_e is constant, the Eckert type parameter C_E is given by

$$C_E = \frac{U_e^2}{I_e} = \frac{(\gamma-1)\ M_e^2}{1 + 0.5(\gamma-1)M_e^2} \tag{2.99}$$

Care must be taken in evaluating the convective terms in Equations (2.96) and (2.97) at the leading edge when $\xi = 0$. The limiting value of

$g^2 F\frac{\partial}{\partial \xi}$ terms is zero as $\xi \to 0$; however, the $g\frac{\partial \psi}{\partial \xi}\frac{\partial}{\partial \eta}$ terms in Equations (2.96) and (2.97) has a finite limit as $\xi \to 0$. To obtain the most accurate numerical solution at the leading edge, a new dependent variable, W, defined as

$$W = - g(\xi) \frac{\partial \psi}{\partial \eta} \tag{2.100}$$

was introduced into Equations (2.96) and (2.97) and the continuity equation, Equation (2.95), was reformulated from Equation (2.85) using W instead of ψ. This procedure was used only at the leading edge. The stream function formulation given by Equations (2.95)-(2.97) was used thereafter. The details of solution procedure at the leading edge are quite similar to those used for the stream function formulation and will not be discussed further.

This transformation was not used to solve the transport equation for the maximum Reynolds stress in the Johnson and King turbulence model because that transport equation is an ordinary differential equation and the transformation offered no advantage.

The corresponding boundary conditions in the transformed coordinates for Equations (2.95)-(2.97) are given as

$$\text{At } \eta = 0, \qquad F = \psi = 0 \tag{2.101}$$

$$G = G_w \quad \text{or} \quad \left.\frac{\partial G}{\partial \eta}\right|_w \text{ specified}$$

$$\text{As } \eta \to \infty, \qquad F = G = 1.0 \tag{2.102}$$

The definition of the displacement thickness, Equation (2.32), gives the value of the stream function at the edge of the boundary layer as

$$\psi_e = g(\xi) \int_0^{\eta_e} (\frac{\rho_e}{\rho})d\eta - m \tag{2.103}$$

where m is the nondimensional mass flux defined as

$$m = \tilde{\rho}_e U_e R_o \tilde{\delta}^* \tag{2.104}$$

and $\tilde{\delta}^*$ is the nondimensional displacement thickness.

Equations (2.96) and (2.97) are parabolic and can be solved in a forward marching manner in the streamwise, ξ, direction as long as $F > 0$. In regions of reversed flow, i.e., $F < 0$, the correct marching direction is the negative direction which is the true "streamwise" direction. With flow reversal, the solution to the complete boundary-layer equations can be advanced in the positive coordinate direction only iteratively and velocities in regions of reversed flow must be stored. In each iterative sweep, the correct difference representation for convective terms is provided through windward differencing which honors the appropriate marching direction. This method has been used successfully by many investigators (Klineberg and Steger, 1974; Carter and Wornom, 1975; Cebeci, 1976).

On the other hand, a much simpler alternative to the multiple sweep procedure was proposed by Reyhner and Flügge-Lotz (1968). According to their suggestion, which is known as the FLARE approximation, the streamwise convective term $F\partial\phi/\partial\xi$ is replaced by $C|F|\partial\phi/\partial\xi$ where C is zero or small positive constant if $F < 0$ and one if $F \geq 0$. This term has been observed to be very small in regions of reversed flow. The validity of the FLARE approximation in the case of small separation

regions has been demonstrated in many calculations (Carter, 1974; Williams, 1975; Cebeci et al., 1979; Kwon and Pletcher, 1981) and also confirmed by the experimental observations of Simpson et al. (1974). Recently, Davis and Carter (1984) showed that the FLARE approximation still gives results comparable to those obtained from the windward differencing scheme with reversed flow velocities even up to 28% of the edge velocity. Throughout the present study, the FLARE approximation was used for most of the calculations. The windward differencing scheme was also employed, but only for limited cases for purposes of comparison.

G. Numerical Method

This section describes the method used to solve the boundary-layer equations developed in the previous section. The continuity and momentum equations were solved in a coupled manner using a fully implicit finite-difference scheme. This results in a block tridiagonal system with the blocks being square matrices of order 2. Kwon and Pletcher (1981) reported that coupling of the continuity and momentum equations eliminated the wiggles in the regions of separation which appeared in the solution when an uncoupled scheme was used. The energy equation and the additional transport equation used in the Johnson and King turbulence model were solved in an uncoupled manner.

Following a discussion of the computational grid, the finite-difference discretization and solution procedures will be presented.

1. Computational grid

A representative example of the finite-difference grid used for this study is shown in Figure 4. However, the mesh shown in Figure 4 is much coarser than those used in the actual calculation. The i index is used to specify the X-position. The point i = 1 corresponds to the leading edge. The j index is used to specify the Y-position with j = 1 corresponding to the points at the wall and j = NJ corresponding to the points at the outer edge of the computational domain. The formulation of the grid can have a significant effect on the convergence and accuracy of the solution. The optimum method of grid formulation is usually achieved through trial and error and is different depending on the flow case. For laminar calculations, an equal grid spacing was used in the normal (η) direction. For turbulent flows, wall functions were not used and the turbulence model was applied directly to the wall as pointed out earlier. Therefore, a variable η grid spacing was used so as to have more grid points concentrated near the wall and to avoid an excessive number of grid points.

In this study, the grid scheme proposed by Cebeci and Smith (1974) was employed. This scheme maintains a constant ratio between two adjacent grid increments as

$$\frac{\Delta\eta_+}{\Delta\eta_-} = K \tag{2.105}$$

where K is constant. In some cases, the accuracy of the solution was somewhat sensitive to the value of K used. A value between 1.05 and 1.10 generally gave the most reliable results. In all turbulent cases,

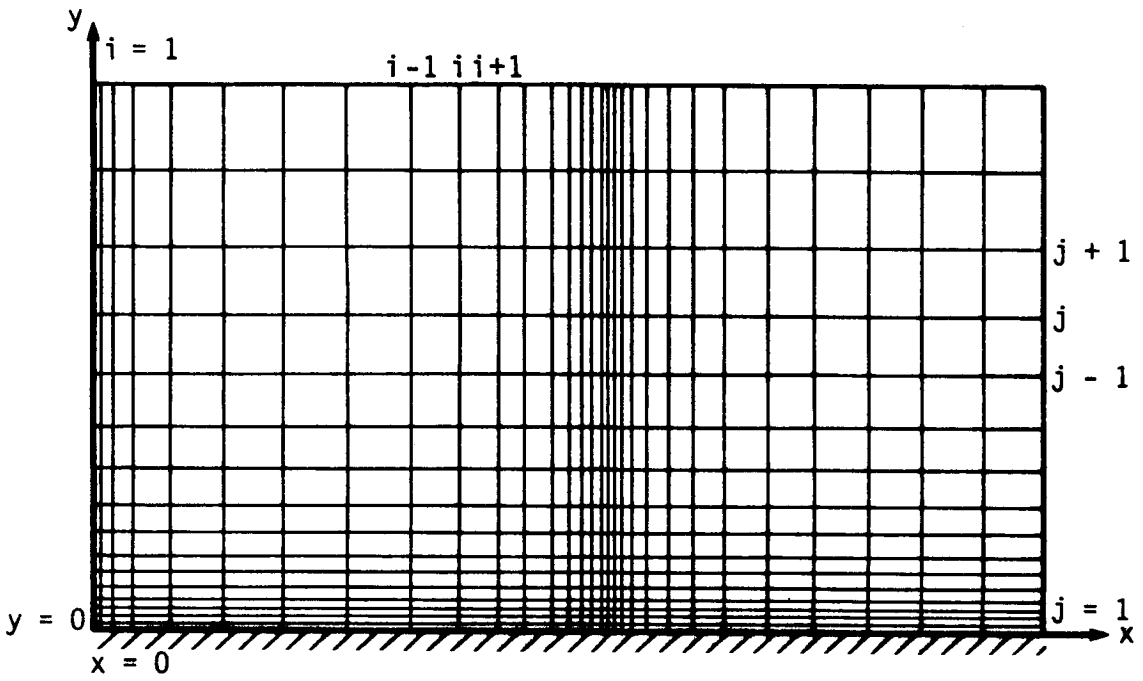

FIGURE 4. Finite-difference grid for the viscous analysis

the grid increment nearest the wall, $\Delta\eta_1$ ($= \eta_2 - \eta_1$), was chosen so that the corresponding Δy^+ did not exceed 1.0, and a number of mesh points, usually 10, were placed within the viscous sublayer.

Variable grid spacing was used in the streamwise (ξ) direction for both laminar and turbulent flows with most of the points concentrated in the region where the strongest pressure gradient was expected. A good example of this would be the concentration of points near an experimentally observed shock position. The simultaneous viscous-inviscid interaction method requires the same grid spacing in ξ direction for both the boundary-layer equations and the potential equation. On the other hand, the two grids can be independent when the semi-inverse viscous-inviscid interaction method is used although the same grid was generally used in the present study. The grid spacing in the ξ direction was generated using a stretching transformation similar to the one proposed by Roberts (1971). This will be discussed in detail in the inviscid analysis section. Outside of the interaction region, the streamwise grid spacing was chosen so as to be approximately proportional to the thickness of the boundary layer. A typical mesh size used 100 increments in the streamwise direction and 50 to 70 in the normal direction.

2. Finite-difference representation

The set of nondimensionalized boundary-layer equations in the transformed coordinates discussed in Section II. F was solved over the region of interest using a fully implicit finite-difference method. In this section, the finite-difference scheme employed to solve the

boundary-layer equations and the equation for turbulence modeling is described.

There have been many finite-difference methods proposed to solve the boundary-layer equations. These can be generally divided into explicit and implicit methods. The explicit method is simple but is often constrained by a stability condition, i.e., suffers from a severe limitation on marching step size. On the other hand, most implicit schemes in common usage are inherently stable. Among them, the Crank-Nicholson implicit scheme is second-order-accurate in both the streamwise and normal directions but barely satisfies the stability condition. This procedure has occasionally been found to be unstable for turbulent flows (Anderson et al., 1984). The fully implicit scheme used in the present study is first-order-accurate in the streamwise direction and second-order-accurate in the normal direction and is also unconditionally stable. When the fully implicit scheme is used, linearization and possible adjustments in the differencing in order to maintain diagonal dominance must be dealt with as in any other implicit scheme. The linearizing procedure is given in the next section.

a. Continuity and momentum equations The finite-difference representation of the continuity and the momentum equations is given as follows.

continuity

$$\frac{g}{2}(F_j^i + F_{j-1}^i) = \frac{1}{\Delta\eta_-}(\psi_j^i - \psi_{j-1}^i) \qquad (2.106)$$

momentum

With the FLARE approximation,

$$Cg^2|F_j^i|\overleftarrow{\delta}_\xi F_j^i - g\overleftarrow{\delta}_\xi \psi_j^i \, \delta_\eta F_j^i = g^2\beta(G_j^i - F_j^{i^2}) + \overleftarrow{\delta}_\eta(N_{j+\frac{1}{2}}\overrightarrow{\delta}_\eta F_j^i) \qquad (2.107)$$

where $C = 1$ if $F \geq 0$ and $C = 0$ if $F < 0$.

With the windward differencing,

$$g^2 F_j^i \overleftrightarrow{\delta}_\xi F_j^i - g\overleftrightarrow{\delta}_\xi \psi_j^i \, \delta_\eta F_j^i = g^2\beta(G_j^i - F_j^{i^2}) + \overleftarrow{\delta}_\eta(N_{j+\frac{1}{2}}\overrightarrow{\delta}_\eta F_j^i) \qquad (2.108)$$

where δ, $\overleftarrow{\delta}$ and $\overrightarrow{\delta}$ are central, backward and forward difference representations in the directions indicated by the subscript, respectively.

$$\delta_\eta \phi_j^i = \frac{1}{(\Delta\eta_+ + \Delta\eta_-)}\left[\frac{\Delta\eta_-}{\Delta\eta_+}(\phi_{j+1}^i - \phi_j^i) + \frac{\Delta\eta_+}{\Delta\eta_-}(\phi_j^i - \phi_{j-1}^i)\right]$$

$$\overrightarrow{\delta}_\eta \phi_j^i = \frac{1}{\Delta\eta_+}(\phi_{j+1}^i - \phi_j^i) \qquad (2.109)$$

$$\overleftarrow{\delta}_\eta \phi_j^i = \frac{1}{\Delta\eta_-}(\phi_j^i - \phi_{j-1}^i)$$

where ϕ is a general dependent variable. A similar representation applies to the operators in the ξ direction.

The double arrow notation in Equation (2.108) on the ξ difference operators means that the difference is always upwind, which is a backward difference when $F > 0$ and a forward difference when $F < 0$. The nondimensional diffusion coefficient $N_{j+\frac{1}{2}}$ was evaluated as the arithmetic average of these quantities at neighboring integer grid points as

$$N_{j+\frac{1}{2}} = \frac{1}{2}(N_j + N_{j+1}) \tag{2.110}$$

where

$$N_j = \left[C_\ell\left(1 + \frac{\mu_t}{\mu}\right)\right]_j \tag{2.111}$$

When the continuity and momentum equations are solved in a coupled manner using an inverse procedure, four variables, F, ψ, g and β are generally treated as unknown quantities, while flow property variables like G, ρ and μ are regarded as known quantities because they are supplied from solutions of the uncoupled equations. Since these unknown variables are included in the coefficients at ith level, the finite-difference equations, Equations (2.106)-(2.108), are algebraically nonlinear. There are several ways to linearize these equations, as discussed in Anderson et al. (1984). Kwon and Pletcher (1981), who studied the effect of several linearization methods for separated flows, reported that among the methods considered only the Newton linearization with coupling of the continuity and momentum equations resulted in a well-behaved solution when large separation regions occurred. The Newton linearization with coupling is also believed to accelerate the convergence of the iterative solution (Keller and Cebeci, 1972; Carter, 1978; Kwon and Pletcher, 1981).

In the present study, the Newton linearization with coupling was used on the nonlinear terms in Equations (2.106)-(2.108). The density and the diffusion terms were iteratively updated after solutions of the energy equation and the turbulence modeling equation were obtained. The

Newton linearization treats the terms which cause the nonlinearity as

$$\phi = \tilde{\phi} + \delta_{\phi} \tag{2.112}$$

where $\tilde{\phi}$ is a provisional value from a previous iteration level and δ_{ϕ} is a change in ϕ between two iterative solutions. First, every unknown variable in Equations (2.106)-(2.108) is replaced by Equation (2.112) and the simple multiplication procedure is carried out. Then terms of power greater than the first in δ_{ϕ} are dropped, and the equations become linear. The provisional values are established by initial guesses for the first iteration and are then iteratively updated at each streamwise station. When the convergence is achieved, i.e., δ_{ϕ} becomes negligibly small, the solution advances to the next streamwise station. The convergence criterion for this local Newton linearization procedure is based on the maximum change in F's and ψ's between two successive iterations, i.e,

$$\varepsilon_c \geq \text{MAX} \left[\, |\delta_{F_j}|, \, |\delta_{\psi_j}|/\psi_e \, \right] \tag{2.113}$$

and ε_c was set equal to 1×10^{-3} in all the present calculations.

The conventional way of providing the initial guess for the provisional value is using the value from the converged solution at the previous station (lagging) and 5-10 iterations were usually required for local convergence in compressible flows. Sometimes, 20-30 iterations were required near the point of separation. In the simultaneous viscous-inviscid interaction method, the viscous calculations take most of the computing time and a large number of local iterations due to the

linearization is undesirable. It was possible to reduce the number of iterations in the simultaneous viscous-inviscid interaction procedure by using a pseudo-time dependent approach, that is, the initial values were taken from solutions of the previous interaction sweep if the overall interaction process was reasonably converged. Convergence for the local Newton linearization procedure was usually obtained if the level of convergence error for the overall interaction process was less than 5%. The convergence criterion for the overall interaction procedure is based on the relative change of the nondimensional mass flux m (see Equation (4.2)). For the first few, usually 10, global interaction sweeps, the initial guesses for the first provisional values were provided conventionally and then switched to the pseudo-time dependent approach. Although this remedy required additional storage for dependent variables, F, ψ and G, over the interaction region, this proved to be so efficient that it required only 2-3 iterations at each streamwise station. Thus, the total computing time was reduced to only about 20% of that needed when lagging from the previous station is used. However, in the semi-inverse interaction method, the savings in computing time was relatively small because the inviscid calculations took the largest portion of the total computing time.

Using the Newton linearization with coupling as described above, Equations (2.106)-(2.108) can be written as

$$b_j F^i_{j-1} + d_j F^i_j - \psi^i_j + \psi^i_{j-1} = h_j \beta + s_j g + c_j \qquad (2.114)$$

$$B_j F^i_{j-1} + D_j F^i_j + A_j F^i_{j+1} + E_j \psi^i_j = H_j \beta + S_j g + C_j \qquad (2.115)$$

The coefficients in the above equations, which are assumed known from the solutions of the previous (i-1) station and previous interaction, are given in Appendix A for both the FLARE approximation scheme and the windward difference scheme.

The appropriate boundary conditions must be given in a discretized form in order to complete the finite-difference system of governing equations. At the wall surface, Equation (2.101) becomes

$$F_1 = \psi_1 = 0 \tag{2.116}$$

In order to maintain the same form as the coefficients of the blocks for $2 \leq j \leq NJ-1$, the coefficients are specified as

$$A_1 = B_1 = H_1 = S_1 = C_1 = b_1 = s_1 = h_1 = c_1 = 0 \tag{2.117-a}$$

$$D_1 = E_1 = d_1 = 1.0 \tag{2.117-b}$$

At the edge of the boundary layer the continuity equation still holds and $F_{NJ} = 1.0$ should be represented in Equation (2.115) by choosing

$$A_{NJ} = B_{NJ} = E_{NJ} = H_{NJ} = S_{NJ} = 0 \tag{2.118-a}$$

$$D_{NJ} = C_{NJ} = 1.0 \tag{2.118-b}$$

The procedure concerning the additional conditions required for the direct and inverse methods will be given in Section II. G. 3.

b. Energy equation As was the case for the momentum equation, convective terms in the energy equation require appropriate treatment to

make forward marching possible in regions of reversed flow. The FLARE approximation was generally used, but windward differencing was also used for the purpose of establishing the validity of the FLARE approximation.

With the FLARE approximation,

$$Cg^2|F_j^i|\overleftarrow{\delta}_\xi G_j^i - g\overleftarrow{\delta}_\xi \psi_j^i \, \delta_\eta G_j^i = \overleftarrow{\delta}_\eta (N_{1,j+\frac{1}{2}} \overrightarrow{\delta}_\eta G_j^i) + C_E \overleftarrow{\delta}_\eta N_{2,j+\frac{1}{2}} \qquad (2.119)$$

With the windward differencing,

$$g^2 F_j^i \overleftrightarrows{\delta}_\xi G_j^i - g\overleftrightarrows{\delta}_\xi \psi_j^i \, \delta_\eta G_j^i = \overleftarrow{\delta}_\eta (N_{1,j+\frac{1}{2}} \overrightarrow{\delta}_\eta G_j^i) + C_E \overleftarrow{\delta}_\eta N_{2,j+\frac{1}{2}} \qquad (2.120)$$

where

$$N_{1,j+\frac{1}{2}} = \frac{C_\ell}{Pr}\left(1 + \frac{\mu_t Pr}{\mu \, Pr_t}\right)_{j+\frac{1}{2}} \qquad (2.121\text{-a})$$

$$N_{2,j+\frac{1}{2}} = C_\ell\left[\left(1 - \frac{1}{Pr}\right) + \left(1 - \frac{1}{Pr_t}\right)\frac{\mu_t}{\mu}\right] F\frac{\partial F}{\partial \eta}\Big|_{j+\frac{1}{2}} \qquad (2.121\text{-b})$$

Since the continuity and momentum equations were solved first uncoupled from the energy equation, the velocity variables, F and ψ, were known. Because of this, the energy equation is linear in G except for the density and the viscous diffusion terms which can be iteratively updated. However, since the diffusion coefficients in the momentum equation are also strong functions of temperature, the energy equation was solved iteratively together with the iterative solution procedure for the continuity and momentum equations.

By grouping coefficients of the unknown G's, Equations (2.119) and (2.120) can be rewritten in tridiagonal form as

$$B_j G^i_{j-1} + D_j G^i_j + A_j G^i_{j+1} = C_j \qquad (2.122)$$

The coefficients are known from intermediate solutions of the continuity and momentum equations and the solution of the energy equation at the previous station and are given in Appendix B. These algebraic equations can be easily solved using the Thomas algorithm.

Boundary conditions for the energy equation should be prescribed in a finite-difference form. When enthalpy is fixed at the wall,

$$B_1 = A_1 = B_{NJ} = A_{NJ} = 0 \qquad (2.123\text{-a})$$

$$D_1 = D_{NJ} = C_{NJ} = 1.0 \qquad C_1 = G_w \qquad (2.123\text{-b})$$

If the heat flux is given, a Taylor series expansion or polynomial fitting can be used to obtain the appropriate finite-difference expression. However, enthalpy was always specified at the wall in the calculations of the present study.

c. Johnson and King turbulence model The transport equation for the maximum Reynolds stress given by Equation (2.75) is discretized with a first-order-accurate backward finite-difference approximation.

$$\delta_x \theta^i = N_3 \theta^i + N_4 \qquad (2.124)$$

where

$$N_3 = - \frac{a_1}{2 u_m L_m \theta_{eq}} \qquad (2.125\text{-a})$$

$$N_4 = - N_3 \theta_{eq} \{1 + \frac{C_{dif} L_m}{a_1 \delta [0.7 - (y/\delta)_m]} |1 - \sigma(x)^{\frac{1}{2}}| \} \qquad (2.125\text{-b})$$

This equation can be rewritten simply as

$$\theta^i = A_i \theta^{i-1} + B_i \tag{2.126}$$

where

$$A_i = \frac{1}{1 - N_3 \Delta x} \qquad B_i = \frac{N_4 \Delta x}{1 - N_3 \Delta x} \tag{2.127}$$

Using an initial condition given by Equation (2.76), Equation (2.126) can be easily integrated along the x coordinate. During the Newton iteration process for the continuity and momentum equations at each local station, Equation (2.126) is also repeatedly solved.

3. Method of solution

In this section, the solution procedure for the boundary-layer equations is presented. As discussed in Section II. G. 2, the continuity and momentum equations are solved in a coupled manner and the energy equation and the transport equation arising in the Johnson-King turbulence model are solved in an uncoupled manner. The pressure gradient, β, is evaluated either directly using the specified edge velocity (direct mode) or indirectly through the specified mass flux, m, (inverse mode). The parameter m is also either known explicitly from the interaction law (semi-inverse procedure), or determined implicitly during the solution procedure coupled with the inviscid scheme (simultaneous procedure).

Equations (2.114) and (2.115) can be rewritten for j = 2 to NJ-1 as

$$\begin{bmatrix} B_j & 0 \\ b_j & 1 \end{bmatrix} \begin{bmatrix} F^i_{j-1} \\ \psi^i_{j-1} \end{bmatrix} + \begin{bmatrix} D_j & E_j \\ d_j & -1 \end{bmatrix} \begin{bmatrix} F^i_j \\ \psi^i_j \end{bmatrix} + \begin{bmatrix} A_j & 0 \\ 0 & 0 \end{bmatrix} \begin{bmatrix} F^i_{j+1} \\ \psi^i_{j+1} \end{bmatrix} = \begin{bmatrix} H_j\beta+S_jg+C_j \\ h_j\beta+s_jg+c_j \end{bmatrix} \quad (2.128)$$

For a given ξ station, these equations form a block tridiagonal system with each block consisting of a two by two matrix as

$$\begin{bmatrix} [\bar{D}]_1 & [\bar{A}]_1 & [0] & & & \\ [\bar{B}]_2 & [\bar{D}]_2 & [\bar{A}]_2 & [0] & & \\ [0] & [\bar{B}]_3 & [\bar{D}]_3 & [\bar{A}]_3 & [0] & \\ & [0] & [\bar{B}]_j & [\bar{D}]_j & [\bar{A}]_j & [0] \\ & & [0] & [\bar{B}]_{NJ} & [\bar{D}]_{NJ} & \end{bmatrix} \begin{bmatrix} [\bar{U}]_1 \\ [\bar{U}]_2 \\ [\bar{U}]_3 \\ \vdots \\ [\bar{U}]_j \\ \vdots \\ [\bar{U}]_{NJ} \end{bmatrix} = \begin{bmatrix} [\bar{C}]_1 \\ [\bar{C}]_2 \\ [\bar{C}]_3 \\ \vdots \\ [\bar{C}]_j \\ \vdots \\ [\bar{C}]_{NJ} \end{bmatrix} \quad (2.129)$$

where

$$[\bar{A}]_j = \begin{bmatrix} A_j & 0 \\ 0 & 0 \end{bmatrix} \quad [\bar{B}]_j = \begin{bmatrix} B_j & 0 \\ b_j & 1 \end{bmatrix} \quad [\bar{D}]_j = \begin{bmatrix} D_j & E_j \\ d_j & -1 \end{bmatrix}$$

$$[\bar{U}]_j = \begin{bmatrix} H_j\beta + S_jg + C_j \\ h_j\beta + s_jg + c_j \end{bmatrix} \quad [\bar{C}]_j = \begin{bmatrix} u^i_j \\ \psi^i_j \end{bmatrix} \quad (2.130)$$

The coefficients in Equation (2.130) are listed in Appendix A.

Equation (2.129) can be solved by using an efficient form of a block elimination procedure which is known as the modified Thomas algorithm (Blottner, 1975). After elimination of the lower diagonal terms, $[\overline{B}]_j$, and rearrangement, the equations are reduced to a bidiagonal recurrence form as

$$F_j^i = A_j^* F_{j+1}^i + H_j^* \beta + S_j^* g + C_j^* \tag{2.131}$$

$$\psi_j^i = a_j^* F_{j+1}^i + h_j^* \beta + s_j^* g + c_j^* \tag{2.132}$$

for j = 1 to NJ-1. The coefficients in Equations (2.131) and (2.132) are given in Appendix C.

Using the no slip boundary condition at the wall, given by Equation (2.117), the coefficients at j = 1 in Equations (2.131) and (2.132) becomes

$$A_1^* = H_1^* = S_1^* = C_1^* = a_1^* = h_1^* = s_1^* = c_1^* = 0 \tag{2.133}$$

Then the coefficients at $2 \leq j \leq NJ-1$ in Equations (2.131) and (2.132) can be calculated from the wall to the outer edge of the computation domain as discussed in Appendix C.

With boundary conditions at j = NJ, given by Equation (2.118), Equation (2.132) becomes

$$F_{NJ}^i = 1.0 \tag{2.134}$$

$$\psi_{NJ}^i = h_{NJ}^* \beta + s_{NJ}^* g + c_{NJ}^* \tag{2.135}$$

Therefore, if the pressure gradient, β, and $g(\xi)$ are known, solutions

for F's and ψ's across the computational domain can be obtained by the simple back-substitution procedure starting from the edge of the boundary at j = NJ using Equations (2.134) and (2.135) and proceeding toward the wall to j = 1 using Equations (2.131) and (2.132).

In the direct mode, the pressure gradient, β, is determined by the edge Mach number, M_e, which can be easily calculated from specified edge velocity, U_e, and $g(\xi)$ is defined as $(2\xi)^{\frac{1}{2}}$ where ξ is fixed at each X location because ξ is a function of X and U_e only.

In the inverse mode, if $g(\xi)$ is set equal to m, the value of ψ_e given by Equation (2.103) can then be written in a finite-difference form as

$$\psi_{NJ}^{i} = m(I_\rho - 1) \tag{2.136}$$

where

$$I_\rho = \int_0^{\eta_e} (\frac{\rho_e}{\rho}) d\eta \tag{2.137}$$

The integral value I_ρ is iteratively updated since the energy equation is solved uncoupled. Also, Equation (2.135) becomes

$$\psi_{NJ}^{i} = h_{NJ}^{*}\beta + s_{NJ}^{*}m + c_{NJ}^{*} \tag{2.138}$$

Elimination of ψ_{NJ}^{i} from Equations (2.136) and (2.138) results in

$$\beta = a_V m + b_V \tag{2.139}$$

where

$$a_V = (I_\rho - 1 - s^*_{NJ}) / h^*_{NJ} \qquad b_V = - c_{NJ} / h^*_{NJ} \tag{2.140}$$

This equation describes the asymptotic relationship between the pressure gradient and the mass flux, m, in the finite-difference form of the boundary-layer equations. If the value of m is known as in the semi-inverse interaction method, β is thus determined and the solution can be obtained through the recurrence formulas, Equations (2.131), (2.132), (2.134) and (2.135) as in the direct method. In the simultaneous interaction method, the value of m is regarded as an unknown quantity and is determined so as to satisfy an additional relationship between β and m obtained from the inviscid analysis. This additional relationship and the associated numerical details will be discussed in Chapter IV.

Since the Newton linearization is used, the solution of the boundary-layer equations is repeated iteratively. Therefore, the coefficients in Equations (2.128)-(2.140) must be updated using the most recent solutions and the solutions obtained from Equations (2.131), (2.132) and (2.135) must converge in order to proceed to the next streamwise station. The convergence criterion was given by Equation (2.113).

This solution procedure can be summarized as follows:

1) Assume the initial distributions of F, ψ and G across the computational domain of the boundary layer using either lagging or the pseudo-time dependent approach.

2) Calculate the turbulent viscosity.

3) Calculate the coefficients in Equations (2.131), (2.132) and (2.135) for the continuity and momentum equations.

4) In case of the direct mode, go to step (7). Otherwise, go to step (5).

5) Determine the value of m in the inverse mode (see Chapter IV).

6) Calculate β using Equation (2.139).

7) Calculate the edge stream function, ψ_{NJ}, using Equation (2.135) in the direct mode and Equation (2.138) in the inverse mode, respectively.

8) Calculate the solutions of F and ψ across the computational domain of the boundary layer using Equations (2.131) and (2.132) by means of back-substitution.

9) Calculate the coefficients in Equation (2.122) for the energy equation.

10) Calculate the solution of G using the Thomas algorithm.

11) Examine convergence of the solutions using Equation (2.113). If the solutions meet the convergence criterion, proceed to the next streamwise station. Otherwise, return to step (2).

III. INVISCID ANALYSIS

In this chapter, the solution procedure for compressible inviscid flow is described. The governing equations and the appropriate boundary conditions are presented. The numerical methods used in solving the governing equations are discussed. Numerical grid generation is also presented. It should be noted that some of the variables used in the inviscid analysis may be denoted by the same symbols as used in the viscous analysis but the symbols may have different meanings. If this occurs, they will be discerned by subscripts i and v for the inviscid and viscous analysis, respectively.

A. Velocity Potential Equation

As discussed in Chapter II, viscosity effects in flows for sufficiently large Reynolds numbers are confined to a thin boundary layer near solid surfaces. As a result, the major portion of the flow region, which is inviscid outside the boundary layer, is governed by a much simpler set of equations. This reduced set of equations, called the Euler equations, can be obtained by neglecting viscous terms in the complete Navier-Stokes equations. The Euler equations consist of a set of first order partial differential equations, generally 4 equations (continuity, two momentum and an energy equations) for 2-dimensional flows.

With an additional assumption of a steady, irrotational and isentropic flow, the Euler equations can be further simplified to a velocity potential equation (sometimes also referred to as the full

potential equation). The velocity potential formulation results in a single second order partial differential equation. If the flow over a slender body is considered, where the freestream is only slightly disturbed, the velocity potential equation can be simplified to form the transonic small disturbance (TSD) potential equation. This formulation provides the advantage of simplicity, especially in the application of the wall boundary conditions. However, the TSD equation suffers restrictions in applications because it is valid only for flows over a thin body. Recent computational evidence (Holst and Ballhaus, 1979; Melnik, 1981; Green and South, 1983) suggests that the velocity potential formulation is the most efficient one among the three (Euler, potential and TSD) formulations in terms of accuracy to cost ratio for a wide range of inviscid transonic applications.

Isentropic flow has been assumed in developing the potential formulation, thus the entropy does not change across a shock wave according to the potential solution. The actual entropy production across the shock wave is proportional to the third power of the shock strength based on the normal component of Mach number (Liepmann and Roshko, 1957) as

$$\Delta S \propto (M_n^2 - 1)^{3/2} \tag{3.1}$$

Therefore, the assumption of no entropy change across the weak shock is reasonable if the normal component of Mach number, M_n is close to one. The velocity potential equation is generally regarded as a reasonable approximation as long as the normal component of Mach number ahead of

the shock wave is less than 1.3.

The potential equation can be written and solved numerically in two forms known as the conservative and the nonconservative forms. South and Jameson (1973) developed a numerical solution scheme for the full potential equation in the nonconservative form using a line relaxation algorithm. This method was implemented into the RAXBOD code by Keller and South (1976) and the computational code has been used widely by many investigators. Newman and South (1976) reported that the nonconservative scheme generated a source of mass at the shock wave, which was caused by switching from the upwind to the central differencing without a proper transition operator. The strength of this mass source is not unique and depends on the local mesh size. A streamline pattern is deflected substantially by this effective mass source downstream of the shock wave so that the global mass balance is destroyed. As a result, the nonconservative scheme produces a weaker shock located upstream of that which would be obtained by a result of the Euler equations (Lock, 1981; Green and South, 1983). It should be noted that the fortuitous good agreement between the nonconservative scheme and experimental observations is due to the fact that this effective mass production happens to simulate the interaction of the shock wave and the viscous layer.

Use of the conservative scheme maintains the conservation of mass, but often results in an overprediction of the shock strength (Steger and Baldwin, 1972; Green and South, 1983). However, there is increasing evidence by Melnik (1978, 1981) and Lax (1954) that a correct approach

should be based on the conservative scheme with viscous interaction used to correct the shock strength and position. In the present study, the velocity potential equation in the fully conservative form is used to describe the inviscid transonic irrotational flow.

With the assumption of a steady isentropic inviscid flow without body forces or external heat transfer, the conservation laws introduced in Section II. A are simplified as

continuity

$$\nabla\cdot(\rho\vec{V}) = 0 \tag{3.2}$$

momentum and energy

$$H = h + \frac{\vec{V}\cdot\vec{V}}{2} = \frac{\gamma}{\gamma-1}\frac{p}{\rho} + \frac{\vec{V}\cdot\vec{V}}{2} \tag{3.3}$$

According to Crocco's theorem, a steady, inviscid, adiabatic, isentropic flow is also irrotational, thus permitting the use of a velocity potential, ϕ, defined as

$$\vec{V} = \nabla\phi \tag{3.4}$$

For the isentropic flow of a perfect gas,

$$\frac{p}{\rho^{\gamma}} = \text{constant} \tag{3.5}$$

$$a = (\gamma RT)^{\frac{1}{2}} \tag{3.6}$$

where a is the speed of the sound in a perfect gas.

1. Coordinate system

The coordinate system chosen for the present inviscid analysis is presented in Figure 5. For axisymmetric external flow, an axisymmetric cylindrical coordinate system is used, where the abscissa, x, is measured along the axis of symmetry and the ordinate, r, is measured in the direction normal to the axis as shown in Figure 5. The velocity components in the x and r direction are noted as u and v, respectively. All the body configurations considered in this study are assumed to extend from the inflow to the outflow boundary. A general computational domain in physical coordinates looks like Figure 6.

2. Governing equations and boundary conditions

a. Governing equations The continuity equation can be written in the aforementioned coordinates as

$$\frac{\partial}{\partial x}(\rho u r) + \frac{\partial}{\partial y}(\rho v r) = 0 \tag{3.7}$$

With the introduction of the velocity potential into the continuity equation, the potential equation is given by

$$(\rho \phi_x r)_x + (\rho \phi_r r)_r = 0 \tag{3.8}$$

b. Boundary conditions A solution of Equation (3.8) can be obtained by prescribing proper boundary conditions along the boundaries of the computational domain as shown in Figure 6.

In the far field with a subsonic freestream, all perturbations are required to vanish as the flow approaches uniform conditions.

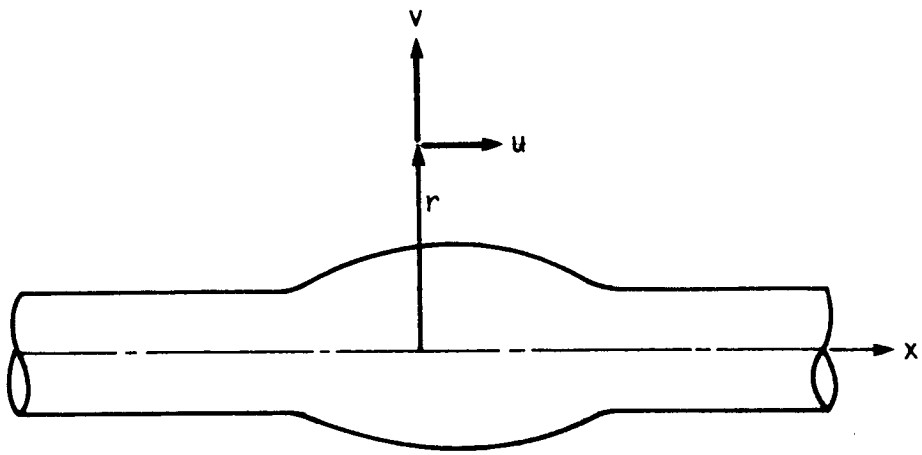

FIGURE 5. Coordinate system for the inviscid analysis

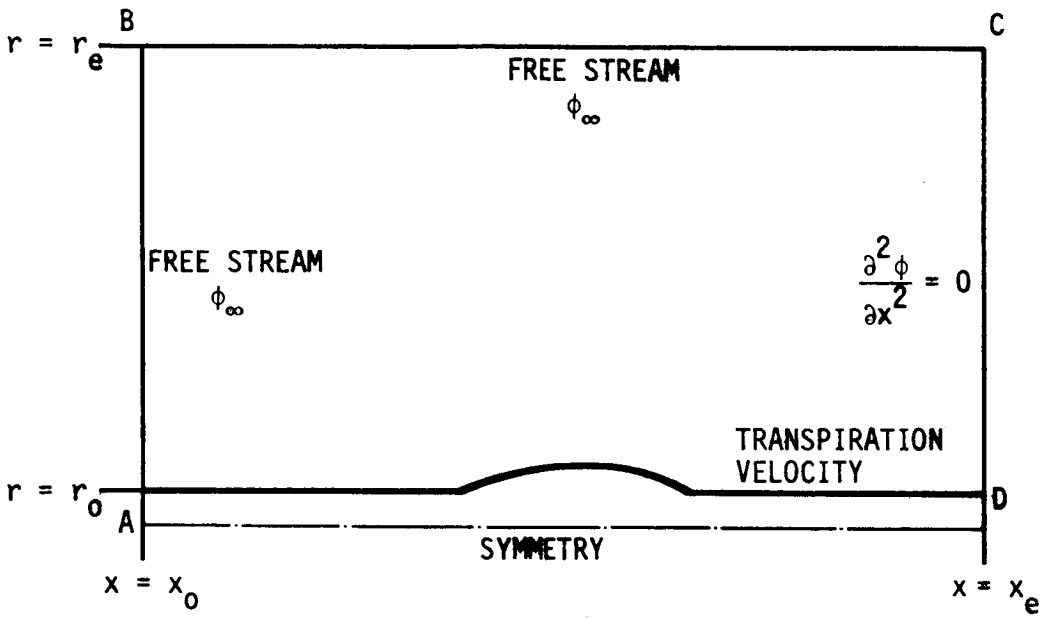

FIGURE 6. Inviscid computational domain in physical coordinates

Therefore, the potentials at the boundaries which are placed sufficiently far from the source of disturbance can be assumed to be held at the fixed values which are determined by the uniform freestream condition. Assuming that the inflow boundary, noted as A-B in Figure 6, is placed far upstream normal to the freestream velocity, u_∞, the boundary condition is expressed in terms of the velocity potential as

$$\phi(x_o,r) = 0 \tag{3.9}$$

The outer boundary is also assumed to be placed sufficiently far from the solid wall so that its effect upon the main structure of the flow is negligible. Hence, the condition at the outer boundary, B-C in Figure 6, is also given as a constant, uniform velocity. When the B-C plane is parallel to the freestream, the velocity potential at $r = r_e$ is given as

$$\phi(x,r_e) = u_\infty(x - x_o) \tag{3.10}$$

The boundary condition at the exit of the computational domain, C-D in Figure 6, needs a careful treatment for convergence of the solution. Since the downstream boundary is positioned such that the outflow can always be assumed to be subsonic, a boundary condition is required. The downstream boundary condition at $x = x_e$ is specified so that the streamwise variation of the flow is zero.

$$\left.\frac{\partial^2\phi}{\partial x^2}\right|_{x=x_e} = 0 \tag{3.11}$$

The boundary condition at the inner boundary surface, D-A in Figure 6, is the key to the viscous-inviscid interaction. Inviscid flows should be computed over an equivalent body, i.e., effective displacement surface due to the viscous effects rather than the actual body surface. This, however, requires repeated generation of the grid because the displacement thickness changes during the interaction process. In order to avoid this computational effort, the coupling procedure is implemented by using a transpiration boundary condition following the incompressible analysis of Lighthill (1958) who suggested that the effect of boundary layer displacement upon the inviscid outer flow could be represented by a distribution of equivalent sources on the physical body surface with strengths given by the streamwise growth of the displacement thickness. This concept has been extended to axisymmetric compressible flow (Gersten, 1974; Lock, 1981) as

$$v_o = \frac{1}{\rho_e r_o} \frac{d}{ds}(\rho_e u_e r_o \delta^*) \tag{3.12}$$

where v_o is the transpiration velocity normal to the body surface, s is the coordinate tangential to the body surface, r_o is the radius of the body, and δ^* is the displacement thickness. In Section II. C, the advantages of using the shear-layer coordinate were explained. When the inviscid flow is solved over the shear-layer coordinate rather than the physical body surface, the displacement thickness in Equation (3.12) should be reduced by the distance between the shear-layer coordinate and the actual body surface (noted as t in Figure 3). As a result, Equation (3.12) becomes

$$v_o = \frac{1}{\rho_e r_o} \frac{d}{ds}(m - m_t) = \frac{1}{\rho_e r_o} \frac{dm^*}{ds} \tag{3.13}$$

where

$$m = \rho_e u_e r_o \delta^* \tag{3.14}$$

$$m_t = \rho_e u_e r_o t \tag{3.15}$$

3. Nondimensionalization

It is convenient to use a dimensionless form of the variables in solving Equation (3.8). The density and velocity components are nondimensionalized by the stagnation density, ρ_o, and by the critical speed of sound, a^*, respectively. Independent variables are normalized by the total length between the inflow and outflow boundary points in the x coordinate, $L_e = x_e - x_o$.

$$\bar{\rho} = \frac{\rho}{\rho_o} \qquad \bar{u} = \frac{u}{a^*} \qquad \bar{v} = \frac{v}{a^*}$$

$$\bar{x} = \frac{x - x_o}{L_e} \qquad \bar{r} = \frac{r}{L_e} \qquad \bar{\phi} = \frac{\phi L_e}{a^*} \tag{3.16}$$

$$\bar{m} = \frac{m}{\rho_o a^* L_e^2} \qquad \bar{m}_t = \frac{m_t}{\rho_o a^* L_e^2} \qquad \bar{m}^* = \frac{m^*}{\rho_o a^* L_e^2}$$

where x_o and x_e are the inflow and outflow boundary position as shown in Figure 6.

With the use of the above dimensionless variables, Equation (3.8) can be rewritten as

$$(\bar{\rho}\bar{\phi}_{\bar{x}}\bar{r})_{\bar{x}} + (\bar{\rho}\bar{\phi}_{\bar{r}}\bar{r})_{\bar{r}} = 0 \tag{3.17}$$

where, using Equations (3.3)-(3.6), the dimensionless density, ρ, can be expressed as

$$\bar{\rho} = [1 - \frac{\gamma-1}{\gamma+1}(\bar{\phi}_{\bar{x}}^2 + \bar{\phi}_{\bar{r}}^2)]^{1/(\gamma-1)} \tag{3.18}$$

The corresponding boundary conditions, given by Equations (3.9)-(3.13), can be rewritten in terms of the dimensionless variables as

$$\bar{\phi}(0,\bar{r}) = 0 \tag{3.19}$$

$$\bar{\phi}(\bar{x},\bar{r}_e) = \bar{u}_\infty \bar{x} \tag{3.20}$$

$$\left.\frac{\partial^2\bar{\phi}}{\partial\bar{x}^2}\right|_{\bar{x}=1} = 0 \tag{3.21}$$

$$\bar{v}_o = \frac{1}{\bar{\rho}_e \bar{r}_o}\frac{d\bar{m}^*}{d\bar{s}} \tag{3.22}$$

Hereafter, bars denoting the inviscid nondimensionalization will be dropped, and all variables are the nondimensional ones unless otherwise specified.

4. Coordinate transformation

The computational domain often becomes irregular in the physical coordinates due to the arbitrary shape of the body configuration. The irregular grid caused by the arbitrariness of the boundaries may increase the truncation error of difference schemes and sometimes greatly affect the stability of the solution procedure. It also takes

considerable effort to implement the boundary conditions on the irregular boundaries. The governing equations are, therefore, usually transformed to a suitable computational domain from the physical coordinates before the solution procedure is applied. Using an independent variable transformation, any arbitrary geometrical surface in the problem can be transformed to a constant coordinate line in the computational set so that the boundary conditions can be implemented with much less effort.

A general independent variable transformation is given as

$$\xi = \xi(x,r) \qquad \eta = \eta(x,r) \tag{3.23}$$

where x and r represent the physical coordinates and ξ and η represent the computational coordinates (see Figure 7). $\xi = 0$ and $\xi = \xi_{max}$ correspond to the points $x = 0$ and $x = 1$, respectively. Likewise, $\eta = 0$ and η_{max} correspond to $r = r_o$ and $r = r_e$, respectively.

Applying this general transformation and maintaining the strong conservative form (Viviand, 1974), Equations (3.17) and (3.18) are transformed into the computational domain as

$$(\frac{\rho Ur}{J})_\xi + (\frac{\rho Vr}{J})_\eta = 0 \tag{3.24}$$

$$\rho = [1 - \frac{\gamma-1}{\gamma+1}(U\phi_\xi + V\phi_\eta)]^{1/(\gamma-1)} \tag{3.25}$$

where U and V are the contravariant velocity components normal to constant ξ and η lines, respectively, and are expressed as

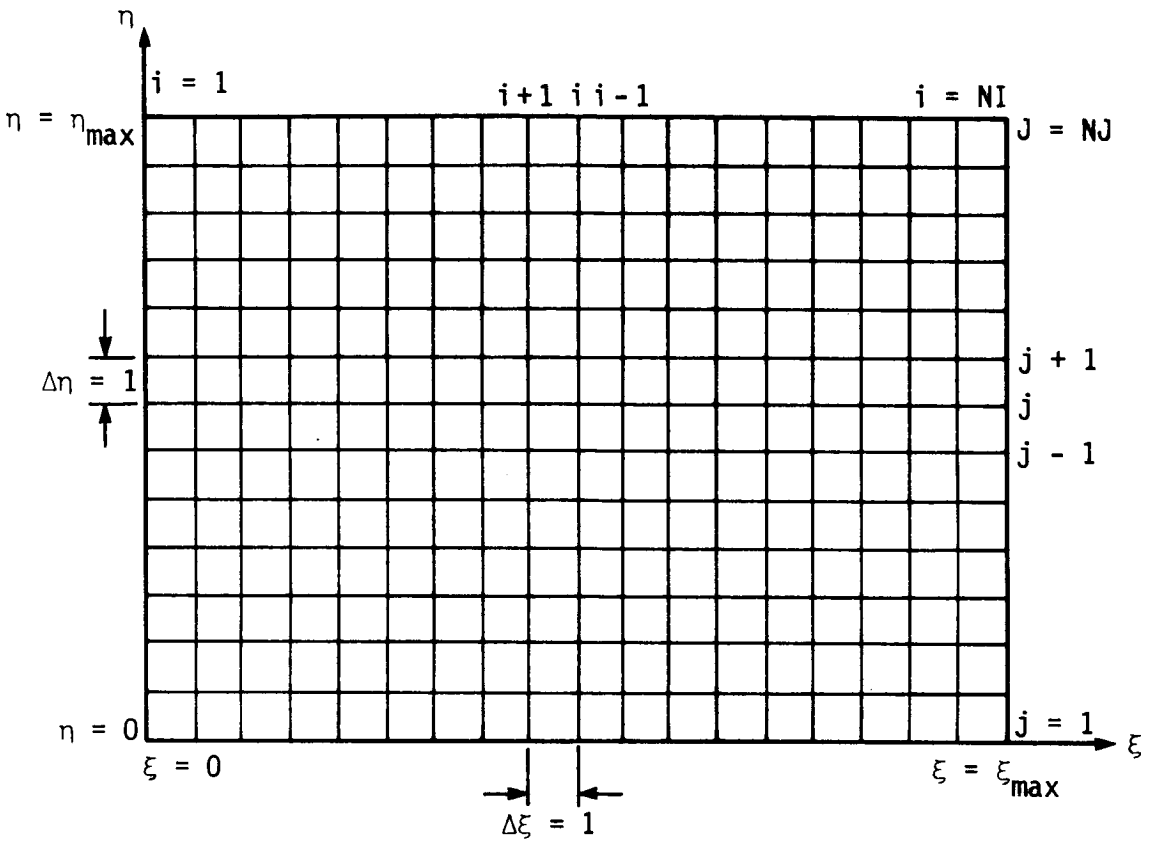

FIGURE 7. Inviscid computational domain in transformed coordinates

$$U = A_1\phi_\xi + A_2\phi_\eta \tag{3.26-a}$$

$$V = A_2\phi_\xi + A_3\phi_\eta \tag{3.26-b}$$

The metric quantities of the transformation are given as

$$\begin{aligned} A_1 &= \xi_x^{\,2} + \xi_r^{\,2} \\ A_2 &= \xi_x\eta_x + \xi_r\eta_r \\ A_3 &= \eta_x^{\,2} + \eta_r^{\,2} \\ J &= \xi_x\eta_r - \xi_r\eta_x \end{aligned} \tag{3.27}$$

where J is the Jacobian of the transformation. These metric quantities can be computed as

$$\begin{aligned} J &= (x_\xi r_\eta - x_\eta r_\xi)^{-1} \\ \xi_x &= J\, r_\eta \qquad \xi_r = -J\, x_\eta \\ \eta_x &= -J\, r_\xi \qquad \eta_r = J\, x_\xi \end{aligned} \tag{3.28}$$

B. Relaxation Methods

It is essential to know the mathematical classification of a governing partial differential equation in order to develop the correct solution procedure. Classification is easier when the potential equation is written in the nonconservative form as

$$(1 - \frac{u^2}{a^2})\phi_{xx} - \frac{2uv}{a^2}\phi_{xr} + (1 - \frac{v^2}{a^2})\phi_{rr} + \frac{1}{r}\phi_r = 0 \qquad (3.29)$$

where a is the local speed of sound. Following the standard classification (Anderson et al., 1984) procedure for second order partial differential equations, it is found that the classification depends upon the signs of the coefficients. This leads to the conclusion that the velocity potential equation becomes

hyperbolic where $q^2 > a^2$ (supersonic)

parabolic where $q^2 = a^2$ (sonic)

elliptic where $q^2 < a^2$ (subsonic)

where $q^2 = \phi_x^2 + \phi_r^2$

Transonic flows, of course, usually include all three of these flow categories. Flow disturbances move very quickly downstream because the propagation velocity is (u + a) and very slowly upstream because the propagation velocity is (u - a). For a disturbance in a downstream region to propagate upstream, it must pass around the supersonic zone. As a result, it is difficult to develop an efficient algorithm for transonic flows. Most of numerical methods for the velocity potential equation have been based on relaxation schemes suitable for an elliptic equation and adjusted for embedded hyperbolic regions because the supersonic region is usually relatively small in transonic flows where the velocity potential equation can be used.

It should also be noted that the velocity potential equation is nonlinear in nature. This makes it almost impossible to use a

noniterative, direct solution procedure because linearization of the velocity potential equation will destroy the mechanism of shock capturing. Therefore, most of the numerical solution procedures for transonic flow use an iterative relaxation method with linearization.

Relaxation methods are generally classified as either point iterative or block iterative. The point iterative scheme is the simplest and the Jacobi and Gauss-Seidel schemes are included in this category. These methods are very simple, but are often relatively slow in convergence, especially as the number of grid points increases. Therefore, they are seldom used in the finite-difference analysis of transonic flows.

In block iterative methods, the unknown variables at a number of grid points are grouped together and solved simultaneously. This is repeated iteratively. The line-Jacobi, line-Gauss-Seidel, successive line overrelaxation (SLOR) and alternating direction implicit (ADI) methods are included in this category. These methods often provide faster convergence than point iterative methods.

Iterative procedures can be accelerated by using a successive overrelaxation (SOR) procedure in which the values obtained from the standard form of any algorithm are arbitrarily modified according to the following format

$$\phi^{n+1} = \phi^{n} + \omega(\phi^{\overline{n+1}} - \phi^{n}) \tag{3.30}$$

where ω is the relaxation parameter. Here, n denotes iteration level and $\phi^{\overline{n+1}}$ is the most recent value of ϕ calculated from the standard

iteration algorithm, ϕ^n is the value from the previous iteration as adjusted by the previous application of this formula, and ϕ^{n+1} is the adjusted (relaxed) value of ϕ at n+1 iteration level. For the iterative procedure to converge, ω must be restricted to values between 0 to 2. When ω ranges between 1.0 and 2.0, the procedure is called overrelaxation. In some cases, underrelaxation is applied with ω ranging from 0 to 1.0.

It is known that the rate of convergence is usually sensitive to the choice of ω and use of the optimum value of ω reduces the computation time greatly. For a simple Laplace equation with simple boundary conditions, it is possible to determine the optimum ω, ω_{opt}, based on the number of mesh points (Young, 1954). For complex nonlinear elliptic equations, it is, however, very difficult to determine the ω_{opt} in advance (Forsythe and Wasow, 1960; Ames, 1977). In such cases, trial-and-error numerical experimentation is often used to determine the value of ω close to ω_{opt}.

The SLOR algorithm is one of the simplest block iterative procedures. Over the years, SLOR algorithms have proved to be reliable and flexible and they are still used in many numerical solution schemes for the potential equation (Jameson et al., 1976; Hafez et al., 1979; Chen and Caughey, 1980; Green and South, 1983). The SLOR procedure was used for part of the calculations in the present study and will be described in more detail below.

An alternating direction implicit (ADI) method (Peaceman and Rachford, 1955) often provides faster convergence than the SLOR scheme.

In the ADI method, a partial differential operator is split into a sequence of an implicit operators in alternating directions, so that the complete iteration cycle consists of consecutive sweeps over all rows and columns. Since each iteration cycle consists of multiple sweeps in different directions, each grid point in the entire mesh can be influenced by every other grid point during each iteration; thus, faster convergence is possible. The ADI method was used in the present study to generate the computational grid and will be described later. The efficiency of the ADI method is usually dependent on flow characteristics and mesh sizes. However, numerous computational results indicate that the ADI method can be as much as 5 ~ 10 times faster than the SLOR method for some problems.

The splitting of the partial differential operator into a sequence of one-dimensional steps as done in traditional ADI methods can also be formulated through an approach known as "approximate factorization". The terminology "approximate factorization (AF)" was used by Yanenko (1971) and adopted by Ballhaus and Steger (1975). In the AF procedure, the implicit differential operator is approximated as a product of factors for multi-dimensional cases. If the original differential operator is nonlinear, it should be linearized before factorization. Each factor usually requires an implicit operator in only one direction; thus, it involves only a simple banded matrix. Then the errors caused by linearization and factorization are corrected in the solution automatically by iterations. Some formulations of ADI schemes are often referred to as AF1 schemes.

A new AF scheme, AF2, was proposed by Ballhaus and Steger (1975) in the study of the unsteady low frequency transonic equation in order to obtain faster convergence than permitted by the ADI scheme. This implicit AF scheme was then applied to the steady TSD equation by Ballhaus et al. (1978) and to the velocity potential equation by Hafez et al. (1979) and Holst and Ballhaus (1979). Since the AF2 scheme is believed to be insensitive to the moving shock instability (Holst, 1983), this scheme is very effective for solving steady transonic flows, especially supercritical cases. In the subcritical case, which does not have supersonic regions, the ADI algorithm generally produces faster convergence than the AF2 scheme (Holst and Ballhaus, 1979).

In the present study, both the SLOR and AF2 schemes were employed for the analysis of inviscid transonic flows. For the semi-inverse interaction method which employs a very simple interaction law, the AF2 scheme was used mainly because of its high convergence speed. In the case of the simultaneous interaction method, the SLOR is preferred to the AF2 scheme since the simpler algebraic formulation of the SLOR reduces the human effort considerably in manipulating the simultaneous interaction laws.

C. Numerical Grid Generation

1. Governing equations

One of the easiest ways of establishing body-fitted coordinates is an analytic method which uses algebraic expressions to stretch or shear the coordinates. This simple procedure is useful for simple geometries

but is difficult to implement for complex geometries. For complex geometries, one of the most popular and highly developed techniques for grid generation establishes a new set of curvilinear coordinates from the numerical solution of appropriately controlled partial differential equations with suitable boundary conditions.

Even though there have been a lot of different numerical grid generation schemes proposed (see Thompson et al., 1982), the most popular one has been the elliptic grid generation scheme based on the Poisson or Laplace equation developed by Thompson et al. (1974, 1977). Some of the schemes proposed more recently are based on hyperbolic equations (Steger and Sorenson, 1980) or parabolic equations (Nakamura, 1982). These have the advantage that the solution can be obtained by simple marching from the initial plane without a time-consuming iteration process. However, they lack a means to control the grid distribution at the end of the marching plane and appear to need further development before they can be used in complex geometries. For the geometries of the present study, a scheme based on the solution of the Laplace equation was adequate to give smooth and nearly orthogonal meshes. Using a Poisson equation would have permitted additional control of the mesh size and skewness but this appeared unnecessary for the present study.

The Laplace equation used to define the coordinate transformation is given by

$$\xi_{xx} + \xi_{rr} = 0 \tag{3.31}$$

$$\eta_{xx} + \eta_{rr} = 0 \tag{3.32}$$

Equations (3.31) and (3.32) are transformed to the computational domain by interchanging the roles of the independent and dependent variables as

$$A\, x_{\xi\xi} - 2B\, x_{\xi\eta} + C\, x_{\eta\eta} = 0 \tag{3.33}$$

$$A\, r_{\xi\xi} - 2B\, r_{\xi\eta} + C\, r_{\eta\eta} = 0 \tag{3.34}$$

where

$$A = x_\eta^2 + r_\eta^2 \qquad B = x_\xi x_\eta + r_\xi r_\eta \qquad C = x_\xi^2 + r_\xi^2 \tag{3.35}$$

A Dirichlet type boundary condition is prescribed at all boundaries as

$$x = x(\xi,\eta) \qquad r = r(\xi,\eta) \tag{3.36}$$

These boundary conditions are very important because they determine the actual grid formulation. The streamwise grid spacing along the body surface was chosen so that more grid points are concentrated where the gradients of flow properties are expected to be large. A transformation formula suggested by Roberts (1971) was used to produce the mesh clustered at some interior point, x_c, along the body surface. This formula is listed in Appendix D. At the outer boundary, the uniform grid spacing was used.

In the normal direction, grid points were concentrated near the body surface. This was done using an exponential stretching type

transformation which is also given in Appendix D. In order to start the relaxation scheme, initial values are needed. Initial values of x and r at interior points were provided by simple linear interpolation between boundary values.

2. Solution procedure

The finite-difference mesh $(x(\xi,\eta), r(\xi,\eta))$ is formed as a solution of Equations (3.33) and (3.34) subject to the boundary conditions given by Equation (3.36). For the finite-difference solution of this elliptic equation, a second-order-accurate central differencing scheme was used. Using operator notation, the finite-difference representation used for Equations (3.33) and (3.34) is

$$L(\ )_{ij} = [A_{ij}\delta_{\xi\xi} - 2B_{ij}\delta_{\xi\eta} + C_{ij}\delta_{\eta\eta}](\ )_{ij} \tag{3.37}$$

where the subscript i and j represent the finite-difference mesh position and the finite-differencing operators are given by

$$\delta_{\xi\xi}(\ )_{i,j} = \frac{1}{\Delta\xi^2}[(\ )_{i+1,j} - 2(\ )_{i,j} + (\ )_{i-1,j}]$$

$$\delta_{\xi\eta}(\ )_{i,j} = \frac{1}{4\Delta\xi\Delta\eta}[(\ )_{i+1,j+1} - (\ )_{i-1,j+1} - (\ )_{i+1,j-1} + (\ )_{i-1,j-1}] \tag{3.38}$$

$$\delta_{\eta\eta}(\ )_{i,j} = \frac{1}{\Delta\eta^2}[(\ )_{i,j+1} - 2(\ )_{i,j} + (\ )_{i,j-1}]$$

for the interior points. Near the boundaries, a one-sided differencing scheme with second-order-accuracy was used. The spacing increments $\Delta\xi$ and $\Delta\eta$ are arbitrary and were set to unity for convenience.

These finite-difference equations can be solved by any standard relaxation procedure. Although the SLOR method is usually used in grid generation, the ADI algorithm was used in the present study in order to improve the convergence rate. For a relaxation problem governed by a PDE in the form of $L\phi = 0$, it is convenient to use a two-level correction scheme given by

$$NC^n + \omega L\phi^n = 0 \tag{3.39}$$

where L is a complete differential operator, N is a linear operator which determines the type of iteration method, C^n is the nth-iteration correction term which is identified as $C^n = \phi^{n+1} - \phi^n$, and the ω is a relaxation parameter. $L\phi^n$ is the nth-iteration residual which indicates the degree of accuracy of the nth-iteration solution, ϕ^n, to the finite-difference equation and is denoted by R^n. Introducing an analogy where the number of steps is proportional to an artificial time (pseudo-time) coordinate t, C is considered as representing $\Delta t\phi_t$. Thus, N should be chosen so that this process converges in time.

In the present study, the Peaceman-Rachford ADI scheme (1955) is reformulated following Ballhaus et al. (1978). The N-operator is approximated as the product of two tridiagonal matrix factors as

$$N = -\frac{1}{\alpha}(\alpha - A\delta_{\xi\xi})(\alpha - C\delta_{\eta\eta}) \tag{3.40}$$

where α is an acceleration parameter which is considered as the inverse of a pseudo-time step, $1/\Delta t$. With the introduction of intermediate correction terms, f and g, Equations (3.33) and (3.34) become

step 1

$$(\alpha - A^n_{i,j}\delta_{\xi\xi})f^n_{i,j} = \alpha\omega Lx^n_{i,j} \tag{3.41-a}$$

$$(\alpha - A^n_{i,j}\delta_{\xi\xi})g^n_{i,j} = \alpha\omega Lr^n_{i,j} \tag{3.41-b}$$

step 2

$$(\alpha - C^n_{i,j}\delta_{\eta\eta})(x^{n+1}_{i,j} - x^n_{i,j}) = f^n_{i,j} \tag{3.42-a}$$

$$(\alpha - C^n_{i,j}\delta_{\eta\eta})(r^{n+1}_{i,j} - r^n_{i,j}) = g^n_{i,j} \tag{3.42-b}$$

In step 1, the values of the f and g arrays are obtained by solving two tridiagonal matrix equations for each η = constant line. Then the new values of x and y are calculated in the second step from the solutions of two tridiagonal matrix equations for each ξ = constant line. These tridiagonal matrix equations can be solved easily by using Thomas algorithm and the actual coefficients of the resulting matrix are given in Appendix E. The stability analysis shows that the ADI method is unconditionally stable as long as $0 \leq \omega \leq 2$ and $\alpha > 0$. In the present calculations, convergence was obtained with a value of ω equal to 2.

To achieve the fastest convergence rate, it is necessary to use a optimum value of α which minimizes the amplification factor of the error. Precise estimation of the optimum α is usually extremely difficult. Following the suggestion of Ballhaus et al. (1978), a sequence of α's is repeated with a predetermined cycle. This sequence is given by

$$\alpha_K = \alpha_H \left(\frac{\alpha_L}{\alpha_H}\right)^{(K-1)/(\ell-1)} \tag{3.43}$$

where ℓ is the number of elements in the sequence. The high end point of the sequence, α_H, is effective in minimizing the high-frequency errors and is chosen between 0.01 and 0.05. The lower end point of the sequence, α_L is effective in reducing the low-frequency errors and recommended values are between 0 and 0.01. The values of these iteration parameters influence the rate of convergence and they are usually optimized by numerical experimentation. The typical values of α_H and α_L used in this study are 0.02 and 0.00001, respectively, and the value of ℓ is 8.

The converged solution is usually obtained for a 100 × 40 grid in 50 iterations using a convergence criterion $\varepsilon_c = 1 \times 10^{-3}$, where ε_c is defined as

$$\varepsilon_c \geq \left|\frac{\text{Rmax}^n}{\text{Rmax}^1}\right| \tag{3.44}$$

where Rmax^k is the maximum residual for both x and y at the kth-iteration level. A typical example of numerically generated meshes is shown in Figure 8.

D. Algorithms for the Velocity Potential Equation

When the flow is subsonic, the velocity potential equation is elliptic. Hence a standard relaxation scheme can be applied after the equation is discretized with second-order-accurate central differencing

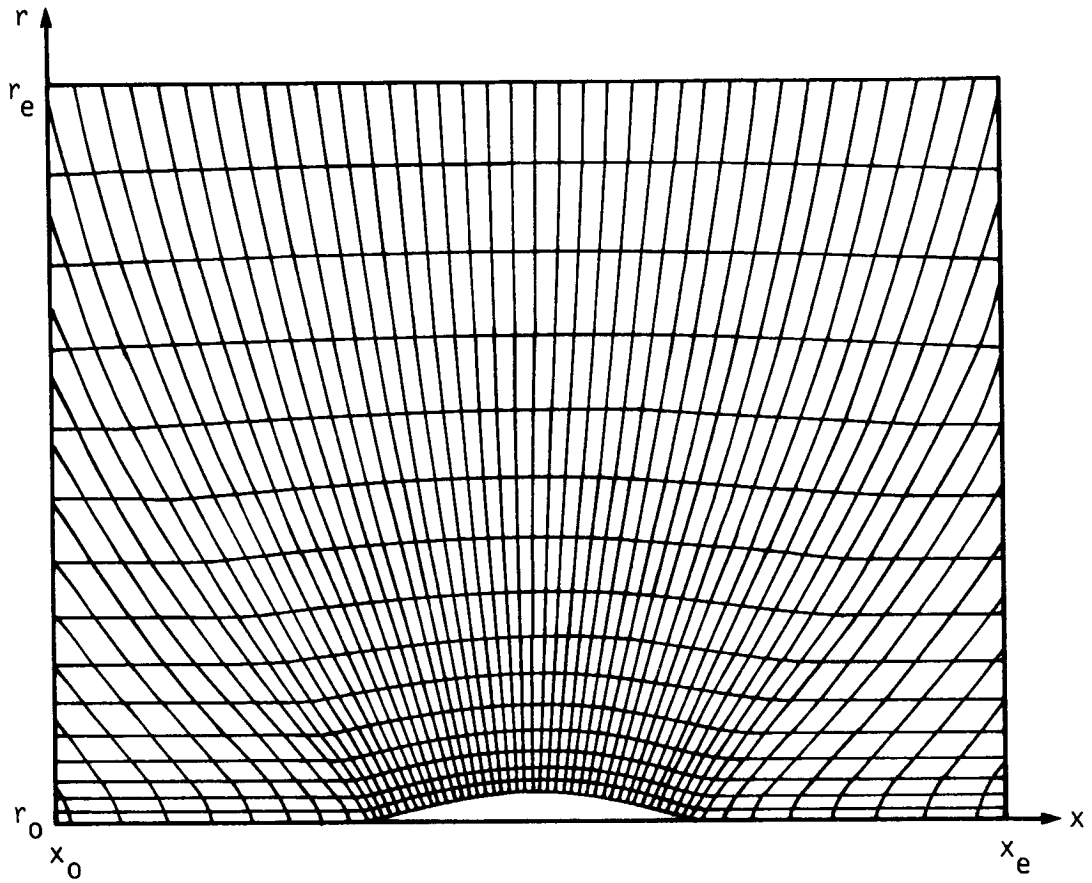

FIGURE 8. Grid system for the inviscid analysis

approximations. The von Neumann stability analysis by Holst (1983) shows that the central differencing scheme is stable for subsonic regions but unstable for supersonic regions. Therefore, modifications are necessary in order to provide a stable solution in supersonic regions.

To deal with this problem, Murman and Cole (1971) introduced a type-dependent, finite-difference relaxation scheme for the transonic small disturbance equation. This scheme has been extended by many others (Steger and Lomax, 1972; Garabedian and Korn, 1972; Jameson, 1974) to solve transonic flows using a variety of formulations. In the type-dependent differencing scheme, a local flow type at each grid point is first determined by centrally differencing the velocity potential. If the local flow type is subsonic, standard second-order-accurate central differencing formulas are used. For supersonic regions which are hyperbolic, first-order-accurate upwind differencing formulas are applied. Hence, the physical domain of dependence is correctly represented by the computational domain of dependence.

For example, assuming that the main flow direction is aligned with the x direction, the expression for the upwind finite-difference representation of the second derivatives at a supersonic point (i,j) becomes

$$\phi_{xx} = \frac{1}{\Delta x^2}(\phi_{i,j} - 2\phi_{i-1,j} + \phi_{i-2,j}) \qquad (3.45\text{-a})$$

$$\phi_{xr} = \frac{1}{2\Delta x \Delta r}(\phi_{i,j+1} - \phi_{i,j-1} + \phi_{i-1,j+1} + \phi_{i-1,j-1}) \qquad (3.45\text{-b})$$

$$\phi_{rr} = \frac{1}{\Delta r^2}(\phi_{i,j+1} - 2\phi_{i,j} + \phi_{i,j-1}) \qquad (3.45\text{-c})$$

Using a Taylor series expansion, it can be shown that an upwind differencing evaluation of the second derivative is first-order-accurate and the leading terms in the truncation error can be regarded as an artificial viscosity which is given by

$$\Delta x(u^2 - a^2)\phi_{xxx} \qquad (3.46)$$

With this artificial viscosity which remains positive when $u^2 > a^2$, supersonic marching becomes stable. However, when the x-component of the velocity is subsonic ($u^2 < a^2$) even though the flow is supersonic ($q^2 > a^2$), the marching scheme might become unstable because the artificial viscosity becomes negative. This instability occurs when the flow is slightly misaligned with the x-axis so that the proper physical domain of dependence is not included in the computational domain of dependence.

The rotated differencing scheme was then introduced by Jameson (1974) to overcome this directional difficulty. The basic idea is to represent the potential equation in a local stream and stream-normal coordinate system. Then type-dependent differencing is used along the local streamline coordinate while the standard central differencing is used along stream-normal coordinate. This produces artificial viscosity which is always positive where the flow is supersonic, thus eliminating the marching instability problem. However, the rotated differencing scheme has several disadvantages, too. Because it must be swept in the

local stream direction, difficulties might arise with general curvilinear meshes. Also, this scheme becomes first-order-accurate in both directions.

The above methods will be referred to as artificial viscosity schemes since the difference molecule is adjusted in supersonic regions to provide the proper zone of dependence. Associated with this modification is a viscosity-like term in the truncation error. The same effect can be achieved by the artificial compressibility (or density) scheme. This idea has been independently developed in several different forms (Eberle, 1978; Harten, 1978; Hafez et al., 1979; Holst and Ballhaus, 1979). In the artificial compressibility scheme, an upwind evaluation of the density is used in supersonic regions to provide the upwind bias which is equivalent to what is accomplished by the artificial viscosity.

In order to illustrate the idea of the artificial compressibility scheme which is used in the present study and to compare it with the artificial viscosity scheme, it is helpful to use a conservative form of the velocity potential equation in one-dimension,

$$(\rho\phi_x)_x = 0 \tag{3.47}$$

With second-order-accurate finite differencing formulas, Equation (3.47) is approximated as

$$(\rho\phi_x)_x = \overleftarrow{\delta}_x(\rho_{i+\frac{1}{2}}\overrightarrow{\delta}_x\phi_i) \tag{3.48}$$

where $\overleftarrow{\delta}_x$ and $\overrightarrow{\delta}_x$ are the backward and forward difference operators for

the first derivative, respectively. This form is satisfactory for subsonic flow regions.

As mentioned before, for the type-dependent differencing scheme, the difference operator is switched to upwind differencing in the supersonic flow region. Following Jameson (1975), this is analogous to the explicit addition of an artificial viscosity to the central differencing. The artificial viscosity is given by

$$-\Delta x(\mu\phi_{xx})_x \tag{3.49}$$

where

$$\mu = \text{MIN}\ [0,\ \rho(1 - \frac{\phi_x^2}{a^2})] \tag{3.50}$$

Jameson also has shown that Equation (3.49) is equivalent to a term with the form of

$$-\Delta x(\nu\rho_x\phi_x)_x \tag{3.51}$$

where

$$\nu = \text{MAX}\ [0,\ (1 - \frac{a^2}{\phi_x^2})] \tag{3.52}$$

When Equation (3.51) is added, Equation (3.47) can be written as

$$(\rho\phi_x)_x \simeq \overleftarrow{\delta}_x(\rho_{i+\frac{1}{2}}\overrightarrow{\delta}_x\phi_i) - \overleftarrow{\delta}_x[\nu_i(\rho_{i+\frac{1}{2}} - \rho_{i-\frac{1}{2}})\overrightarrow{\delta}_x\phi_i] \tag{3.53}$$

In subsonic regions, this scheme is second-order-accurate and centrally differenced. For supersonic regions, it becomes a combination of

second-order-accurate central differencing and first-order-accurate upwind differencing due to the addition of the artificial viscosity.

In the artificial compressibility approach, the difference expression given by Equation (3.53) has been rearranged by Holst and Ballhaus (1979) to give

$$(\rho\phi_x)_x \simeq \overleftarrow{\delta}_x(\tilde{\rho}_{i+\frac{1}{2}}\overrightarrow{\delta}_x\phi_i) \tag{3.54}$$

where

$$\tilde{\rho}_{i+\frac{1}{2}} = (1 - \nu_i)\rho_{i+\frac{1}{2}} + \nu_i\rho_{i-\frac{1}{2}} \tag{3.55}$$

Comparison of Equations (3.53) and (3.54) shows that the explicit addition of the artificial viscosity is equivalent to using a retarded density. The differencing becomes more strongly retarded in the upwind direction as the flow becomes more supersonic. If the above scheme is applied in both directions for two-dimensional flows, it provides the upwind biasing for the streamwise term in supersonic regions, thus giving nearly the same effect as obtained by the rotated difference scheme.

One difficulty in using the artificial compressibility scheme is the choice of a switching function, ν, because ν affects significantly the accuracy and stability of the solution, especially, the strength of shock waves as supersonic regions become larger. When ν is not properly chosen (see Equation (3.45)), a large pre-shock oscillation can be observed (Holst and Ballhaus, 1979), which often results in a numerical instability. This can be avoided by modifying the way in which ν and ρ

are computed (Holst, 1983). The details will be given in a following section.

E. Numerical Method

In the present section a finite-difference representation of the velocity potential equation and its solution procedure are presented.

1. Finite-difference representation

a. Governing equations After applying second-order-accurate finite-difference approximations, Equation (3.24) is written as

$$\overleftarrow{\delta}_\xi \left(\frac{\tilde{\rho} Ur}{J}\right)_{i+\frac{1}{2},j} + \overleftarrow{\delta}_\eta \left(\frac{\bar{\rho} Vr}{J}\right)_{i,j+\frac{1}{2}} = 0 \tag{3.56}$$

where the contravariant velocity components are computed using second-order-accurate finite difference formulas given by

$$\left(\frac{U}{J}\right)_{i+\frac{1}{2},j} = \left(\frac{A_1}{J}\right)_{i+\frac{1}{2},j} \vec{\delta}_\xi \phi_{i,j} + \frac{1}{2}\left(\frac{A_2}{J}\right)_{i+1,j} \delta_\eta \phi_{i+1,j} + \frac{1}{2}\left(\frac{A_2}{J}\right)_{i,j} \delta_\eta \phi_{i,j} \tag{3.57-a}$$

$$\left(\frac{V}{J}\right)_{i,j+\frac{1}{2}} = \frac{1}{2}\left(\frac{A_2}{J}\right)_{i,j} \delta_\xi \phi_{i,j} + \frac{1}{2}\left(\frac{A_2}{J}\right)_{i,j+1} \delta_\xi \phi_{i,j+1} + \left(\frac{A_3}{J}\right)_{i,j+\frac{1}{2}} \vec{\delta}_\eta \phi_{i,j} \tag{3.57-b}$$

The values of the Jacobian, J, and the transformation metric quantities, A_1, A_2 and A_3, are first evaluated at integer mesh nodes (i,j) using

fourth-order-accurate central finite-difference formulas. Then the values of the metric quantities at half integer points are obtained by fourth-order-accurate interpolations.

Using the artificial compressibility scheme mentioned in the previous section, this formulation becomes valid for supersonic regions as well as subsonic regions. Instead of direct addition of the artificial retarded density given by Equation (3.51) which makes the analysis difficult due to the general ξ-η coordinate system, an approximate implementation is achieved by using the following form

$$- \Delta\xi\left(\nu\rho_{\xi}\frac{|U|}{J}\right)_{\xi} \tag{3.58}$$

where ν is still the same switching function (Holst, 1979). To simulate the full effect of the rotated differencing scheme, the same form of the artificial retarded density was added in the η direction (Holst and Albert, 1979)

$$- \Delta\eta\left(\nu\rho_{\eta}\frac{|V|}{J}\right)_{\eta} \tag{3.59}$$

Then the retarded density coefficients are expressed as

$$\tilde{\rho}_{i+\frac{1}{2},j} = (1 - \nu_{i+k,j})\rho_{i+\frac{1}{2},j} + \nu_{i+k,j}\rho_{i+2k-\frac{1}{2},j} \tag{3.60-a}$$

$$\bar{\rho}_{i,j+\frac{1}{2}} = (1 - \nu_{i,j+\ell})\rho_{i,j+\frac{1}{2}} + \nu_{i,j+\ell}\rho_{i,j+2\ell-\frac{1}{2}} \tag{3.60-b}$$

where

$$k = \begin{cases} 0 & \text{when } U_{i+\frac{1}{2},j} > 0 \\ 1 & \text{when } U_{i+\frac{1}{2},j} < 0 \end{cases} \qquad (3.61)$$

$$\ell = \begin{cases} 0 & \text{when } V_{i,j+\frac{1}{2}} > 0 \\ 1 & \text{when } V_{i,j+\frac{1}{2}} < 0 \end{cases}$$

The density given in Equation (3.24) can be rewritten as

$$\rho = (1 - \frac{\gamma-1}{\gamma+1}Q)^{-(\gamma-1)} \qquad (3.62)$$

where $Q = A_1\phi_\xi^2 + 2A_2\phi_\xi\phi_\eta + A_3\phi_\eta^2$. In the TAIR code written by Dougherty et al. (1981), the density values are computed using a binomial series expansion of Equation (3.62). When the first four terms are retained, the density becomes

$$\rho = 1 + C_1Q + C_2Q^2 + C_3Q^3 \qquad (3.63)$$

where

$$C_1 = -\frac{1}{\gamma+1} \qquad C_2 = \frac{2-\gamma}{2(\gamma+1)^2} \qquad C_3 = -\frac{(2-\gamma)(3-2\gamma)}{6(\gamma+1)^3} \qquad (3.64)$$

where γ is the ratio of specific heats.

According to Dougherty et al. (1981), this approximation is very accurate and saves significant computation time compared to the exponentiation operation. Values of the density are calculated and stored at the centers of the mesh cell, $(i+\frac{1}{2},j+\frac{1}{2})$, based on the suggestion of South and Jameson (see Holst, 1983) who found that the pre-shock oscillation can be reduced in this way. The values needed at $(i+\frac{1}{2},j)$ and $(i,j+\frac{1}{2})$ are obtained by simple arithmetic averaging.

The magnitude of the artificial viscosity, i.e., switching function ν, is very important for the accuracy and the stability of the solution. Since the expression given by Equation (3.52) proved to be inadequate for flows with large supersonic regions, a formulation suggested by Holst (1979) was used in the present study:

$$\nu_{i,j} = \text{MAX}\ [0,\ (M_{i,j}^{2} - 1)C_{\nu}] \tag{3.65}$$

where $M_{i,j}$ is the local Mach number and C_{ν} is a constant. With this formulation, it is easier to select an appropriate value for ν. C_{ν} is usually set between 1.0 and 2.0 and should be carefully determined by trial-and-error depending on the strength of shock waves and relaxation schemes employed. The smaller values of C_{ν} usually produce sharper, less-smeared shock profiles and should be used for weak shock wave flows. The accuracy and stability of the solution seem more sensitive to the choice of C_{ν} in the SLOR method than in the AF2 method. This is believed to be due to the effect of an added artificial time-dependent dissipation term in the AF2 scheme. The typical value of C_{ν} for a stable solution is 0.8 for the SLOR method and 1.2 for the AF2 scheme. Values of ν are actually computed at the centers of the mesh cell $(i+\frac{1}{2},j+\frac{1}{2})$, like the density, and simple arithmetic averaging is used to obtain the value at (i,j).

b. Boundary conditions The boundary conditions at the inflow and outer boundaries become

$$\phi(1,j) = 0 \qquad \phi(i,NJ) = \phi_{\infty}(i,NJ) \tag{3.66}$$

where ϕ_∞ is the velocity potential of the undisturbed freestream and can be calculated easily from Equation (3.20).

The exit boundary condition is approximated as

$$(\frac{\rho Ur}{J})_{NI-\frac{1}{2},j} = (\frac{\rho Ur}{J})_{NI,j} = (\frac{\rho Ur}{J})_{NI+\frac{1}{2},j} \tag{3.67}$$

because the ξ coordinate is assumed to be almost parallel to the x coordinate in the vicinity of the exit plane. This approximation makes it much simpler to implement the boundary condition without serious error. The difference approximation for ϕ_ξ at i = NI appearing in the expression of $(V/J)_{NI,j+\frac{1}{2}}$ can be obtained from the boundary condition instead of using a one-sided differencing. From Equation (3.26-a), ϕ_ξ becomes

$$\phi_\xi\Big|_{NI,j+\frac{1}{2}} = (\frac{U}{A_1} - \frac{A_2}{A_1}\phi_\eta)_{NI,j+\frac{1}{2}} \tag{3.68}$$

Consequently,

$$(\frac{\bar{\rho}Vr}{J})_{NI,j+\frac{1}{2}} = \{\bar{\rho}r[(\frac{A_3}{J} - \frac{A_2^2}{A_1 J})\phi_\eta + \frac{A_2}{A_1}\frac{U}{J}]\}_{NI,j+\frac{1}{2}} \tag{3.69}$$

Using Equations (3.67) and (3.69), the L-operator is constructed maintaining second-order-accuracy.

A simple mathematical operation based on the coordinate transformation and the definition of the contravariant velocity shows that the transpiration velocity boundary condition at the solid surface, given by Equation (3.22), can be expressed as

$$v_o = \frac{V}{J}\xi_s\Big|_{j=1} \tag{3.70}$$

Combining Equations (3.22) and (3.70) gives

$$\left(\frac{\rho Vr}{J}\right)_{i,1} = \left.\frac{dm^*}{d\xi}\right|_i \tag{3.71}$$

This boundary condition is implemented through the control volume approach by assuming

$$\left(\frac{\rho Vr}{J}\right)_{i,1+\frac{1}{2}} + \left(\frac{\rho Vr}{J}\right)_{i,1-\frac{1}{2}} = 2\left(\frac{\rho Vr}{J}\right)_{i,1} \tag{3.72}$$

Therefore,

$$\left(\frac{\rho Vr}{J}\right)_{i,1-\frac{1}{2}} = 2\left.\frac{dm^*}{d\xi}\right|_i - \left(\frac{\rho Vr}{J}\right)_{i,1+\frac{1}{2}} \tag{3.73}$$

Also, the difference approximation for ϕ_η at the wall appears in the expression for $(U/J)_{i+\frac{1}{2},1}$. As for the exit boundary, Equation (3.26-b) is used to give

$$\left.\phi_\eta\right|_{i+\frac{1}{2},1} = \left(\frac{V}{A_3} - \frac{A_2}{A_3}\phi_\xi\right)_{i+\frac{1}{2},1} \tag{3.74}$$

Using this expression,

$$\left(\frac{\tilde{\rho}Ur}{J}\right)_{i+\frac{1}{2},1} = \left[\tilde{\rho}r\left(\frac{A_1}{J} - \frac{A_2^2}{A_3 J}\right)\phi_\xi + \frac{A_2}{A_3}\frac{dm^*}{d\xi}\right]_{i+\frac{1}{2},1} \tag{3.75}$$

Equations (3.73) and (3.75) are then incorporated into Equation (3.53) to construct the L-operator using second-order-accurate central differencing formulas just as for interior points.

As discussed before, the distribution of the mass flux, m^*, is assumed to be unknown in the simultaneous interaction method. Therefore, m^* must be treated as an unknown variable in developing the

general procedure for the velocity potential equation. This was difficult to achieve with the two step AF2 algorithm so only the SLOR scheme was utilized for the simultaneous interaction method and m^* was assumed to be known before each iteration for the AF2 scheme.

2. Method of solution

In this section, the relaxation procedures used in solving a finite-difference form of the velocity potential equation given by Equation (3.56) is presented. The present analysis employs two different relaxation algorithms: the SLOR and AF2 schemes.

Just as in the numerical grid generation scheme, a two-level correction in pseudo-time given by Equation (3.39) was used. With this approach, the discrete linear operator N should be chosen so that this iterative relaxation process converges in pseudo-time. This often requires the addition of time-dependent terms to embed the steady-state equation in a convergent time-dependent process. With the definition of C^n and Equation (3.30), the provisional value can be written as

$$\overline{\phi^{n+1}} = \frac{1}{\omega} C^n + \phi^n \tag{3.76}$$

By using this expression, overrelaxation can be implemented as a part of the solution algorithm, not as a separate step.

a. SLOR method The standard successive line overrelaxation (SLOR) procedure was applied to Equation (3.56). Even though the SLOR method is often much slower than the AF2 scheme, it is used for the simultaneous viscous-inviscid interaction method because of its simplicity. The simultaneous interaction method requires a relation

between the velocity potential and the mass flux. With the SLOR scheme it is simple to derive such a relation because the calculation procedure consists of only a single sweep in each iteration. When Equation (3.57) is incorporated into Equation (3.56), the resulting difference molecule is composed of nine points as shown in Figure 9. Since the sweep direction for the present SLOR scheme is aligned with the main stream (ξ) direction, ϕ's at the downstream column, i+1, are all evaluated at the nth-iteration level, and ϕ's at the ith column are all treated as unknown quantities at the (n+1)th-iteration level. The ϕ's at the upstream column, i-1, are all treated as known quantities at the (n+1)th-iteration level.

Using Equations (3.39) and (3.76), the resulting N is expressed as

$$NC^{n}_{i,j} = [-(R_i + R_{i-1}) + \omega R_{i-1} E_\xi^{-1} + \overleftarrow{\delta}_\eta R_j \overrightarrow{\delta}_\eta]\, C^{n}_{i,j} \qquad (3.77)$$

$$+ [\text{Cross Product Terms}]$$

The cross product terms are due to the skewness of the mesh cell and are represented as

$$\{\frac{1}{2}(\frac{A_2}{J})_{i,j} \overleftarrow{\delta}_\xi (\tilde{\rho}r)_{i+\frac{1}{2},j} \delta_\eta - \frac{\omega}{2} E_\xi^{-1}[(\frac{A_2}{J})_{i,j} (\tilde{\rho}r)_{i+\frac{1}{2},j} \delta_\eta]$$

$$- \frac{\omega}{4} E_\xi^{-1}[\overleftarrow{\delta}_\eta (\bar{\rho}r)_{i,j+\frac{1}{2}} (1 + E_\eta^{+1})(\frac{A_2}{J})_{i,j}]\}\, C^{n}_{i,j} \qquad (3.78)$$

where

$$R_i = (\frac{\tilde{\rho} A_1 r}{J})_{i+\frac{1}{2},j} \qquad R_j = (\frac{\bar{\rho} A_3 r}{J})_{i,j+\frac{1}{2}} \qquad (3.79)$$

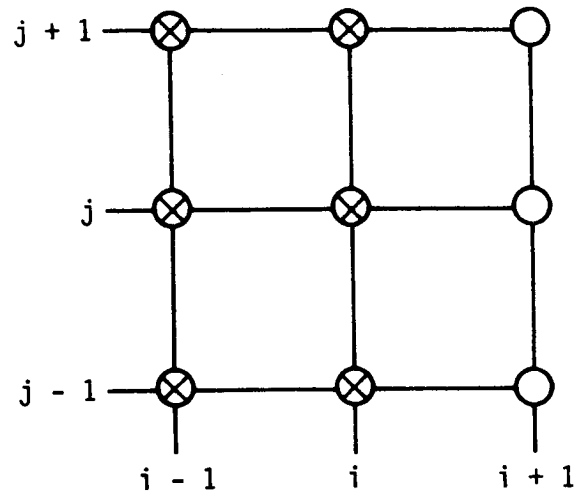

SLOR

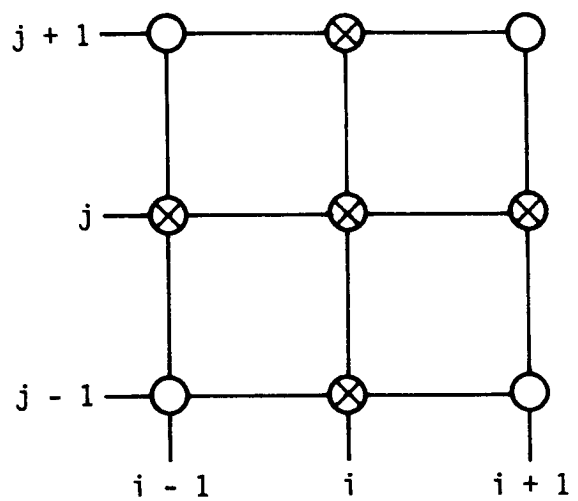

AF2

○ DIFFERENCING MOLECULE FOR L OPERATOR
× DIFFERENCING MOLECULE FOR N OPERATOR

FIGURE 9. Differencing molecule for operators

and E_{ξ}^{-1} and E_{η}^{+1} are defined as

$$E_{\xi}^{-1}\,(\,)_{i,j} = (\,)_{i-1,j} \qquad E_{\eta}^{+1}\,(\,)_{i,j} = (\,)_{i,j+1} \tag{3.80}$$

Although the correct zone of dependence is reflected on the computational domain through the artificial compressibility scheme, stability problems have been experienced near the sonic lines (where M is close to one) when the potential equation is solved (Jameson, 1974). This difficulty can usually be avoided by adding the time-dependent dissipation-like terms to numerical schemes (Holst, 1983). The first three terms in Equation (3.77) act like a time-dependent dissipation term ($\phi_{\xi t}$) in the pseudo-time analysis so that the SLOR scheme is usually stable for most of the transonic regime without an additional dissipation term. However, the SLOR scheme begins to show signs of a numerical instability as Mach number increases in supercritical cases. This instability problem at high Mach numbers might be avoided by adding additional time-dissipation terms (Jameson, 1974). At the present time, however, such an additional time-dependent dissipation term was not necessary when the velocity potential equation was solved coupled with the boundary-layer equations.

The most important single factor determining the rate of convergence of the SLOR solution is the relaxation parameter, ω. The optimum value of ω is usually very close to 2, but decreases slightly as the Mach number increases. The typical value of ω is between 1.90 and 1.95 for moderate shock wave flows. Because of stability requirements, ω was always set to unity in supersonic regions.

A complete η direction operator is included in N so that this scheme is implicit in the η direction. On the other hand, N involves only the lower diagonal part of the ξ direction operator, so this scheme is explicit in the ξ direction. This implies that each grid point is influenced by only a single grid point to the right in the ξ direction during one sweep so that the rate of convergence is relatively slower than the ADI or AF schemes. This set of N results in a tridiagonal matrix equation for each ξ = constant line. The resulting expression for the tridiagonal system written for the unknown quantities at the ith-column becomes

$$B_j C^n_{i,j-1} + D_j C^n_{i,j} + A_j C^n_{i,j+1} = E_j \tag{3.81}$$

The coefficients of Equation (3.81), A_j, B_j, D_j and E_j are functions of the already known C's at the adjacent columns, ϕ's from the previous iteration level, and the density. These coefficients are given in Appendix F. Note that only E_1 includes $dm^*/d\xi$ explicitly.

Equation (3.81) can be solved easily by eliminating either the upper or lower diagonal terms from the tridiagonal matrix using a standard Thomas algorithm. Elimination of the upper diagonal terms in the coefficient matrix results in the following bidiagonal recurrence relationships:

$$C^n_{i,1} = p_1 \tag{3.82-a}$$

$$C^n_{i,j} = p_j + q_j C^n_{i,j-1} \tag{3.82-b}$$

The coefficients, p_j and q_j, are also listed in Appendix F and are calculated recursively from j = NJ to j = 1. After elimination of the upper diagonal terms, only p_1 includes $dm^*/d\xi$ explicitly. A closer look at p_1 reveals the relation between $C^n_{i,1}$ and $dm^*/d\xi$ as

$$C^n_{i,1} = p_{10} + p_{11}(\frac{dm^*}{d\xi})_{i-\frac{1}{2}} + p_{12}(\frac{dm^*}{d\xi})_i + p_{13}(\frac{dm^*}{d\xi})_{i+\frac{1}{2}} \qquad (3.83)$$

If the distribution of m^* is known, then all $C^n_{i,j}$ at the ith column can be calculated using recurrence relationships, Equations (3.82)-(3.83).

The SLOR solution procedure then proceeds to the next (i+1) column and consequently completes one streamwise sweep column by column. This process is repeated through multiple sweeps until convergence has been achieved. The evaluation of convergence is based on the degree of accuracy of the residual as given by Equation (3.44). The convergence criterion, ε_c, was typically set equal to 1×10^{-3}. A typical inviscid flow calculation for a supercritical transonic case requires about 300 ~ 500 iterations. The solution procedure of the simultaneous interaction which treats both $C^n_{i,1}$ and $dm^*/d\xi$ as unknown variables will be explained in Chapter IV.

b. AF2 method In the approximate factorization scheme for a two-dimensional flow, the N-operator is usually approximated as a product of two factors as

$$N = N_1 N_2 \simeq L \qquad (3.84)$$

The factors N_1 and N_2 are chosen so that their product is a close

approximation to L and each factor requires only simple matrix operations and the overall scheme is stable. Several versions of the AF2 scheme, which differ only slightly, (Ballhaus and Steger, 1975; Ballhaus et al., 1978; Holst and Ballhaus, 1979; Flores et al., 1984) have been suggested. The present approximate factorization scheme is based on the AF2 scheme which was developed by Holst (1979) and used in TAIR computer code.

In the present study, the N-operator is factored as

$$NC^{n}_{i,j} = -\frac{1}{\alpha}(\alpha + \overleftarrow{\delta}_{\eta}R_{j})(-\alpha\vec{\delta}_{\eta} \mp \alpha\beta\vec{\vec{\delta}}_{\xi} - \overleftarrow{\delta}_{\xi}R_{i}\vec{\delta}_{\xi})\, C^{n}_{i,j} \tag{3.85}$$

where R_i and R_j are given by Equation (3.79). A free parameter α is interpreted as the inverse of an artificial time-step, $1/\Delta t$, as in the ADI method given in Equation (3.40). This AF2 scheme can be implemented in a two-step format as

step 1

$$(\alpha + \overleftarrow{\delta}_{\eta}R_{j})f^{n}_{i,j} = \alpha\omega L\phi^{n}_{i,j} \tag{3.86}$$

step 2

$$(-\alpha\vec{\delta}_{\eta} \mp \alpha\lambda\vec{\vec{\delta}}_{\xi} - \overleftarrow{\delta}_{\xi}R_{i}\vec{\delta}_{\xi})C^{n}_{i,j} = f^{n}_{i,j} \tag{3.87}$$

where $f^{n}_{i,j}$ is an intermediate result between alternative sweeps. The main difference between the present and Holst's scheme is that a regular right-hand coordinate system is used in the present analysis while Holst used a left-hand coordinate system. Therefore, some of signs in N_1 and N_2 in Holst's algorithm are different than those in the present

analysis.

In step 1, Equation (3.86) results in a set of simple bidiagonal matrix equations for the f array along the η direction. The second step consists of a set of tridiagonal matrix equations for the correction array, C, along the ξ direction. The resulting sets of matrix equations become

step 1

$$b_j f^n_{i,j-1} + d_j f^n_{i,j} = e_j \tag{3.88}$$

step 2

$$B_i C^n_{i-1,j} + D_i C^n_{i,j} + A_i C^n_{i+1,j} = E_i \tag{3.89}$$

The coefficients in these equations are given in Appendix G. Equation (3.88) can be solved easily by back-substitution if the boundary condition of f at j = 1 is known. The coefficients in Equation (3.89) form the familiar tridiagonal matrix that can be solved by the Thomas algorithm after all f^n's are obtained.

The most distinctive feature of the present AF2 scheme is that the difference approximation in the η direction is split between two steps. This provides a $\phi_{\eta t}$-type term which is thought to be helpful for the convergence process of the iteration scheme as the time-dependent dissipation term. This also places a restriction on a sweep direction in both steps. The sweep direction should be in the positive η direction, i.e., from j = 1 to j = NJ, for the first step and in the negative η direction, i.e., from j = NJ to j = 1, for the second step.

No restriction is imposed on sweep direction due to the flow direction in either of the two steps.

In order to avoid the instability problem occurring near sonic lines, a $\phi_{\xi t}$ term can be added explicitly, if necessary, in the appropriate factor insuring upwind differencing. In the present study, the $\phi_{\xi t}$-type term is included by adding $\pm \alpha\lambda\vec{\bar{\delta}}_{\xi}$ in the second step to provide time-dependent dissipation in the ξ direction. The difference direction of this term is always upwind with the flow direction as indicated by the double arrow notation and the sign is chosen so as to increase the size of the diagonal term of the matrix in Equation (3.89) ensuring diagonal dominance. This additional dissipation term only influenced stability and did not affect the values of the solution.

The magnitude of the $\phi_{\xi t}$ term is controlled by a parameter λ using special logic suggested by Dougherty et al. (1981). The value of λ is fixed at 0.3 in subsonic regions. In supersonic regions, λ is first initialized depending on the shock strength. Generally, the initial value of λ is small ($\sim$ 1.0) for small supersonic regions, moderate (3.0 $\sim$ 4.0) for moderate supersonic regions, large ($\geq$ 4.5) for large supersonic regions. Then λ is updated appropriately by monitoring the phase of solution convergence based on the average and maximum residual, i.e., if the solution is converging satisfactorily, λ is decreased; if not, λ is increased. In addition to this logic, λ is adjusted depending on how much time-dependent dissipation is required for the solution. This method developed by Dougherty et al. (1981) monitors the growth rate of the number of supersonic points, and if they grow fast, then λ

is increased; if they grow slowly, then λ is decreased.

The standard von Neumann stability analysis applied to a linearly simplified AF2 scheme (Holst, 1983) shows that this fully implicit iteration scheme is generally unconditionally stable as long as $0 \leq \omega \leq 2$ and $\alpha \geq 0$. Treating the iteration level as pseudo-time, which can be done by considering α as $1/\Delta t$, naturally suggests that fast convergence can be obtained with a small value of α, i.e., large time step. This is, however, effective for reducing only the low-frequency errors but not the high-frequency errors (Ballhaus et al., 1978). As was done in the ADI method used for grid generation, α is cycled over a sequence of values, given by Equation (3.43). Identifying the correct values for the high and low limits of α, i.e., α_H and α_L, is not easy and is again based on trial-and-error numerical experimentation. Suggested values for α_H and α_L are 1.5 and 0.07, respectively, and the value of ℓ is 8.

Implementation of the boundary conditions outlined in the previous section can be done without altering the form of factors N_1 and N_2 even at the wall. However, a few details need attention. First, the boundary condition on f at j = 1 is required at the beginning of the first sweep. Since the intermediate variable f has little physical meaning related to ϕ, it is not obvious how to provide a meaningful boundary value for f. Constructing the N-operator from the L-operator at the wall based on its boundary condition suggests that $f_\eta = 0$ seems to be a good approximation. This choice of boundary condition on f is also consistent with the fact that the value of f approaches zero as the

iteration process drives the solution to a steady state.

Associated with the solid surface boundary condition, there is an additional stability condition for the present AF2 scheme. The parameter α has to be restricted to some minimum value in the region close to the solid surface when the aforementioned wall boundary condition is used (Holst, 1983). Usually the value of α is multiplied by a factor of 10 in the vicinity of the wall surface. At the exit boundary, the second derivative term in the ξ direction in the second step, $(\overleftarrow{\delta}_{\xi} R_i \overrightarrow{\delta}_{\xi}) C^n_{i,j}$, is assumed to be zero according to the boundary condition.

When the distribution of m^* is known, C^n and ϕ^{n+1} are determined after two sweeps of Equations (3.88) and (3.89). This process is repeated iteratively until convergence is achieved. The convergence criterion is also evaluated by Equation (3.44) and the typical value of ε_c was 1×10^{-2}. The AF2 scheme seems to converge about 10 times faster than the SLOR method for transonic problems. Holst and Ballhaus (1979) observed that even with the same level of ε_c, the AF2 scheme provides the solution significantly closer to the finally converged solution than the SLOR scheme. This is because the average residual drops more slowly than the maximum residual in the SLOR scheme, while both maximum and average residual decrease with nearly the same speed in the AF2 scheme.

Holst and Ballhaus (1979) suggested that the reason for this behavior is due to the fact that the AF2 scheme reduces all error components efficiently whereas the SLOR scheme treats only the high-frequency error components efficiently and the maximum residual is

highly influenced by the high-frequency errors. They also suggested that the root mean square error is a better criterion with which to compare convergence performance between different relaxation algorithms. Since the maximum residual is the convenient way to monitor convergence of the solution, the AF2 algorithm can use a larger convergence criterion than the SLOR scheme to provide approximately the same average degree of accuracy in both converged solutions.

IV. VISCOUS-INVISCID INTERACTION METHOD

In the previous chapters, the solution procedures for the viscous and inviscid flow equations were presented. Hence, the solutions for each region can be obtained separately if the appropriate boundary conditions are provided. This zonal approach reduces the effort of solving the governing equations compared to the effort needed to solve the Navier-Strokes equations in the complete flow domain. However, in an interaction analysis, the solution in one region is permitted to influence the solution in another. In the present problem, this is carried out through the displacement effect of the viscous flow. This displacement effect causes a change in the boundary conditions for the inviscid flow as proposed by Lighthill (1958) and discussed in Section III. A. The zonal approach requires that the solutions from each zone match in some manner. This is usually implemented through the requirement that the surface pressure distribution obtained from the two solutions be identical. A coupling algorithm is needed to specify the way in which the boundary conditions for the viscous and inviscid flow will be altered from one iteration to the next in order to drive the solutions toward the matched condition.

There have been several interaction schemes proposed and these can be generally classified as direct, inverse, semi-inverse and simultaneous (see Figure 10). In Chapter I, some of the previous studies employed the interaction method were reviewed briefly and were summarized in Table 1. If the interaction between the viscous and inviscid flow is weak, i.e., the viscous effect upon the pressure field

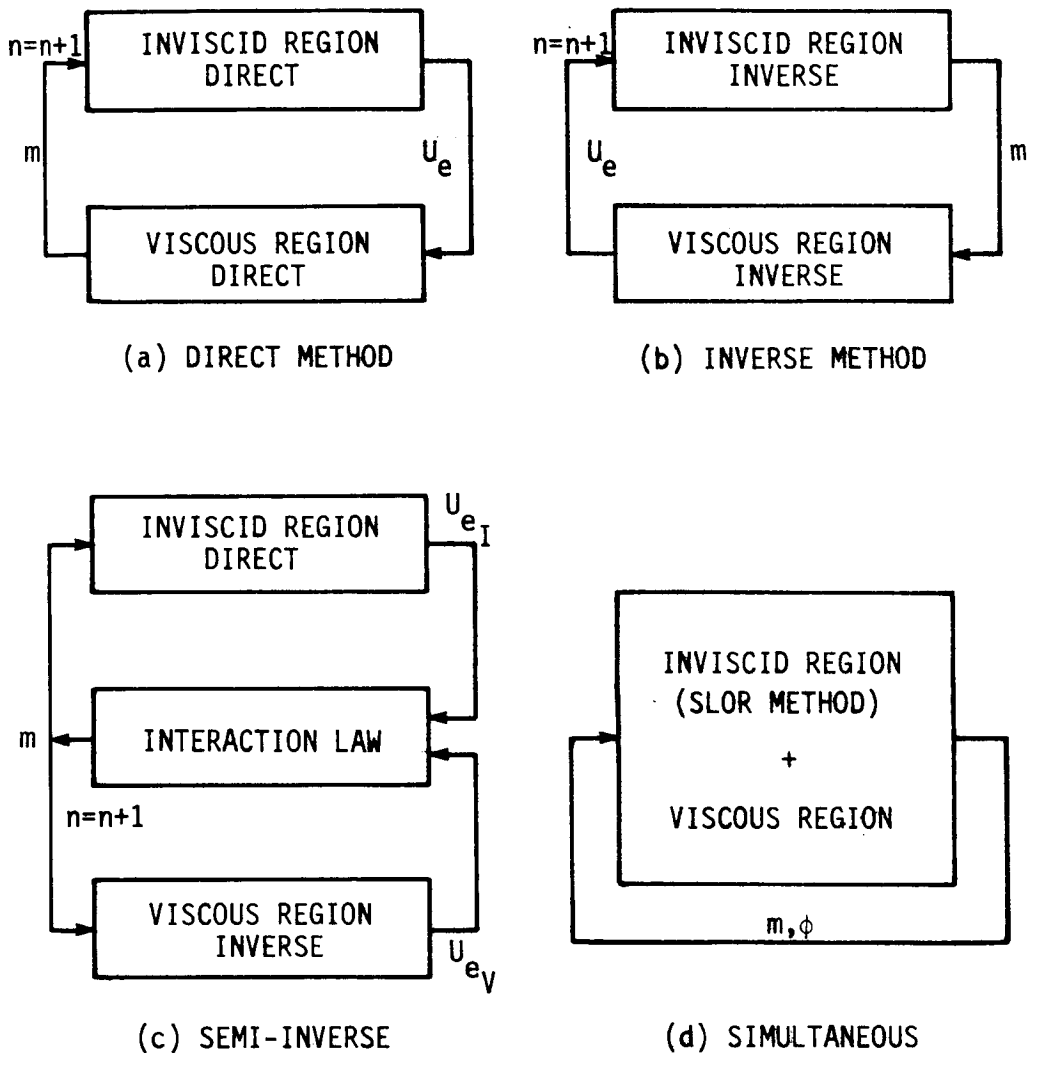

FIGURE 10. Coupling algorithms for the interaction method

is small, then the classical direct interaction method can be used. As sketched in Figure 10-a, in the direct interaction method, the solution is obtained in the viscous and inviscid regions sequentially in the direct mode, i.e., the boundary-layer equations are solved with a prescribed pressure field obtained from the inviscid solution to give the distribution of the displacement thickness and the inviscid flow is solved over the prescribed displacement thickness obtained from the boundary-layer solution to provide the pressure field. This procedure is repeated iteratively until both solutions converge. This method usually requires underrelaxation and converges slowly. The main shortcoming of the direct interaction method is, however, that the solution of the boundary-layer equations in the direct mode leads to a singularity at the point of separation as discussed earlier and consequently destroys the interaction process.

This difficulty can be overcome by using the inverse interaction method in which the role of the pressure and the displacement thickness is reversed from the direct method. In the inverse interaction method, the boundary-layer equations are solved with the prescribed displacement thickness and the inviscid region is solved with the prescribed pressure field (see Figure 10-b). However, it is difficult to develop an inverse solution procedure for transonic inviscid flow. Also, it is necessary to use a severe underrelaxation factor even for a simple case so that the whole iterative procedure is very slow to converge (Carter and Wornom, 1975).

The semi-inverse interaction method proposed by Le Balleur (1978) offered advantages over the inverse method. In the semi-inverse interaction method, the boundary-layer equations are solved inversely and the inviscid flow is solved in the direct mode. Therefore, solutions including the pressure distribution in both regions can be obtained with the same prescribed displacement thickness. A coupling algorithm (denoted as interaction law in Figure 10-c) is then devised to update the displacement thickness in a manner which will reduce the difference between the pressure distributions from the two solutions at the next iteration. The semi-inverse strategy is shown in Figure 10-c. The same idea was successfully used by Carter (1979) and Kwon and Pletcher (1979) for incompressible interacting flows but their coupling algorithm was different from the one used by Le Balleur (1978). This method was also applied to transonic flow calculations by Whitfield et al. (1981), Carter (1981) and Van Dalsem and Steger (1983) and Melnik et al. (1983).

However, the coupling algorithms used in the semi-inverse methods to date have been rather arbitrary and lack a rigorous theoretical background, although Carter (1979) gave a somewhat formal justification for his coupling algorithm based on the von Karman momentum integral relation. Also, according to the von Neumann stability analysis done by Wigton and Holt (1981), the semi-inverse method becomes unstable for supersonic separated flow due to the amplification of the high frequency Fourier components in the solution. Such an instability has also been experienced in the calculation of transonic flows with large separated

regions in the present study.

Since the viscous and inviscid flow regions are solved separately at each global iteration in the above method, only a weak coupling of the two regions is provided. For strongly interacting flows where the viscous and inviscid flow regions are locally coupled, a localized implicit treatment of coupling between the viscous and inviscid regions seems to be preferable. This type of approach which seeks a simultaneous solution of the the viscous and inviscid flow regions is classified broadly as a simultaneous interaction method (see Figure 10-d). This approach is further divided into the quasi-simultaneous and the (fully) simultaneous method depending on whether the simultaneous solution procedure is used partially or not. In the quasi-simultaneous method, the simultaneous solution procedure is used only in updating the boundary conditions needed for coupling, and either the boundary-layer or inviscid equations are solved separately. In the fully simultaneous interaction method, the full description of the viscous and inviscid flow regions are embedded together and are solved simultaneously instead of using a separate simple local relation.

Most of the quasi-simultaneous and simultaneous methods developed to date have used integral methods for either the viscous or inviscid flow equations. At this time, the work of Edwards and Carter (1985) seems to be the only one which utilized the finite-difference method for both viscous and inviscid flow equations for incompressible flows. No solution schemes of this kind have been noted for transonic flows. In the present study, a simultaneous interaction method was developed for

the finite-difference representation of the boundary-layer and potential equations for transonic flow. The semi-inverse interaction method was also utilized in the present study.

A. Semi-Inverse Method

The semi-inverse interaction procedure used in the present study solved the boundary-layer equations in the inverse mode inside the interaction region and used the AF2 scheme to solve the potential equation for the inviscid flow. These solution procedures have been outlined in previous chapters.

The coupling algorithm used in the present semi-inverse procedure is based on ideas introduced by Carter (1978) and Kwon and Pletcher (1979). In these earlier procedures, the displacement thickness distribution was updated based on the mismatch of edge velocities in the viscous and inviscid solutions employing a constant relaxation factor. This coupling algorithm allows use of overrelaxation which can increase the rate of convergence in some cases. However, it requires significant underrelaxation for flows with large separated regions as pointed by Melnik et al. (1983). This procedure is also expected to be unstable in supersonic separated flows according to Wigton and Holt (1981). In Le Balleur's semi-inverse method (1978, 1981a, 1981b), error measurement is based on the velocity gradient and locally optimum relaxation factors were applied. The preliminary calculations in the present study also confirmed that the use of streamwise variation in the relaxation factor improves the convergence rate. However, the choice of the turbulence

model also seems to influence the convergence behavior, sometimes requiring careful treatment of the relaxation factor for convergence.

In this study, a modification of the coupling algorithm was developed which resulted in a reduction of 10-40% in the number of viscous-inviscid global iterations required for a given convergence level. The new coupling algorithm is given as

$$m^{n+1} = m^{n}\left[(1 - \omega) + \omega\left(\frac{Ue_V}{Ue_I}\right)^{b}\right] \tag{4.1}$$

where Ue_V is the edge velocity obtained from the boundary-layer solution, Ue_I is the tangential velocity at the surface obtained from the solution of the potential equation, n is the global iteration level, ω is a relaxation factor and b is a parameter (the modification referred to previously) which has been taken as 1.0 in the previous studies. The typical value of ω used in the present calculation ranged from 0.2 to 1.0. Letting b take on values greater than 1.0 gives greater weight to the local discrepancy between the viscous and inviscid solutions and has been found to accelerate convergence significantly without jeopardizing stability. In this work, values of b ranging from 1.2 to 1.7 were used. It should be noted that this modified form of the coupling algorithm generally improves the rate of convergence but not the stability condition of the original algorithm.

In order to start the present semi-inverse interaction algorithm, an initial distribution of m is needed. This was obtained by solving boundary-layer equations in the direct mode using pressure data from the inviscid solution without the viscous effect. Usually, the adverse

pressure gradient from the fully converged inviscid solution is strong enough to cause separation in the boundary-layer calculations. Thus, only a few iterations were used in the inviscid solution in order to obtain a mild pressure gradient which did not cause boundary-layer separation. The distribution of $dm/d\xi$ used in evaluation of the transpiration velocity for the potential equation was obtained by applying a cubic spline interpolation method to the m distribution. Before applying the interpolation, m is adjusted by the distance t between the shear-layer coordinate and the body surface if necessary (see Equation (3.13)). It was also found that the computing time could be reduced considerably by not requiring full convergence of the inviscid solution at each global iteration. The number of inviscid solution iterations between each global viscous-inviscid iteration used in this work was 20 ~ 50.

The convergence of the interaction process was determined by the convergence of m, i.e.,

$$\varepsilon \geq \text{MAX} \left[\left| \frac{m^{n+1} - m^{n}}{m^{n}} \right| \right] \tag{4.2}$$

The typical convergence criterion was $\varepsilon = 1 \times 10^{-3}$. The number of global iterations to obtain the above convergence varied significantly from case to case and will be discussed in the next chapter.

The solution procedure of the above semi-inverse method is summarized as follows:

1) Assume the position of the shear-layer coordinate, if necessary.

2) Calculate the asymptotic solution of inviscid flow with zero

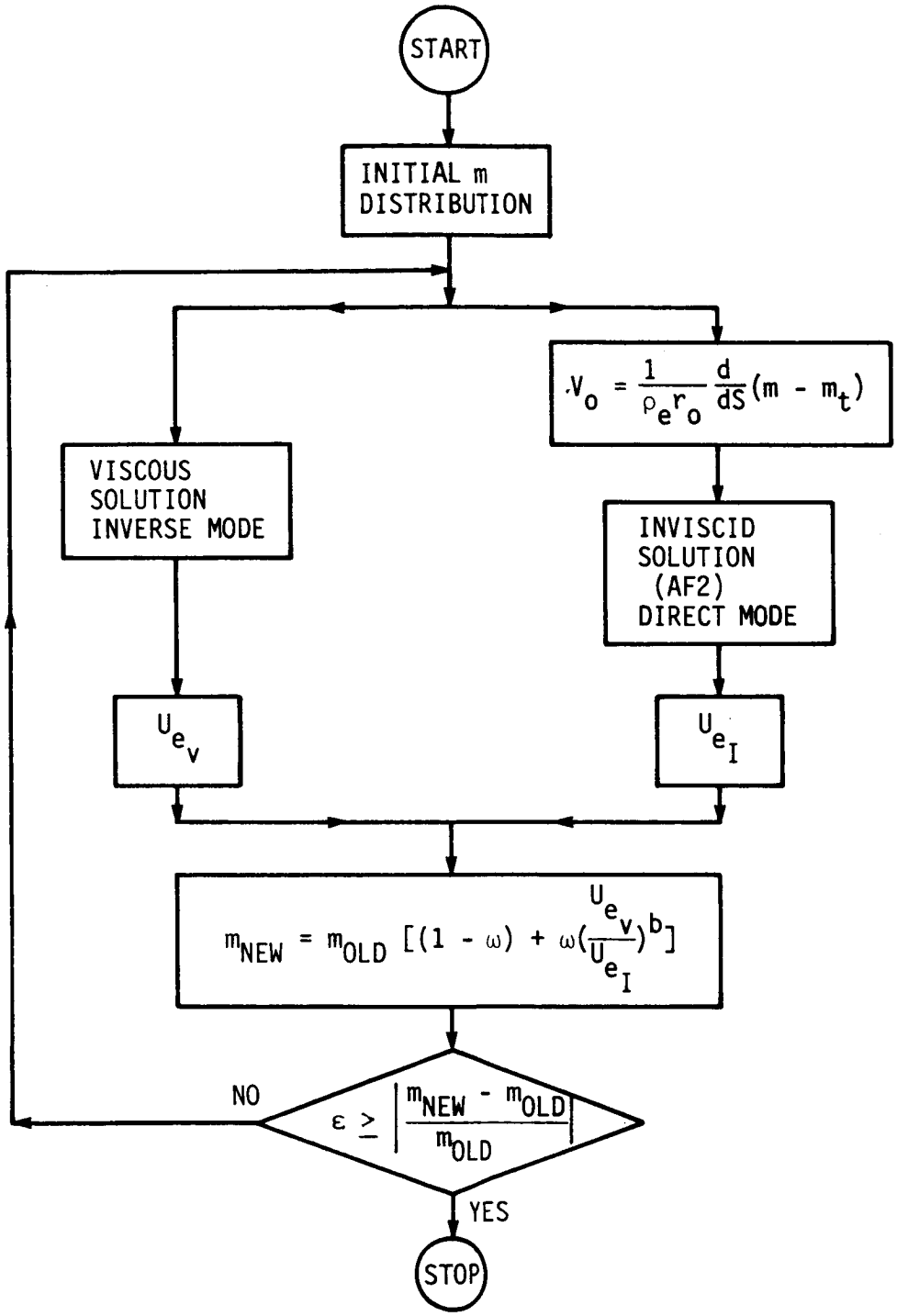

FIGURE 11. Flow chart for the semi-inverse method

transpiration velocity using the AF2 scheme to obtain the initial guess of the pressure distribution.

3) Using the initial pressure distribution, calculate the boundary-layer solution in the direct mode to obtain the initial m distribution.

4) With the m distribution, calculate the boundary-layer solution in the inverse mode.

5) If the shear-layer coordinate system was used, adjust the m distribution with the distance t (see Equation (3.13)).

6) Using the adjusted m distribution, solve the potential equation for inviscid flow using the AF2 scheme.

7) Examine convergence using Equation (4.2). If the solution meets the convergence criterion, terminate the calculation. Otherwise, proceed to step (8).

8) Update the m distribution using Equation (4.1).

9) Return to step (4).

The organization of this calculation procedure is also shown in Figure 11.

B. Simultaneous Method

When the simultaneous interaction method is used, the potential equation is solved using the SLOR scheme so that the boundary-layer equations and potential equation are solved along the same sweep direction. In the solution procedure of the boundary-layer equations, the local relation between the pressure gradient parameter, β, and the nondimensional mass flux m_v was given by Equation (2.139). Also, in the

SLOR procedure for the potential equation, the explicit local relation between the correction array at the wall, $C^n_{i,1}$, and $dm^*_I/d\xi$ was provided by Equation (3.83).

By using a finite-difference approximation for $dm^*/d\xi$, $C^n_{i,1}$ can be written in terms of m^*. The optimum choice of the finite-difference expression for $dm^*/d\xi$ was not clear but was chosen by trial-and-error. The expressions used for $dm^*/d\xi$ are given as

$$\left.\frac{dm^*}{d\xi}\right|_i = \frac{1}{2\Delta\xi}(3m^{*n+1}_i - 4m^{*n+1}_{i-1} + m^{*n+1}_{i-2})$$

$$\left.\frac{dm^*}{d\xi}\right|_{i-\frac{1}{2}} = \frac{1}{24\Delta\xi}(-m^{*n}_{i+1} + 27m^{*n+1}_i - 27m^{*n+1}_{i-1} + m^{*n+1}_{i-2}) \qquad (4.3)$$

$$\left.\frac{dm^*}{d\xi}\right|_{i+\frac{1}{2}} = \frac{1}{24\Delta\xi}(-m^{*n}_{i+2} + 27m^{*n}_{i+1} - 27m^{*n}_i + m^{*n}_{i-1})$$

Hereafter, $\Delta\xi_I$ will be omitted because $\Delta\xi_I$ was set to unity (see Section III. C. 2). The finite-difference expression for $(dm^*/d\xi)_i$ is most important in obtaining the stable solution, because this term is directly associated with the transpiration velocity, v_o. This term was approximated by a second-order-accurate backward differencing formula. The other two terms at $(i-\frac{1}{2})$ and $(i+\frac{1}{2})$ stations usually have little effect on the accuracy and stability of the solution, since these terms appear due to the skewness of the mesh cell at the wall. They are approximated by fourth-order-accurate central differencing formulas. Especially, $(dm^*/d\xi)_{i+\frac{1}{2}}$ was evaluated based on the previously known distribution of m^* at the nth-iteration level so that this term was treated as known quantity.

Since the sweep direction is along the positive ξ direction, the values of variables for $i \leq i-1$ are already known at the (n+1)th-iteration level and the values of the variables for $i \geq i+1$ can be evaluated at the nth-iteration level. Therefore, by combining Equation (4.3) and Equation (3.83), $C^n_{i,1}$ can be expressed as a function of m^{*n}_i as

$$C^n_{i,1} = \lambda_1 m^{*n}_i + \lambda_2 \tag{4.4}$$

The pressure gradient parameter, β, defined in Equation (2.98) can be rewritten as

$$\beta = C_M \frac{dM^*}{d\xi_V} \tag{4.5}$$

where

$$M^* = u_e / a^* \tag{4.6}$$

$$C_M = [(1 - \frac{\gamma-1}{\gamma+1}M^{*2})M^*]^{-1} \tag{4.7}$$

and ξ_V is the transformed ξ coordinate used in the analysis of the boundary-layer equations. Using a velocity potential, M^* is given as

$$M^*_{i+\frac{1}{2}} = R_{\ell_i} \phi_{\xi_I}\Big|_{i+\frac{1}{2}} \tag{4.8}$$

where

$$R_{\ell_i} = [(\frac{J}{A_3})_{i+\frac{1}{2},1}]^{\frac{1}{2}} \tag{4.9}$$

where J and A_3 are the Jacobian and metric quantity of the transformation used in the inviscid flow analysis and were given by Equation (3.27).

Applying a central difference approximation, the pressure gradient parameter at ith streamwise station can also expressed in terms of velocity potential as follows:

$$\beta_I = C_M \frac{\Delta\xi_I}{\Delta\xi_V} \frac{dM^*}{d\xi_I}$$

$$\simeq \frac{C_M}{\Delta\xi_V} (\overleftarrow{\delta}_{\xi_I} R_{\ell_i} \overrightarrow{\delta}_{\xi_I}) \phi_{i,1} \tag{4.10}$$

$$\simeq \frac{C_M}{\Delta\xi_V} [R_{\ell_i} (\phi^n_{i+1,1} - \phi^n_{i,1}) - R_{\ell_{i-1}} (\phi^{n+1}_{i,1} - \phi^{n+1}_{i-1,1})]$$

where M^* in the C_M is approximated by values at the nth-iteration level. Substituting Equation (4.4) into Equation (4.10) and combining all known quantities, the pressure gradient parameter in the inviscid flow field based on the SLOR scheme can be approximated in the following form,

$$\beta_I = a^*_I m^* + b^*_I \tag{4.11}$$

where

$$a^*_I = - \frac{C_M}{\Delta\xi_V} R_{\ell_{i-1}} \lambda_1 \tag{4.12-a}$$

$$b^*_I = \frac{C_M}{\Delta\xi_V} [R_{\ell_i} (\phi^n_{i+1,1} - \phi^n_{i,1}) - R_{\ell_{i-1}} (\phi^n_{i,1} + \lambda_2 - \phi^{n+1}_{i-1,1}] \tag{4.12-b}$$

By nondimensionalizing m^*_I in the same way as m_V, and treating m_t in Equation (3.13) as a known quantity, the inviscid pressure gradient parameter, Equation (4.11), can be rewritten in terms of m as follows.

$$\beta_I = a_I m + b_I \tag{4.13}$$

Requiring that both pressure gradient parameters be the same, i.e., $\beta_V = \beta_I$, the new value of m can be determined from Equation (2.139) and (4.13) as

$$m = \frac{b_V - b_I}{a_I - a_V} \tag{4.14}$$

When m and β are determined, the velocity profile in the boundary layer, F^i_j and ψ^i_j are easily calculated using Equations (2.131), (2.132), (2.134) and (2.135). Since the Newton linearization procedure was applied to the boundary-layer equations, the coefficients a_V and b_V must be iteratively updated. Therefore, m also has to be iteratively determined at each local streamwise station until a local boundary-layer solution converges.

On the other hand, the local inviscid relation given by Equation (4.11) does not need to be iteratively updated because the potential equation analysis does not include linearization except for the density term which is updated at the end of each streamwise sweep. When m converges, $C^n_{i,1}$ can be obtained by Equation (4.4). Before calculating $C^n_{i,1}$, the relaxation factor, ω, is applied to the new m. The global iteration process is very sensitive to the choice of ω and the optimum value of ω determined by trial-and-error ranged from 0.2 to 0.7. Given the value of $C^n_{i,1}$, the rest of the correction array, $C^n_{i,j}$, are calculated by back-substitution using the recurrence relation, Equation (3.82).

The above procedure is then advanced to the next streamwise (i+1)

station. This overall sweep procedure is repeated until the solutions converge. The skeleton flow chart for this simultaneous interaction method is shown in Figure 12. The convergence criterion used in the present simultaneous interaction method was also based on the convergence of m, which was given by Equation (4.2). The typical value of ε ranged from 1×10^{-3} to 5×10^{-4}. The initial distribution of m needed to start the interaction was provided in the same way as in the semi-inverse method.

The calculation procedure for the simultaneous interaction method is summarized as follows:

1) Assume the position of the shear-layer coordinate, if necessary.
2) Calculate the asymptotic solution of the inviscid flow with zero transpiration velocity using the SLOR scheme to obtain the initial guess for the pressure distribution.
3) Using the initial pressure distribution, calculate the boundary-layer solution in the direct mode to obtain the initial m distribution.
4) With the m distribution, start the streamwise sweep of the boundary-layer equation and the SLOR procedure for the potential equation.
5) Calculate the recurrence formula for $C^n_{i,j}$ and the relation between β_I and m at the ith streamwise station from the SLOR solution procedure.
6) Obtain the relations between β_V and m from the recurrence formula at the ith streamwise station from the boundary-layer solution procedure.

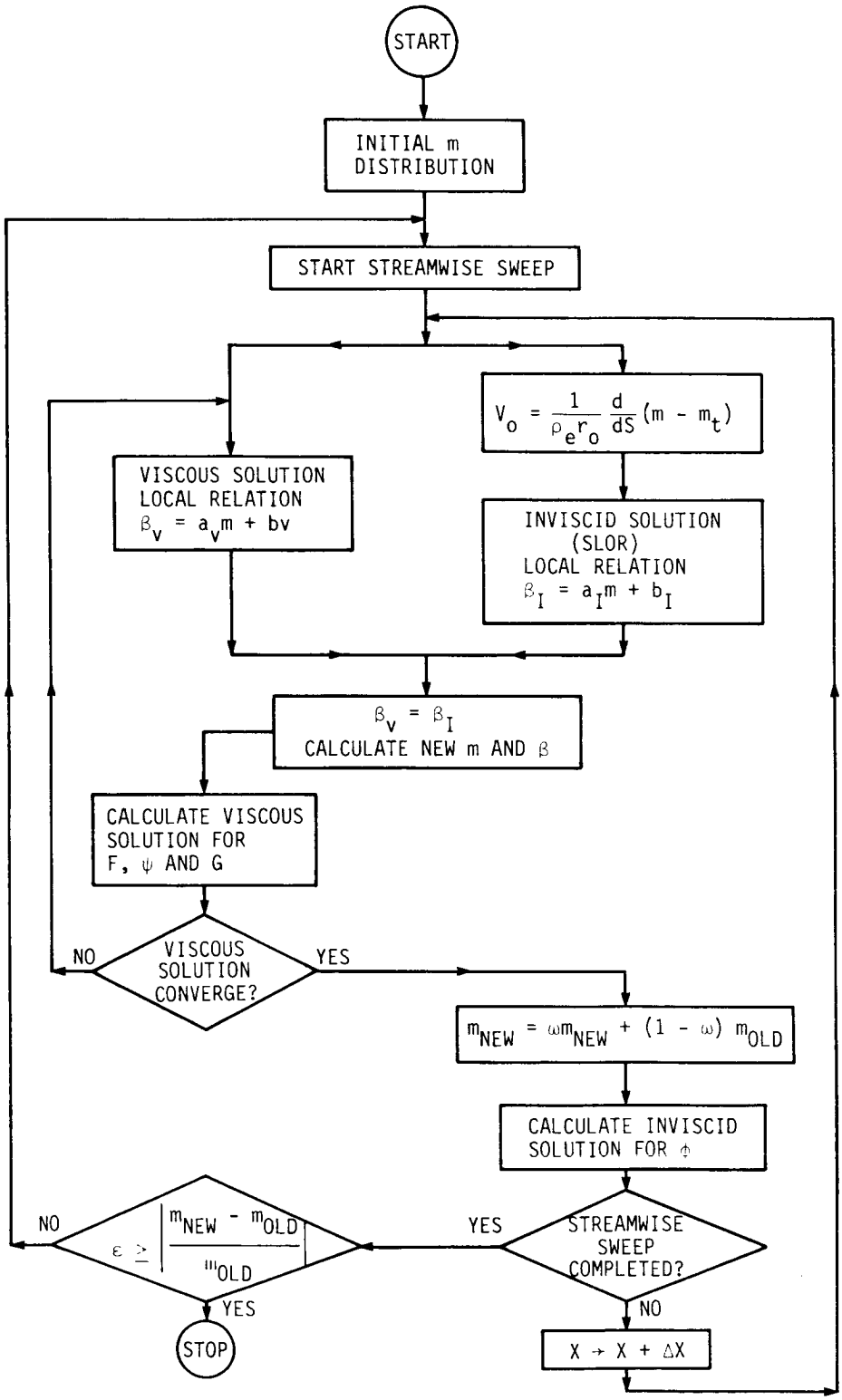

FIGURE 12. Flow chart for the simultaneous method

7) Calculate the new m by letting $\beta_V = \beta_I$.

8) Examine convergence of m and the boundary-layer solutions. If the convergence criteria are met, proceed to step 9. Otherwise, return to step 6.

9) Apply the underrelaxation to the converged m.

10) Calculate the correction array, $C^n_{i,j}$ with the relaxed m.

11) Proceed to the next streamwise (i+1) station.

12) At the end of each streamwise sweep, examine convergence using Equation (4.2). If the solutions meet the convergence criterion, terminate the calculation. Otherwise, return to step 4.

V. RESULTS AND DISCUSSION

This chapter presents the results of the present study. The results are mainly divided into two categories: incompressible and transonic flows. First, predictions of incompressible laminar separated flow are presented. These were obtained as part of a preliminary study to test the basic performance of the present viscous-inviscid interaction methods. Second, the computational results for transonic turbulent flows with separation are presented in order to fully evaluate the capabilities of the present interaction schemes.

Before the present numerical algorithm was applied to interaction problems, the viscous and inviscid solution procedures were tested separately for simple boundary layer and inviscid problems. The inverse solution procedure for the boundary-layer equations was verified by solving two laminar separated flows which have been studied numerically by many others; 1) linearly retarded flows studied by Howarth (1938), Briley (1971), Klineberg and Steger (1974), Carter (1975), Murphy (1977), Cebeci and Stewartson (1983), and Halim and Hafez (1984); 2) incompressible flows studied by Carter (1975) and Cebeci et al. (1979). The inverse solutions obtained by the present method for these flows provided good agreement with the other available solutions obtained based on the boundary-layer equations. The solution procedure for the inviscid flow was checked by comparing solutions for boattail and bump flows with available inviscid solutions (Wilmoth, 1977; Carter, 1981). The inviscid solutions obtained by the present methods (SLOR, AF2) also showed good agreement with the other inviscid solutions. A detailed

description of above comparisons is, however, not included here.

A. Incompressible Laminar Flow

The present viscous-inviscid interaction methods are demonstrated by recalculating one of flows studied by Carter and Wornom (1975). They analyzed a two-dimensional, incompressible, laminar, separated flow over a flat plate with a trough located downstream of the leading edge using a conventional inverse viscous-inviscid interaction method. The surface is prescribed as

$$y = - t_a \, \mathrm{sech}(4x - 10) \tag{5.1}$$

where t_a is the depth of the trough as shown in Figure 13 and was set to 0.03 m in the present calculation. This provides essentially a flat surface far upstream and downstream of x = 2.5 m. The leading edge of the plate is set at x = 0 m. The Reynolds number based on freestream conditions and the unit length is $Re_\infty = 8 \times 10^4$. In their solution procedure, the boundary layer was calculated in a inverse mode using vorticity transport and stream function equations and the inviscid flow was computed by the inverse Cauchy integral formulation based on small disturbance theory.

This flow over a trough configuration has also been analyzed by many other investigators including Kwon and Pletcher (1981), Veldman (1981), Davis and Werle (1981), Carter and Vasta (1982b), and Edwards and Carter (1985). This separated flow is a good benchmark case to test the interaction scheme for incompressible flow, since all of the above

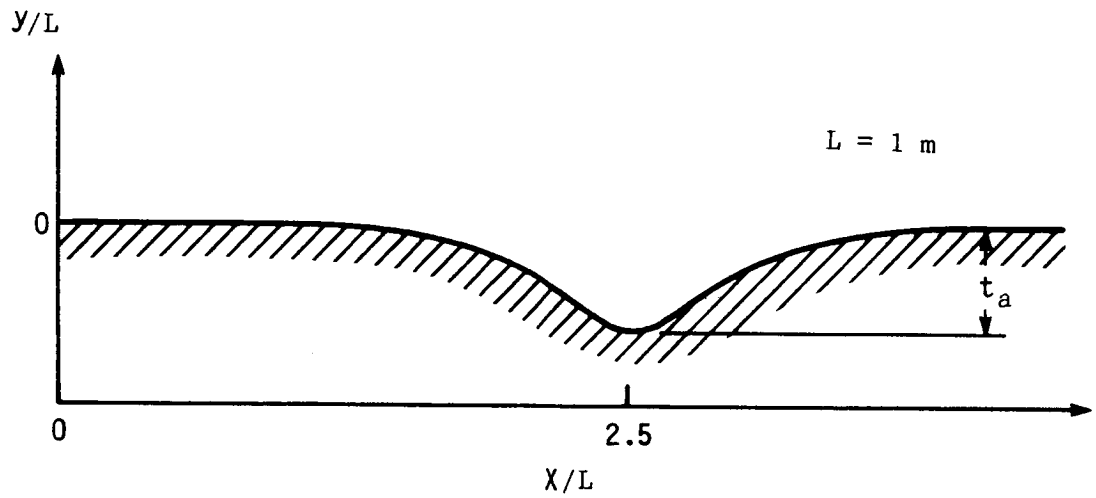

FIGURE 13. Geometric configuration of a flat plate with a trough

results are in good agreement. Kwon and Pletcher (1981) and Carter and Vasta (1982b) used the semi-inverse interaction method, and Veldman (1981) and Davis and Werle (1981) used the quasi-simultaneous interaction method. All these analyses employed the direct Cauchy integral formulation for the inviscid flow region. Edwards and Carter (1985) utilized the semi-inverse and the quasi-simultaneous interaction methods employing a finite-difference solution procedure for the Laplace equation for stream function in the inviscid flow region. All the above works used finite-difference solutions for the viscous region. In the present study, the semi-inverse and simultaneous interaction methods employed finite-difference methods for both the viscous and inviscid regions.

The description of the present method given in Chapters II-IV was for the general case of compressible flow. For the incompressible computations, the velocity potential equation was nondimensionalized using freestream conditions rather than the critical speed of sound and stagnation density. The rest of the solution procedure essentially remains the same. In the present calculation, the inflow and outflow boundary were set to $x = -2.5$ m and $x = 7.5$ m, respectively and the outer boundary was set to $y = 5$ m for the inviscid flow field. The inviscid solution was obtained with a mesh of 101×31 grid points in the streamwise and transverse directions, respectively. These mesh points were formed with nonuniform spacing so that a concentration of grid points occurred near $x = 2.5$ m and $y = 0$ m. The interaction region extended from $x = 1.0$ m to $x = 4.0$ m and 65 grid increments were used in

the streamwise direction. Inside the interaction region, the mesh for the boundary-layer solution used the same streamwise grid points as the inviscid mesh and 60 points were placed uniformly in the normal direction. The boundary-layer equation was started at x = 0 m from the uniform freestream conditions. Since the flow was assumed to be isothermal, the energy equation was not solved and the density and viscosity were assumed constant. A shear-layer coordinate was not used and the FLARE approximation was always used in the reversed flow regions.

The same initial distribution of displacement thickness as used by Carter and Wornom (1975) was assumed to start the interaction procedure. For the semi-inverse method, the relaxation factor was set to 0.7 and parameter b in Equation (4.1) was set to 1.5. For the simultaneous method, the relaxation factor was set to 0.5. With the semi-inverse method, approximately 20 global iterations were required to satisfy the convergence criterion $\varepsilon = 1 \times 10^{-3}$ (see Equation (4.2)). For the same convergence level, the simultaneous method converged in about 80 iterations. However, each global iteration cycle in the semi-inverse method required 50 iterations for the intermediate inviscid solution to converge. Therefore, the simultaneous method required only about half the computing time required by the semi-inverse method. However, no effort was made to optimize the convergence process of either interaction scheme for this flow case.

Some results calculated with the present interaction methods are compared with the predictions of Carter and Wornom (1975) in Figures

14-16. The results of other investigators were not plotted because all seem to agree very well within graphical accuracy. The predicted distributions of the surface pressure are shown in Figure 14. The present solutions are in good agreement with those of Carter and Wornom. Also, the semi-inverse and simultaneous methods gave almost identical results as expected. However, a slight difference in the prediction of the maximum pressure recovery at the bottom of the trough is noticeable. This difference is believed to be due to the different inviscid solution procedures used in the two interaction methods.

Figure 15 shows the comparison of the predicted displacement thickness distributions. Although the present solutions agree well with that of Carter and Wornom (1975), the displacement thickness downstream of the trough is slightly overpredicted. A similar tendency was observed by Kwon and Pletcher (1981) and a detailed discussion about this can be found in their paper. The predicted skin-friction distribution is shown in Figure 16 along with the Blasius similarity solution of a flat plate. The present results show that the predicted values return to the Blasius solution toward the end of the interaction region and they are also in excellent agreement with the prediction of Carter and Wornom except in the vicinity of the reattachment point. This disagreement near the reattachment point may be due to differences in the grid spacing. The present mesh spacing in the streamwise directions was almost twice as large as that used by Carter and Wornom.

A careful comparison of the present results with solutions of other viscous-inviscid interaction schemes for this laminar flow suggests that

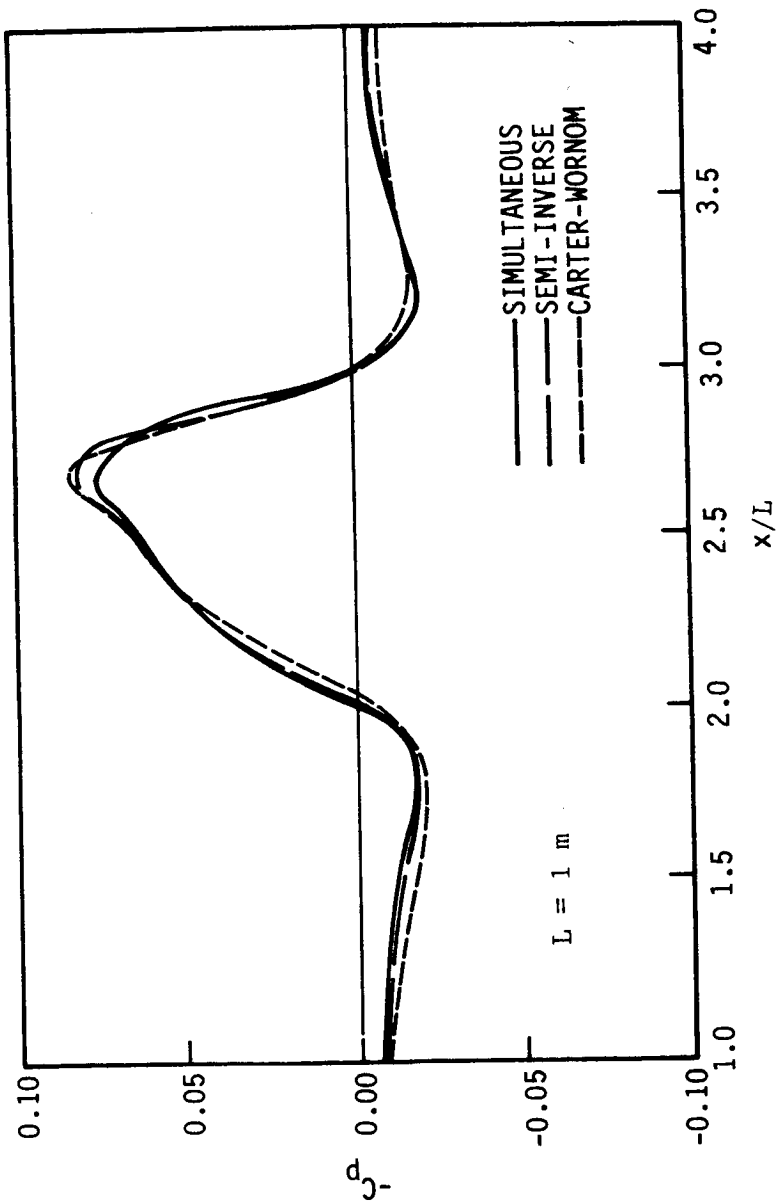

FIGURE 14. Pressure coefficient distribution for an incompressible laminar separation bubble flow over a flat plate with a trough ($Re_\infty = 8 \times 10^4$)

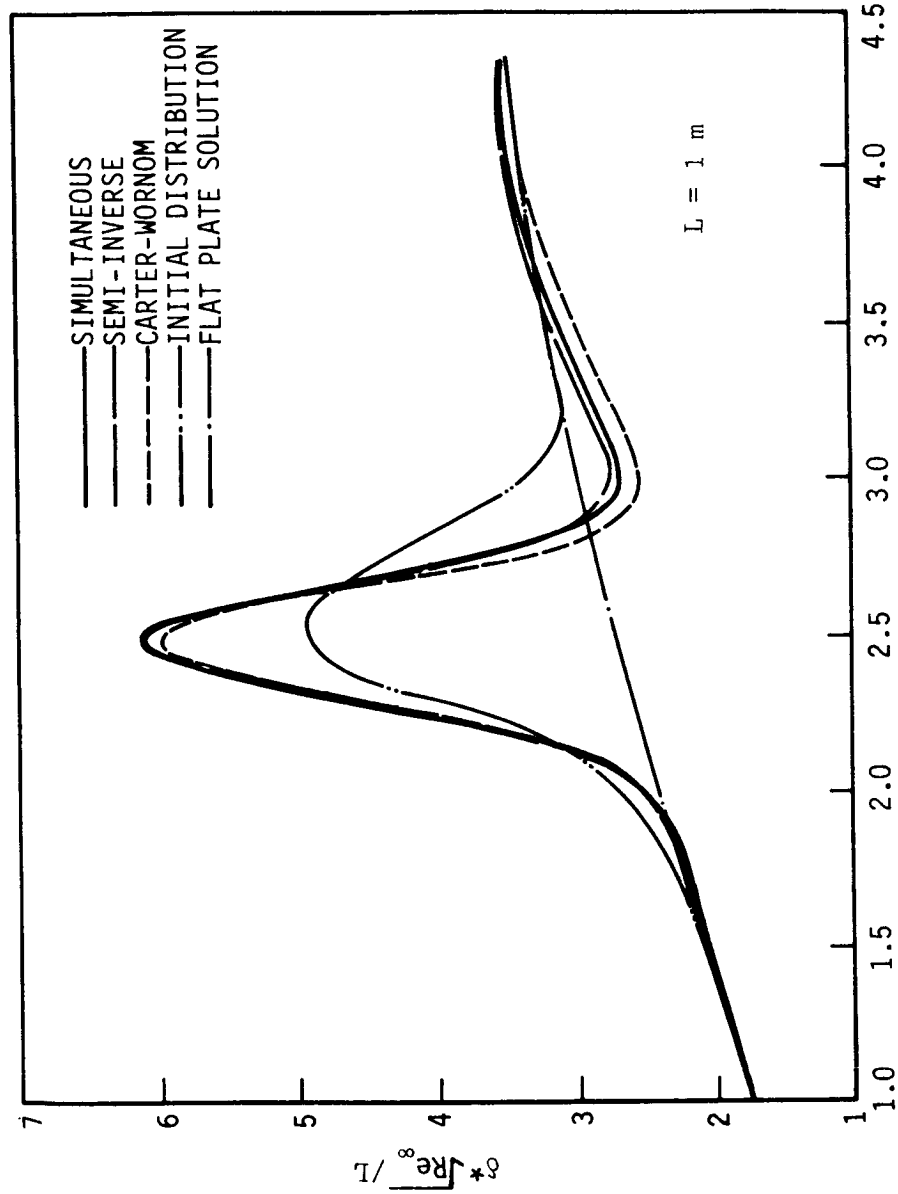

FIGURE 15. Displacement thickness distribution for an incompressible laminar separation bubble flow over a flat plate with a trough ($Re_\infty = 8 \times 10^4$)

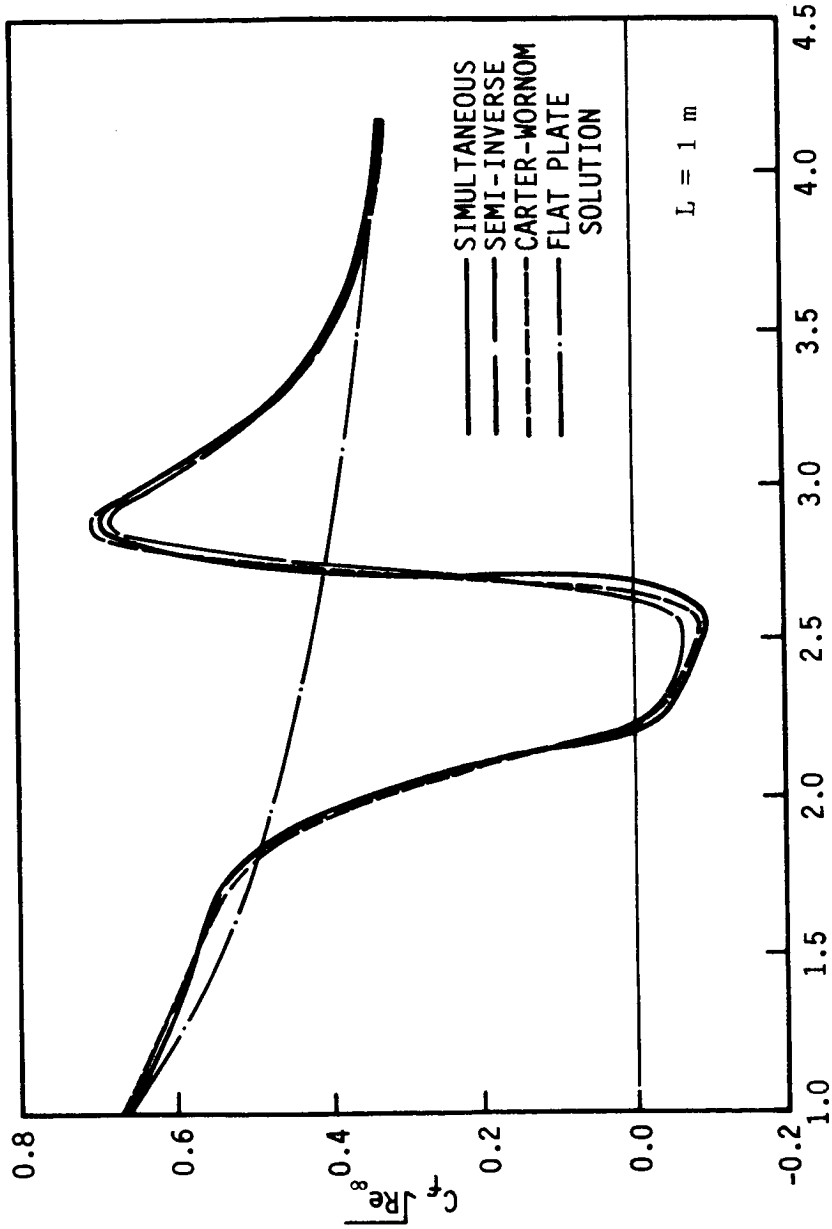

FIGURE 16. Skin-friction coefficient distribution for an incompressible laminar separation bubble flow over a flat plate with a trough ($Re_\infty = 8 \times 10^4$)

the present interaction schemes, both the modified semi-inverse and simultaneous schemes, are capable of predicting the separated flows very accurately and they are also very consistent with each other. However, the present interaction methods were designed primarily for the transonic regime and have not been optimized for incompressible flows. The incompressible flow case was included to verify that the present algorithms do produce solutions that agree with established results in the incompressible limit. This was considered essential before proceeding to more complex transonic flow cases.

B. Transonic Turbulent Flow

Further evaluation of the present interaction schemes was made by computing transonic turbulent flows with significant separation which involved strong interaction between inviscid and viscous regions. Comparisons will be presented for two different body configurations.

1. Boattail flow

The first to be considered is the transonic flow over an axisymmetric circular-arc boattail with a solid cylindrical plume simulator studied experimentally by Reubush (1974). This experiment was conducted in the NASA Langley 16 foot transonic wind tunnel in order to determine the effectiveness of utilizing solid circular cylinders to simulate real jet exhaust plumes. Extensive measurements of surface pressures and boattail drag were obtained over a freestream Mach number range of 0.40 to 1.3 for several configurations. The boattail configuration is shown in Figure 17 and more detailed information can be

found in an article by Reubush (1974).

In the calculations by the present methods, the computational domain for the inviscid flow solution, shown in Figure 18, varied with the body configuration; the upstream boundary was always set at $x/d_m = -3.0$ and the downstream boundary was set at $x/d_m = 4.0$ and 5.5 for configurations 1 and 2, respectively. The outer boundary was always set at 5 d_m. The coordinate x was measured from the starting point of boattail and d_m is the maximum boattail diameter. The inviscid solution was obtained with a mesh of 101 × 31 grid points in the streamwise and transverse directions, respectively. These grid points were nonuniformly distributed so that about a third of total gird points were placed along the boattail region and a concentration of mesh points was placed at the boattail-sting juncture. The interaction region was assumed to extend from $x/d_m = -1.0$ to $x/d_m = 2.5$ for the configuration 1 boattail and from $x/d_m = -1.0$ to $x/d_m = 3.5$ for the configuration 2 boattail. Inside the interaction region, the same streamwise grid spacing was used at the body surface for both the inviscid and viscous solutions and 61 ~ 65 grid points were used. In the transverse direction, 70 boundary-layer grid points were nonuniformly distributed based on Equation (2.105). The ratio between two adjacent grid spacing, K, was 1.05.

A velocity profile at the upstream boundary was obtained from the direct boundary-layer solution starting from the leading edge ($x/d_m = -6.64$) using the pressure obtained from the undisturbed inviscid solution. This inflow velocity profile was not updated during the

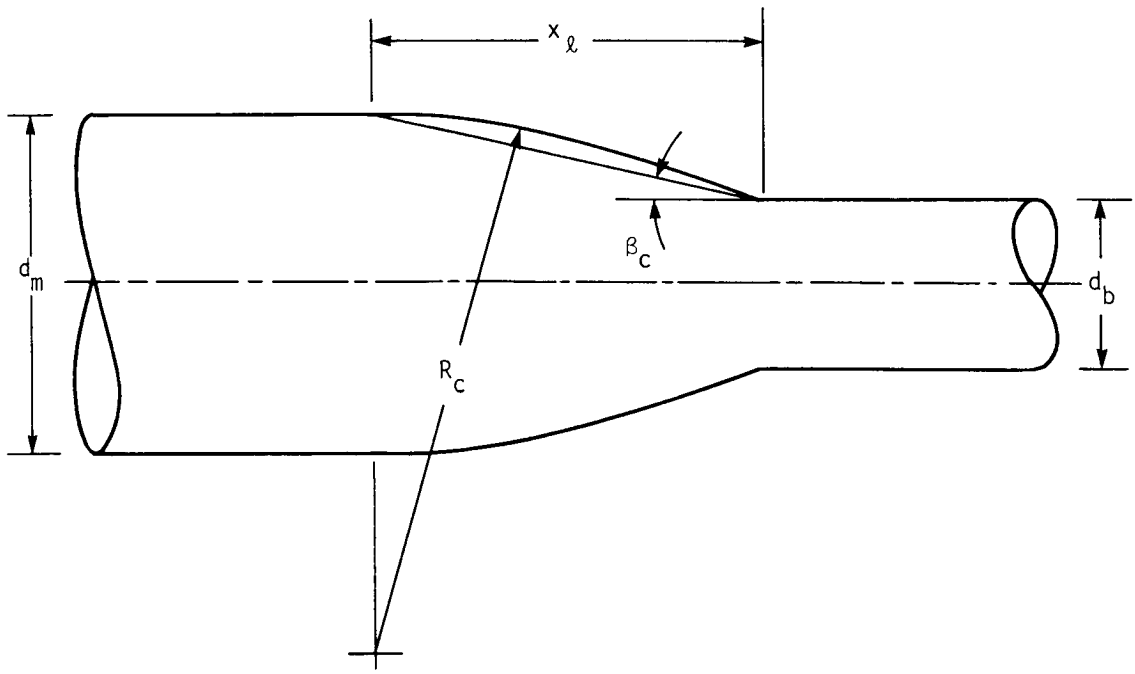

BOATTAIL GEOMETRIC PARAMETERS

CONF.	x_ℓ/d_m	d_b/d_m	R_c/d_m	β_c, deg
1	0.800	0.51	1.429	17.027
2	1.000	0.51	2.163	13.766
3	1.768	0.51	6.500	7.891

FIGURE 17. Geometric configuration of a boattail

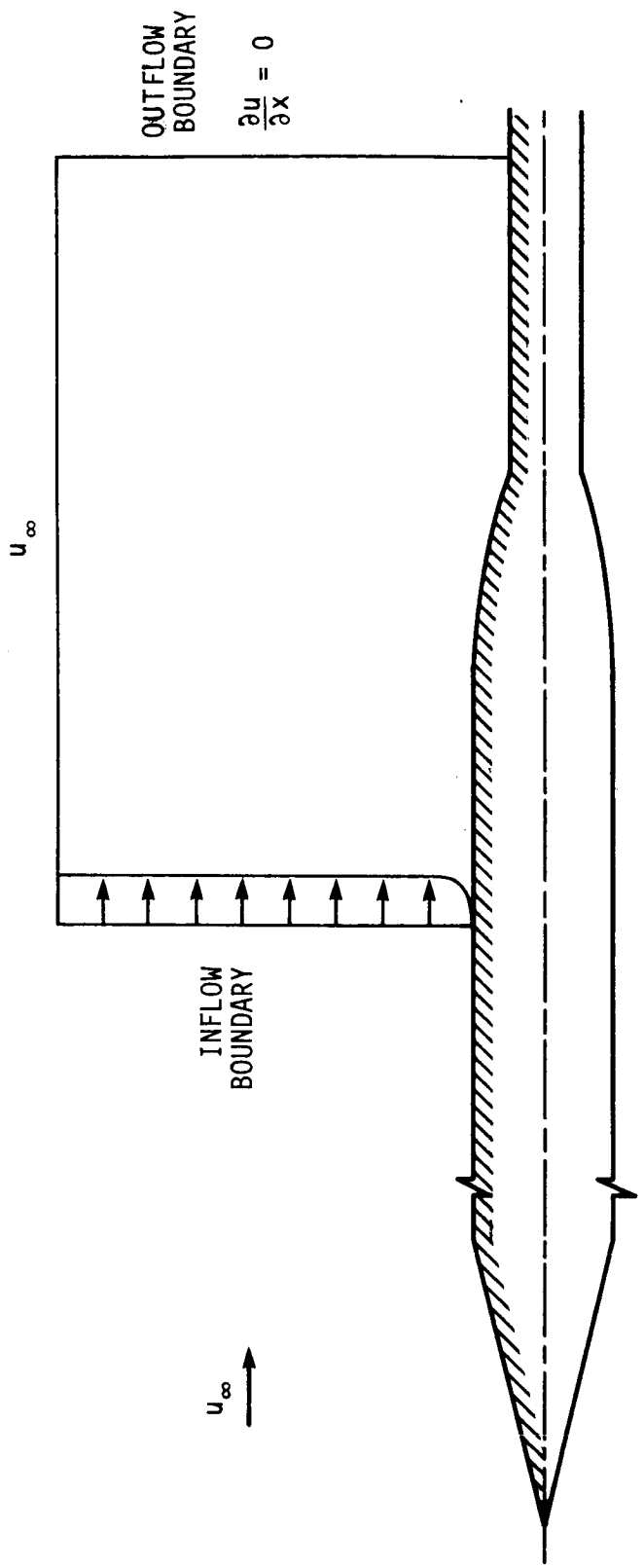

FIGURE 18. Computational domain for the inviscid solution of the boattail flow

interaction process because the pressure distribution upstream of the interaction region obtained from the interacted inviscid solution remained nearly unchanged. The effect of the cone-cylinder forebody was neglected in the present calculations. The initial distribution of the mass flux, m, was obtained by the boundary-layer solution in the direct mode using the pressure data provided by the undisturbed inviscid solution of the AF2 scheme with only 10 iterations. The distribution of m downstream of the interaction region was iteratively calculated by assuming that dm/dx in that region decreased linearly from the value at the interaction boundary to zero at the exit boundary.

In every turbulent flow calculation for this configuration, transition from laminar to turbulent flow was assumed to occur near the leading edge at $x/d_m = -6.0$ and the algebraic Cebeci-Smith and Johnson-King turbulence models were used. When the Johnson-King model was used, it was initiated at $x/d_m = -1.1$ after starting with the Cebeci-Smith model. In the figures to follow, the results of the simultaneous and semi-inverse methods obtained with the Johnson-King turbulence model will be shown with the results of the simultaneous method obtained with the Cebeci-Smith model. Since the results of the semi-inverse interaction methods obtained with the Cebeci-Smith model were always in good agreement with those of the simultaneous method obtained with the same model, they will not be displayed. In the region of reversed flow, the FLARE approximation was always used.

Even though Reubush (1974) performed extensive measurements for a wide range of Mach numbers, Reynolds numbers and boattail

configurations, only a few representative cases were calculated in the present study. The first comparison was made for the configuration 2 boattail case at $M_\infty = 0.8$ and $Re_\infty = 1.22 \times 10^7$, which resulted in a fully attached flow over a smooth boattail surface without the appearance of a shock wave. Because of the smooth body surface, the shear-layer coordinate was not used in this case. With the semi-inverse method, the relaxation factor was set to 1.2 and the value for parameter b in Equation (4.1) was also set to 1.5. The solution converged nicely in 30 iterations to $\varepsilon = 1 \times 10^{-3}$. Each global iteration cycle in the semi-inverse method required about 90 seconds on a Perkin-Elmer 3240 computer, which is similar to a VAX-11/780. For the simultaneous interaction method, a relaxation factor of 0.75 was used and 110 iterations were required for the same convergence criterion. Approximately 20 seconds were required to complete one iteration cycle. As a result, both interaction methods took about the same overall computing time for this case.

The predicted distribution of surface pressure is shown in Figure 19 and is compared with the solutions of Wilmoth (1977) and Swanson et al. (1983). As discussed earlier, the solutions of Wilmoth (1977) were obtained using the direct viscous-inviscid interaction method with experimentally determined separation and reattachment points. Swanson et al. (1983) solved the Navier-Stokes equations with the composite velocity formulation and used an algebraic Cebeci-Smith turbulence model with a relaxation formula of Shang et al. (1976). The comparison shows that the present solutions with the Johnson-King model are in the best

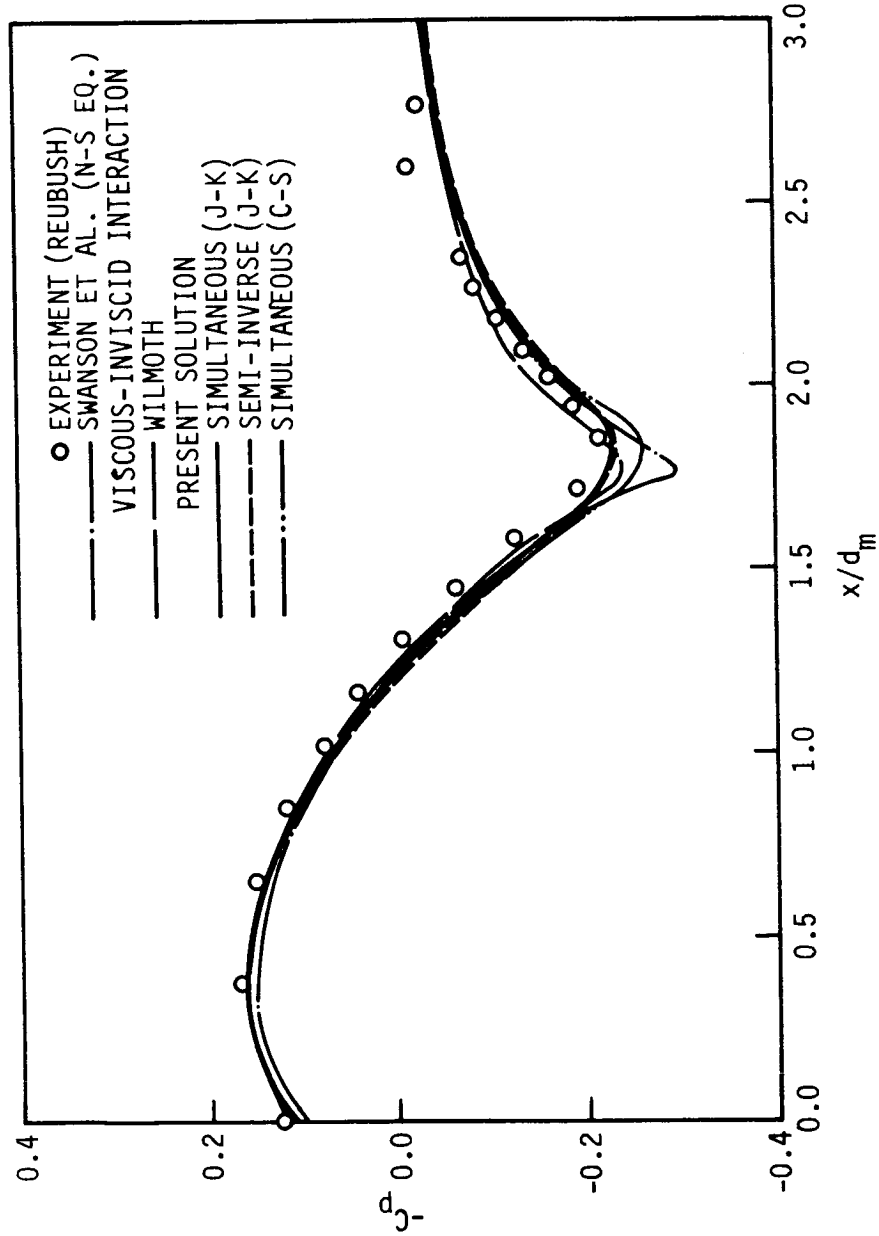

FIGURE 19. Pressure coefficient distribution for a transonic turbulent flow over a boattail (Config. 3, $M_\infty = 0.8$, $Re_\infty = 1.22 \times 10^7$)

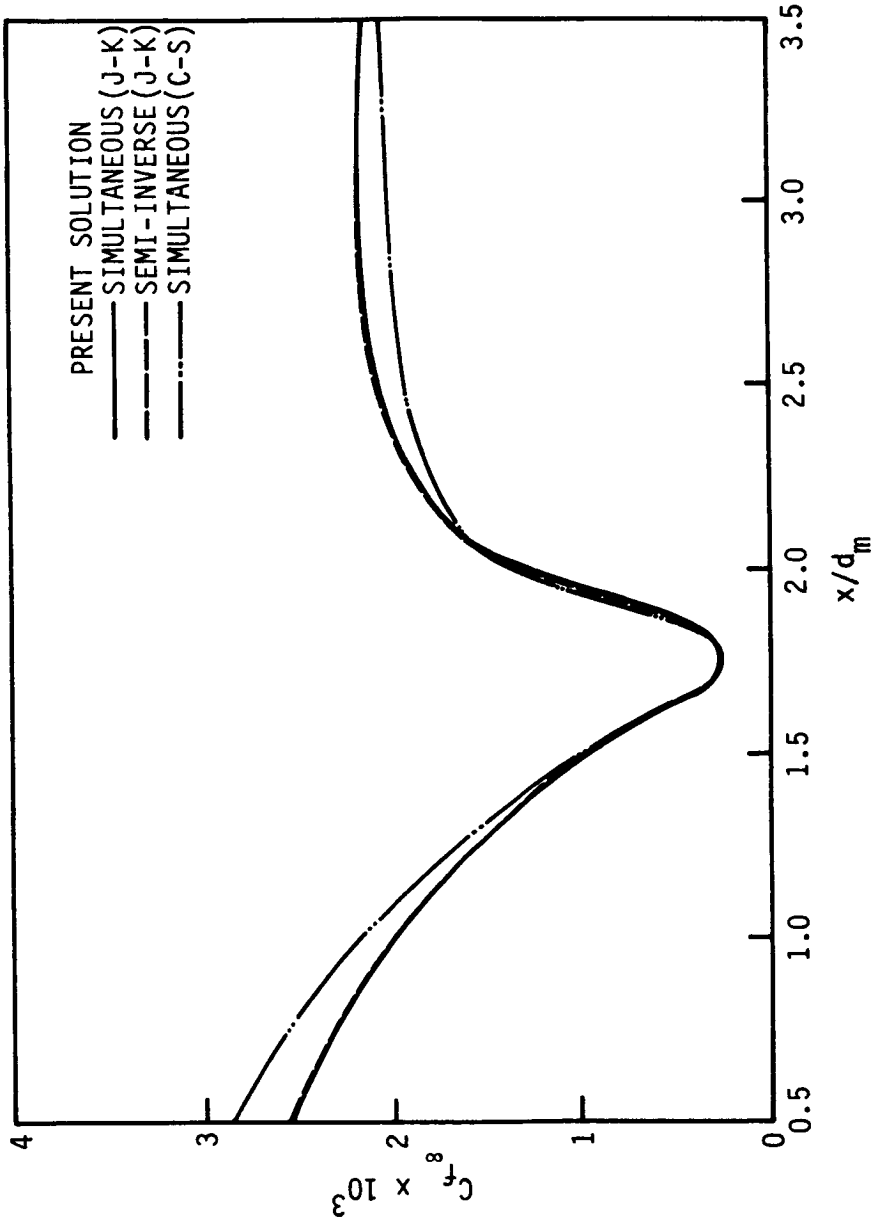

FIGURE 20. Skin-friction coefficient distribution for a transonic turbulent flow over a boattail (Config. 3, $M_\infty = 0.8$, $Re_\infty = 1.22 \times 10^7$)

agreement with the experimental data. The results of the Cebeci-Smith model in the present analysis and Navier-Stokes solution by Swanson et al. (1983) show a slight overprediction of the pressure in the vicinity of $x/d_m = 1.7$. The predicted skin friction for this flow is given in Figure 20. Unfortunately, experimental data were not available for comparison. As in the comparison of the pressure distribution, the predictions from both the simultaneous and semi-inverse method with the Johnson-King model are indistinguishable. However, the predictions of the Cebeci-Smith model differ from the others upstream and again downstream of the boattail. The Johnson-King model predicts the lower skin friction upstream of the boattail but higher skin friction in the downstream region. The same tendency was observed in every other calculation in the present study. This difference is nearly insensitive to the choice of the starting point for the Johnson-King model.

The next comparison is for the separated flow over the configuration 1 boattail, the most steep boattail tested by Reubush (1974), at the subcritical conditions of $M_\infty = 0.7$ and $Re_\infty = 1.16 \times 10^7$. Experimental data indicated that a pressure plateau was formed over the last 30% of boattail followed by a trailing edge compression without the appearance of a shock wave. The separation point determined from oil flow visualization studies by Abeyounis (1977) on the same flow model was $x/d_m = 0.51$.

In the present calculations, the relaxation factor was set to 0.35 and 0.50 for the semi-inverse and simultaneous interaction methods, respectively. The convergence behavior of the iteration process

depended on the turbulence model used. In the semi-inverse interaction method with the same convergence criterion as used in the previous case, the Cebeci-Smith model required about 70 ~ 80 iterations and the Johnson-King model required 100 ~ 120 iterations. In the simultaneous interaction method, the turbulence models used had little effect on the convergence behavior and the solutions converged in 170 ~ 200 iterations. In terms of total computing time, the simultaneous method required only about 40 ~ 50% of that needed in the semi-inverse method.

Figure 21 compares the surface pressure distribution predicted by the present interaction schemes with experimental data. Also shown in Figure 21 are the Navier-Stokes solutions obtained by Swanson et al. (1983) and the viscous-inviscid interaction results of Wilmoth (1977). Figure 22 shows the calculated variation of the skin-friction coefficient and the Navier-Stokes solution of Swanson et al. (1983). No experimental skin-friction data are available at the present time for comparison. The present solutions obtained with the algebraic Cebeci-Smith model significantly overpredict the surface pressure variation in the vicinity of the boattail-sting juncture. The predictions of the separation and reattachment points (x/d_m = 0.64 and 0.88, respectively) by the Cebeci-Smith model are also very poor. The Navier-Stokes solutions obtained with the Shang-Hankey turbulence model provide better predictions than the present solution obtained with the Cebeci-Smith model. The prediction of surface pressure in the reversed flow region is, however, still much higher than the experimental data, and the solution does not seem to capture the pressure plateau which is

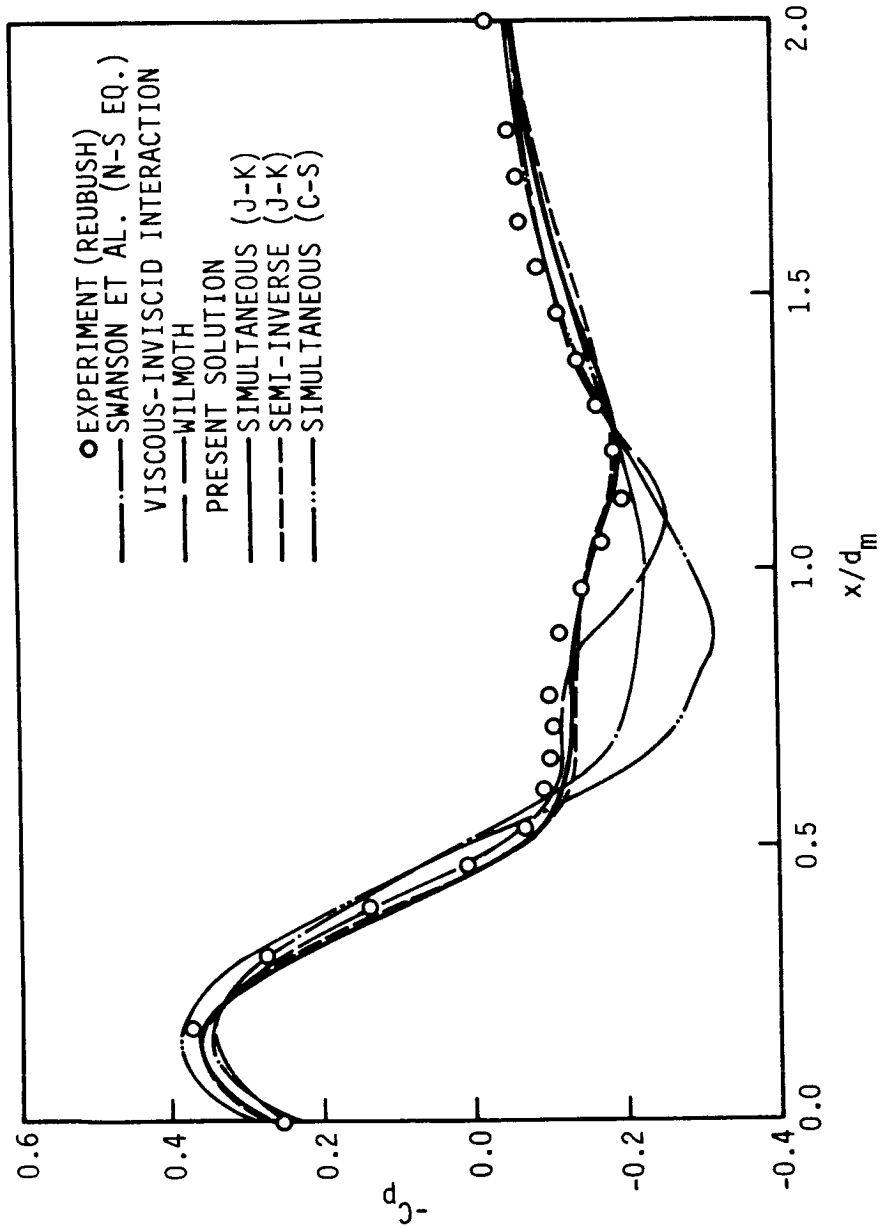

FIGURE 21. Pressure coefficient distribution for a transonic turbulent flow over a boattail (Config. 1, $M_\infty = 0.7$, $Re_\infty = 1.16 \times 10^7$)

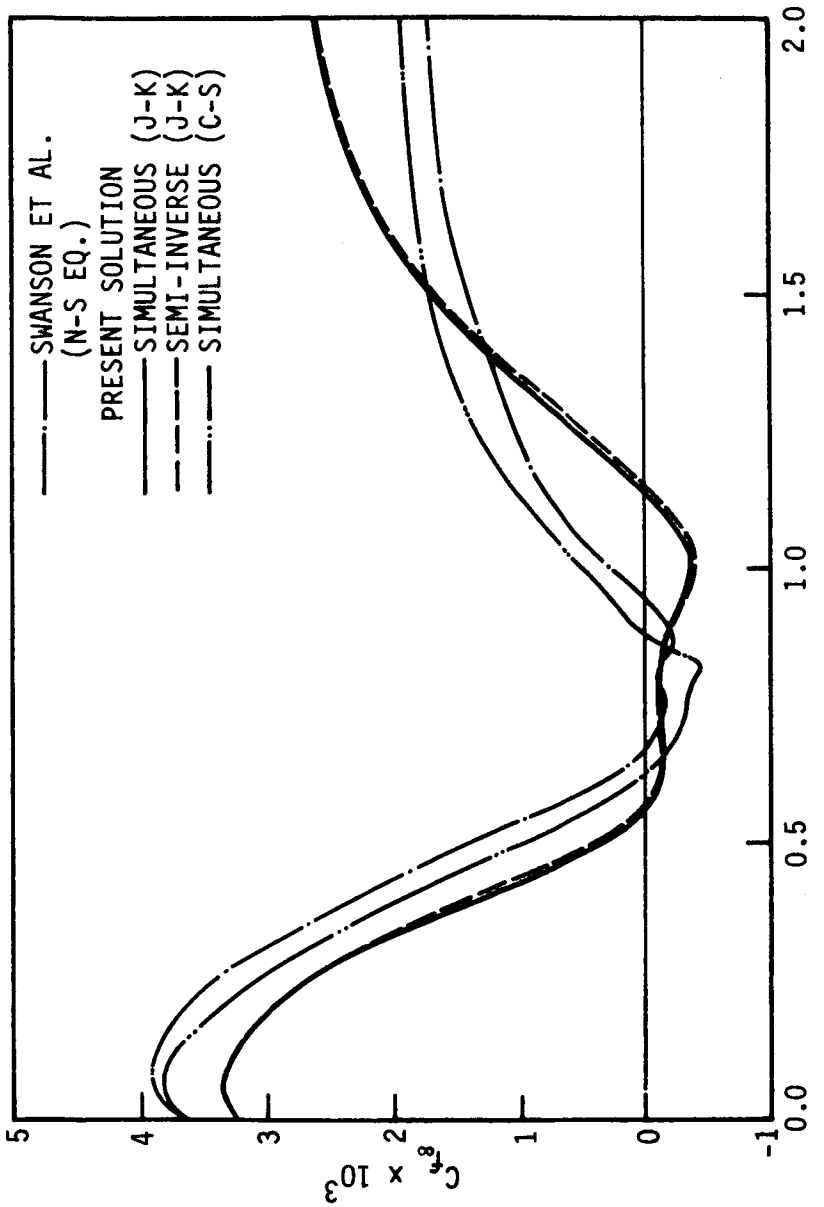

FIGURE 22. Skin-friction coefficient distribution for a transonic turbulent flow over a boattail (Config. 1, $M_\infty = 0.7$, $Re_\infty = 1.16 \times 10^7$)

characteristic of the extensive separation. Also, the prediction of the separated region is not much better than present prediction obtained with the algebraic Cebeci-Smith model. The interaction results by Wilmoth show better agreement with the experimental data than the above results and clearly exhibit the general characteristics of the pressure plateau but show a rapid pressure increase in the second recovery region.

On the other hand, the present prediction based on the Johnson-King turbulence model generally agrees very well with the experimentally observed data. Especially, the prediction of the separation point ($x/d_m = 0.56$) is much better and the predicted reversed flow region is almost twice as large as given by the other solutions. Since the experimentally observed data for the reattachment point are not available, it is difficult to argue which prediction is better. However, based on the view of the other experimental data considered in the present study, the reattachment point usually occurs near the point of maximum pressure. On this basis, the prediction of the reattachment point by the Johnson-King model is believed to be better than the other solutions.

Figures 23-25 show the distributions of the displacement thickness, maximum Reynolds stress and the mean velocity profiles calculated by the Cebeci-Smith and Johnson-King models for the same separated boattail flow. Experimental and other numerical data were not available for comparison. The displacement thickness predicted by the Johnson-King model is larger by as much as 30% than that predicted by the Cebeci-

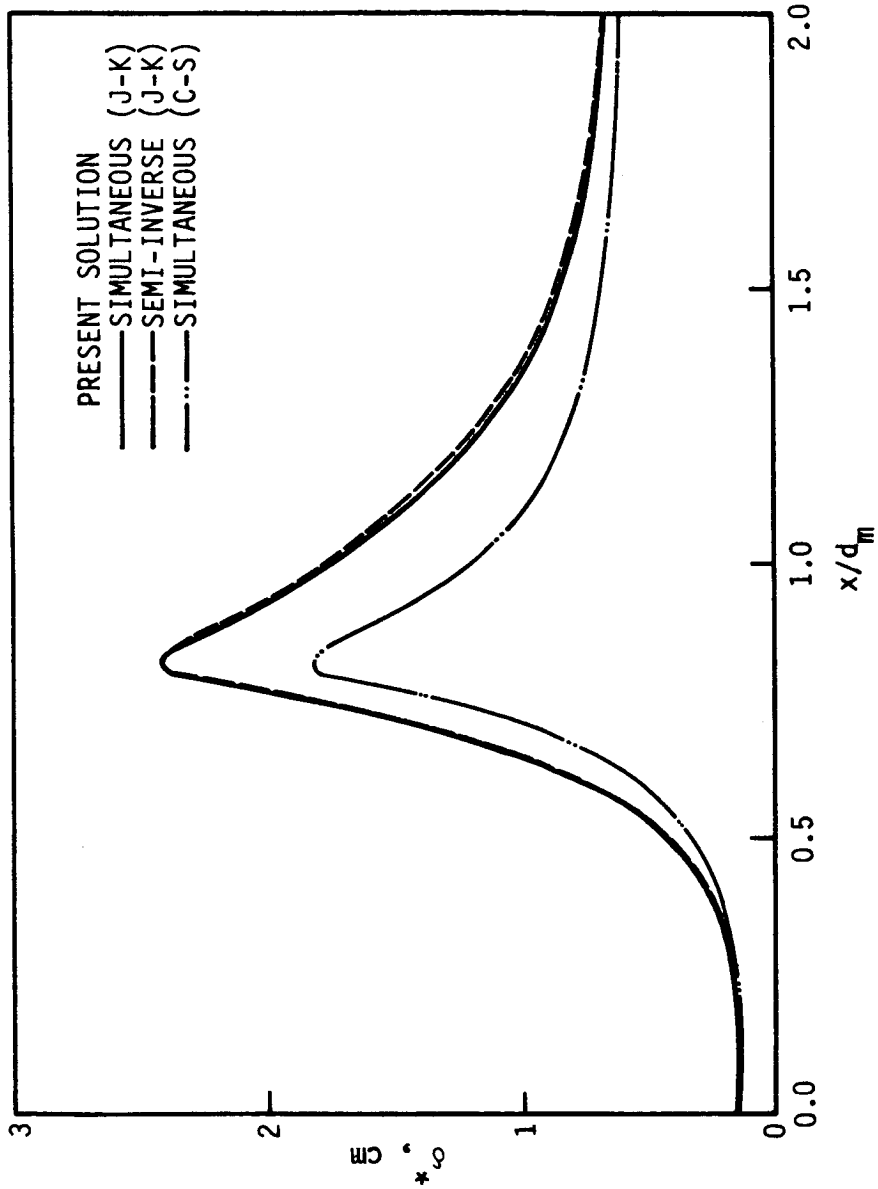

FIGURE 23. Displacement thickness distribution for a transonic turbulent flow over a boattail (Config. 1, $M_\infty = 0.7$, $Re_\infty = 1.16 \times 10^7$)

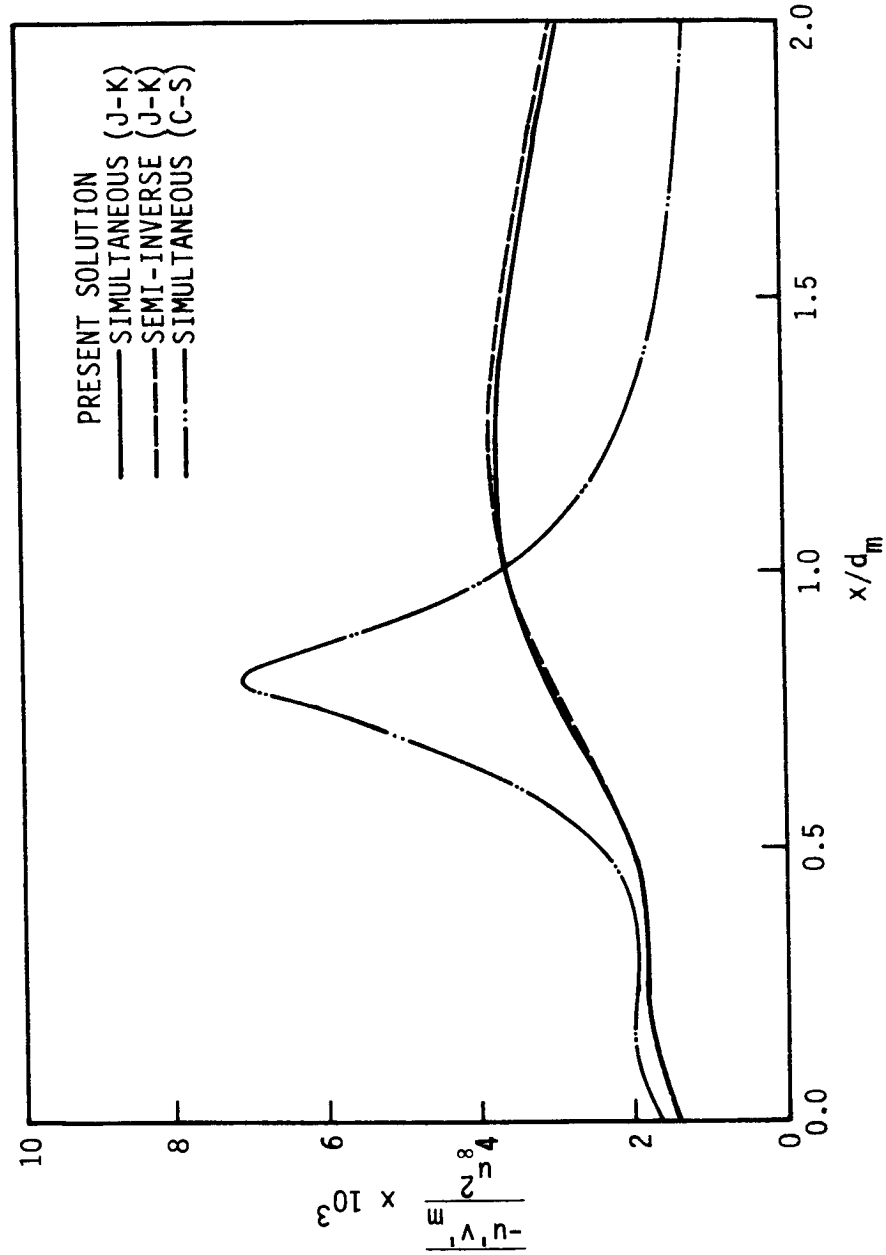

FIGURE 24. Maximum Reynolds shear stress distribution for a transonic turbulent flow over a boattail (Config. 1, $M_\infty = 0.7$, $Re_\infty = 1.16 \times 10^7$)

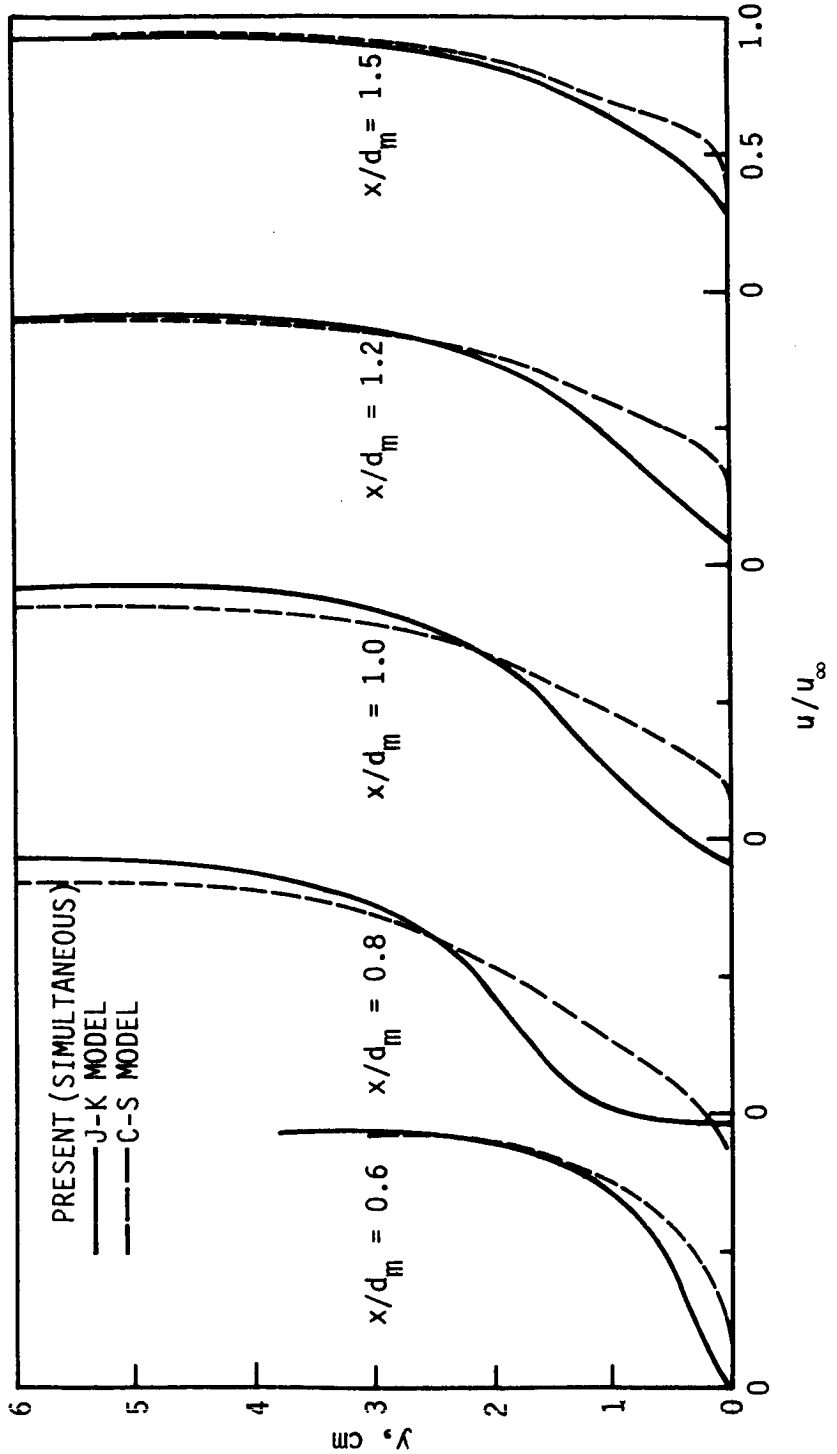

FIGURE 25. Mean velocity profiles for a transonic turbulent flow over a boattail (Config. 1, $M_\infty = 0.7$, $Re_\infty = 1.16 \times 10^7$)

Smith model. This is consistent with the smaller pressure recovery predicted by the Johnson-King model downstream of the boattail.

The most striking difference between the two models can be found in the comparison of the calculated variations of the maximum Reynolds stresses displayed in Figure 24. The Cebeci-Smith model predicts a sharp peak in $-\overline{u'v'}_m$, which suggests that the turbulence field is strongly dependent upon the local flow conditions. On the other hand, $-\overline{u'v'}_m$ predicted by the Johnson-King model shows more gradual increase over a longer streamwise distance, which is responsible for the thick displacement thickness and smaller pressure recovery. From the velocity profiles shown in Figure 25, a major difference can be observed in the inner part of the boundary layer: the Johnson-King model predicts much larger separation bubble than the Cebeci-Smith model.

The results for the boattail case presented in Figures 19-25 were obtained using a body surface oriented coordinate system for the viscous calculation. Guided by these results, the calculations were repeated using two different shear-layer coordinate systems. First, a dividing streamline ($\psi = 0$) from the previous results was chosen as the shear-layer coordinate. A second choice of shear-layer coordinate was made so as to align the coordinate with the displacement surface in the reversed flow region. The coordinate then asymptotically approached the body surface. A comparison of the calculations using both shear-layer coordinates with the previous results obtained using the body-oriented coordinate shows differences too small to be drawn on the figures, and suggests that the use of the shear-layer coordinate system provides no

important advantage in the calculation.

From viewing the results of this subcritical flow case, it becomes obvious that the new simultaneous viscous-inviscid interaction method can usually predict flows with pressure driven separation more economically than the semi-inverse method, for the same degree of accuracy. It was also found that the accuracy of the solutions is more strongly dependent on the turbulence modeling than the interaction algorithm. The Johnson-King turbulence model produced much better predictions than the algebraic Cebeci-Smith model for separated flows with viscous-inviscid interaction.

2. Bump flow

The next case to be presented is the shock interacted flow field about an axisymmetric circular-arc bump studied experimentally by Bachalo and Johnson (1979). This flow served as the primary test case for the present study because of the availability of extensive experimental data. This flow configuration, shown in Figure 26, consists of an axisymmetric circular-arc bump attached to a circular cylinder placed parallel to the flow direction. The cylinder, 15.2 cm in outside diameter, extends 61 cm upstream of the bump leading edge. The bump has a chord of 20.32 cm and is 1.9 cm in thickness. The bump leading edge is smoothed by a small fillet, of radius 18.3 cm, to prevent separation at the leading edge. The model was initially tested at a freestream Mach number, $M_\infty = 0.875$ and freestream Reynolds number, $Re_\infty = 1.36 \times 10^7$ in the NASA Ames 2 × 2 foot transonic wind tunnel.

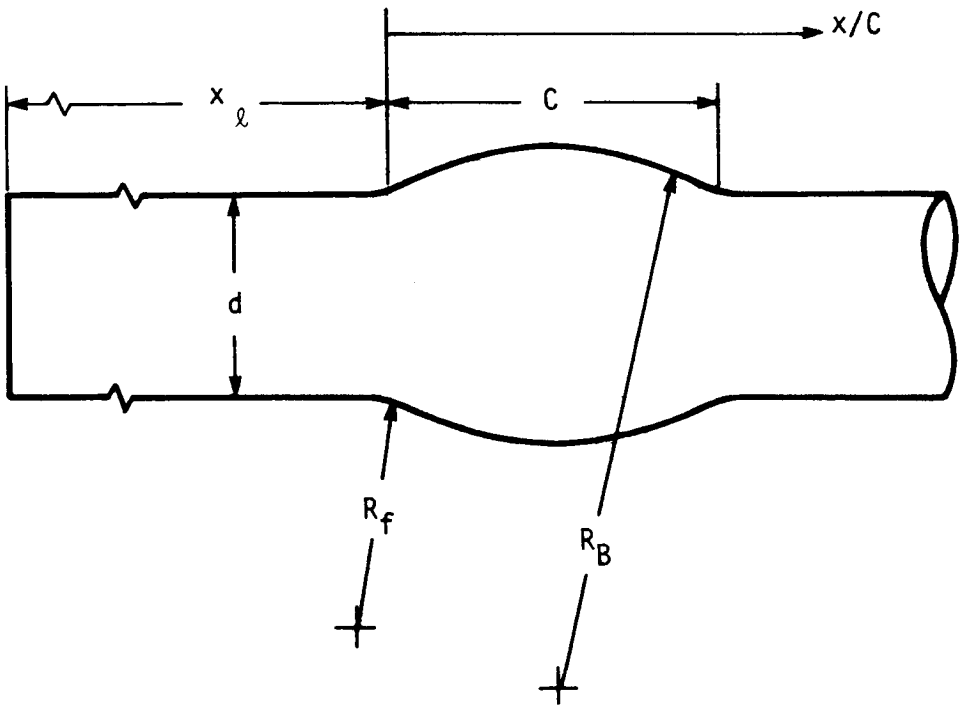

BUMP GEOMETRIC PARAMETERS			
x_ℓ	=	61.00	cm
C	=	20.32	cm
d	=	15.34	cm
R_f	=	18.30	cm
R_B	=	28.05	cm

FIGURE 26. Geometric configuration of a bump

Later, Horstman and Johnson (1984) reported the measurements for the same body configuration obtained in the 6 × 6 foot supersonic wind tunnel over a range of freestream Mach numbers from 0.4 to 0.94. This experiment was carried out in order to evaluate the importance of the interference effect of the wind tunnel walls. For $M_\infty = 0.875$, both results agreed well on general aspects of the flow including the distribution of the surface pressure. However, a slight difference was noticeable in the location of the shock wave; the shock wave in the larger wind tunnel was located about 0.01 chord length upstream of that measured in the smaller wind tunnel. Also, the pressure recovery downstream of the shock in the larger wind tunnel was slightly smaller than that observed in the smaller wind tunnel as shown in Figure 27.

Their experimental data can be summarized as follows. For a Mach number up to 0.8, the flow was subcritical (no shock wave appears) and a small separation bubble was present near the bump-sting juncture. The locations of the separation and reattachment points were somewhat insensitive to the Mach number in subcritical cases. As the Mach number passes 0.8, the flow becomes supercritical and the shock wave forms approximately at $x/C = 0.65$ (x is referenced to the forward intersection point of the arc of the bump with the cylinder and measured parallel to the cylinder and C is the chord length of the bump). As the Mach number is increased further, the location of the shock wave moves very slightly downstream and a large pressure plateau is formed in the vicinity of the bump-sting juncture followed by the smooth compression after the juncture. The separation bubble also begins to grow very rapidly; the

separation point moves upstream toward the shock wave location and the reattachment point moves farther downstream. For example, at $M_\infty = 0.875$, the shock wave is located approximately at $x/C = 0.67$ and the separation and reattachment points are located at $x/C \simeq 0.69$ and $x/C \simeq 1.17$. The extent of the separated region was determined by oil-flow visualization. Considerable uncertainty was reported to exist in interpretation of these observations, especially the reattachment point.

Johnson et al. (1982) performed numerical computations using the Navier-Stokes equations with the algebraic Cebeci-Smith and Wilcox-Rubesin (k-ω^2) two-equation turbulence models. Their results indicated that the shock location and the separation point were predicted substantially downstream of the experimentally observed position and the more sophisticated two-equation model did not provide significantly better predictions than the simple algebraic model. Horstman and Johnson (1984) used the k-ε turbulence model developed by Jones and Launder (1972) in their Navier-Stokes solutions and obtained a slight improvement in the predictions of the shock location and the separation point over the results of Johnson et al. (1982). Most of the improvement was, however, due to the new outer boundary condition: they used the freestream outer boundary condition instead of the solid wall boundary condition based on the experimental data which indicated that the flow was almost free of the wind tunnel wall effects. However, this resulted in an overprediction of surface pressure downstream of the bump trailing edge region. Recently, Johnson (1985) solved the same bump flow using the Navier-Stokes equations with the Johnson-King turbulence

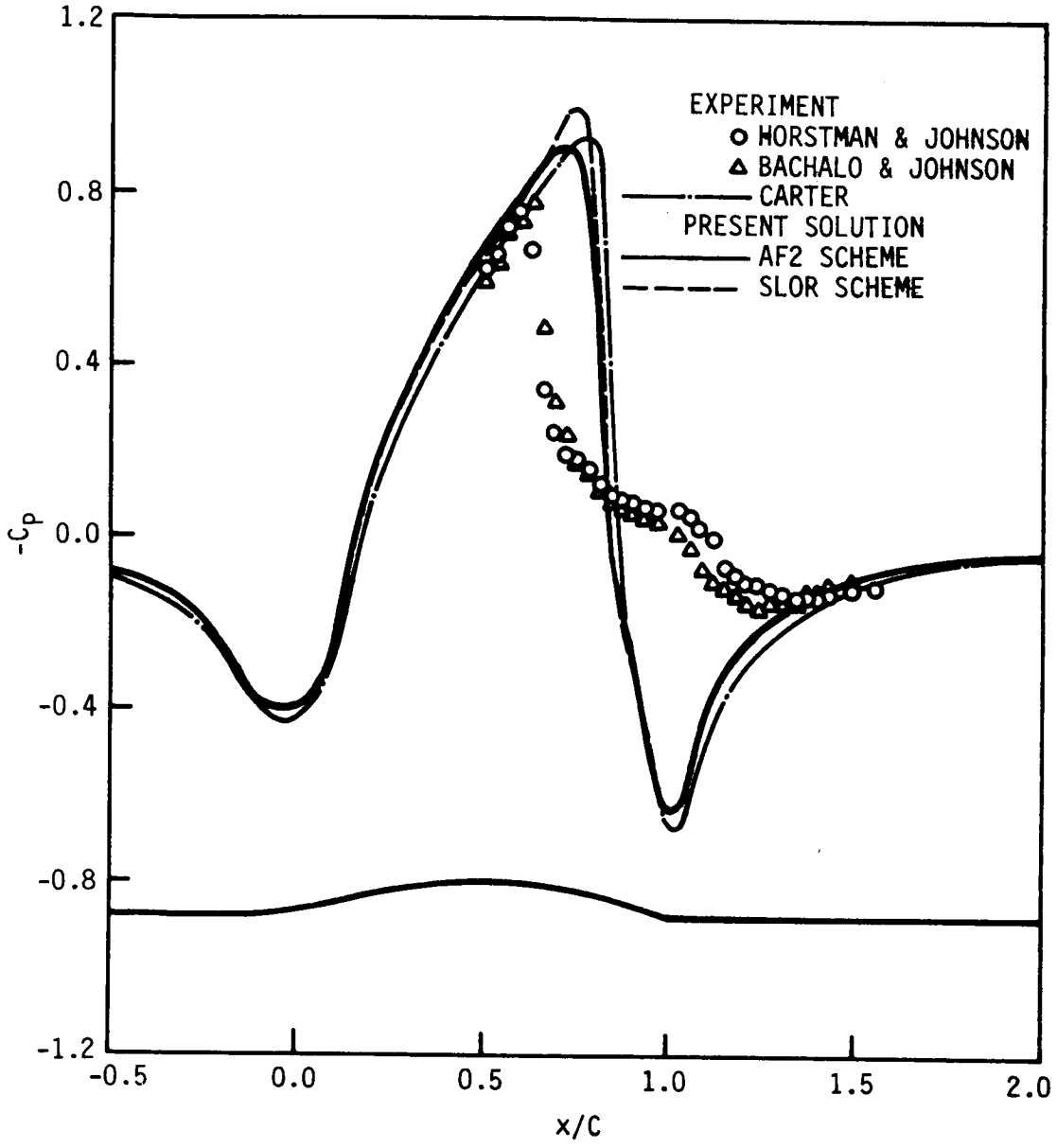

FIGURE 27. Comparison of measured pressure coefficients with predictions for inviscid flow for a transonic turbulent flow over a bump ($M_\infty = 0.875$)

model. The overall predictions were in much better agreement with the measurements than the above Navier-Stokes solutions based on the algebraic and two-equation models.

The semi-inverse viscous-inviscid interaction approach was applied to the same flow by Carter (1981) and Carter and Vasta (1982a). The solution was obtained with the algebraic Cebeci-Smith model and predicts the shock location better than the previous Navier-Stokes solutions but the pressure plateau was not captured at all and the pressure at the bump trailing edge region was substantially overpredicted. It was also reported that the predictions were improved by reducing the Clauser constant of the Cebeci-Smith model by half (Carter, 1981) and by using the relaxation formula of Shang and Hankey (1975) (Carter and Vasta, 1982a).

In the present calculations, 101 × 41 mesh points were nonuniformly distributed over the inviscid computational domain which extended from $x/C = -2.0$ to $x/C = 3.0$ in the streamwise direction and 2.5 chord lengths in the transverse direction. Preliminary calculations were performed with several different computational domains and mesh sizes. The computational domain and the number of grid points were reduced to the smallest values that still provided mesh independent interaction solutions. About 40% of the mesh points along the body surface were placed over the bump ($0 \leq x/C \leq 1.0$) with the greatest concentration near $x/C = 0.65$. The smallest mesh spacing was $\Delta x/C = 0.015$. The viscous-inviscid interaction region extended from $x/C = -0.5$ to $x/C = 1.5$ and occupied 61 mesh points in the streamwise direction. For

the viscous mesh inside the interaction region, the inviscid mesh spacing along the wall was used in the streamwise direction and 70 points were distributed nonuniformly across the boundary layer with K = 1.09 (see Equation (2.105)).

The incoming velocity profile for the boundary-layer analysis was again obtained from the direct solution of the boundary-layer equations starting from the nose of cylinder (x/C = -3.0) using the pressure obtained from the undisturbed inviscid solution. The initial distribution of m was provided by the direct solution of the boundary-layer equations with the pressure data obtained by the undisturbed solution of the potential equation using the AF2 scheme with 10 iterations. The distribution of m downstream of the interaction region was obtained in the same way as in the boattail flow calculations. Transition from laminar to turbulent flow was made at x/C = -2.8. Calculations were made using both the Cebeci-Smith and Johnson-King turbulence models. The switching point for the Johnson-King model was x/C = -0.6.

The convergence behavior of the viscous-inviscid iterative procedure was found to be very sensitive to the choice of turbulence model and the freestream Mach number. This implies that convergence of the interaction process is strongly dependent on the size of the separated flow region. The relaxation parameter was decided by a trial-and-error method. In subcritical cases which resulted in small separation regions, a relatively large value of the relaxation factor was used regardless of the turbulence models (0.7 ~ 1.0 for the semi-

inverse method and 0.6 ~ 0.75 for the simultaneous method) and the solutions usually converged very well for both interaction methods (35 ~ 50 iterations for the semi-inverse method and about 100 iterations for the simultaneous method). When the semi-inverse method was used for supercritical cases with the Mach number less than 0.9, a relaxation factor of 0.4 ~ 0.6 was used with the Cebeci-Smith model and convergence to $\varepsilon = 1 \times 10^{-3}$ was achieved in 100 ~ 150 iterations. Each global iteration cycle in the semi-inverse method required about 2 minutes. When the Johnson-King model was used in the semi-inverse method, a smaller value of the relaxation factor (0.2 ~ 0.3) was necessary to obtain convergence. However, the solutions converged to only about $\varepsilon = 1 \times 10^{-2}$ after 40 ~ 50 iterations. It has not been possible to reduce the residual further due to the occurrence of oscillatory behavior in the convergence pattern. For $M_\infty = 0.9$, the solution by the semi-inverse method diverged even with a small relaxation factor (0.1). On the other hand, with the simultaneous method for the supercritical cases with the Mach number up to 0.9, the convergence was still obtained with a relatively large value of relaxation factor (0.4 ~ 0.7) regardless of the turbulence model and 150 ~ 250 iterations were needed for $\varepsilon = 1 \times 10^{-3}$. A typical calculation with the simultaneous interaction method requires 60 ~ 80 minutes on a Perkin-Elmer 3240 minicomputer.

Before the interaction method was applied, the present numerical algorithm was carefully tested especially for the inviscid flow calculation. In order to obtain a meaningful comparison of the semi-

inverse and simultaneous interaction methods, the AF2 and SLOR schemes must provide nearly the same inviscid flow solutions. For subcritical cases, the undisturbed inviscid solutions of the SLOR and AF2 schemes were found to be almost identical. When the artificial compressibility approach is used in the solution procedure of the full potential equation for supercritical cases, it is already known that the prediction of the shock strength is very sensitive to the magnitude of density biasing. Therefore, the density biasing magnitude must be decided carefully. This was done by numerical experiments and comparison with the results of the other inviscid code and available solutions in the literature. Figure 27 compares the undisturbed solutions of the SLOR and AF2 schemes for $M_\infty = 0.875$. Also shown in Figure 27 is the inviscid solution of Carter (1981) for comparison. Both solutions are in good agreement except that the SLOR solution shows a slightly stronger shock than the AF2 solution. This difference disappears when the viscous effect is included.

Figures 28-31 compare the calculated surface pressure distributions with the experimental data taken from the 6 × 6 foot wind tunnel at $M_\infty = 0.6$, 0.8, 0.875 and 0.9 by Horstman and Johnson (1984). The Navier-Stokes solutions obtained by Johnson (1985) using the Johnson-King turbulence model are also compared for all the above Mach numbers. For $M_\infty = 0.875$, the experimental data of the 2 × 2 foot wind tunnel (Bachalo and Johnson, 1979) and the Navier-Stokes solutions obtained by Horstman and Johnson (1984) based on the Cebeci-Smith and k-ε turbulence models are also displayed. The Cebeci-Smith model used in the present

interaction scheme overpredicts the pressure in the separated region and does not capture the pressure plateau characteristics at all. The same trend is also observed in the Navier-Stokes solutions of Horstman and Johnson (1984) using the same Cebeci-Smith turbulence model, but the present predictions of the shock position seem to agree slightly better with the experimental data than the Navier-Stokes solutions based on the same Cebeci-Smith turbulence model. The overall predictions of the present interaction method using the Johnson-King model are observed to agree very well with the experimental data and the Navier-Stokes solutions of Johnson (1985) with the same Johnson-King turbulence model.

The present semi-inverse and simultaneous interaction methods again give almost identical final solutions except for $M_\infty = 0.9$ for which the semi-inverse method failed to converge. The shock position is reasonably well predicted and the pressure plateau behavior is well described by the Johnson-King turbulence model for all Mach numbers. However, in the supercritical cases, the shock strength is slightly underpredicted and the shock location is predicted upstream of the measured data by both the semi-inverse and simultaneous interaction method. The difference between the solutions obtained by the present interaction method and the Navier-Stokes solutions based on the same Johnson-King model becomes larger as the Mach number is increased. One interesting observation can be made for the $M_\infty = 0.875$ case. While the Navier-Stokes solutions of Johnson (1985) agreed very well with the experimental data of the 2 × 2 foot wind tunnel, the present predictions agree better with the 6 × 6 foot wind tunnel data. Considering that the

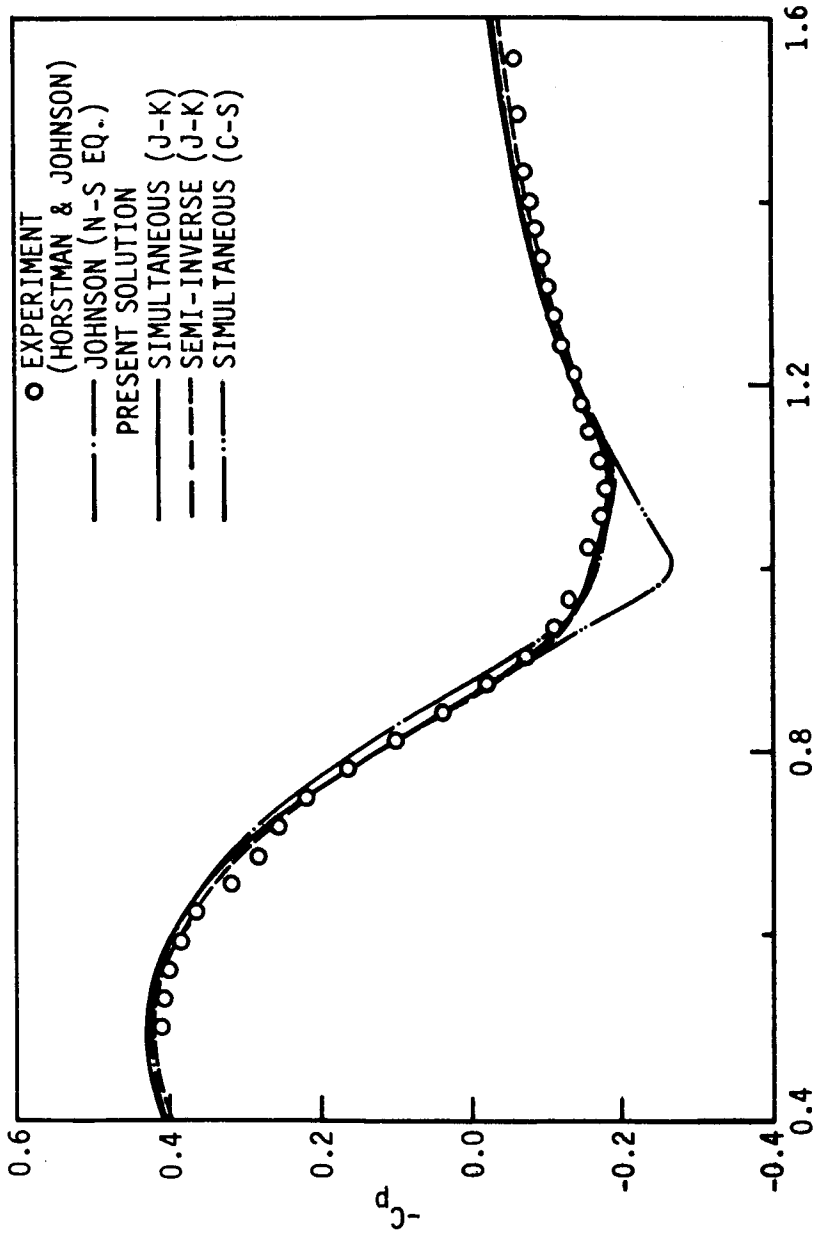

FIGURE 28. Pressure coefficient distribution for a transonic turbulent flow over a bump ($M_\infty = 0.6$)

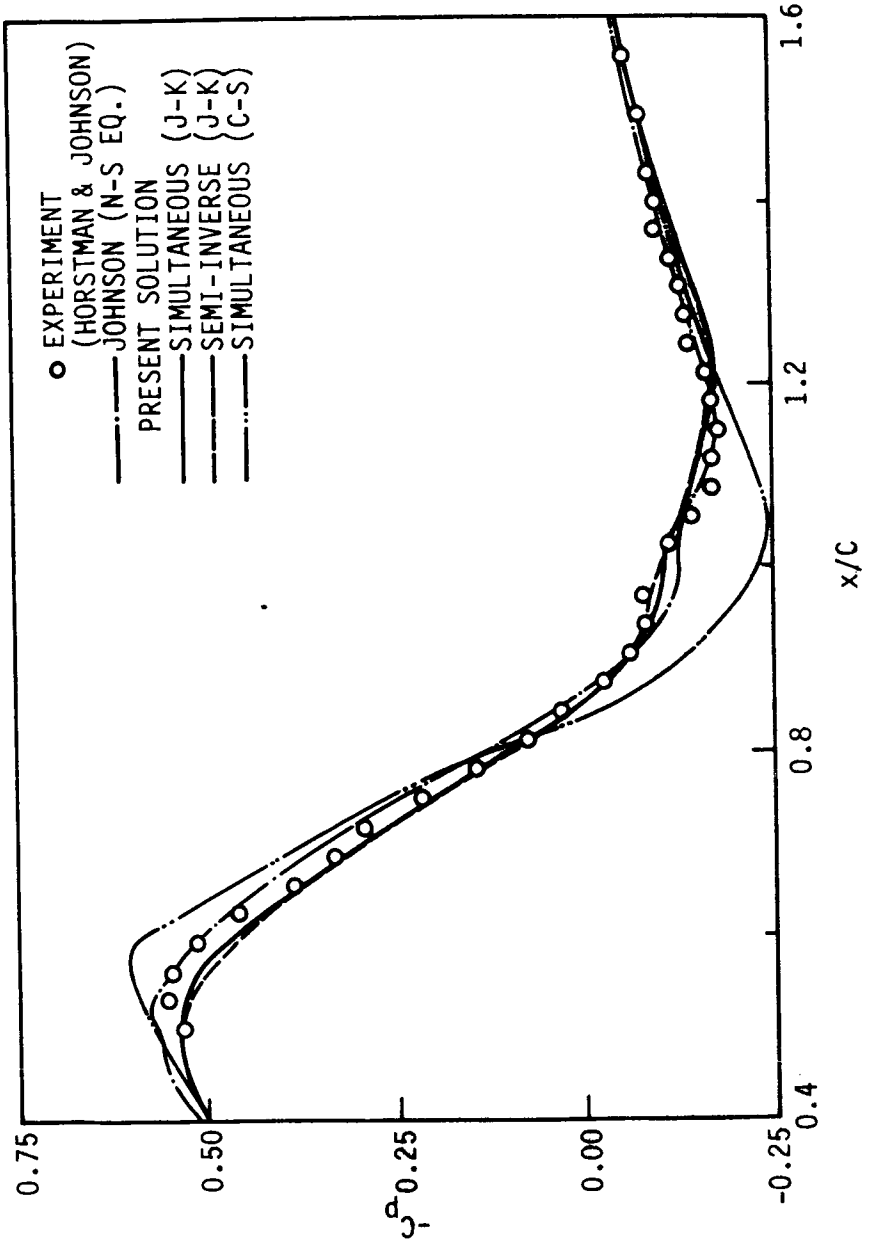

FIGURE 29. Pressure coefficient distribution for a transonic turbulent flow over a bump ($M_\infty = 0.8$)

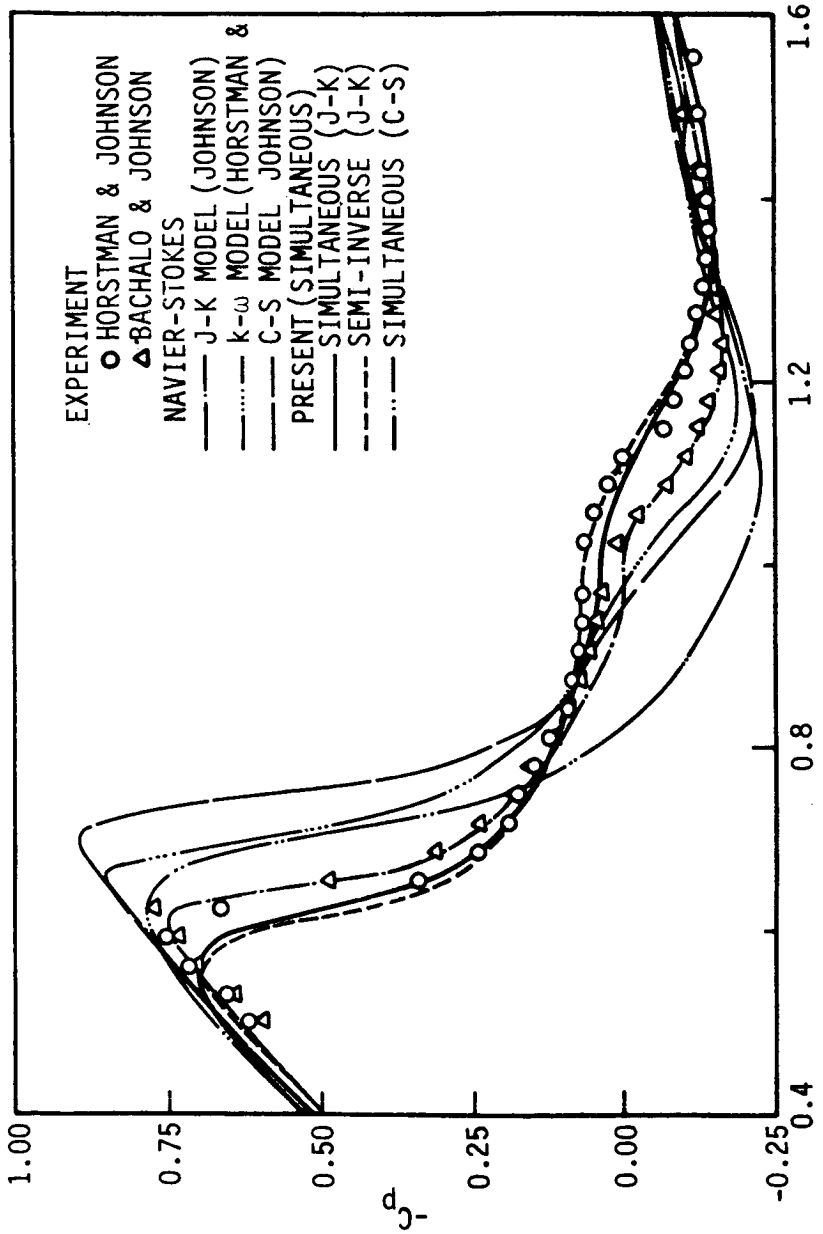

FIGURE 30. Pressure coefficient distribution for a transonic turbulent flow over a bump (M_∞ = 0.875)

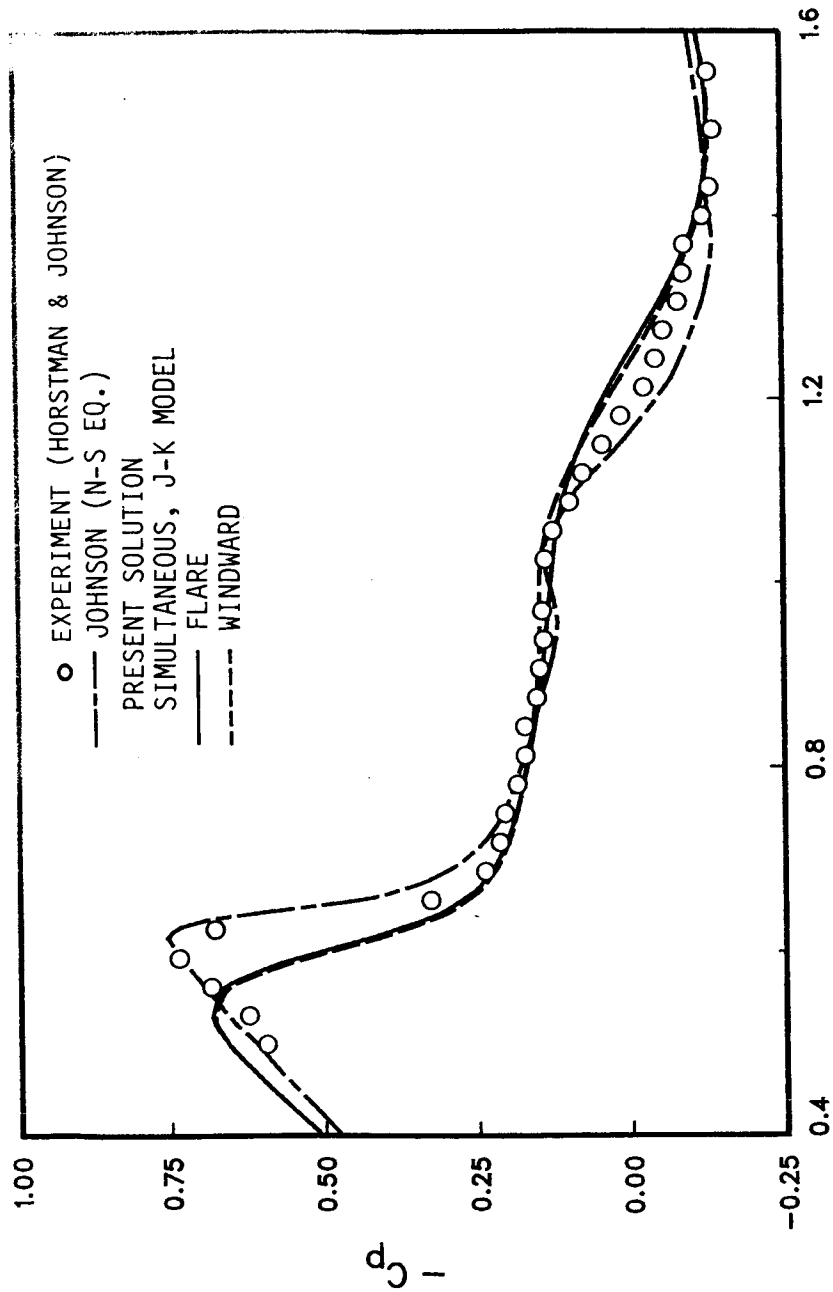

FIGURE 31. Pressure coefficient distribution for a transonic turbulent flow over a bump ($M_\infty = 0.9$)

wind tunnel wall effect should be much smaller in the larger wind tunnel, it could be argued that the present interaction solutions provide the best agreement with the experimental data.

In the present calculations for this flow case, solutions were obtained using both the FLARE approximation and the windward differencing scheme in the boundary-layer equations. Figure 31 compares the pressure coefficient predicted using the FLARE approximation with the predictions using the windward differencing for the flow at $M_\infty = 0.9$. This flow has the largest separation bubble among flows considered in the present study. The two solutions gave nearly identical results. The convergence behavior seems to be insensitive to the use of the FLARE approximation and the windward differencing scheme.

The skin-friction coefficient predicted by the present interaction scheme using the Cebeci-Smith and Johnson-King models for $M_\infty = 0.6$, 0.875 and 0.9 are shown in Figures 32-34. Experimental data and other numerical solutions for skin friction are not available at the present time. Again, there is little difference between the solutions of the semi-inverse and simultaneous method. For $M_\infty = 0.6$, the difference between the predictions of the Cebeci-Smith and Johnson-King turbulence models is very small and the predicted separation and reattachment points are in good agreement with the experimental data.

For $M_\infty = 0.875$, the difference between the Cebeci-Smith and Johnson-King turbulence model becomes evident. The Cebeci-Smith model results in a much smaller separation region and the separation and reattachment points predicted by the Johnson-King model are seen to be

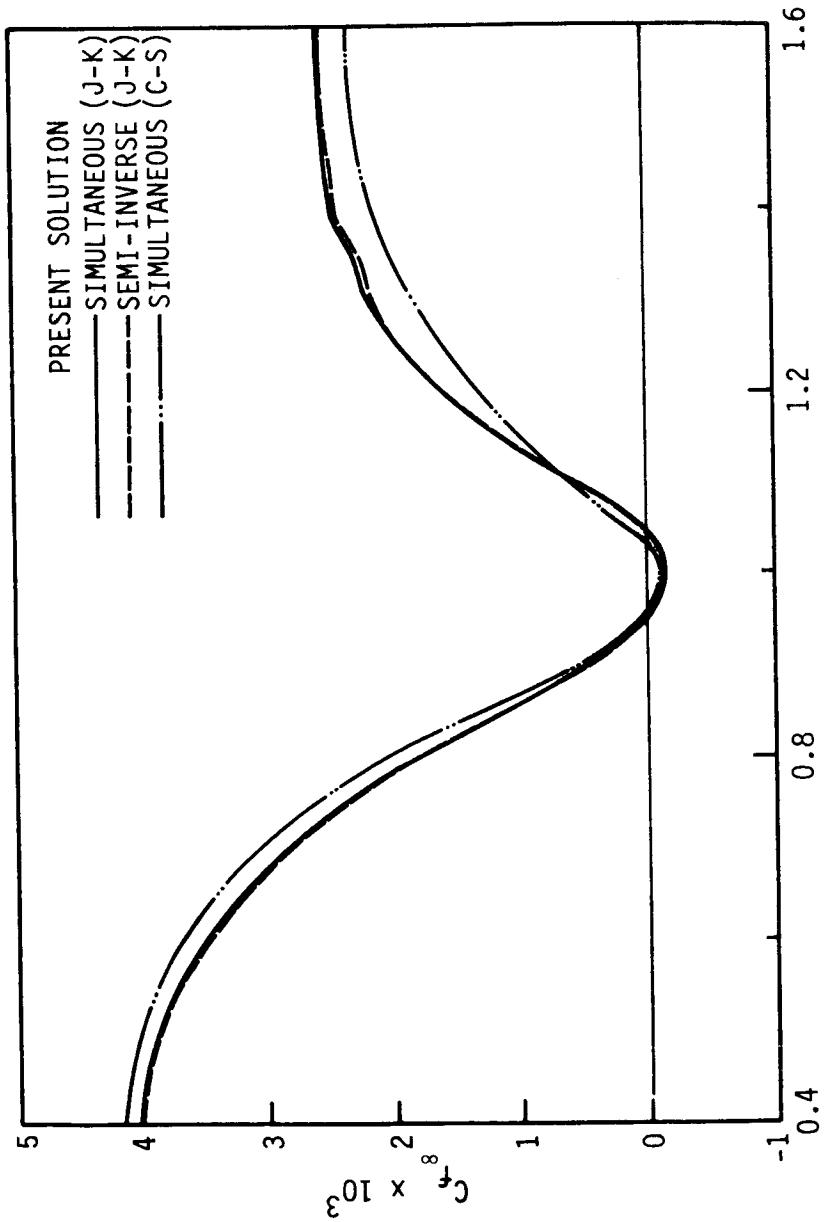

FIGURE 32. Skin-friction coefficient distribution for a transonic turbulent flow over a bump ($M_\infty = 0.6$)

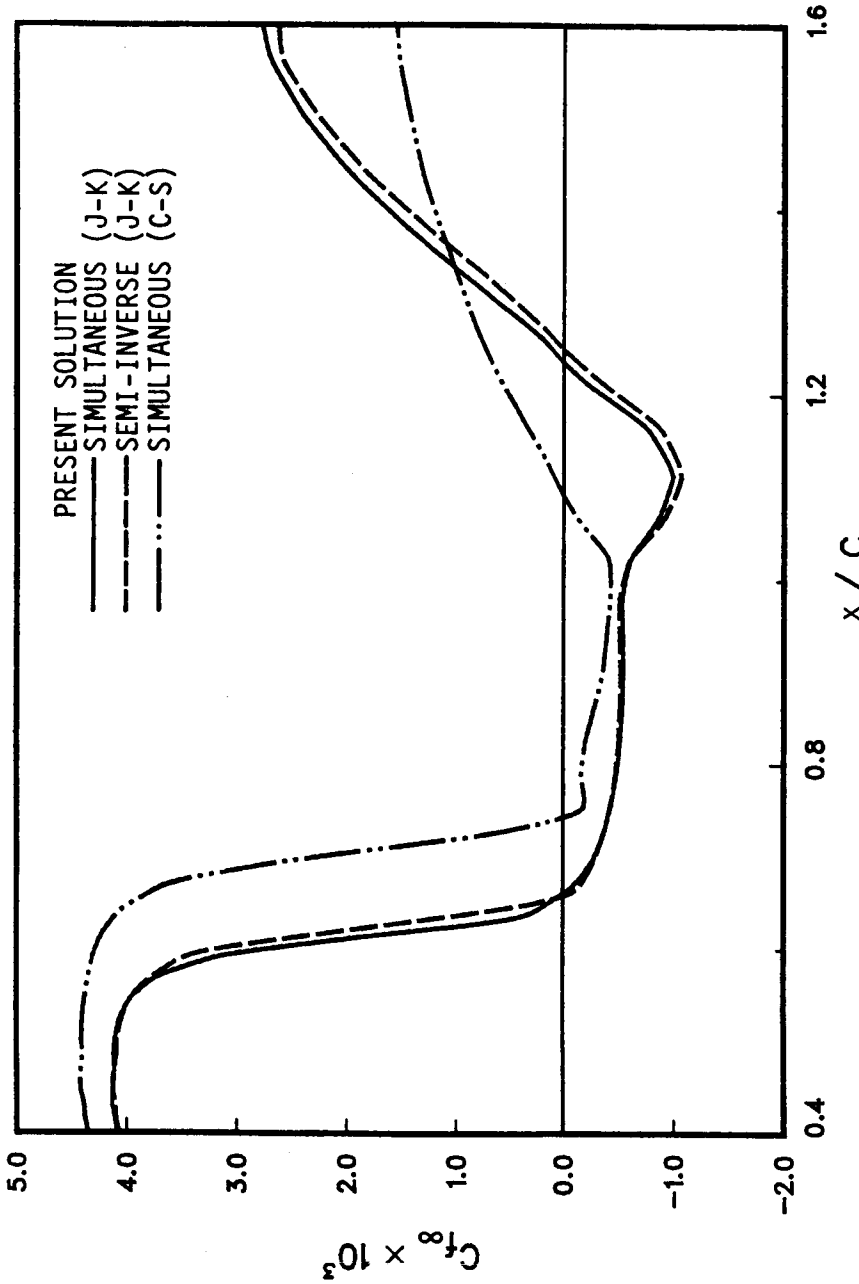

FIGURE 33. Skin-friction coefficient distribution for a transonic turbulent flow over a bump ($M_\infty = 0.875$)

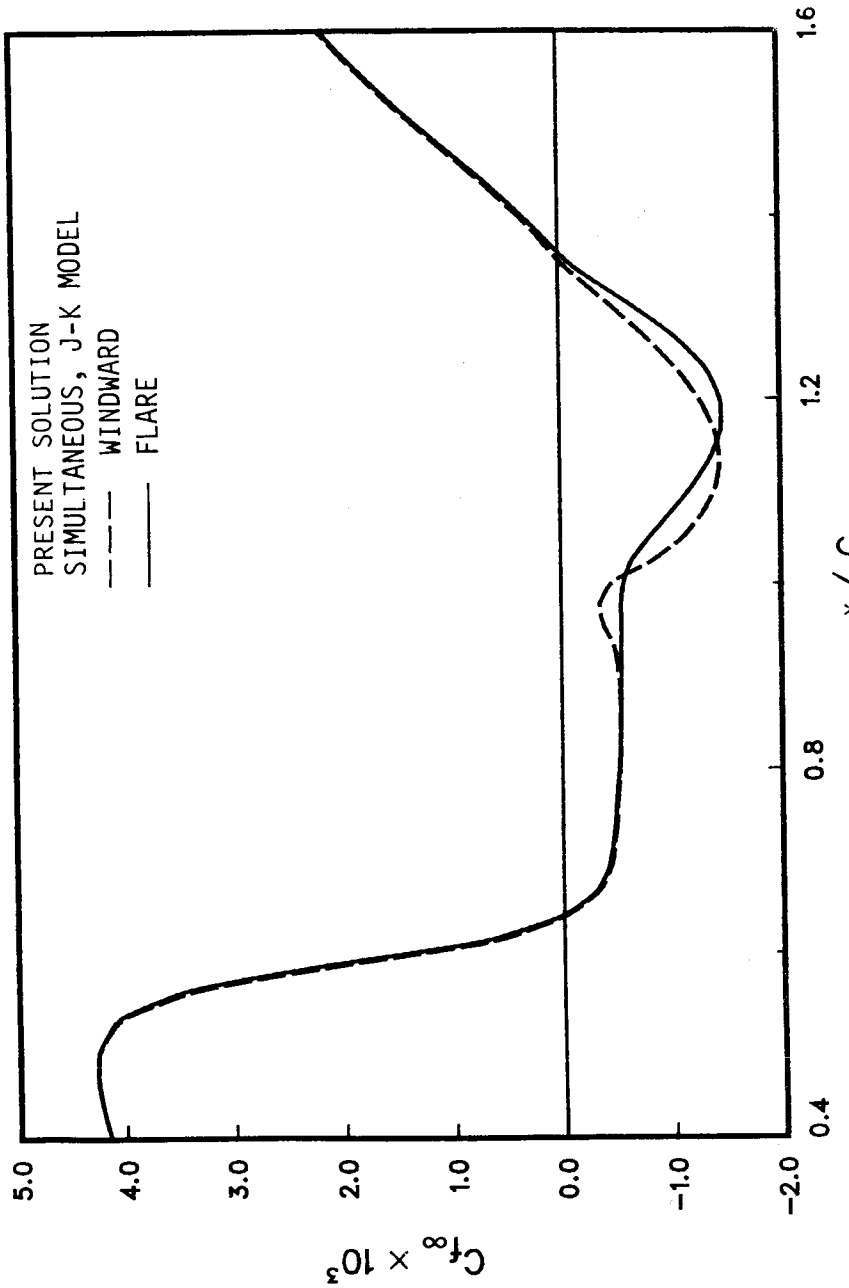

FIGURE 34. Skin-friction coefficient distribution for a transonic turbulent flow over a bump ($M_\infty = 0.9$)

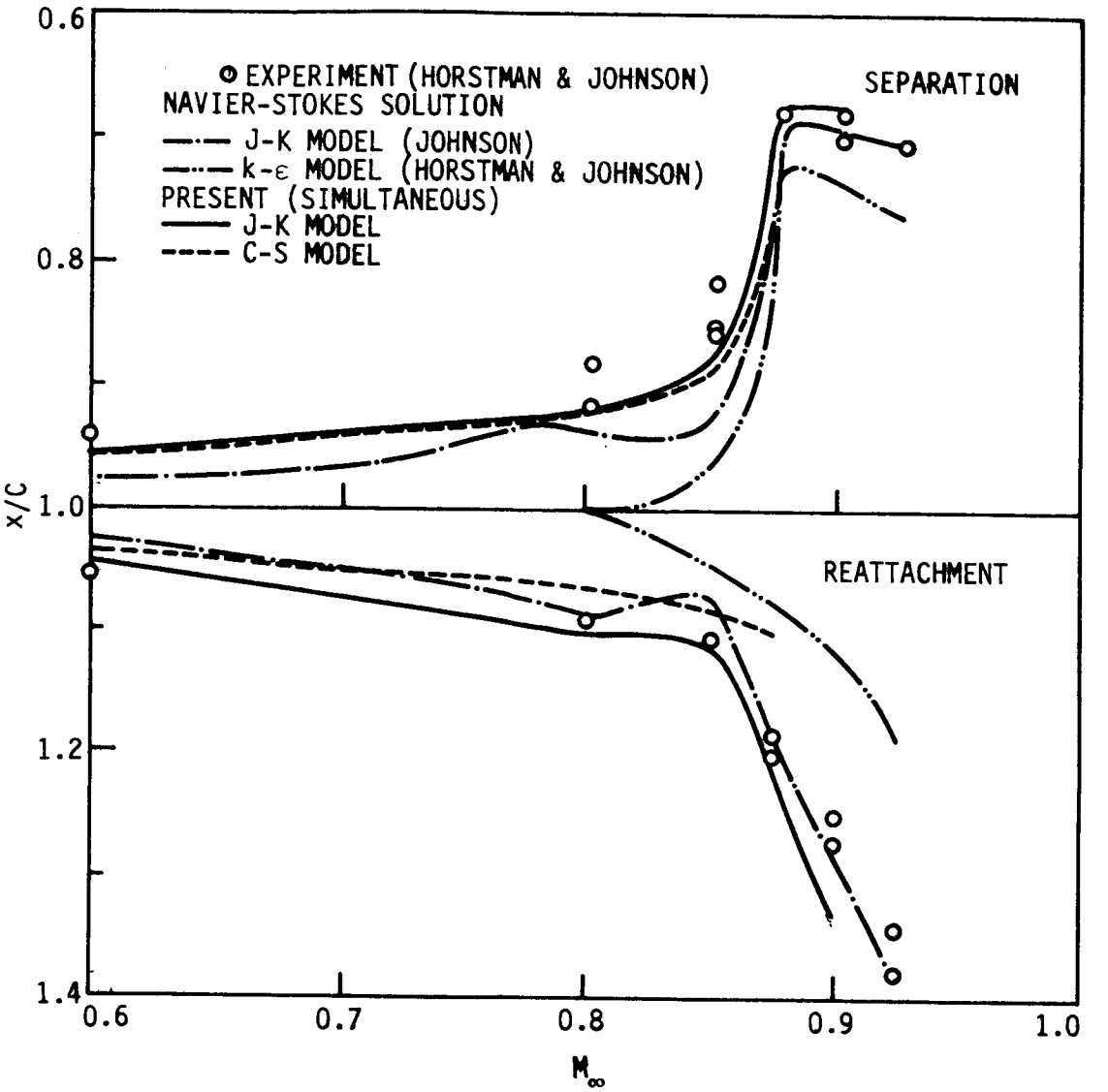

FIGURE 35. Comparison of separation and reattachment locations for a transonic turbulent flow over a bump

in fairly good agreement with the measurements. As was observed in the calculation of the boattail flow, the skin friction predicted by the Johnson-King model shows a more rapid increase after the reattachment point than the prediction by the Cebeci-Smith model. In Figure 34, the predictions of skin friction by the FLARE approximation and windward differencing are compared for $M_\infty = 0.9$. Some differences can be observed in the region before the reattachment point but overall, the agreement is reasonably good and the predictions of the separation and reattachment points agree very well. Therefore, it was felt that the use of the FLARE approximation was justified for the flows considered in the present study.

Figure 35 compares the predicted separation and reattachment points with the experimentally observed values and values from the Navier-Stokes solutions obtained using the Jones-Launder (k-ε) turbulence model (Horstman and Johnson, 1984) and Johnson-King turbulence model (Johnson, 1985). The predictions obtained by the present simultaneous interaction method with the Johnson-King model is generally in good agreement with the measurements. The reattachment point is predicted slightly downstream of the measured value. The predictions by the Cebeci-Smith model are relatively good in lower Mach numbers, but the disagreement with the measurements becomes larger as the Mach number is increased above 0.85. On the other hand, the Navier-Stokes solutions by Johnson (1985) with the Johnson-King model are observed to significantly underpredict the separation point compared to the measurements and the present results with the same model. It is also interesting to note

that the Navier-Stokes solutions with the k-ε two-equation model failed to predict separation when the freestream Mach number was less than 0.8.

Note that the experimental data of the $M_\infty = 0.875$ case shown in the figures to follow are the measurements taken in the 2 × 2 foot transonic wind tunnel. Measurements from the 6 × 6 foot wind tunnel are not available except for the surface pressure distribution at the present time. The predicted and measured displacement thickness distributions of the boundary layer for $M_\infty = 0.6$ and 0.875 are compared in Figures 36 and 37. None of the predictions agree really well with the measurements over the full extent of the flow. Discrepancies are especially evident after the bump-sting juncture ($x/C = 1.0$). The difference becomes larger at the supercritical Mach numbers. The present solutions based on the Johnson-King model predict the largest displacement thickness. This is also consistent with the fact that the pressure recovery along the bump trailing edge predicted by the Johnson-King model in the present study is relatively the smallest.

Figures 38 and 39 show the comparisons of the predicted maximum Reynolds stresses and the experimental data for $M_\infty = 0.6$ and 0.875. In the comparison of the Reynolds shear stress of the boundary-layer calculations with the measurements, the effect for the rotation of coordinate along the body surface may be significant and must be corrected. The experimental data shown in Figures 38 and 36 are the values recalculated by Johnson (1985) from the measurements of Bachalo and Johnson (1979) by performing a coordinate transformation from the rectangular measurement coordinates to shear-layer coordinates. This

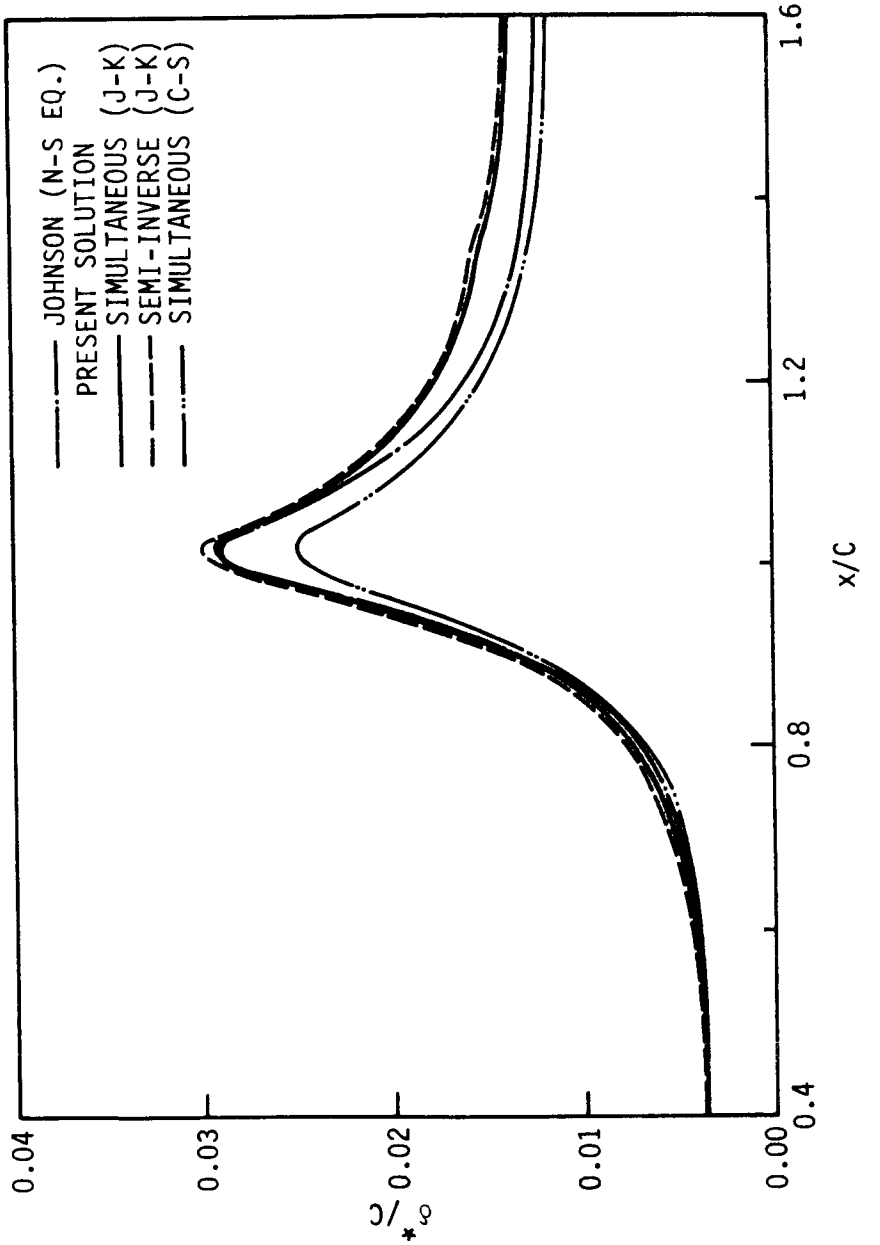

FIGURE 36. Displacement thickness distribution for a transonic turbulent flow over a bump ($M_\infty = 0.6$)

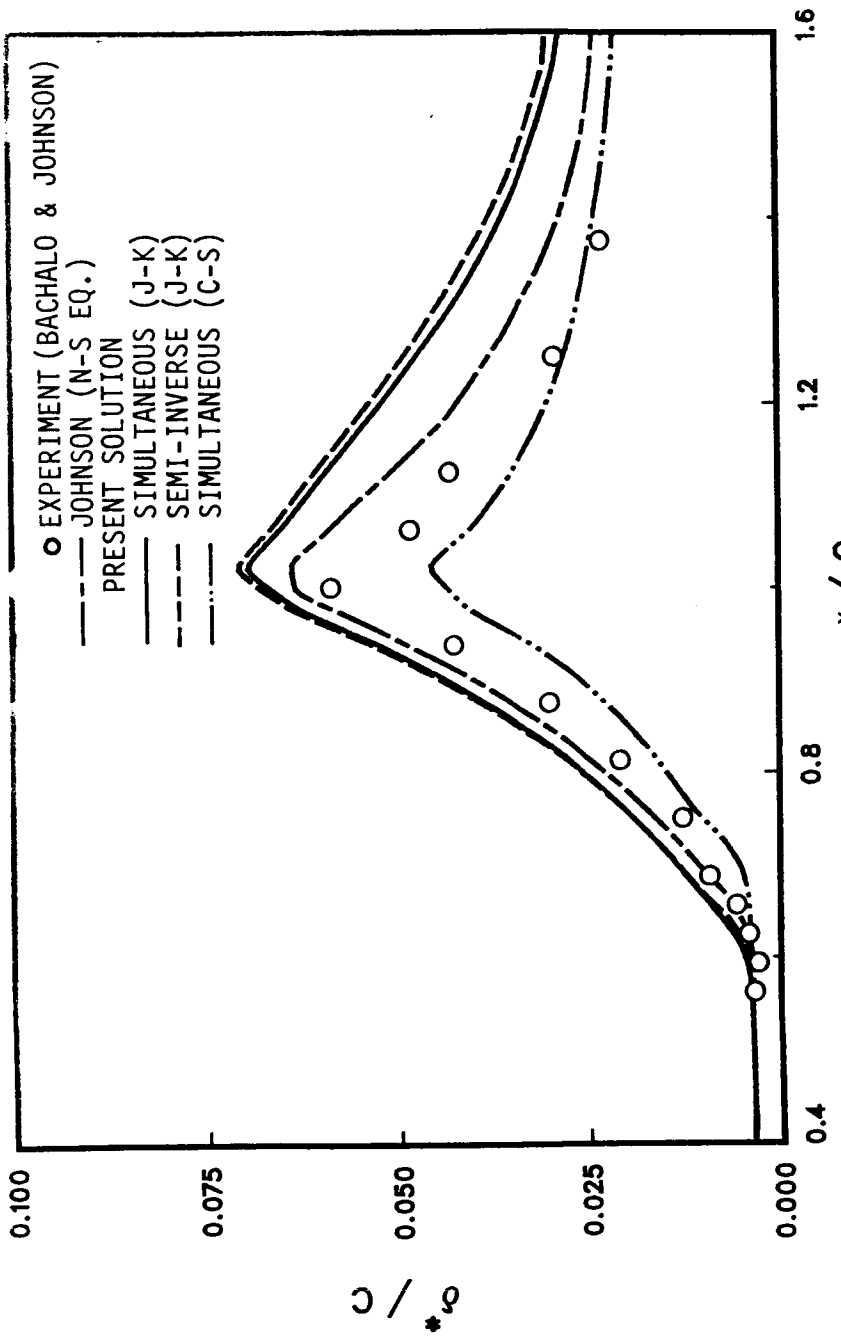

FIGURE 37. Displacement thickness distribution for a transonic turbulent flow over a bump ($M_\infty = 0.875$)

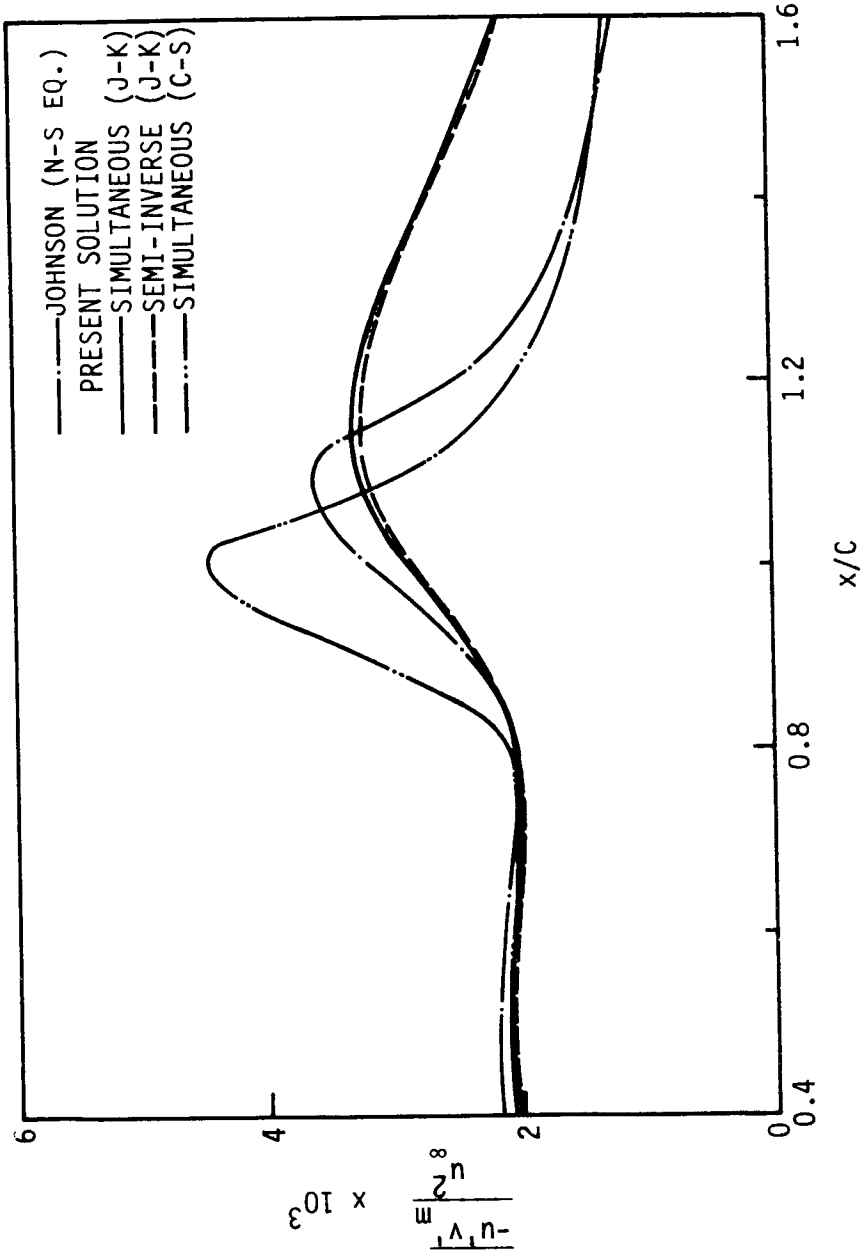

FIGURE 38. Maximum Reynolds shear stress distribution for a transonic turbulent flow over a bump ($M_\infty = 0.6$)

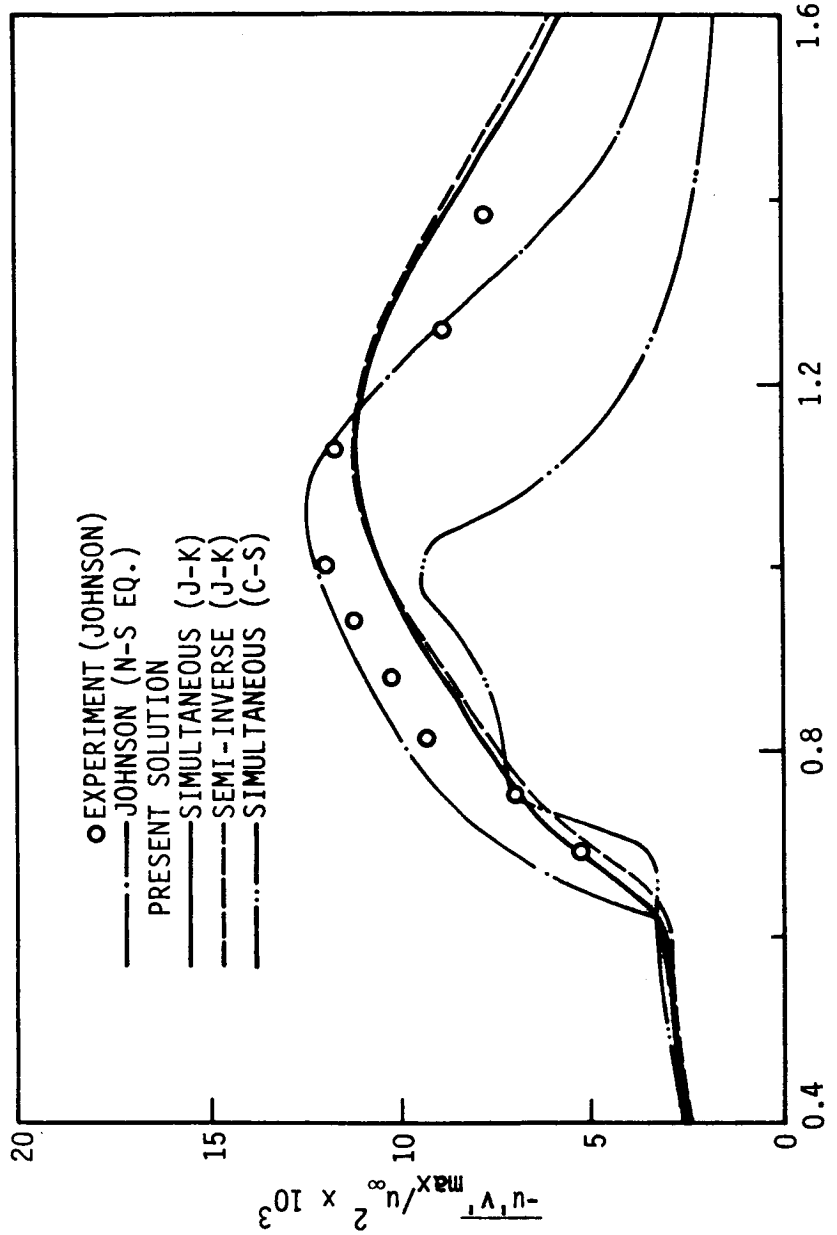

FIGURE 39. Maximum Reynolds shear stress distribution for a transonic turbulent flow over a bump ($M_\infty = 0.875$)

comparison shows the most striking difference between the algebraic Cebeci-Smith and Johnson-King model. The Cebeci-Smith model shows more rapid increase and abrupt decrease in $-\overline{u'v'}_m$, while the Johnson-King model provides more accurate prediction near the shock wave and smoother development across the flow field. One thing to notice is that the present predictions with the Johnson-King model indicates a slower decay downstream of the reattachment point than do the Navier-Stokes solutions obtained by Johnson using the same model. This slower decay is believed to be the cause of the rapid increase in the skin-friction coefficient after the reattachment point predicted by the Johnson-King model in the present method. In his Navier-Stokes solutions, Johnson (1985) found that this slow decay in the maximum Reynolds stresses was due to the fact that the value of $\sigma(x)$ in Equation (2.73) grew to unrealistically high values downstream of the reattachment point where a local equilibrium state was expected to be almost restored. The reason for this behavior is believed to be an underestimation of the turbulent viscosity length scales in the inner part of the boundary layer as pointed out by Johnson (1985). Since $\sigma(x)$ is the measure of nonequilibrium effects, it was initially expected to be close to unity after the reattachment point. However, the use of $\sigma(x) = 1.0$ after the reattachment point resulted in the decay of the maximum Reynolds stresses being too rapid after the reattachment point. Therefore, Johnson suggested that the value of $\sigma(x)$ be limited by an upper bound such as 3.0. However, such a limit was not used in the present calculations because the value of $\sigma(x)$ did not grow as fast as in the

Navier-Stokes solutions of Johnson. It never exceeded a value of about 3.5.

The velocity profiles predicted by the Johnson-King and Cebeci-Smith models for $M_\infty = 0.875$ are compared with the measurements and Navier-Stokes solutions obtained by the Johnson-King model in Figures 40 and 41. The agreement between predictions of the Johnson-King model and the measurements is especially good in the separated flow region. After the reattachment point, the predictions of the Cebeci-Smith model agree better with the measurements. This slow flow recovery downstream of the reattachment point predicted by the Johnson-King model appears to be a shortcoming that requires improvement. However, the effect of this discrepancy on the prediction of the surface pressure distribution is small. The difference in the predicted velocity profiles obtained by the FLARE approximation and windward differencing scheme is negligibly small. Figures 42 and 43 compare the profiles of Reynolds shear stress calculated by the present method with the measurements and the Navier-Stokes solutions obtained with the Johnson-King model for $M_\infty = 0.875$. Overall, the predictions of the Johnson-King model show better agreement with the measurements than predictions of the Cebeci-Smith model, especially downstream of the bump-sting juncture. However, in the outer region of the boundary layer, the Reynolds stresses predicted by the Johnson-King model decrease too slowly.

Figure 44 presents a Mach contour plot obtained by the present simultaneous interaction method with the Johnson-King model at $M_\infty = 0.875$. Note that the plot does not take into account viscous

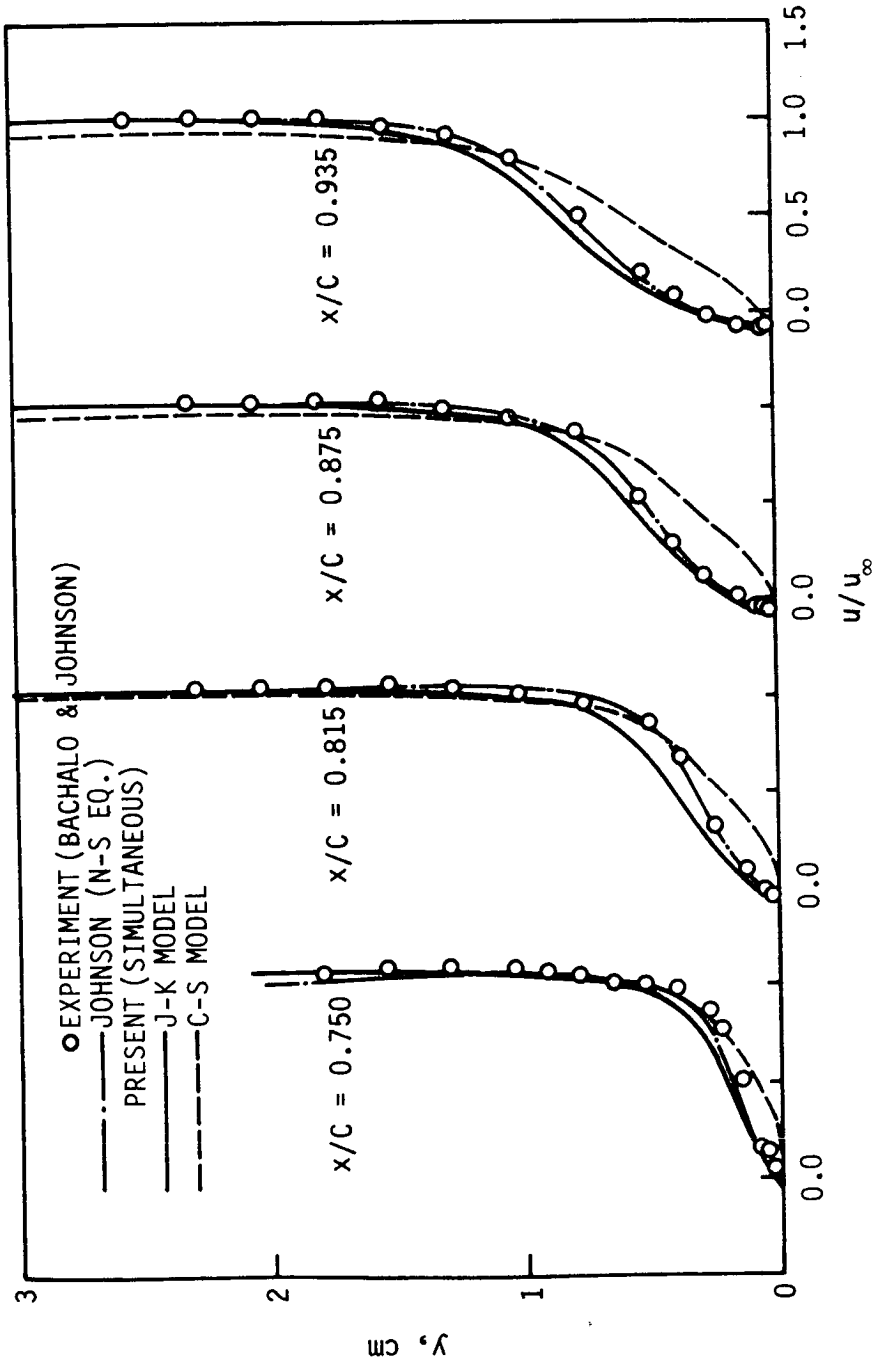

FIGURE 40. Mean velocity profiles for a transonic turbulent flow over a bump (1) ($M_\infty = 0.875$)

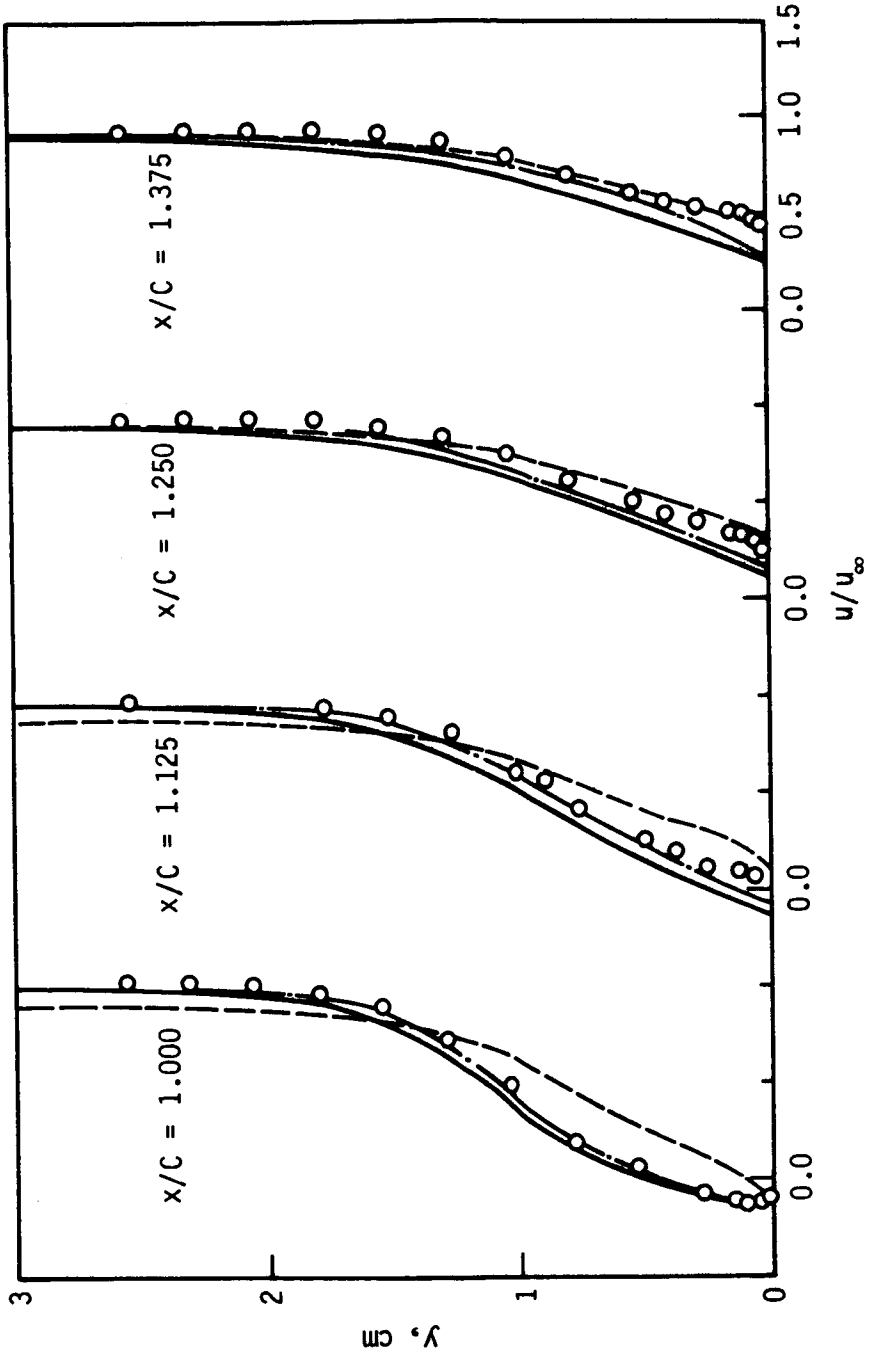

FIGURE 41. Mean velocity profiles for a transonic turbulent flow over a bump (2) ($M_\infty = 0.875$)

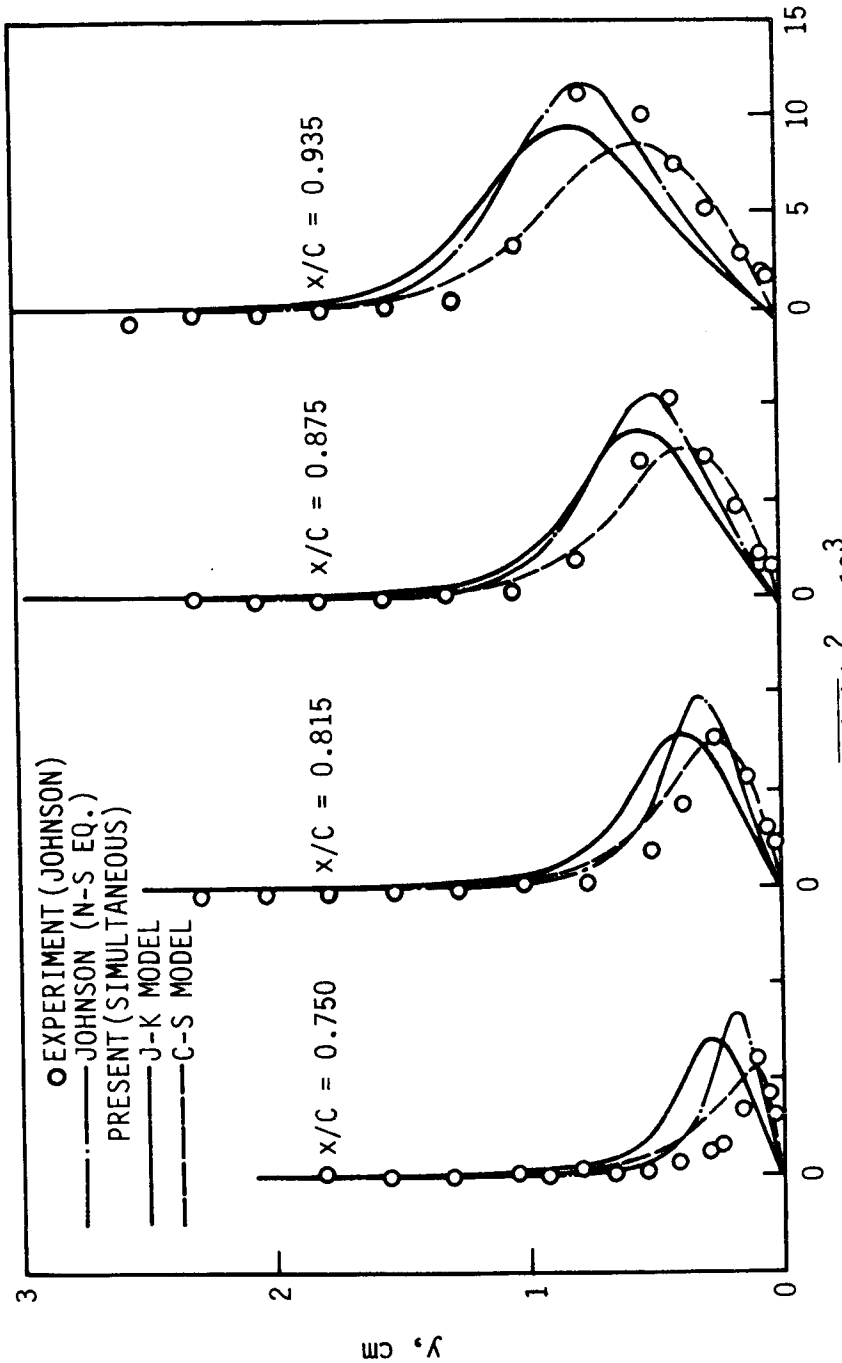

FIGURE 42. Reynolds shear stress profiles for a transonic turbulent flow over a bump (1) ($M_\infty = 0.875$)

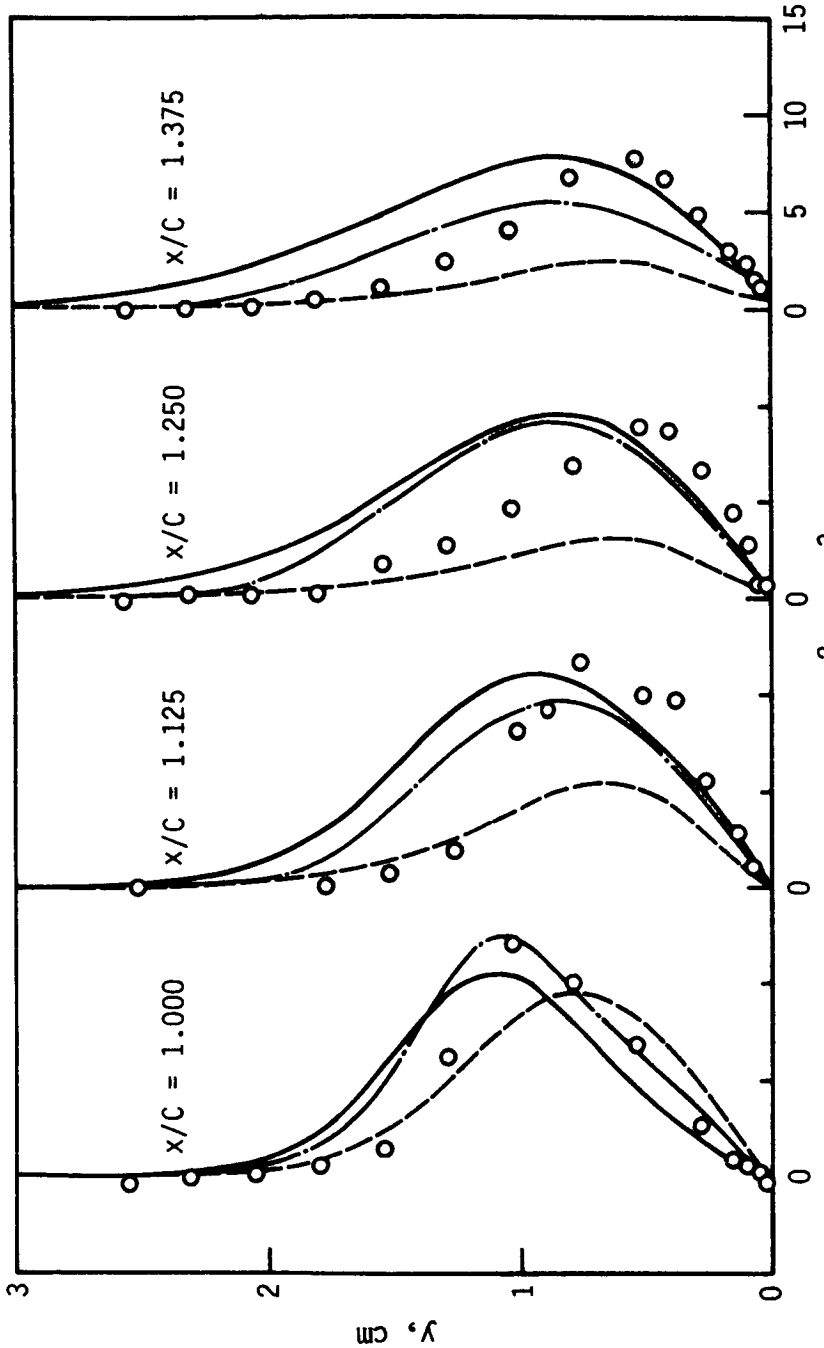

FIGURE 43. Reynolds shear stress profiles for a transonic turbulent flow over a bump (2) ($M_\infty = 0.875$)

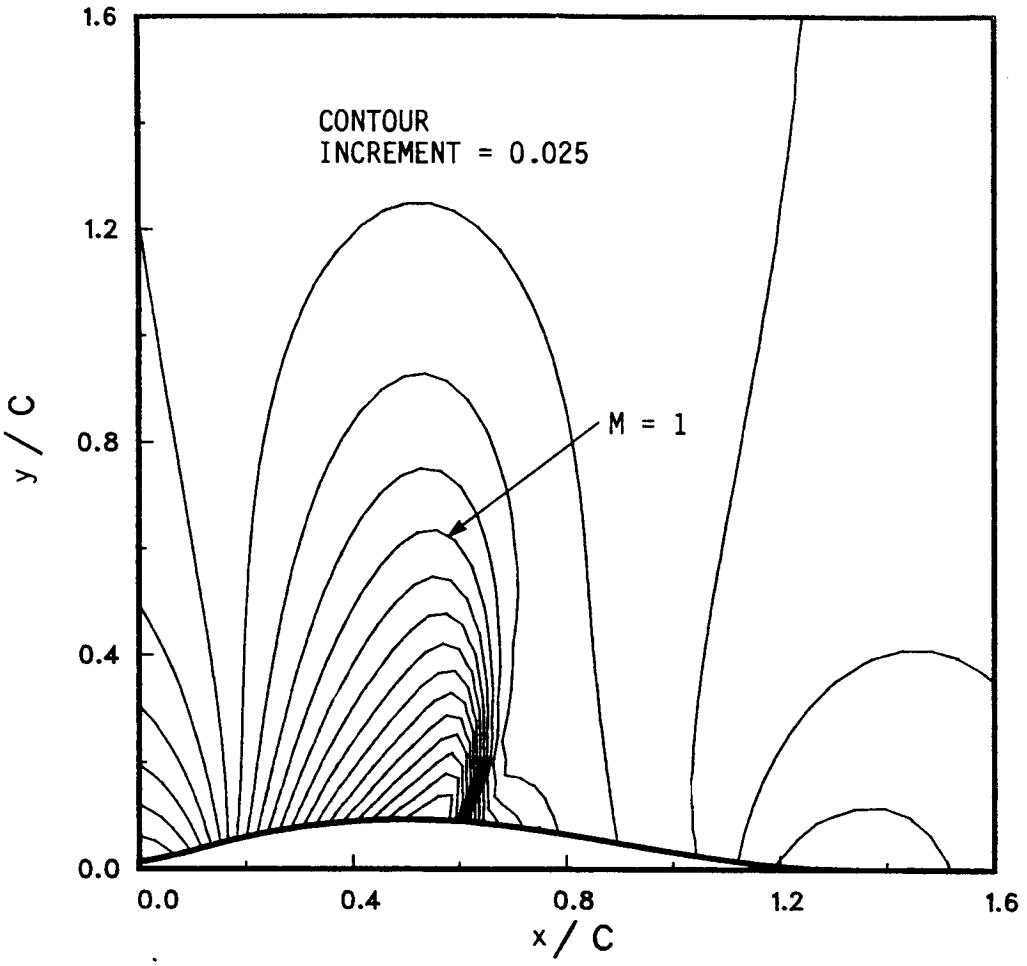

FIGURE 44. Mach contour plot for a transonic turbulent flow over a bump ($M_\infty = 0.875$)

regions explicitly because it was made based only on the inviscid part of the interacted solution. The body surface shown in this figure does not represents the actual body surface but the shear-layer coordinate used in the present calculation. The predicted shock location is in good agreement with the measurements as shown in the surface pressure comparison. The experimental observations and the Navier-Stokes solutions by Johnson (1985) indicated that the shock is highly curved in the inviscid region so that the shock wave far from the body surface is nearly aligned with the bump-sting juncture. However, the present solution shows almost vertical shock wave formation. This is believed to be due to the error caused by the velocity potential formulation for the inviscid flow. The source of the error is likely the neglect of the entropy rise across the shock in the potential flow analysis. To be more accurate, the inviscid analysis should satisfy the Rankine-Hugoniot relation rather than the isentropic relation across the shock wave and the effect of the rotational flow generated by the curved shock should be accounted for.

In the early stage of the present study, the effect of changing the modeling constants of the Johnson-King model, a_1 and C_{dif}, was evaluated using the simultaneous interaction method. As discussed by Johnson and King (1985), the interaction solution was found to be insensitive to the choice of C_{dif}. On the other hand, the effect of varying a_1 upon the prediction is noticeable. Some of the present calculations were performed using several different values of a_1. The typical value deduced from experimental measurements for compressible flows ranges

between 0.2 and 0.3. Figures 45-48 compare predictions with different values of a_1 in the range 0.25 ~ 0.4 for the flow at $M_\infty = 0.875$. Note that all the Johnson-King model results shown in the previous figures were obtained with $a_1 = 0.25$.

As can be seen in these figures, the results upstream of the shock wave seem insensitive to the value of a_1, but differences become evident downstream of the shock wave. Figure 45 shows that the shock position moves very slowly in the downstream direction and the pressure recovery in the bump trailing edge region increases with increasing values of a_1. Interestingly, predictions of the surface pressure with the larger a_1 (0.35 ~ 0.40) are in better agreement with the measurements of the 2 × 2 foot wind tunnel, while the prediction with a smaller value (0.25) of a_1 agrees much better with the measurements of the 6 × 6 foot wind tunnel.

The predicted location of the separation point does not seem to be very sensitive to the value used for a_1. The location of the reattachment point, however, does exhibit a dependence upon a_1. With a larger value of a_1, the predicted reattachment point moves upstream. As shown by Figures 47 and 48, increasing the value of a_1 from 0.25 to 0.35 appears to give improved predictions for the displacement thickness and the maximum Reynolds stresses distributions. However, considering the fact that these measurements were taken in the 2 × 2 foot wind tunnel and recalling the observation made in the comparison of the surface pressure, these variations are thought to be within the range of errors associated with the experimental data. Therefore, it is difficult to conclude which value of a_1 gives the best overall predictions. It seems

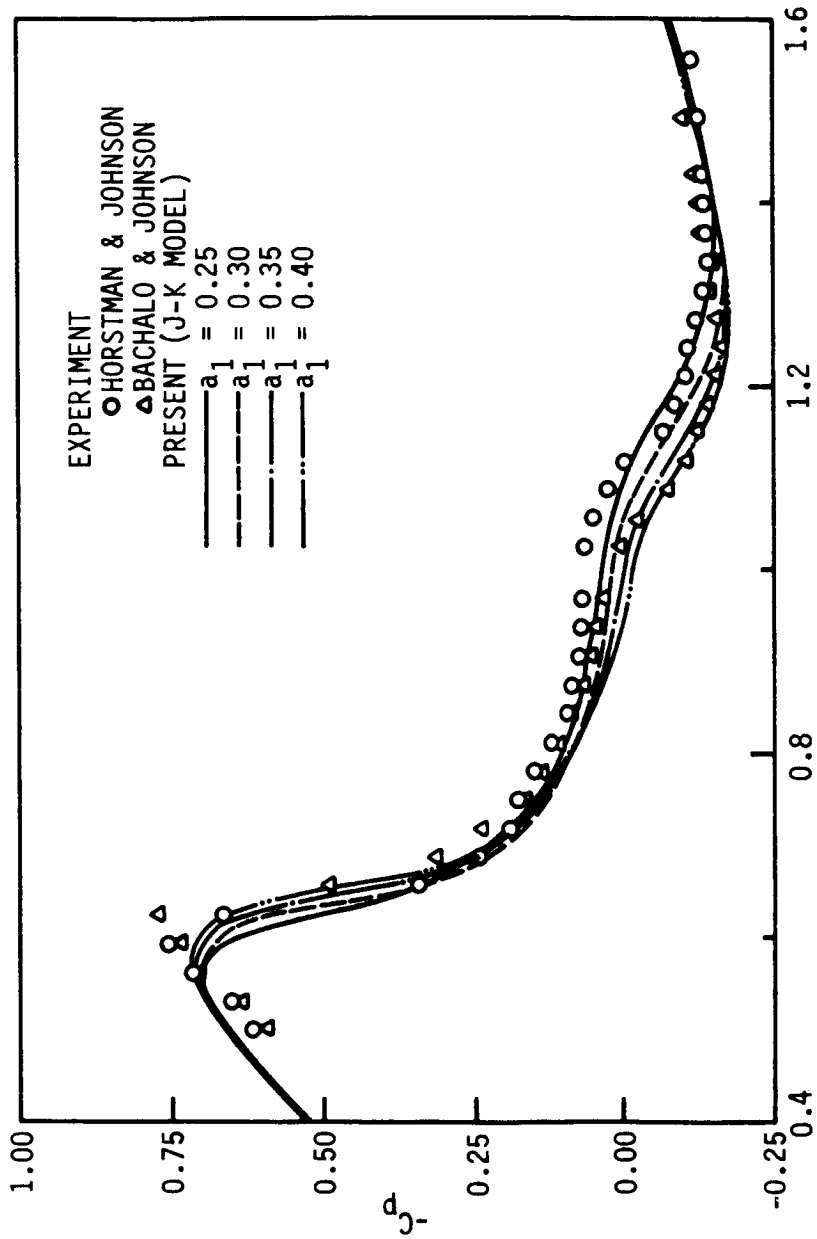

FIGURE 45. Pressure coefficient distribution with varying a_1 for a transonic turbulent flow over a bump ($M_\infty = 0.875$)

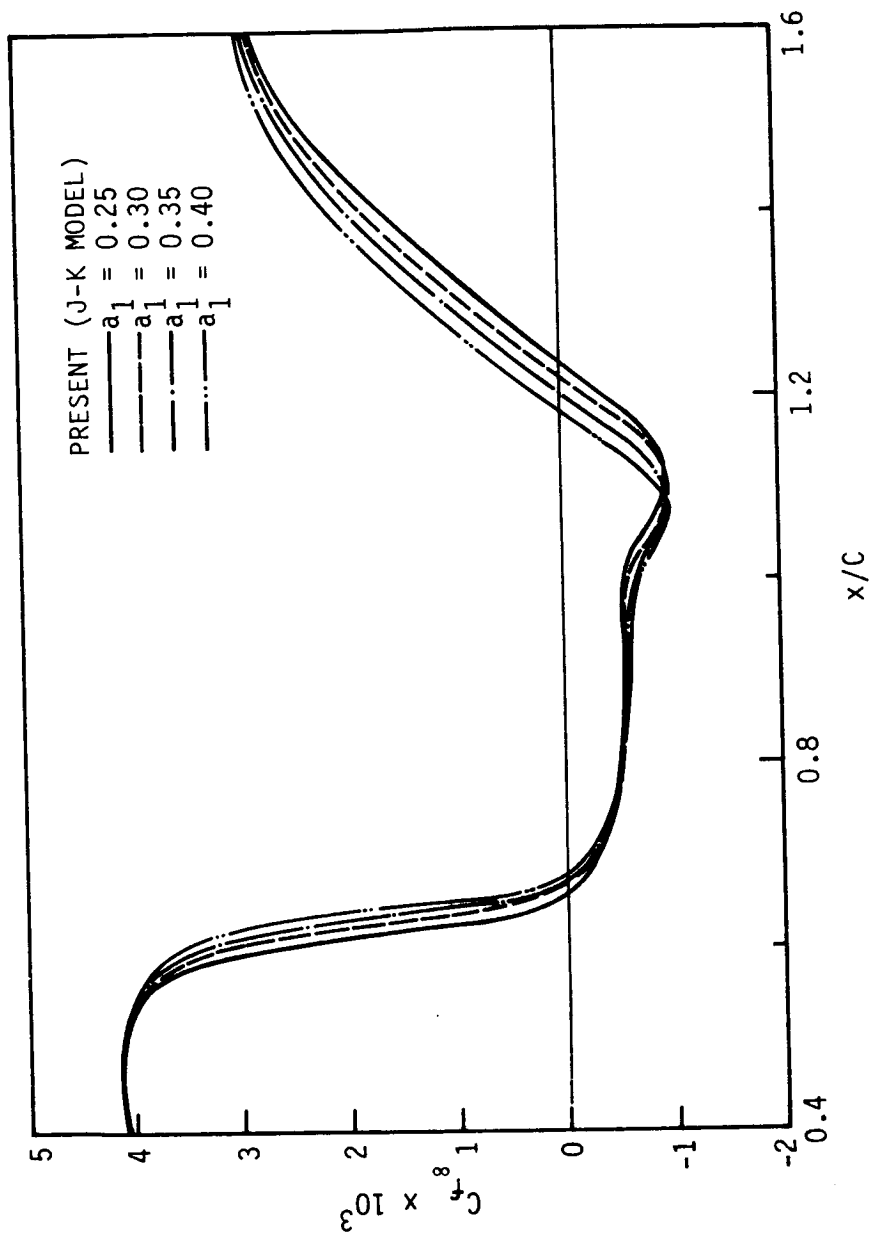

FIGURE 46. Skin-friction coefficient distribution with varying a_1 for a transonic turbulent flow over a bump ($M_\infty = 0.875$)

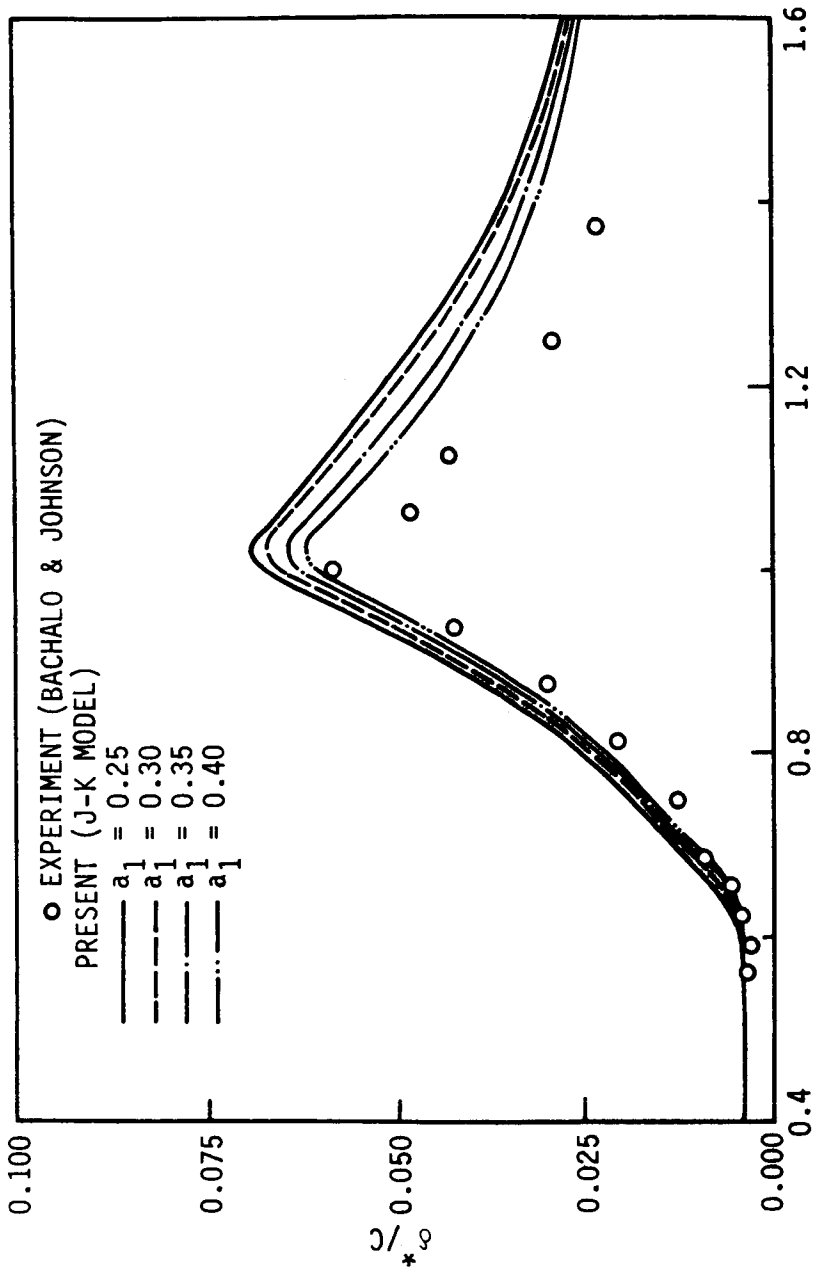

FIGURE 47. Displacement thickness distribution with varying a_1 for a transonic turbulent flow over a bump ($M_\infty = 0.875$)

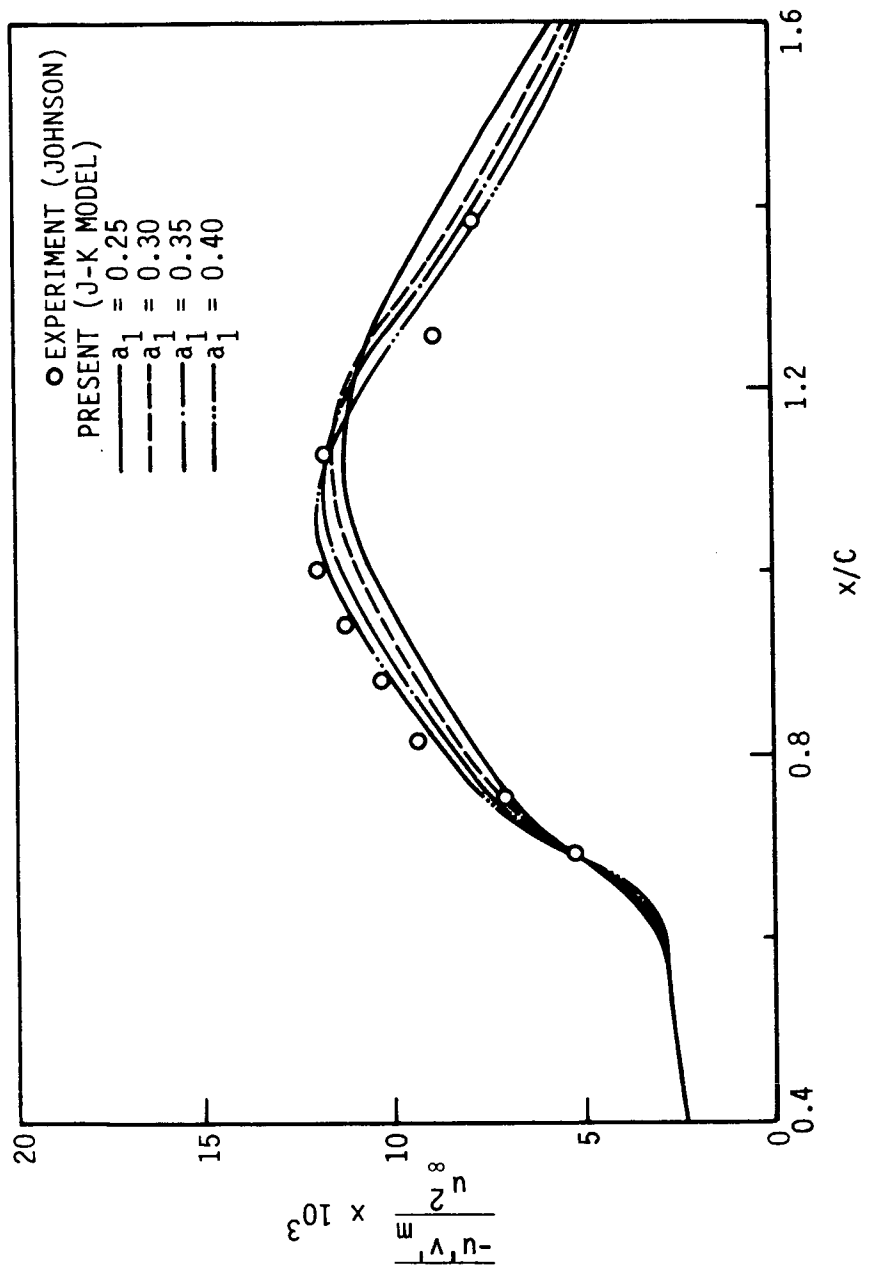

FIGURE 48. Maximum Reynolds shear stress distribution with varying a_1 for a transonic turbulent flow over a bump (M_∞ = 0.875)

clear that values of a_1 in the range $0.2 \sim 0.3$ give reasonably good predictions for most of the turbulent flow calculations in this study.

VI. CONCLUSIONS

A. Concluding Remarks

Two new viscous-inviscid interaction procedures have been developed and evaluated for transonic flows. Both employ an inverse finite-difference solution of the boundary-layer equations and a direct finite-difference solution to the conservative form of the full potential equation. The boundary-layer equations are solved in a fully implicit manner using Newton linearization with coupling of the continuity and momentum equations. The solution procedures have been developed using both the SLOR and AF2 schemes to solve the full potential equation. The two interaction procedures employ different coupling algorithms; one is similar to the procedure developed by Carter (1979) (the semi-inverse scheme) and the other, known as the simultaneous methods, is new as applied to finite-difference forms of the boundary-layer and full potential equations for transonic flows. The Cebeci-Smith and Johnson-King turbulence models were used for turbulent flow calculations. The present schemes were applied to predict flows over three different configurations in which significant flow separations occurred; incompressible laminar flow over a flat plate with a trough, transonic flow over an axisymmetric circular-arc boattail, and transonic flow over an axisymmetric circular-arc bump attached to a circular cylinder. From the study described in the previous chapters, the following conclusions can be made.

1. A modification to the semi-inverse interaction method proposed by Carter (1979) has been introduced and resulted in a reduction of 30 ~ 50% in the number of global iterations required for a specified level of convergence for the cases considered in this paper. The semi-inverse method is found to be stable for calculations of the subcritical flow with separation. However, it becomes less stable in supercritical flow with increasing size of the separated region so that a smaller value of the relaxation factor is required to obtain convergence. The value of the relaxation factor required seemed to depend upon the turbulence model used. The Johnson-King model required the use of a smaller relaxation factor than was needed for the Cebeci-Smith model and a larger number of global iterations was generally required for convergence. This apparent sensitivity to turbulence models may actually be only a sensitivity to the viscous solution being obtained, which was significantly different for each of the two models. The Johnson-King model tended to predict a larger separated region which could be the major cause for the requirement of a smaller relaxation factor and more global iterations for convergence. In attempting the calculation of the bump flow at $M_\infty \geq 0.9$, the semi-inverse method failed to provide convergence regardless of the turbulence model used.

2. A new simultaneous interaction method has been developed by obtaining the solutions of the boundary-layer equations and the SLOR procedure of the potential equation simultaneously. The predictions from this interaction method are in good agreement with those from the semi-inverse method when the latter gives a converged solution. For the

calculation of subcritical flows with a relatively small separated region, the simultaneous interaction method is usually about twice as efficient as the semi-inverse method. Additionally, the simultaneous interaction method was found to be stable over a wider range of flows than the semi-inverse method. Also, the simultaneous interaction method seems to be relatively insensitive to the turbulence model used. Moreover, by employing a pseudo-time dependent approach in the iterative procedure of the Newton linearization method for the boundary-layer equation, the simultaneous method takes only 20 ~ 30% of the total computing time required by the semi-inverse method for supercritical flow calculations.

3. The predictions for turbulent flows are quite dependent upon the turbulence model used. Of the two models evaluated, the algebraic Cebeci-Smith model generally predicted very poorly for separated flows at both subcritical and supercritical Mach numbers. The present solutions with the Cebeci-Smith model significantly overpredicted the pressure recovery and underpredicted the size of the separation bubble and the displacement thickness. The position of the shock wave is predicted reasonably well by the Cebeci-Smith model. The turbulence model proposed by Johnson and King (1985) was found to provide generally better predictions than the algebraic Cebeci-Smith and more sophisticated two-equation models for the transonic separated flows considered. The predicted locations of the shock wave, separation and reattachment points using the Johnson-King model agree very well with the experimental data. The displacement thickness is underpredicted in

the largely separated flow region and the flow recovery toward the equilibrium stage after the reattachment point is also underpredicted by the Johnson-King model. The effect of varying the a_1 parameter in the Johnson-King model was investigated. The value of $a_1 = 0.25$ (used by Johnson and King (1985)) is found to give generally satisfactory predictions; however, for each separated case computed, it was possible to obtained slightly improved predictions by adjusting the a_1 value. Clearly, the Johnson-King model provides much better predictions than the algebraic Cebeci-Smith model for these flows. Yet some room for improvement in the turbulence modeling for separated flows remains.

4. The predictions obtained by the FLARE approximation showed good agreement with those obtained by the windward differencing scheme.

B. Recommendations for Future Study

The present viscous-inviscid interaction method generally provides good predictions for flows considered in the present study. However, improvement appears possible in several areas in order to provide better predictions for flows with strong interaction. Although the velocity potential formulation is accurate enough for most of the transonic flow regime, errors associated with the isentropic assumption for the shock jump conditions increase with increasing strength of the shock wave. This error can be completely eliminated by using the full Euler equations, but then computational efficiency must be sacrificed. Instead, the full potential formulation can be modified by using an entropy correction approach suggested by Klopfer and Nixon (1983) and

Hafez and Lovell (1983, 1984). This approach is expected to be effective in reducing the error caused by the isentropic assumptions.

The present simultaneous interaction method is based on the SLOR solution procedure for the inviscid flow region. Improvement in the rate of convergence might be possible by employing a faster iterative relaxation algorithm like the ADI or AF2 schemes as in the case of the semi-inverse interaction method. Recently, significant progress has been made in improving the efficiency of solution algorithms for the time-averaged Navier-Stokes equations. Work should continue on Navier-Stokes algorithms and these, too, should be useful in predicting complex transonic flow with strong viscous-inviscid interaction.

The newly proposed Johnson-King model is very simple to use and shows great promise for accurately predicting flows with large separated regions. However, improvement appears possible. A better description of flow recovery toward the equilibrium state, and better modeling of the diffusion terms in the transport equation for the maximum Reynolds stress are two areas where further work should be done.

VII. REFERENCES

Abeyounis, W. K. 1977. "Boundary-Layer Separation on Isolated Boattail Nozzles." NASA CR-152703.

Ackeret, J., Feldmann, F., and Rott, N. 1947. "Investigation of Compression Shocks and Boundary Layers in Gases Moving at High Speed." NACA TM-1113.

Alber, I. E., Bacon, J. W., Masson, B. S., and Collins, D. J. 1973. "An Experimental Investigation of Turbulent Transonic Viscous-Inviscid Interactions." AIAA J. 11, No. 5: 620-627.

Altstatt, M. C. 1977. "An Experimental and Analytical Investigation of a Transonic Shock-Wave/Boundary-Layer Interaction." AEDC TR-77-47. Arnold Air Force Station, Tennessee.

Ames, W. F. 1977. Numerical Methods for Partial Differential Equations. 2nd ed. Academic Press, New York.

Anderson, D. A., Tannehill, J. C., and Pletcher, R. H. 1984. Computational Fluid Mechanics and Heat Transfer. McGraw-Hill, New York.

Bachalo, W. D. and Johnson, D. A. 1979. "An Investigation of Transonic Turbulent Boundary Layer Separation Generated on an Axisymmetric Flow Model." AIAA Paper 79-1479. Williamsburg, Virginia.

Bailey, F. R. and Ballhaus, W. F. 1972. "Relaxation Methods for Transonic Flow about Wing-Cylinder Combinations and Lifting Swept Wings." Lecture Notes in Physics. Vol. 19. Springer-Verlag, New York.

Baldwin, B. S. and Lomax, H. 1978. "Thin Layer Approximation and Algebraic Model for Separated Turbulent Flows." AIAA Paper 78-257. Huntsville, Alabama.

Baldwin, B. S. and MacCormack, R. W. 1976. "Modifications of the Law of the Wall and Algebraic Turbulence Modelling for Separated Boundary Layers." AIAA Paper 76-3540. San Diego, California.

Baldwin, B. S. and Rose, W. C. 1975. "Calculation of Shock-Separated Turbulent Boundary Layers." NASA SP-347.

Baldwin, B. S., MacCormack, R. W., and Deiwert, G. S. 1975. "Numerical Techniques for the Solution of the Compressible Navier-Stokes Equation and Implementation of Turbulence Models." AGARD LSP-73.

Ballhaus, W. F., Jameson, A., and Albert, J. 1978. "Implicit Approximate-Factorization Schemes for Steady Transonic Flow Problems." AIAA J. 16, No. 6: 573-579.

Ballhaus, W. F. and Steger, J. L. 1975. "Implicit Approximate-Factorization Schemes for the Low-Frequency Transonic Equation." NASA TM X-73082.

Bauer, F. P., Garabedian, D., Korn, D., and Jameson, A. 1975. "Supercritical Wing Section II." Lecture Notes in Economics and Mathematical Systems. Vol. 108. Springer-Verlag, Berlin.

Bavitz, P. C. 1975. "An Analysis Method for Two Dimensional Transonic Viscous Flow." NASA TN D-7718.

Benek, J. A. 1979. "Separated and Nonseparated Turbulent Flows about Axisymmetric Nozzle Afterbodies, Part I. Detailed Surface Measurement." AEDC TR 78-49.; "Part II. Detailed Flow Measurement." AEDC TR 79-22. Arnold Air Force Station, Tennessee.

Bertram, M. H. 1968. "Compressible Turbulent Boundary Layers." NASA SP-216.

Blottner, F. G. 1975. "Investigation of Some Finite-Difference Techniques for Solving the Boundary Layer Equations." Computer Methods in Applied Mechanics and Engineering 6: 1-30.

Boussinesq, J. 1877. "Essai Sur La Theorie Des Eaux Courantes." Mem. Pres. Acad. Sci. 23: 46.

Bradshaw, P. 1972. "The Understanding and Prediction of Turbulent Flow." Aeronautical J. 6: 403-418.

Bradshaw, P. 1977. "Compressible Turbulent Shear Layers." Ann. Rev. Fluid Mech. 9: 33-54.

Bradshaw, P. and Ferriss, D. H. 1971. "Calculation of Boundary-Layer Development Using the Turbulent Energy Equation: Compressible Flow on Adiabatic Walls." J. Fluid Mechanics 46, Part 1: 83-110.

Bradshaw, P. and Wong, F. Y. F. 1972. "The Reattachment and Relaxation of a Turbulent Shear Layer." J. Fluid Mechanics 52, Part 1: 113-135.

Bradshaw, P., Ferriss, D. H., and Atwell, N. P. 1967. "Calculation of Boundary-Layer Development Using the Turbulent Energy Equation." J. Fluid Mechanics 28, Part 3: 593-616.

Briley, W. R. 1971. "A Numerical Study of Laminar Separation Bubbles using the Navier-Stokes Equations." J. Fluid Mechanics 47, Part 4: 713-736.

Brown, S. N. and Stewartson, K. 1969. "Laminar Separation." Ann. Rev. Fluid Mech. 1: 45-72.

Carter, J. E. 1974. "Solutions for Laminar Boundary Layers with Separation and Reattachment." AIAA Paper 74-5. Washington, D. C.

Carter, J. E. 1975. "Inverse Solutions for Laminar Boundary-Layer Flows with Separation and Reattachment." NASA TR R-447.

Carter, J. E. 1978. "Inverse Boundary-Layer Theory and Comparison with Experiment." NASA TP-1208.

Carter, J. E. 1979. "A New Boundary-Layer Inviscid Iteration Technique for Separated Flow." AIAA Paper 79-1450. Williamsburg, Virginia.

Carter, J. E. 1981. "Viscous-Inviscid Interaction Analysis of Transonic Turbulent Separated Flow." AIAA Paper 81-1241. Palo Alto, California.

Carter, J. E. and Hafez, M. M. 1982. "Analysis of Imbedded Transonic Shock Wave Influence on Turbulent Boundary Layer Separation." Annual Report. Air Force Office of Scientific Research Contract F49620-81-C-0041.

Carter, J. E. and Vasta, V. N. 1982a. "Analysis of Separated Boundary-Layer Flows." 8th International Conference on Numerical Methods in Fluid Dynamics, Aachen, West Germany.

Carter, J. E. and Vasta, V. N. 1982b. "Analysis of Airfoil Leading Edge Separation Bubbles." NASA CR-165935.

Carter, J. E. and Wornom, S. F. 1975. "Solutions for Incompressible Separated Boundary Layers Including Viscous-Inviscid Interaction." NASA SP-347.

Carter, J. E., Edwards, D. E., and Hafez, M. M. 1983. "Analysis of Transonic Shock Induced Separated Flow Including Normal Pressure Gradients." Final Report. Air Force Office of Scientific Research Contract F49620-81-C-0041.

Catherall, D. and Mangler, K. W. 1966. "The Integration of the Two-Dimensional Laminar Boundary-Layer Equations past the Point of Vanishing Skin Friction." J. Fluid Mechanics 26, Part 1: 163-182.

Cebeci, T. 1970. "Behavior of Turbulent Flow near a Porous Wall with Pressure Gradient." AIAA J. 8, No. 12: 2152-2156.

Cebeci, T. 1971. "Wall Curvature and Transition Effects in Turbulent Boundary Layers." AIAA J. 9, No. 9: 1868-1870.

Cebeci, T. 1973. "Variation of the Van Driest Damping Parameter with Mass Transfer." AIAA J. 11, No. 2: 237-238.

Cebeci, T. 1976. "Separated Flows and Their Representation by Boundary Layer Equations." Report ONR-CR215-234-2. Office of Naval Research, Arlington, Virginia.

Cebeci, T. and Smith, A. M. O. 1974. Analysis of Turbulent Boundary Layers. Academic Press, New York.

Cebeci, T. and Stewartson, K. 1983. "On the Calculation of Separation Bubbles." J. Fluid Mechanics 133: 287-296.

Cebeci, T., Keller, H. B., and Williams, P. G. 1979. "Separating Boundary-Layer Flow Calculations." J. Computational Physics 31: 363-378.

Chan, Y. Y. 1972. "Compressible Turbulent Boundary Layer Computations Based on an Extended Mixing Length Approach." Canadian Aeronautics and Space Institute Transactions 5: 21-27.

Chapman, D. R. and Rubesin, M. W. 1949. "Temperature and Velocity Profiles in the Compressible Laminar Boundary Layer with Arbitrary Distribution of Surface Temperature." J. Aeronautical Sciences 16: 547-565.

Chen, L. T. and Caughey, D. A. 1980. "Calculation of Transonic Inlet Flowfields Using Generalized Coordinates." J. Aircraft 17, No. 3: 167-174.

Chien, K. Y. 1982. "Predictions of Channel and Boundary-Layer Flows with a Low-Reynolds-Number Turbulence Model." AIAA J. 20, No. 1: 33-38.

Chow, W. L., Bober, L. J., and Anderson, B. H. 1975. "Numerical Calculation of Transonic Boattail Flow." NASA TN D-7984.

Clauser, F. H. 1956. "The Turbulent Boundary Layer." Advan. Appl. Mech. 4: 1-51.

Coakley, T. J. and Viegas, J. R. 1977. "Turbulence Modeling of Shock Separated Boundary-Layer Flows." Symposium on Turbulent Shear Flows, University Park, Pennsylvania.

Coles, D. 1962. "The Turbulent Boundary Layer in a Compressible Fluid." Phys. Fluids 7, No. 9: 1403-1423.

Collyer, M. R. and Lock, R. C. 1979. "Prediction of Viscous Effects in Steady Transonic Flow past an Aerofoil." Aeronautical Quarterly 30: 485-505.

Cosner, R. R. and Bower, W. W. 1977. "A Patched Solution of the Transonic Flowfields About an Axisymmetric Boattail." AIAA Paper 77-227. Los Angeles, California.

Crimi, P. and Reeves, B. L. 1976. "Analysis of Leading-Edge Separation Bubbles on Airfoils." AIAA J. 14, No. 11: 1548-1555.

Dash, S. M. and Pergament, H. S. 1978. "A COmputational Model for the Prediction of Jet Entrainment in the Vicinity of Nozzle Boattails (The BOAT Code)." NASA CR-3075.

Davis, R. T. 1984. "A Procedure for Solving the Compressible Interacting Boundary-Layer Equations for Subsonic and Supersonic Flows." AIAA Paper 84-1614. Snowmass, Colorado.

Davis, R. T. and Carter, J. E. 1984. "Analysis of Airfoil Transitional Separation Bubbles." AIAA Paper 84-1613. Snowmass, Colorado.

Davis, R. T. and Werle, M. J. 1981. "Progress on Interacting Boundary-Layer Computations at High Reynolds Number." Proc. 1st Symposium on Numerical and Physical Aspects of Aerodynamic Flow, Long Beach, California.

Deardorff, J. W. 1970. "A Numerical Study of Three-Dimensional Turbulent Channel Flow at Large Reynolds Numbers." J. Fluid Mechanics 41, Part 2: 453-480.

Deiwert, G. S. 1976. "Computation of Separated Transonic Turbulent Flows." AIAA J. 14, No. 6: 735-740.

Deiwert, G. S. 1981. "Numerical Simulation of Three-Dimensional Boattail Afterbody Flowfields." AIAA J. 19, No. 5: 582-588.

Delery, J. M. 1983. "Experimental Investigation of Turbulence Properties in Transonic Shock/Boundary-Layer Interactions." AIAA J. 21, No. 2: 180-185.

Delery, J. M., Chattot, J. J., and Le Balleur, J. C. 1976. "Viscous Interaction with Separation in Transonic Flow." NASA TT F-17187.

Dougherty, F. C., Holst, T. L., Gundy, K. L., and Thomas, S. C. 1981. "TAIR - A Transonic Airfoil Analysis Computer Code." NASA TM-81296.

Eberle, A. 1978. "A Finite Volume Method for Calculating Transonic Potential Flow around Wings from the Pressure Minimum Integral." NASA TM-75324.

Edwards, D. E. and Carter, J. E. 1985. "A Quasi-Simultaneous Finite Difference Approach for Strongly Interacting Flow." Proc. 3rd Symposium on Numerical and Physical Aspects of Aerodynamic Flows, Long Beach, California.

Favre, A. 1965. "Equations des Gaz Turbulents Compressibles: 1. Formes Generales." J. de Mecanique 4: 361-390.

Flores, J., Holst, T. L., Kwak, D., and Batiste, D. M. 1984. "A New Consistent Spatial Differencing Scheme for the Transonic Full-Potential Equation." AIAA J. 22, No. 8: 1027-1034.

Forsythe, G. E. and Wasow, W. 1960. Finite Difference Methods for Partial Differential Equations. Wiley, New York.

Garabedian, P. R. and Korn, D. 1972. "Analysis of Transonic Airfoils." Comm. Pure Appl. Math. 24: 841-851.

Gersten, K. 1974. "Die Verdrangungsclicke bei Grenzschichten Hoherer Ordnung (Displacement Thickness in Higher Order Boundary Layers)." Z. Angew. Math. Mech. 54: 165-171.

Glauert, M. B. 1957. "A Boundary Layer Theorem, with Applications to Rotating Cylinders." J. Fluid Mechanics 2, Part 1: 89-99.

Goldstein, S. 1948. "On Laminar Boundary Layer Flow near a Position of Separation." Q. J. Mech. Appl. Math. 1: 43-69.

Green, J. E. 1968. "Reflection of an Oblique Shock Wave by a Turbulent Boundary Layer." J. Fluid Mechanics 40, Part 1: 81-95.

Green, J. E. 1970. "Interaction between Shock Waves and Turbulent Boundary Layers." Progress in Aerospace Sciences 11: 235-340.

Green, L. L. and South, J. C., Jr. 1983. "Conservative Full-Potential Calculations for Axisymmetric, Transonic Flow." AIAA J. 21, No. 11: 1492-1499.

Hafez, M. and Lovell, D. 1983. "Entropy and Vorticity Corrections for Transonic Flows." AIAA Paper 83-1926. Danvers, Massachusetts.

Hafez, M. and Lovell, D. 1984. "Transonic Small DIsturbance Calculations Including Corrections." Numerical and Physical Aspects of Aerodynamic Flows II, (T. Cebeci, ed.), Springer-Verlag, New York, pp.337-350.

Hafez, M., South, J. C., Jr., and Murman, E. 1979. "Artificial Compressibility Methods for Numerical Solutions of Transonic Full Potential Equation." AIAA J. 17, No. 8: 838-844.

Halim, A. and Hafez, M. 1984. "Calculation of Separation Bubbles using Boundary-Layer-Type Equations - Part I." Recent Advances in Numerical Methods in Fluids, Vol. 3, Viscous Flow Computational Methods, (W. G. Habashi, ed.), Pineridge, Swansea, pp.395-415.

Hanjalic, K. and Launder, B. E. 1972. "A Reynolds Stress Model of Turbulence and Its Application to Axisymmetric Shear Flows." J. Fluid Mechanics 52, Part 4: 609-638.

Harlow, F. H. and Nakayama, P. I. 1967. "Turbulence Transport Equations." Phys. Fluids 10, No. 11: 2323-2332.

Harten, A. 1978. "The Artificial Compression Method for Computation of Shocks and Contact Discontinuities: III. Self-Adjusting Hybrid Schemes." Math. Comput. 32: 363-389.

Hess, J. L. and Smith, A. M. O. 1967. "Calculation of Potential Flow about Arbitrary Bodies." Progress in Aeronautical Sciences 8: 1-138

Hinze, J. O. 1975. Turbulence. 2nd ed. McGraw-Hill, New York.

Holst, T. L. 1977. "Numerical Solution of Axisymmetric Boattail Fields with Plume Simulators." AIAA Paper 77-224. Los Angeles, California.

Holst, T. L. 1979. "Implicit Algorithm for the Conservative Transonic Full-Potential Equation Using an Arbitrary Mesh." AIAA J. 17, No. 10: 1038-1045.

Holst, T. L. 1983. "Numerical Computation of Transonic Flow Governed by the Full-Potential Equation." von Karman Institute Lecture Series. Rhode-St-Genese, Belgium.

Holst, T. L. and Albert, J. 1979. "An Implicit Algorithm for the Conservative, Transonic Full-Potential Equation with Effective Rotated Differencing." NASA TM-78570.

Holst, T. L. and Ballhaus, W. F. 1979. "Fast, Conservative Schemes for the Full Potential Equation Applied to Transonic Flows." AIAA J. 17, No. 2: 145-152.

Horstman, C. C. 1976. "A Turbulence Model for Nonequilibrium Adverse Pressure Gradient Flows." AIAA Paper 76-412. San Diego, California.

Horstman, C. C. 1983. "Prediction of Separated Asymmetric Trailing-Edge Flows at Transonic Mach Numbers." AIAA J. 21, No. 9: 1255-1261.

Horstman, C. C. and Johnson, D. A. 1984. "Prediction of Transonic Flows." AIAA J. 22, No. 7: 1001-1003.

Houwink, R. and Veldman, A. E. P. 1984. "Steady and Unsteady Separated Flow Computations for Transonic Airfoils." AIAA Paper 84-1618. Snowmass, Colorado.

Howarth, L. 1938. "On the Solution of the Laminar Boundary Layer Equations." Proc. Roy. Soc. London A 164: 547-579.

Illingworth, C. R. 1950. "Some Solutions of the Equations of Flow of a Viscous Compressible Fluid." Proc. Camb. Phil. Soc. 46: 469-478.

Jameson, A. 1974. "Iterative Solution of Transonic Flows over Airfoils and Wings, Including Flows at Mach 1." Commun. Pure Appl. Math. 27: 283-309.

Jameson, A. 1975. "Transonic Potential Flow Calculations using Conservative Form." Proc. AIAA 2nd Computational Fluid Dynamics Conference, Hartford, Connecticut: 148-161.

Jameson, A., Caughey, D. A., Newman, P. A., and Davis, R. M. 1976. "A Brief Description of the Jameson-Caughey NYU Transonic Swept-Wing Computer Program FLO22." NASA TM X-73996.

Johnson, D. A. 1985. "Predictions of Transonic Separated Flow with an Eddy-Viscosity/Reynolds-Shear-Stress Closure Model." AIAA Paper 85-1683. Cincinnati, Ohio.

Johnson, D. A. and Bachalo, W. D. 1980. "Transonic Flow past a Symmetrical Airfoil-Inviscid and Turbulent Flow Properties." AIAA J. 18, No. 1: 16-24.

Johnson, D. A. and King, L. S. 1985. "A Mathematically Simple Turbulence Closure Model for Attached and Separated Turbulent Boundary Layers." AIAA J. 23, No. 11: 1684-1692. (see also "A New Turbulence Closure Model for Boundary Layer Flows with Strong Adverse Pressure Gradients and Separation." AIAA Paper 84-0175. Reno, Nevada.)

Johnson, D. A., Horstman, C. C., and Bachalo, W. D. 1982. "Comparison Between Experiment and Prediction for Transonic Turbulent Separated Flow." AIAA J. 20, No. 6: 737-744.

Jones, W. P. and Launder, B. E. 1972. "The Prediction of Laminarization with a Two-Equation Model of Turbulence." Int. J. Heat Mass Transfer 15: 301-314.

Kays, K. M., Moffat, R. J., and Thielbahr, W. H. 1970. "Heat Transfer to the Highly Accelerated Turbulent Boundary Layer with and without Mass Addition." J. Heat Transfer 92: 499-505.

Keller, H. B. and Cebeci, T. 1972. "Accurate Numerical Methods for Boundary-Layer Flows. II: Two-Dimensional Turbulent Flows." AIAA J. 10, No. 9: 1193-1199.

Keller, J. D. and South, J. C., Jr. 1976. "RAXBOD: A Fortran Program for Inviscid Transonic Flow over Axisymmetric Bodies." NASA TM X-72831.

Khosla, P. K. and Lai, H. T. 1984. "Global PNS Solutions for Transonic Strong Interaction Flows." AIAA Paper 84-0458. Reno, Nevada.

Khosla, P. K. and Rubin 1983. "A Composite Velocity Procedure for the Compressible Navier-Stokes Equations." AIAA J. 21, No. 11: 1546-1551.

Kistler, A. L. and Chen, W. S. 1963. "The Fluctuating Pressure Field in a Supersonic Turbulent Boundary Layer." J. Fluid Mechanics 16, Part 1: 41-64.

Klebanoff, P. S. 1954. "Characteristics of Turbulence in a Boundary Layer with Zero Pressure Gradient." NACA TN-3178.

Klebanoff, P. S. and Diehl, Z. W. 1952. 'Some features of Artificially Thickened Fully Developed Turbulent Boundary Layers with Zero Pressure Gradient." NACA Rep. 1110.

Klineberg J. M. and Steger, J. L. 1974. "On Laminar Boundary-Layer Separation." AIAA Paper 74-94. Washington, D. C.

Klopfer, G. H. and Nixon, D. 1983. "Non-Isentropic Potential Formulation for Transonic Flows." AIAA Paper 83-0375. Reno, Nevada.

Kuhn, G. D. 1980. "Calculation of Separated Turbulent Flows on Axisymmetric Afterbodies Including Exhaust Plume Effects." AIAA J. 18, No. 3: 235-242.

Kwon, O. K. and Pletcher, R. H. 1979. "Prediction of Incompressible Separated Boundary Layers Including Viscous-Inviscid Interaction." J. Fluids Engineering 101: 466-472.

Kwon, O. K, and Pletcher, R. H. 1981. "Prediction of the Incompressible Flow over a Rearward-Facing Step." Technical Report HTL-26, CFD-4, ISU-ERI-82019. Engineering Research Institute, Iowa State University, Ames, Iowa.

Lax, P. D. 1954. "Weak Solutions of Nonlinear Hyperbolic Equations and their Numerical Computation." Comm. Pure Appl. Math. 7: 159-193.

Le Balleur, J. C. 1978. "Couplage Visqueux-Non Visqueux: Methode Numerique et Applications Aux Ecoulements Bidimensionnels Transsoniques et Supersoniques." La Recherche Aerospatiale No. 1978-2: 65-76.

Le Balleur, J. C. 1981a. "Calcul des Ecoulements a Forte Interaction Visqueuse au Moyen de Method de Couplage." AGARD CP-291, paper 1, Colorado Springs, Colorado.

Le Balleur, J. C. 1981b. "Strong Matching Method for Computing Transonic Viscous Flows Including Wakes and Separations, Lifting Airfoils." La Recherche Aerospatiale No. 1981-3 (English Edition): 21-45.

Le Balleur, J. C. 1984. "A Semi-Implicit and Unsteady Numerical Method of Viscous-Inviscid Interaction for Transonic Separated Flows." La Recherche Aerospatiale No. 1984-1 (English Edition): 15-37.

Lee, D. S. and Pletcher, R. H. 1985. "Application of a Viscous-Inviscid Interaction Method to Predict Transonic Separated Flows." Proc. 3rd Symposium on Numerical and Physical Aspects of Aerodynamic Flows, Long Beach, California.

Lee, S. C., and Van Dalsem, W. R. 1981. "Numerical Simulation of Steady Transonic Flow about Airfoils." AIAA Paper 81-1002. Palo Alto, California.

Lees, L. 1956. "Laminar Heat Transfer over Blunt-Nosed Bodies at Hypersonic Flight Speeds." Jet Propul. 26, No. 4: 259-269, 274.

Lees, L. and Reeves, B. L. 1964. "Supersonic Separated and Reattaching Laminar Flows: I. General Theory and Application to Adiabatic Boundary-Layer/Shock-Wave Interactions." AIAA J. 2, No. 11: 1907-1920.

Levy, L. L., Jr. 1978. "Experimental and Computational Steady and Unsteady Transonic Flows about a Thick Airfoil." AIAA J. 16, No. 6: 564-572.

Liepmann, H. W. 1946. "The Interaction between Boundary Layer and Shock Waves in Transonic Flow." J. Aeronautical Sciences 13, No. 12: 623-637.

Liepmann, H. W. and Roshko, A. 1957. Elements of Gas Dynamics. Wiley, New York.

Lighthill, M. J. 1958. "On Displacement Thickness." J. Fluid Mechanics 4, Part 4: 383-392.

Lock, R. C. 1981. "A Review of Methods for Predicting Viscous Effects on Aerofoils and Wings at Transonic Speeds." AGARD CP-291, Paper 2, Colorado Springs, Colorado.

Magnus, R. and Yoshihara, H. 1970. "Inviscid Transonic Flow over Airfoils." AIAA J. 8, No. 12: 2157-2162.

Maise, G. and McDonald, H. 1968. "Mixing Length and Kinematic Eddy Viscosity in a Compressible Boundary Layer." AIAA J. 6, No. 1: 73-80.

Mangler, W. 1948. "Zusammenhang Zwischen Ebenen und Rotationssymmetrischen Grenzschichten in Kompressiblen Flussigkeiten." Z. Angew. Math. Mech. 28: 97-103.

McDevitt, J. B., Levy, L. L., Jr., and Deiwert, G. S. 1976. "Transonic Flow about a Thick Circular-Arc Airfoil." AIAA J. 14, No. 5: 606-613.

McDonald, M. and Kreskovsky, J. P. 1974. "Effect of Free Stream Turbulence on the Turbulent Boundary Layer." Int. J. Heat Mass Transfer 17: 705-716.

Mehta, U. and Lomax, H. 1982. "Reynolds Averaged Navier-Stokes Computations of Transonic Flows - the State-of-the-Art." Progress in Astronautics and Aeronautics, Vol. 81, Transonic Aerodynamics (D. Nixon, ed.), AIAA, New York, pp.297-375.

Melnik, R. E. 1978. "Wake Curvature and Trailing Edge Interaction Effects in Viscous Flow over Airfoils." Advanced Technology Airfoil Research Conference, CP-2045.

Melnik, R. E. 1981. "Turbulent Interactions on Airfoils at Transonic Speeds-Recent Developments." AGARD CP-291, Paper 10, Colorado Springs, Colorado.

Melnik, R. E. and Brook, J. W. 1985. "The Computation of Viscid/Inviscid Interaction on Airfoils with Separated Flow." Proc. 3rd Symposium on Numerical and Physical Aspects of Aerodynamic Flows, Long Beach, California.

Melnik, R. E., Mead, H. R., and Jameson, A. 1983. "A Multi-Grid Method for the Computation of Viscid/Inviscid Interaction on Airfoils." AIAA Paper 83-0234. Reno, Nevada.

Moses, H. L., Jones, R. R. III., O'Brien, W. F., Jr., and Peterson, R. S. 1978. "Simultaneous Solution of the Boundary Layer and Freestream with Separated Flow." AIAA J. 16, No. 1: 61-66.

Murman, E. M. and Bussing, T. R. A. 1984. "On the Coupling of Boundary-Layer and Euler Equation Solutions." Numerical and Physical Aspects of Aerodynamic Flows II, (T. Cebeci, ed.), Springer-Verlag, New York, pp.313-325.

Murman, E. M. and Cole, J. D. 1971. "Calculation of Plane Steady Transonic Flows." AIAA J. 9, No. 1: 114-121.

Murphy, J. D. 1977. "An Efficient Numerical Method for Solving the Incompressible Navier-Stokes Equations." AIAA J. 15, No. 9: 1307-1314.

Murphy, J. D. and King, L. S. 1983. "Airfoil Flow-Field Calculations with Coupled Boundary-Layer Potential Codes." Proc. 2nd Symposium on Numerical and Physical Aspects of Aerodynamic Flows, Long Beach, California.

Nakamura, S. 1982. "Noniterative Grid Generation Using Parabolic Difference Equations for Fuselage-Wing Flow Calculations." Proc. 8th Int. Conf. Num. Methods Fluid Dyn. Aachen, W. Germany.

Newman, P. A. and South, J. C., Jr. 1976. "Conservative versus Nonconservative Differencing: Transonic Streamline Shape Effects." NASA TM X-72827.

Ng, K. H. and Spalding, D. B. 1972. "Turbulence Model for Boundary Layers Near Walls." Phys. Fluids 15, No. 1: 20-30.

Nixon, D. and Kerlick, G. D. 1982. "Potential Equation Methods for Transonic Flow Prediction." Progress in Astronautics and Aeronautics, Vol. 81, Transonic Aerodynamics, (D. Nixon, ed.), AIAA, New York, pp.239-296.

Page, R. H. 1961. "A Theory for Incipient Separation." Developments in Mechanics 1, (J. E. Lay and L. E. Malvern, ed.), Plenum Press, New York, pp.563-577.

Patankar, S. V. and Spalding, D. B. 1967. Heat and Mass Transfer in Boundary Layers. Morgam-Grampiar Press, London.

Peaceman, D. W. and Rachford, H. H. 1955. "The Numerical Solution of Parabolic and Elliptic Differential Equations." J. Soc. Ind. Appl. Math. 3: 28-41.

Pearcey, H. H., Osborne, J., and Haines, A. B. 1968. "The Interaction between Local Effects at the Shock and Rear Separation - a Source of Significant Scale Effects in Wind-Tunnel Tests on Aerofoils and Wings." AGARD CP-35, Part II.

Perry, A. E. and Schofield, W. H. 1973. "Mean Velocity and Shear Stress Distributions in Turbulent Boundary Layers." Phys. Fluids 16, No. 12: 2068-2081.

Pletcher, R. H. 1976. "Prediction of Turbulent Boundary Layers at Low Reynolds Numbers." AIAA J. 14, No. 5: 696-698.

Pletcher, R. H. 1978. "Prediction of Incompressible Turbulent Separating Flow." J. Fluids Engineering 100: 427-433.

Prandtl, L. 1926. "Ueber die Ausgebildete Turbulenz." Proc. 2nd Int. Cong. Appl. Mech. Zurich: 62-74.

Prandtl, L. 1938. "Zur Berechnung der Grenzschichten." Z. Angew. Math. Mech. 18: 77-82.

Presz, W. M., Jr. 1974. "Turbulent Boundary Layer Separation of Axisymmetric Afterbodies." Ph.D. Thesis, University of Connecticut.

Presz, W. M., Jr., King, R. W., and Buteau, J. D. 1978. "An Improved Analytical Model of the Separated Region on Boattail Nozzles at Subsonic Speeds." NASA CR-3028.

Probstein, R. F. and Elliott, D. 1956. "The Transverse Curvature Effect in Compressible Axially Symmetric Laminar Boundary-Layer Flow." J. Aeronautical Sciences 23, No.½: 208-224.

Pulliam, T. H. and Steger, J. L. 1980. "Implicit Finite-Difference Simulations of Three-Dimensional Compressible Flow." AIAA J. 18, No. 2: 159-167.

Reshotko, E. and Tucker, M. 1957. "Approximate Calculation of the Compressible Turbulent Boundary Layer with Heat Transfer and Arbitrary Pressure Gradient." NACA TN-4154.

Reubush, D. E. 1974. "Experimental Study of the Effectiveness of Cylindrical Plume Simulators for Predicting Jet-On Boattail Drag at Mach Numbers up to 1.30." NASA TN D-7795.

Reubush, D. E. and Putnam, L. E. 1976. "An Experimental and Analytical Investigation of the Effect on Isolated Boattail Drag of Varying Reynolds Number." NASA TN D-8210.

Reyhner, T. A. 1968. "Finite-Difference Solution of the Compressible Turbulent Boundary Layer Equations." Proc. Computation of Turbulent Boundary Layer, AFOSR-IFP-Stanford Conference, Vol. 1, Palo Alto, California, pp.375-383.

Reyhner, T. A. and Flugge-Lotz, I. 1968. "The Interaction of a Shock Wave with a Laminar Boundary Layer." Int. J. Non-Linear Mechanics 3, No. 2: 173-199.

Reynolds, A. J. 1974. Turbulent Flows in Engineering. Wiley, New York.

Roberts, G. O. 1971. "Computational Meshes for Boundary Layer Problems." Proc. 2nd Int. Conf. Num. Methods Fluid Dyn. Lecture Notes in Physics. Vol. 8. Springer-Verlag, New York, pp.171-177.

Rotta, J. 1951. "Statistische Theorie Nichthomogener Turbulenz." Z. Phys. 129: 547-572.

Rudman, S. and Rubin, S. G. 1968. "Hypersonic Viscous Flow over Slender Bodies with Sharp Leading Edges." AIAA J. 6, No. 10: 1883-1890.

Sahu, J. and Danberg, J. E. 1985. "Navier-Stokes Computations of Axisymmetric Transonic Flows with a Two-Equation Model of Turbulence." AIAA Paper 85-0373. Reno, Nevada.

Seddon, J. 1960. "The Flow Produced by Interaction of a Turbulent Boundary Layer with a Normal Shock Wave of Strength Sufficient to Cause Separation." ARC RM No. 3502.

Seegmiller, H. L., Marvin, J. G., and Levy, L. L., Jr. 1978. "Steady and Unsteady Transonic Flow." AIAA J. 16, No. 12: 1262-1270.

Shang, J. S. and Hankey, W. L., Jr. 1975. "Numerical Solution for Supersonic Turbulent Flow over a Compression Ramp." AIAA J. 13, No. 10: 1368-1374. (see also "Supersonic Turbulent Separated Flows Utilizing the Navier-Stokes Equations." AGARD CP-168, Paper 23.)

Shang, J. S., Hankey, W. L., Jr., and Herbert, L. C. 1976. "Numerical Simulation of Shock Wave-Turbulent Boundary Layer Interaction." AIAA Paper 76-95. San Diego, California.

Shrewsbury, G. D. 1968. "Effect of Boattail Juncture Shape on Pressure Drag Coefficients of Isolated Afterbodies." NASA TM X-1517.

Simpson, R. L. 1979. "A Review of Some Phenomena in Turbulent Flow Separation." Proc. Turbulent Boundary Layers - 1979 the Joint ASME-CSME Applied Mechanics, Fluid Engineering and Bioengineering Conference, pp.1-14.

Simpson, R. L., Strickland, J. H., and Barr, P. W. 1974. "Laser and Hot-Film Anemometer Measurements in a Separating Turbulent Boundary Layer." Thermal and Fluid Center, Southern Methodist University, TR WT-3.

Simpson, R. L., Strickland, J. H., and Barr, P. W. 1977. "Features of a Separating Turbulent Boundary Layer in the Vicinity of Separation." J. Fluid Mechanics 79, Part 3: 553-594.

South, J. C., Jr. 1985. "A Historical Perspective and Overview of Computational Transonics." Recent Advances in Numerical Methods in Fluids, Vol. 4, Advances in Computational Transonics, (W. G. Habashi, ed.), Pineridge, Swansea, pp.1-20.

South, J. C., Jr. and Jameson, A. 1973. "Relaxation Solutions for Inviscid Axisymmetric Transonic Flow over Blunt or Pointed Bodies." Proc. AIAA Computational Fluid Dynamics Conference, Palm Spring, California, pp.8-17.

Spreiter, J. R. 1982. "Transonic Aerodynamics - History and Statement of Problem." Progress in Astronautics and Aeronautics, Vol. 81, Transonic Aerodynamics, (D. Nixon, ed.), AIAA, New York, pp.3-79.

Steger, J. L. and Baldwin, B. S. 1972. "Shock Waves and Drag in the Numerical Calculation of Isentropic Transonic Flow." NASA TN D-6997.

Steger, J. L. and Lomax, H. 1972. "Numerical Calculation of Transonic Flow about Two-Dimensional Airfoils by Relaxation Procedures." AIAA J. 10, No. 1: 49-54.

Steger, J. L. and Sorenson, R. L. 1980. "Use of Hyperbolic Partial Differential Equations to Generate Body Fitted Coordinates." Numerical Grid Generation Techniques, NASA CP-2166, pp.463-478.

Swanson, R. C. 1980. "Numerical Solutions of the Navier-Stokes Equations for Transonic Afterbody Flows." NASA TP-1784.

Swanson, R. C., Rubin, S. G., and Khosla, P. K. 1983. "Calculation of Afterbody Flows with Composite Velocity Formulation." AIAA Paper 83-1736. Danvers, Massachusetts.

Thompson, J. F., Thames, F. C., and Mastin, C. W. 1974. "Automatic Numerical Generation of Body-Fitted Curvilinear Coordinate System for Field Containing Any Number of Arbitrary Two-Dimensional Bodies." J. Computational Physics 15: 299-319.

Thompson, J. F., Thames, F. C., and Mastin, C. W. 1977. "TOMCAT-A Code for Numerical Generation of Boundary-Fitted Curvilinear Coordinate Systems on Fields Containing Any Number of Arbitrary Two-Dimensional Bodies." J. Computational Physics 24: 274-302.

Thompson, J. F., Warsi, U. A., and Mastin, C. W. 1982. "Boundary-Fitted Coordinate Systems for Numerical Solution of Partial Differential Equations-A Review." J. Computational Physics 47: 1-108.

Townsend, A. A. 1976. The Structure of Turbulent Shear Flow. Cambridge University Press, Cambridge.

Van Dalsem, W. R. and Steger, J. L. 1983. "Finite-Difference Simulation of Transonic Separated Flow Using a Full Potential-Boundary Layer Interaction Approach." AIAA Paper 83-1689. Danvers, Massachusetts.

Van Driest, E. R. 1951. "Turbulent Boundary Layer in Compressible Fluids." J. Aeronautical Sciences 18, No. 3: 145-160.

Van Driest, E. R. 1956. "On Turbulent Flow Near a Wall." J. Aeronautical Sciences 23, No. 11: 1007-1011.

Veldman, A. E. P. 1979. "A Numerical Method for the Calculation of Laminar, Incompressible Boundary Layers with Strong Viscous-Inviscid Interaction." National Aerospace Laboratory, NLR TR 79023 U.

Veldman, A. E. P. 1981. "New, Quasi-Simultaneous Method to Calculate Interacting Boundary Layers." AIAA J. 19, No. 1: 79-85.

Veldman, A. E. P. and Lindhout, J. P. F. 1983. "A Quasi-Simultaneous Calculation Method for Strongly Interacting Viscous FLow around an Infinite Swept Wing." Proc. 2nd Symposium on Numerical and Physical Aspects of Aerodynamic Flow, Long Beach, California.

Viegas, J. R. and Coakley, T. J. 1978. "Numerical Investigation of Turbulence Models for Shock Separated Boundary-Layer Flows." AIAA J. 16, No. 4: 293-294.

Viegas, J. R. and Horstman, C. C. 1979. "Comparison of Multiequation Turbulence Models for Several Shock Boundary-Layer Interaction Flows." AIAA J. 17, No. 8: 811-820.

Viegas, J. R. and Rubesin, M. W. 1983. "Wall-Function Boundary Conditions in the Solution of the Navier-Stokes Equations for Complex Compressible Flows." AIAA Paper 83-1694. Danvers, Massachusetts.

Viviand, H. 1974. "Conservative Forms of Gas Dynamic Equations." La Recherche Aerospatiale No. 1974-1: 65-68.

Wai, J. C. and Yoshihara, H. 1981. "Planar Transonic Airfoil Computations with Viscous Interactions." AGARD CP-291, Paper 9, Colorado Springs, Colorado.

Werle, M. J. and Verdon, J. M. 1980. "Viscid/Inviscid Interaction for Symmetric Trailing Edges." Technical Report. Naval Air Systems Command Contract N00019-78-C0604.

White, F. M. 1974. Viscous Fluid Flow. McGraw-Hill, New York.

Whitfield, D. L., Swafford, T. W., and Jacocks, J. L. 1981. "Calculation of Turbulent Boundary Layers with Separation and Viscous-Inviscid Interaction." AIAA J. 19, No. 10: 1315-1322.

Wigton, L. B. and Holt, M. 1981. "Viscous-Inviscid Interaction in Transonic Flow." AIAA Paper 81-1003. Palo Alto, California.

Wilcox, D. C. and Rubesin, M. W. 1980. "Progress in Turbulence Modeling for Complex Flow Fields Including Effects of Compressibility." NASA TP-1517.

Williams, P. G. 1975. "A Reverse Flow Computation in the Theory of Self-Induced Separation." Lecture Notes in Physics. Vol. 35. Springer-Verlag, New York, pp.445-451.

Wilmoth, R. G. 1977. "Computation of Transonic Boattail Flow with Separation." NASA TP-1070.

Yanenko, N. N. 1971. The Method of Fractional Steps. Springer-Verlag, New York.

Yoshihara, H. and Spee, B. M. 1982. "Applied Computational Transonic Aerodynamics." AGARD AG-226.

Young, D. 1954. "Iterative Methods for Solving Partial Difference Equations of Elliptic Type." Trans. Amer. Math. Soc. 76: 92-111.

VIII. ACKNOWLEDGMENTS

This material was based upon work supported by the National Aeronautics and Space Administration Ames Research Center under Grant NAG-2-152 and the Engineering Research Institute at Iowa State University.

The authors wish to express their appreciation to Terry L. Holst, Dennis A. Johnson, and John D. Murphy of NASA Ames Research Center for their interest, suggestions, and cooperation.

IX. APPENDIX A: COEFFICIENTS IN THE FINITE-DIFFERENCE REPRESENTATIONS OF THE CONTINUITY AND MOMENTUM EQUATIONS

The coefficients in the finite-difference representation of the continuity equation, given by Equation (2.114), are

$$a_j = \frac{1}{2}\,\Delta\eta_-\tilde{g}$$

$$d_j = b_j$$

$$h_j = 0$$

$$s_j = -\frac{1}{2}\,\Delta\eta_-(\tilde{F}_j + \tilde{F}_{j-1})$$

$$c_j = -\tilde{g}s_j$$

When the FLARE approximation is used, the coefficients of the finite-difference representation of the momentum equation, given by Equation (2.115), are

$$A_j = \frac{1}{\Delta\eta_-(K+1)}\left[\frac{\tilde{g}}{K\Delta\xi_-}(\psi_j^{i-1} - \tilde{\psi}_j) - \frac{2}{\Delta\eta_+}N_{j+\frac{1}{2}}\right]$$

$$B_j = \frac{1}{\Delta\eta_-(K+1)}\left[K\frac{\tilde{g}}{\Delta\xi_-}(\tilde{\psi}_j - \psi_j^{i-1}) - \frac{2}{\Delta\eta_-}N_{j-\frac{1}{2}}\right]$$

$$C_j = \frac{C}{\Delta\xi_-}\tilde{g}^2\tilde{F}_j(3\tilde{F}_j - 2F_j^{i-1}) + 2\tilde{g}^2\tilde{\beta}(2\tilde{F}_j^{\,2} - \tilde{G}_j)$$

$$- \frac{\tilde{g}^2}{\Delta\eta_-(K+1)\Delta\xi_-}(2\tilde{\psi}_j - \psi_j^{i-1})\left[\frac{1}{K}(\tilde{F}_{j+1} - \tilde{F}_j) + K(\tilde{F}_j - \tilde{F}_{j-1})\right]$$

$$D_j = -(A_j + B_j) + \frac{C}{\Delta\xi_-}\tilde{g}^2(2\tilde{F}_j - F_j^{i-1}) + 2\tilde{g}^2\tilde{\beta}\tilde{F}_j$$

$$E_j = \frac{-\tilde{g}}{\Delta\eta_-(K+1)\Delta\xi_-}[\frac{1}{K}(\tilde{F}_{j+1} - \tilde{F}_j) + K(\tilde{F}_j - \tilde{F}_{j-1})]$$

$$H_j = \tilde{g}^2(\tilde{G}_j - \tilde{F}_j^2)$$

$$S_j = \frac{1}{\Delta\eta_-(K+1)\Delta\xi_-}(\tilde{\psi}_j - \psi_j^{i-1})[\frac{1}{K}(\tilde{F}_{j+1} - \tilde{F}_j) + K(\tilde{F}_j - \tilde{F}_{j-1})]$$

$$+ \frac{2C}{\Delta\xi_-}\tilde{g}\tilde{F}_j(F_j^{i-1} - \tilde{F}_j) + 2\tilde{g}\tilde{\beta}(\tilde{G}_j - \tilde{F}_j^2)$$

When the windward differencing is used, the coefficients of the finite-difference representation of the momentum equation, given by Equation (2.115), are

$$A_j = \frac{1}{\Delta\eta_-(K+1)}[\frac{\tilde{g}}{K\Delta\xi_+}(\tilde{\psi}_j - \psi_j^{i+1}) - \frac{2}{\Delta\eta_+}N_{j+\frac{1}{2}}]$$

$$B_j = \frac{1}{\Delta\eta_-(K+1)}[K\frac{\tilde{g}}{\Delta\xi_+}(\psi_j^{i+1} - \tilde{\psi}_j) - \frac{2}{\Delta\eta_-}N_{j-\frac{1}{2}}]$$

$$C_j = \frac{1}{\Delta\xi_+}\tilde{g}^2\tilde{F}_j(2F_j^{i+1} - 3\tilde{F}_j) + 2\tilde{g}^2\tilde{\beta}(2\tilde{F}_j^2 - \tilde{G}_j)$$

$$+ \frac{\tilde{g}^2}{\Delta\eta_-(K+1)\Delta\xi_+}(2\tilde{\psi}_j - \psi_j^{i+1})[\frac{1}{K}(\tilde{F}_{j+1} - \tilde{F}_j) + K(\tilde{F}_j - \tilde{F}_{j-1})]$$

$$D_j = -(A_j + B_j) - \frac{1}{\Delta\xi_+}\tilde{g}^2(2\tilde{F}_j - F_j^{i+1}) + 2\tilde{g}^2\tilde{\beta}\tilde{F}_j$$

$$E_j = \frac{\tilde{g}}{\Delta\eta_-(K+1)\Delta\xi_+}[\frac{1}{K}(\tilde{F}_{j+1} - \tilde{F}_j) + K(\tilde{F}_j - \tilde{F}_{j-1})]$$

$$H_j = \tilde{g}^2(\tilde{G}_j - \tilde{F}_j^2)$$

$$S_j = \frac{1}{\Delta\eta_-(K+1)\Delta\xi_+}(\psi_j^{i+1} - \tilde{\psi}_j)[\frac{1}{K}(\tilde{F}_{j+1} - \tilde{F}_j) + K(\tilde{F}_j - \tilde{F}_{j-1})]$$

$$- \frac{2}{\Delta\xi_+}\tilde{g}\tilde{F}_j(F_j^{i+1} - \tilde{F}_j) + 2\tilde{g}\tilde{\beta}(\tilde{G}_j - \tilde{F}_j^2)$$

Note that the provisional values with tilde (~) are always evaluated at ith streamwise station.

X. APPENDIX B: COEFFICIENTS IN THE FINITE-DIFFERENCE REPRESENTATION OF THE ENERGY EQUATION

When the FLARE approximation is used, the coefficients in the finite-difference representation of the energy equation, given by Equation (2.122), are

$$A_j = \frac{1}{\Delta\eta_-(K+1)}\left[\frac{g}{K\Delta\xi_-}(\psi_j^{i-1} - \psi_j^i) - \frac{2}{\Delta\eta_+}N_{1,j+\frac{1}{2}}\right]$$

$$B_j = \frac{1}{\Delta\eta_-(K+1)}\left[K\frac{g}{\Delta\xi_-}(\psi_j^{i} - \psi_j^{i-1}) - \frac{2}{\Delta\eta_-}N_{1,j-\frac{1}{2}}\right]$$

$$C_j = \frac{C}{\Delta\xi_-}g^2F_j^iG_j^{i-1} + \frac{2}{\Delta\eta_-(K+1)}(N_{2,j+\frac{1}{2}} - N_{2,j-\frac{1}{2}})$$

$$D_j = -(A_j + B_j) + \frac{C}{\Delta\xi_-}g^2F_j^i$$

When the windward differencing is used, the coefficients in the finite-difference representation of the energy equation, given by Equation (2.122), are

$$A_j = \frac{1}{\Delta\eta_-(K+1)}\left[\frac{g}{K\Delta\xi_+}(\psi_j^{i} - \psi_j^{i+1}) - \frac{2}{\Delta\eta_+}N_{1,j+\frac{1}{2}}\right]$$

$$B_j = \frac{1}{\Delta\eta_-(K+1)}\left[K\frac{g}{\Delta\xi_+}(\psi_j^{i+1} - \psi_j^{i}) - \frac{2}{\Delta\eta_-}N_{1,j-\frac{1}{2}}\right]$$

$$C_j = -\frac{1}{\Delta\xi_+}g^2F_j^iG_j^{i+1} + \frac{2}{\Delta\eta_-(K+1)}(N_{2,j+\frac{1}{2}} - N_{2,j-\frac{1}{2}})$$

$$D_j = -(A_j + B_j) - \frac{1}{\Delta\xi_+}g^2F_j^i$$

XI. APPENDIX C: RESULTING COEFFICIENTS BY THE USE OF THE MODIFIED THOMAS ALGORITHM

A system of block tridiagonal equations, Equation (2.129), is reduced to a set of bidiagonal equations, Equations (2.131) and (2.132), by using the modified Thomas algorithm. The coefficients for $2 \leq j \leq NJ$ in Equations (2.131) and (2.132) are given as

$$A_j^* = -\frac{A_j}{Q_2}$$

$$C_j^* = \frac{1}{Q_2}[C_j - C_{j-1}^*(B_j + E_j b_j) + E_j(c_j - c_{j-1}^*)]$$

$$H_j^* = \frac{1}{Q_2}[H_j - H_{j-1}^*(B_j + E_j b_j) + E_j(h_j - h_{j-1}^*)]$$

$$S_j^* = \frac{1}{Q_2}[S_j - S_{j-1}^*(B_j + E_j b_j) + E_j(s_j - s_{j-1}^*)]$$

$$a_j^* = A_j^* Q_1$$

$$c_j^* = C_j^* Q_1 + C_{j-1}^* b_j - c_j + c_{j-1}^*$$

$$h_j^* = H_j^* Q_1 + H_{j-1}^* b_j - h_j + h_{j-1}^*$$

$$s_j^* = S_j^* Q_1 + S_{j-1}^* b_j - s_j + s_{j-1}^*$$

$$Q_1 = d_j + A_{j-1}^* b_j + a_{j-1}^*$$

$$Q_2 = D_j + A_{j-1}^* B_j + E_j Q_1$$

The corresponding values at $j = 1$ are given by Equation (2.133).

XII. APPENDIX D: TRANSFORMATION FORMULAS USED FOR THE BOUNDARY CONDITIONS IN THE NUMERICAL GRID GENERATION

The solution procedure for the numerical grid generation was presented in Section III. C. It required a Dirichlet type boundary condition at all boundaries of the computational domain. In the streamwise direction along the body surface, the grid points are controlled by the transformation formula suggested by Roberts (1971).

$$x = x_c \{1 + \frac{\sinh[\alpha_1(\xi/\xi_{max} - \alpha_2)]}{\sinh(\alpha_1\alpha_2)}\}$$

where

$$\alpha_2 = \frac{1}{2\alpha_1} \ln[\frac{1 + (e^{\alpha_1} - 1)x_c}{1 + (e^{-\alpha_1} + 1)x_c}]$$

$$0 < \alpha_1 < \infty$$

More points are clustered near x_c as the stretching parameter α_1 becomes larger. Values of α_1 closer to zero result in the grid distribution being close to the equal spacing. The typical value of α_1 was between 2 and 5. At the outer boundary, the grid spacing was set uniform.

In the normal direction, grid points were concentrated toward the wall by the use of an exponential stretching type transformation given as

$$r = r_o + \frac{(\alpha_3 + 1) - (\alpha_3 - 1)\left(\frac{\alpha_3 + 1}{\alpha_3 - 1}\right)^{1-\frac{\eta}{\eta_{max}}}}{\left(\frac{\alpha_3 + 1}{\alpha_3 - 1}\right)^{1-\frac{\eta}{\eta_{max}}} + 1}$$

$$1 < \alpha_3 < \infty$$

This stretching transformation clusters more points near $r = r_o$ as the stretching parameter α_3 approaches unity. A value of α_3 much larger than 1 produces a mesh with approximately uniform spacing. In this study, the typical value ranged from 1.05 to 1.1.

XII. APPENDIX E: COEFFICIENTS IN THE FINITE-DIFFERENCE REPRESENTATIONS USED IN THE NUMERICAL GRID GENERATION

The Laplace equation which is used to define the coordinate transformation is discretized by using a second-order-accurate central differencing scheme. The finite-difference representation of the Laplace equation in the ADI scheme constructs two sets of tridiagonal matrix equations for x and r, Equations (3.41) and (3.42). Since the coefficients for x and r are almost identical, only the coefficients for x are described explicitly.

By rearranging the coefficients of the unknown variables, Equations (3.41) and (3.42) can be rewritten as

step 1

$$BX_i f^n_{i-1,j} + DX_i f^n_{i,j} + AX_i f^n_{i+1,j} = CX_i \tag{12.1}$$

step 2

$$BY_j C^n_{i,j-1} + DY_j C^n_{i,j} + AY_j C^n_{i,j+1} = CY_j \tag{12.2}$$

where

$$C^n_{i,j} = x^{n+1}_{i,j} - x^n_{i,j} \tag{12.3}$$

The coefficients in Equations (12.1) and (12.2) for $2 \le i \le NI-1$ and $2 \le j \le NJ-1$ are

$$AX_i = BX_i = -A^n_{i,j}$$

$$DX_i = \alpha + 2A^n_{i,j}$$

$$CX_i = \alpha\omega Lx^n_{i,j}$$

$$AY_j = BY_j = -C^n_{i,j}$$

$$DY_j = \alpha + 2C^n_{i,j}$$

$$CY_j = f^n_{i,j}$$

At the surrounding boundaries of the computational domain, the Dirichlet boundary condition is prescribed. Therefore, the coefficients in Equations (12.1) and (12.2) at the boundaries are

$$AX_1 = BX_1 = CX_1 = AX_{NI} = BX_{NI} = CX_{NI} = 0$$

$$DX_1 = DX_{NI} = 1.0$$

$$AY_1 = BY_1 = CY_1 = AY_{NJ} = BY_{NJ} = CY_{NJ} = 0$$

$$DY_1 = DY_{NJ} = 1.0$$

In the above expressions, $\Delta\xi$ and $\Delta\eta$ are omitted because $\Delta\xi = \Delta\eta = 1.0$ everywhere. The coefficients in the matrix equation for r is easily obtained by simply replacing the $f^n_{i,j}$ and x with $g^n_{i,j}$ and r, respectively, from the expressions for the above coefficients.

XIII. APPENDIX F: COEFFICIENTS IN THE FINITE-DIFFERENCE REPRESENTATION OF THE POTENTIAL EQUATION OBTAINED BY THE SLOR SCHEME

The resulting coefficients in the tridiagonal matrix equations, Equation (3.81), obtained from the full potential equation by using the SLOR scheme are given as follows.

For $2 \le j \le NJ-1$ at ith streamwise station,

$$A_j = - [A2_{i,j} \overleftarrow{\delta}_\xi (\tilde{\rho} r)_{i+\frac{1}{2}} + R_j]$$

$$B_j = A2_{i,j} \overleftarrow{\delta}_\xi (\tilde{\rho} r)_{i+\frac{1}{2}} - R_{j-1}$$

$$D_j = R_i + R_{i-1} + R_j + R_{j-1}$$

$$E_j = b_j C^n_{i-1,j-1} + d_j C^n_{i-1,j} + a_j C^n_{i-1,j+1} + \omega L\phi^n_{i,j}$$

$$a_j = - \omega[(\tilde{\rho} r)_{i-\frac{1}{2},j} A2_{i-1,j} + (\bar{\rho} r)_{i,j+\frac{1}{2}} A2_{i,j+1}]$$

$$b_j = \omega[(\tilde{\rho} r)_{i-\frac{1}{2},j} A2_{i-1,j} + (\bar{\rho} r)_{i,j-\frac{1}{2}} A2_{i,j-1}]$$

$$d_j = \omega[R_{i-1} - A2_{i,j} \overleftarrow{\delta}_\eta (\bar{\rho} r)_{i,j+\frac{1}{2}}]$$

where

$$A2_{i,j} = \frac{1}{4} \left(\frac{A_2}{J}\right)_{i,j} \tag{13.1}$$

and R_i and R_j are given by Equation (3.79).

At the outer boundary, j = NJ, the potential is fixed by the freestream value. Therefore, $C^n_{i,NJ} = 0$. The corresponding coefficients are given as

$$A_{NJ} = B_{NJ} = E_{NJ} = 0$$

$$D_{NJ} = 1.0$$

At the wall surface, j = 1, the transpiration velocity boundary condition is prescribed. The resulting coefficients are

$$A_1 = - \theta_r R_1$$

$$B_1 = 0$$

$$D_1 = A4_i + A4_{i-1} + \theta_r R_1$$

$$E_1 = d_1 C^n_{i-1,1} + a_1 C^n_{i-1,2} + \omega L\phi^n_{i,1}$$

$$a_1 = - \omega\theta_r (\bar{\rho}r)_{i,1+\frac{1}{2}} A2_{1,2}$$

$$d_1 = \omega[A4_{i-1} - \theta_r (\bar{\rho}r)_{i,1+\frac{1}{2}} A2_{i,1}]$$

where

$$A4_i = \left[(\bar{\rho}r)\left(\frac{A_1}{J} - \frac{A_2^2}{A_3 J}\right)\right]_{i+\frac{1}{2},1} \tag{13.2}$$

$$\theta_r = 1 + \frac{r_{i,1-\frac{1}{2}}}{r_{i,1+\frac{1}{2}}} \tag{13.3}$$

A closer look at $L\phi^n_{i,1}$ reveals the new relation between E_1 and $dm^*/d\xi$ as follows.

$$E_1 = e_0 + e_1\left(\frac{dm^*}{d\xi}\right)_{i-\frac{1}{2}} + e_2\left(\frac{dm^*}{d\xi}\right)_i + e_3\left(\frac{dm^*}{d\xi}\right)_{i+\frac{1}{2}} \tag{13.4}$$

where

$$e_0 = d_1 C^n_{i-1,1} + a_1 C^n_{i-1,2}$$

$$+\omega[\overleftarrow{\delta}_\xi A4_i \overrightarrow{\delta}_\xi + \theta_r(\bar{\rho}r)_{i,1+\frac{1}{2}}(1 + E^{+1}_\eta)\delta_\xi + \theta_r R_1 \overrightarrow{\delta}_\eta]\ \phi^n_{i,1}$$

$$e_1 = -\ \omega A5_{i-1}(\frac{\tilde{\rho}}{\rho})_{i-\frac{1}{2},1}$$

$$e_2 = -\ 2\omega\ \frac{r_{i,1-\frac{1}{2}}}{r_{i,1}}(\frac{\bar{\rho}}{\rho})_{i,1}$$

$$e_3 = \omega A5_i(\frac{\tilde{\rho}}{\rho})_{i+\frac{1}{2},1}$$

and

$$A5_i = (\frac{A_2}{A_3})_{i+\frac{1}{2},1} \tag{13.5}$$

By eliminating the upper diagonal terms using a standard Thomas algorithm, Equation (3.81) becomes the bidiagonal recurrence relationships, given by Equation (3.82). The coefficients of Equation (3.82) are given as

$$p_j = E^*_j\ /\ D^*_j$$

$$q_j = -\ B_j\ /\ D^*_j$$

$$D^*_j = D_j - A_j B_{j+1}\ /\ D^*_{j+1}$$

$$E^*_j = E_j - A_j E^*_{j+1}\ /\ D^*_{j+1}$$

As given by Equation (3.83), the coefficient p_1 can be more specific in terms of $dm^*/d\xi$ using the relation given by Equation (13.4). The coefficients of Equation (3.83) are then given as

$$p_{10} = [e_0 - A_1 E_2^* / D_2^*] / D_1^*$$

$$p_{11} = e_1 / D_1^* \qquad p_{12} = e_2 / D_1^* \qquad p_{13} = e_3 / D_1^*$$

XIV. APPENDIX G: COEFFICIENTS IN THE FINITE-DIFFERENCE REPRESENTATION OF THE POTENTIAL EQUATION OBTAINED BY THE AF2 SCHEME

The AF2 scheme consists of a two-step procedure. When the main flow direction is along the positive ξ direction, coefficients in Equations (3.88) and (3.89) are given as

$$b_j = -R_{j-1}$$

$$d_j = (\alpha + R_j)$$

$$e_j = \alpha\omega L\phi^n_{i,j}$$

$$A_i = -R_i$$

$$B_i = -(\alpha\lambda + R_{i-1})$$

$$D_i = \alpha + \alpha\lambda + R_i + R_{i-1}$$

$$E_i = f^n_{i,j} + \alpha C^n_{i,j+1}$$

When the flow is in the negative ξ direction, A_i and B_i change based on the windward differencing scheme. In such a case,

$$A_j = -(\alpha\lambda + R_i)$$

$$B_j = -R_{i-1}$$

END DATE

JAN. 9, 1987